TABLE OF CONTENTS

Page

LIST OF TABLES

LIST OF FIGURES

LIST OF ABREVIATIONS

DRV	Dynamic Recovery
DRX	Dynamic Recrystallization
DT	Dynamic Transformation
MDRX	Metadynamic Recrystallization
T_m	Melting Point in ˚C
BCC	Body Centered Cubic
FCC	Face Centered Cubic
BCT	Body Centered Tetragonal
SFE	Stacking Fault Energy
HAGB	High Angle Grain Boundary
LAGB	Low Angle Grain Boundary
EBSD	Electron Back Scattered Diffraction
G.S.	Grain Size
TMCP	Thermomechanical Controlled Processing
FEM	Finite Element Modeling
R	Correlation coefficient
ARRE	Average absolute relative error
KAM	Kernel average misorientation
FEG-SEM	Field Emission Gun-Scanning Electron Microscope
GB	Grain Boundary
PAGB	Prior austenite grain boundaries

LIST OF SYMBOLS

Symbol	Description	Unit
γ	Austenite	
α	Ferrite	
δ	Delta Ferrite	
T	Temperature	˚C
$\dot{\varepsilon}$	Strain Rate	s^{-1}
ε	Strain	
σ	Stress	MPa
A, m_1, m_2, m_3, m_4, m_5, m_6, m_7, m_8, m_9	Parameters of the Hansel-Spittel equation	
ΔT	Change in temperature	
$\int \sigma d\varepsilon$	Area under the uncorrected stress- strain curve	
ρ	Density	Kg/m^3
C_p	Specific heat	J/Kg/°K
Z	Zener – Hollomon parameter	
Q	Activation energy	$KJmol^{-1}$
R	Universal gas constant	$8.314Jmol^{-1}K^{-1}$
A, n_1, n, α, β	Arrhenius Equation Material Constants	
Δ	Absolute average error	
σ_E	Experimental flow stress	MPa
σ_P	Predicted flow stress	MPa
$\bar{\sigma}_E$	Average values of experimental flow stress	
$\bar{\sigma}_P$	Average values of predicted flow stress	
σ_m	Flow stress at the end point in the first hit deformation	MPa
σ_1	The offset yield flow stress for the first hit	MPa
σ_2	The offset yield flow stress for the second hit	MPa
$\boldsymbol{X_m}$	Metadynamic softening fraction	%
t	Interpass time	s
n	Material dependent constant	
$t_{0.5}$	Time for metadynamic softening fraction of 50%	s
θ	Strain hardening rate	
D_{eff}	Effective diffusion	
D_L	Lattice diffusion coefficients	$\frac{m^2}{s}$
D_P	Pipe diffusion coefficients	$\frac{m^2}{s}$
f_L	Fraction of atoms participating in the lattice diffusion processes	
f_p	Fraction of atoms participating in the pipe	

	diffusion processes	
μ	Shear modulus	MPa
b	Burgers vector	m
K	Bulk Modulus	MPa
$\frac{d\mu}{d\sigma_s}$	Pressure Dependence	
$\frac{T_M dK}{K_0 dT}$	Temperature Dependence	
V_p^*	Activation Volume	$\frac{m^3}{mole}$
$a_p D_{0p}$	Pre-Exponential of pipe diffusion,	$\frac{m^4}{s}$
Q_{p0}	Activation energy of pipe diffusion	$\frac{KJ}{mole}$
D_{0L}	Pre-exponential of lattice diffusion for Carbon	$\frac{m^2}{s}$

INTRODUCTION

During the last 30 years a large number of structural components such as bumpers, dashboards, rear doors, etc. have been produced using plastic injection or plastic extrusion technologies. Metallic dies, made of high strength steels are generally used to fabricate molds and die (Lin, Chen et Zhong, 2008e). In recent years there has been a continuous demand for larger components by the transport industry and as a result, larger and larger dies need to be produced. The die manufacturing starts with casting process where liquid metal is transformed into an ingot. During the casting process, there is temperature gradient between the liquid metal and the mold which leads to the formation of inhomogeneities in the microstructure such as chill zone, columnar zone and equiaxed zone. In addition to it, when the metal solidifies in the mold, segregation of the alloying elements occurs which leads to lower or higher concentration of elements. The segregation occurs usually at the center and top regions of the ingot. These imperfections become more significant when manufacturing larger dies and molds for which, even larger cast ingots must be produced. With the increase in the size of ingot, there is also an increase in inhomogeneity of microstructure (as-cast structure) and chemical composition (segregation) (Moore et Shah, 1983). The presence of these inhomogeneities leads to low workability of the cast ingot structure. Improper selection of deformation parameter can lead to initiation of cracks along the grain boundaries. In order to break these inhomogeneities, ingot breakdown process is done, in which, the ingot is deformed by repetitive blows at temperatures around 0.75 of the melting point. Deformation at lower temperatures may lead to precipitation of the alloying elements which tend to pin the dislocations, thereby causing grain boundary failure. On the other hand, deformation at temperatures near to the melting point may cause local melting and grain boundary cracking. The local melting may further be promoted at higher strain rates due to deformation heating. Therefore, as-cast structures have a short window of workability and accurate parameters are necessary in order to deform them to wrought structure components.

During hot working of metals specifically, steels, various dynamic and static softening mechanisms occur. The processes that occur during deformation are termed as dynamic process, whereas, those that occur between intervals of deformation or after deformation is completed, are termed as static processes. Dynamic softening process like dynamic recovery, dynamic recrystallization, meta dynamic recrystallization and dynamic transformation, occur during the deformation at high temperatures. Dynamic recovery results from the annihilation of dislocations due to ease of cross slip, climb, and dislocation unpinning at the hot working temperature. During the recovery process, subgrains are formed which act as sinks for moving dislocations. These subgrains have low misorientations across their boundaries and are usually located within primary grains. The stress-strain curve for a metal undergoing dynamic recovery shows an increase in flow stress up to a steady-state value that corresponds to the development of a steady state substructure. In some alloys e.g. steel, where dynamic recovery occurs at a lower rate, dislocation climb is difficult. This leads to higher densities of dislocations in some grains. With the increase in temperature, the grain boundary mobility is also increased. Therefore, the difference in the dislocation density in grains coupled with higher grain boundary mobility leads to the nucleation and growth of strain free grains. This process is termed as discontinuous dynamic recrystallization (DDRX) (Rollett et al., 2004).

Metadynamic recrystallization (MDRX) occurs during the time interval between hot deformation steps or at the end of the deformation process. During MDRX, the nuclei formed due to DDRX undergo a very rapid growth. In recent years, another softening mechanism which occurs in steels known as dynamic transformation (DT) of austenite has gained tremendous attention. It is well known that austenite can be readily transformed into ferrite during deformation between the Ae_3 and Ar_3 temperatures. This phenomenon is referred to as "Dynamic Strain Induced Transformation" (DSIT) (Beladi et al., 2004) and is an effective means for the production of ultrafine ferrite microstructures (Choo et al., 2001; Dong, 2001). But in the case of the dynamic transformation of austenite *above* the Ae_3, DSIT also involves ferrite formation during deformation. It has been observed that ferrite nucleation occurs continuously during straining (Zheng et al., 2009) and leads to the formation of Widmanstätten Ferrite (WF).

The softening mechanisms explained briefly above have been studied mainly for wrought structured alloys and very limited research is available on the effects of these mechanisms on the mechanical behavior of as-cast structured alloys. Considering the importance of the evolution of the as-cast structure on the mechanical properties of the final component and the lack of information in this domain, the focus of the present study will be on the effect of hot deformation parameters on fundamental softening mechanisms governing microstructure evolution of medium carbon low alloy steels.

There are very few studies which focus on the development of precise models for predicting the flow behavior of as-cast structures and using them in FEM simulations in order to optimize the forging parameters of large components. Therefore, the design of the thermomechanical process in order to better engineer the starting as as-cast structure, of the medium carbon low alloy steel, is another objective of the present thesis.
The present thesis is organized into 7 chapters as detailed below:

1. Chapters 2 and 3 focus on the development of constitutive models for *as-cast* structured medium carbon low alloy steels. Arrhenius and Hansel-Spittel models are two phenomenological models which are extensively used to predict stress-strain curves. Hansel-Spittel model with FEM software has been used by many researchers for wrought alloys, whereas Arrhenius model has been used only to predict stress-strain curves and never been used to simulate using FEM simulation.

2. Chapter 4 focusses on the softening behavior of *as-cast* medium carbon low alloy steel and the microstructure evolution due to hot compression process. The chapter also provides a detailed comparison between two models already developed in Chapters 2 and 3 and thus provides the best model to predict stress-strain curves as well as FEM simulation of the process.

3. Chapter 5 discusses microstructure evolution due to Dynamic Transformation of austenite in as-cast structures which is reported for the first time. The study proves the presence of ferrite in the microstructure of the hot deformed samples in the austenitic regions by various techniques. The study shows the effect of strain rate on the diffusion of carbon and its resulting effect on the microstructure. This study provides a novel model of dynamic transformation of austenite with the support of microstructure and diffusional analysis.

4. Chapter 6 brings original information on the effect of addition of Chromium on the dynamic transformation of austenite. In all previous studies done, no study involves the effect of addition of Chromium on the kinetics of DT. The present study successfully correlates with the driving force model considering the effect of elements like Chromium, Silicon, and Manganese on the phenomenon of DT with the diffusional study of each contributing element.

5. Annex I focus on the effect of double hit deformation on Metadynamic Recrystallization (MDRX) kinetics. Ingot breakdown process often consists of several successive deformation steps with high interpass times, during which MDRX occurs. Two-stage isothermal compression tests were carried out at 1150 °C and 1200 °C with strain rates of 0.25-2 s^{-1} and interpass times of 5-25 s. Based on the experimental results, a material model for MDRX is proposed. The constitutive model was implemented in Forge NxT 1.1® software to simulate the multistage compression. The predicted results from the material model are found to be consistent with the numerical analysis and experimental results, which indicated that the proposed kinetic equations can give precise softening behavior for hot deformed as-cast medium carbon low alloy steel.

CHAPTER 1

LITERATURE REVIEW

1.1 Casting

It is a unique metal forming process which has the capability to produce complex components of an alloy. Different types of casting process like sand casting, investment casting, die casting etc. are used for manufacturing different types of shapes and sizes of a workpiece according to their desired applications. Most of the alloys solidify with dendritic structures in a mold. When the molten metal comes in contact with the walls of the mold, small equiaxed grains, or the chill crystals, start to form, as shown in Fig. 1.1 (Maidorn et Blind, 1985).

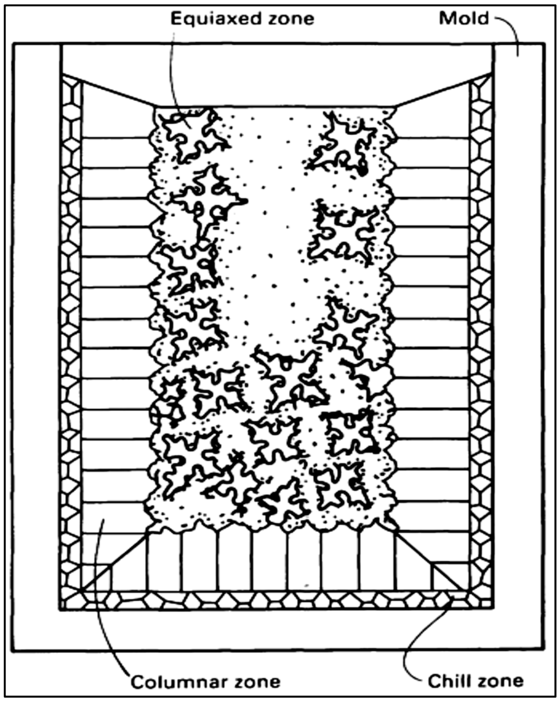

Figure 1.1 Schematic of microstructure zone formation in castings (Maidorn et Blind, 1985)

The undercooling of the melt is reduced by the latent crystallization heat, which is liberated from the crystallizing metal which depresses fast grain growth. Due to this, some grains start to grow in the direction opposition to the direction of the heat flow, thus resulting in columnar grains. Further cooling of the molten metal in the central area causes a formation of large equiaxed grains.

1.2 As-cast Microstructure

During the solidification of molten metal in the mold, various physical and chemical processes occur. These processes are explained as below:

- The elements have different solubility in solid and liquid phases which is entirely temperature dependent.
- Reactions between metal, slag, and gases.
- Temperature gradient in horizontal and vertical direction.
- Shrinkage during solidification and further cooling of molds.

These phenomenon during solidification cause segregation. The segregation may be microscopic or macroscopic regions of the ingot having different a chemical composition, non-metallic inclusions and cavities, cracks, pores etc. (Maidorn et Blind, 1985). Due to macrosegregation, various patterns are observed in the ingot like “A” segregation, “V” segregation, Negative segregation, Hot top segregation etc. (Fig. 1.2).

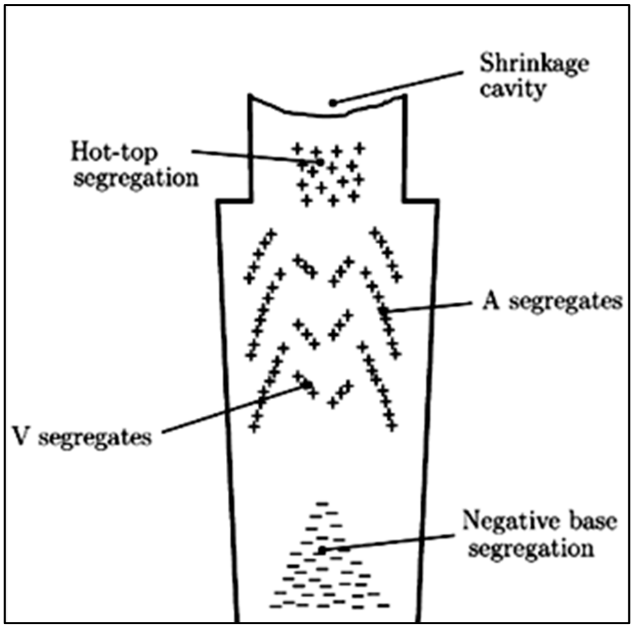

Figure 1.2 Different types of macrosegregation found in cast ingot (Pickering, 2013)

1.3 Bulk Metal Forming Process

Metal forming process consists of series of deformation steps in which a metal billet or blank, received after casting is shaped by tools or dies. The pattern and mastery of such processes depend on an understanding of the features of the workpiece material, the conditions at the tool/workpiece interface, the mechanics of plastic deformation (metal flow), the equipment used, and the finished-product requirements (Hurtuk). These elements determine the choice of tool geometry and material as well as processing conditions (e.g., workpiece and die temperatures and lubrication). Due to the complexity of many metalworking operations, analytical, physical, or numerical models are often relied upon to design such processes. Metal-forming processes are usually classified according to two broad categories:

- Bulk, or massive, forming operations
- Sheet forming operations

In both of these processes, the surfaces of the deforming metal and the tools are in contact. The friction between the metal and the tool have a major influence on material flow during deformation. In bulk forming process, the input material is in billet, rod, or slab form, and the surface to volume ratio in the formed part increases considerably under the action of high compressive loading. Whereas, in the sheet forming process, a piece of sheet metal is plastically deformed by tensile loads into a 3D shape, often without significant changes in sheet thickness (Dieter, Kuhn et Semiatin, 2003).

1.3.1 Forging

It is a bulk deformation process in which the shape of a material is changed by squeezing i.e. with a mechanical or hydraulic press or by hammering (Fig. 1.3). The deformation breaks down the cast microstructure and the resultant directional alignment of the fiber make the forged ingot stronger and more ductile than casting process which results in greater resistance to shock and fatigue (Dieter, Kuhn et Semiatin, 2003). Forging is basically of two types, Closed Die forging and Open Die Forging.

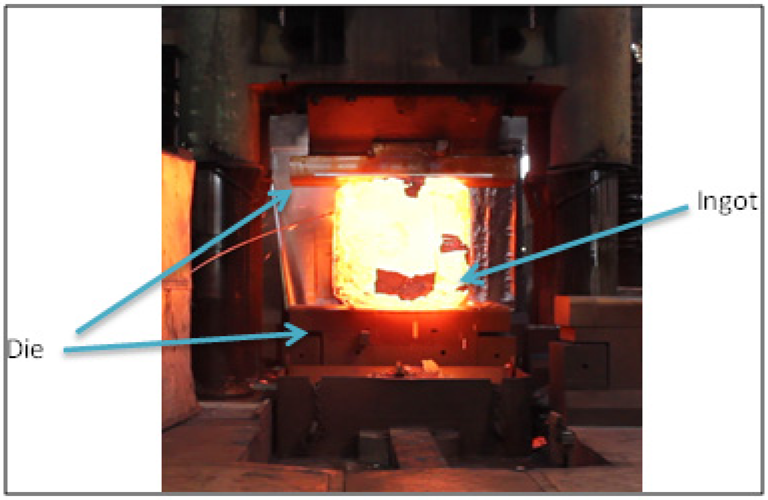

Figure 1.3 Forging Process in 5000-ton capacity press

1.3.2 Closed Die

The forging partially closes the workpiece material and thus restricts the flow of the metal. Fig. 1.4 illustrates the closed die forging process. The hot metal is enclosed in the dies of a predefined shape (Step 1). The force is applied to the dies to give the impression to the hot metal (Steps 2 & 3).

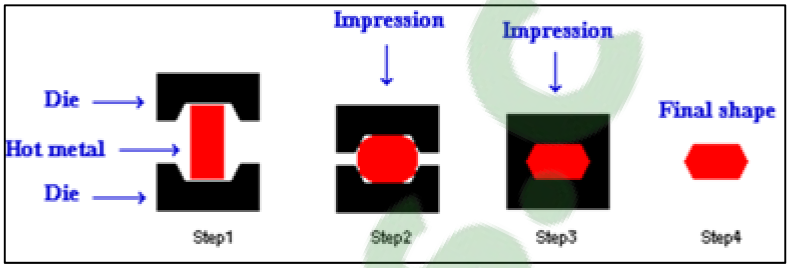

Figure 1.4 Schematic of Closed Die Forging process

1.3.3 Open Die

The hot metal is squeezed or hammered between flat, V-shaped or circular dies. The metal flow is not completely restricted due to the fact that the work piece is not enclosed as shown in Fig. 1.5. Open die forging is usually used when the size of the forging is too large to be produced in a closed die.

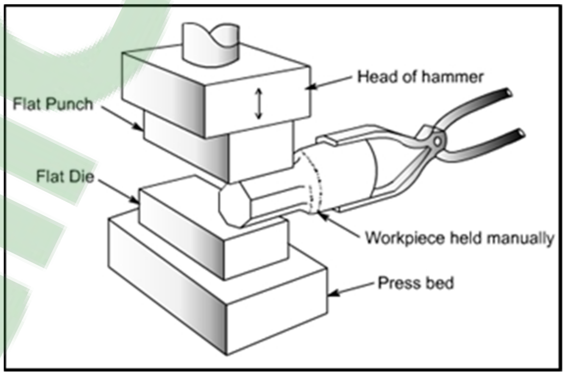

Figure 1.5 Schematic of Open Die Forging process (Nakao et Miura, 2011)

1.4 Ingot Breakdown Process

In order to break down the initial cast microstructure which is composed of the chill zone, columnar zone, and equiaxed zone, to wrought structure, open die forging is used to deform the large ingot into a short wide ingot by the action of repetitive die blows. This process is known as ingot breakdown process (Dieter, Kuhn et Semiatin, 2003). This process not only converts large, non-uniform grains (cast microstructure) to wrought microstructure but also is useful for reducing chemical heterogeneities present due to segregation of various elements due to diffusion process of alloying elements. In the case of steels, the ingot breakdown process is usually conducted in the austenite phase (Fig. 1.6). The operation consists in heating the ingot and held for ~24hrs in a furnace to about 1260 °C. It is then transferred to the forging press where through a multi-hit process incremental deformation is applied to the ingot. Due to this, various microstructural changes occur, like dynamic softening such as dynamic recovery (DRV), dynamic recrystallization (DRX), dynamic transformation (DT) and metadynamic recrystallization, MDRX. To attain the final shape of the ingot, deformation is done along the various axis of the ingot.

During the ingot breakdown process, the ingot is deformed above the $0.75T_m$ (T_m = Melting Point in °C) as shown in Fig. 1.7, to reduce the forging load. Forging at low temperatures may lead to precipitation of carbides that pin matrix dislocations and cause grain boundary failure.

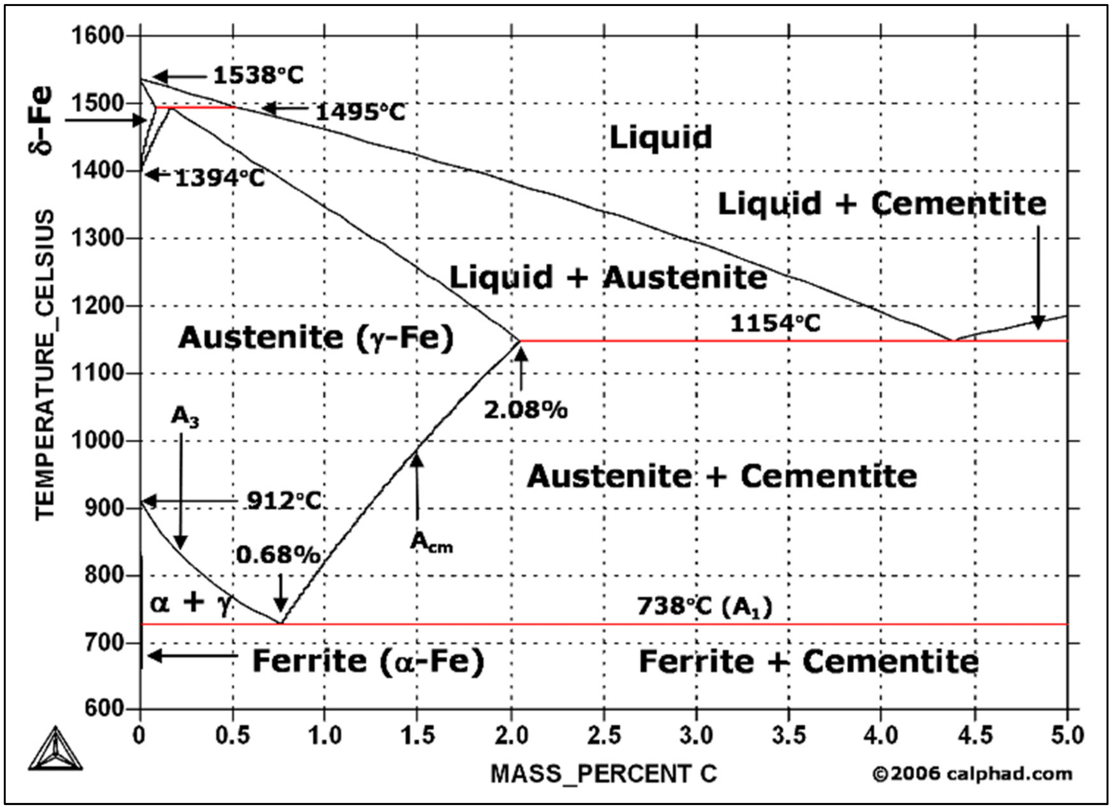

Figure 1.6 Illustration of ϒ solvus line in Fe-C phase diagram.
(http://www.calphad.com/iron-carbon.html)

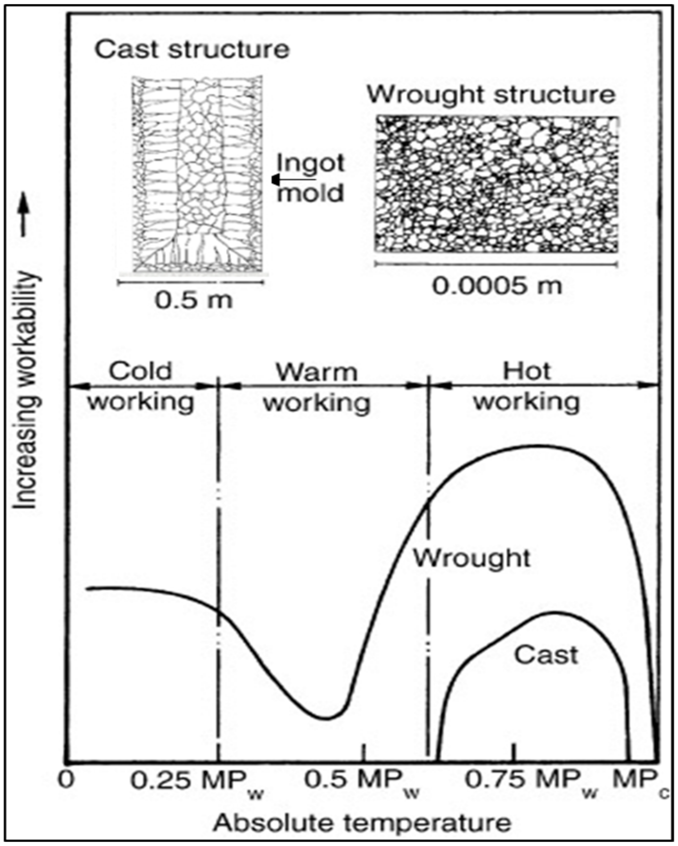

Figure 1.7 Schematic of relative workability
of cast metals and wrought metals at
cold, warm, and hot working temperatures.
The melting point is denoted as
MP$_c$ (cast metals) or MP$_w$ (wrought metals)
(Dieter, Kuhn et Semiatin, 2003)

1.5 Iron Carbon Phase Diagram

Fig. 1.6 shows the Iron-Carbon phase diagram, showing the equilibrium phases that are present at each temperature. Upon heating pure iron to 910 °C, the crystal structure transforms from body-centered cubic (BCC) to the face-centered cubic (FCC) structure known as austenite or γ iron. This structure or phase of iron is fully austenitic up to 1390 °C. Above 1394 °C, the FCC structure of iron transforms back into the BCC structure, known as δ iron, which remains ferritic until it melts at 1538 °C. The austenitizing temperature lowers down to 723 °C upon the addition of carbon as an alloying element when it nears the eutectoid point with 0.8 wt.% carbon content.

Some important boundaries at single-phase fields have been given special names.

These include:

- A_1: Eutectoid temperature, which is the minimum temperature for austenite.
- A_3: The lower-temperature boundary of the austenite region at low carbon contents; i.e., the gamma/gamma + ferrite boundary.
- A_{cm}: The counterpart boundary for high-carbon contents; i.e., the gamma / gamma + Fe_3C boundary (Bhadeshia, 2002).

Sometimes the letters **c**, **e**, or **r** are included e.g. Ae_1 or Ae_3.

The boundary between the initial formation of ferrite and pure austenite is known as the Ae_3 temperature, which is a very important temperature in the present study. As the temperature slowly decreases, all the austenite transforms into a ferrite + pearlite microstructure at the Ae_1 temperature or 723 °C. Pearlite microstructure consists of a lamellar structure of ferrite and cementite (Fe_3C). The maximum solubility of carbon in the ferrite and austenite phase is 0.02 wt.% and 2.14 wt.% respectively. This solubility limit depends on the crystal structure and the conditions of the interstitial sites available for the carbon atoms to fill.

The addition of other alloying elements significantly changes the Fe-C phase diagram, especially with regard to the constancy of the ferrite and austenite phases. The concentration of these alloying elements results in the shifting of phase boundaries. Alloying elements such as C, Co, Cu, Mn, N, and Ni are known as the austenite stabilizers. They lower the eutectoid temperature and widen the range of temperature over which the austenite phase is stable. In contrast, alloying elements such as Al, Cr, Mo, Si, and W are known as ferrite formers, increase the eutectoid temperature thereby restricting the formation of the austenite phase. The addition of alloying elements also improves material properties such as the corrosion resistance (Aranas Jr et Jonas, 2015).

This kind of the phase diagram is usually determined based on orthoequilibrium conditions. This involves the diffusion of both the substitutional and interstitial atoms (Ortho-equilibrium) (Hillert et Ågren, 2004) during transformation, which usually takes a considerable amount of time. It has been found that the diffusional movement of interstitial elements such as C and N is orders of magnitudes faster than that of the substitutional elements (Hillert et Ågren, 2004). On the other hand, paraequilibrium is a condition where only partial equilibrium is attained (Hultgren, 1947). In this situation, only the interstitial elements are able to partition due to time limitations. The paraequilibrium temperatures are lower than the orthoequilibrium temperatures by about 5 °C to 30 °C, depending on the alloying element. In the present work, transformation occurs under paraequilibrium conditions.

1.5.1 Transformation of Austenite

As discussed above, Fe-C equilibrium phase diagram gives the phases which are present due to equilibrium cooling conditions. For most of the applications, the material is cooled under non-equilibrium conditions in order to modify the mechanical properties. Due to this, actual cooling rates may be too fast for actual equilibrium to be achieved and various types of microstructures are developed in many alloys, specifically steels. Due to this, various non-equilibrium phases are formed. The development of microstructure in steels can be divided into two types of mechanism; i) displacive and ii) diffusional. These are described briefly:

1.5.2 Displacive Transformation

Austenite as a parent crystal structure transforms to another crystal structure by deformation without any diffusion of atoms taking place (Fig. 1.8). Deformation rate will change the parent crystal structure to product crystal structure. There is invariant plain strain shape deformation with a large shear component. Examples of this transformation are Widmanstätten ferrite, bainite or acicular ferrite and martensite.

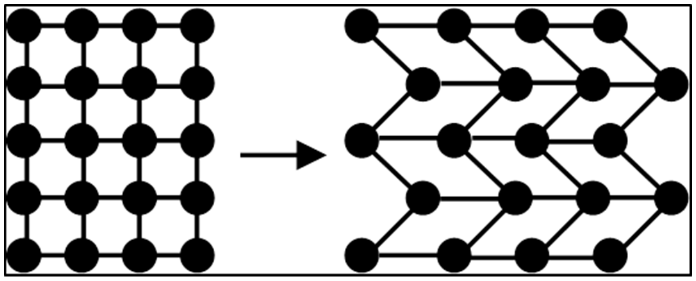

Figure 1.8 Schematic of displacive mechanism

1.5.2.1 Martensite

Martensite is a non-equilibrium phase structure formed by rapid cooling or quenching austenite to a low temperature. It is formed by a diffusionless or displacive transformation. The initial FCC austenite undergoes polymorphic transformation to the body-centered tetragonal (BCT) martensite phase. This transformation increases the volume because the austenite is denser than the martensite. High cooling rates prevent the carbon atoms from diffusing, thus inhibiting the formation of ferrite or cementite. Martensite has supersaturated solid solution of carbon due to the fact that the carbon atoms remain in the interstices thus causing lattice strain and distortion.

Martensite is brittle and is considered as the hardest phase of steel with needle-like grains. Fig. 1.9 shows an example of martensite taken from an optical microscope. The toughness can be recovered by tempering the as-quenched martensite between 250 °C – 600 °C. The microstructure transforms into tempered martensite with better mechanical properties (Krauss, 1999).

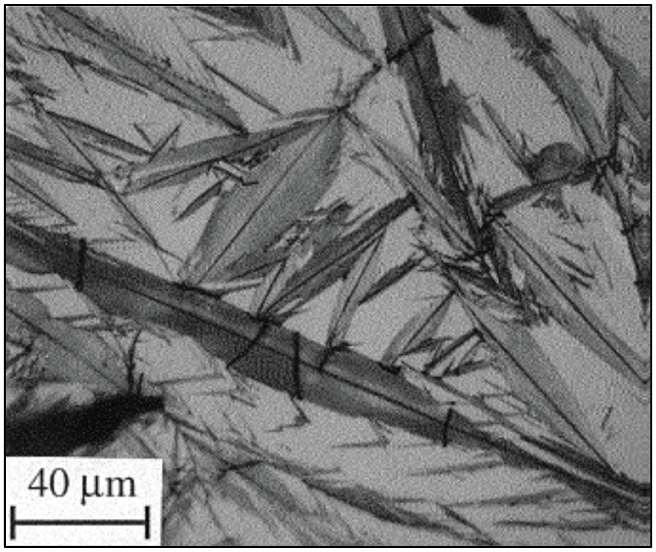

Figure 1.9 Microstructure of plate martensite
in Fe–1.86 wt.% C alloy (Krauss, 1999)

1.5.2.2 Widmanstätten Ferrite

Widmanstätten ferrite consists of long and thin, pointed plates of ferrite which involve the simultaneous growth of pairs of plates as shown in Fig. 1.10. It is usually nucleated at high temperatures, usually just below the Ae_3 temperature. The development and length of the ferrite plate depend on the paraequilibrium condition of carbon diffusion in the austenite. The ferrite plates which nucleate on an austenite grain boundary, are known as *primary Widmanstätten ferrite* and the ones which form from allotriomorphic ferrite (Sec 1.5.3.1 and Fig. 1.12), are known as *secondary Widmanstätten ferrite*. The plates grow by diffusion control mechanism, but they nucleate by a displacive mechanism. Fig. 1.10 illustrates the nucleation of Widmanstätten ferrite according to these two types of transformation (Bhadeshia, 2010b). A part of the present work is also concerned with the formation of Widmanstätten ferrite, however, formation takes place entirely *above* the Ae_3 temperature.

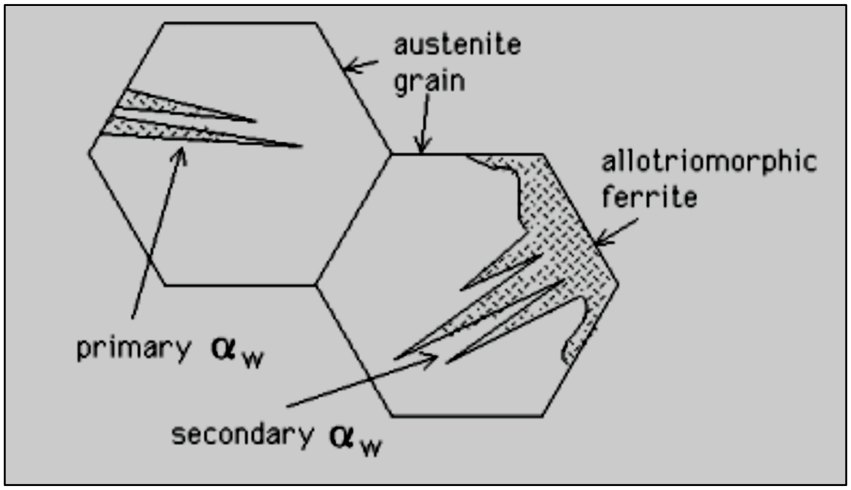

Figure 1.10 Nucleation of primary and secondary Widmanstätten ferrite (Bhadeshia, 2010b)

1.5.3 Diffusional or Reconstructive Transformation

Transformation starts with a parent crystal structure where the atoms rearrange themselves in a different pattern and the product phase can (although it need not) be of a different composition from the parent phase (Fig. 1.11). This process requires diffusion and mobility of the atoms. The rate at which an interface move depends both on its intrinsic mobility (related to the process of atom transfer across the interface) and on the ease with which any alloying elements partitioned during transformation diffuse ahead of the moving interface (Bhadeshia, 1987). Due to this, there is also a composition change because of some atoms partitioning from the parent phase to the product phase. This process requires very slow cooling from the austenitic region to temperatures below the Ae_3 and Ae_1 lines. Examples of this type of transformation are allotriomorphic ferrite, idiomorphic ferrite, massive ferrite, and pearlite.

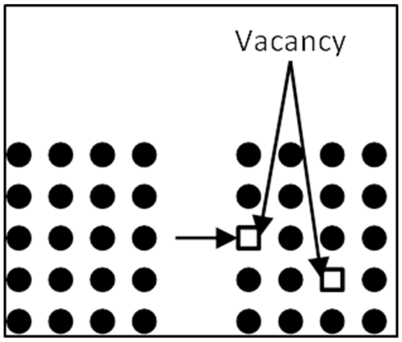

Figure 1.11 Schematic of reconstructive mechanism

1.5.3.1 Ferrite

Ferrite is the thermodynamic stable phase of steel below the Ae_3 temperature. It nucleates within austenite grains during cooling from temperatures above the Ae_3 and is usually seen as equiaxed shapes. When the nucleation of the ferrite phase occurs at the grain boundaries, it is known as *Allotriomorphic Ferrite (Bhadeshia, 2010a).* When the nucleation is inside the austenite grains *Idiomorphic Ferrite* forms. Nucleation of ferrite usually occurs at the austenite grain boundaries and the surfaces of inclusions. Ferrite which forms inside grains usually nucleates heterogeneously on non-metallic inclusions present in the steel. Fig. 1.12 illustrates the formation of ferrite.

1.5.3.2 Pearlite

Pearlite consists of a lamellar structure of ferrite and cementite. Steel is fully austenitic at temperatures above the Ae_3. Pearlite formation starts when the austenite reaches the Ae_1 temperature. Carbon solubility in ferrite is only 0.02%, and any surplus is passed up into the austenite. This results in cementite formation on both edges of the ferrite plate. As the concentration of carbon on both edges of the cementite plate drops, this leads to the development of a new ferrite plate. This is the sidewise nucleation of sets of lamellae responsible for the pearlite structure. The microstructure is shaped by a reconstructive transformation, where the atomic movement of carbon is significantly high and there is sufficient time for all the atoms to diffuse. Fig. 1.13 shows a depiction of the pearlite structure in steel (Callister et Rethwisch, 2011).

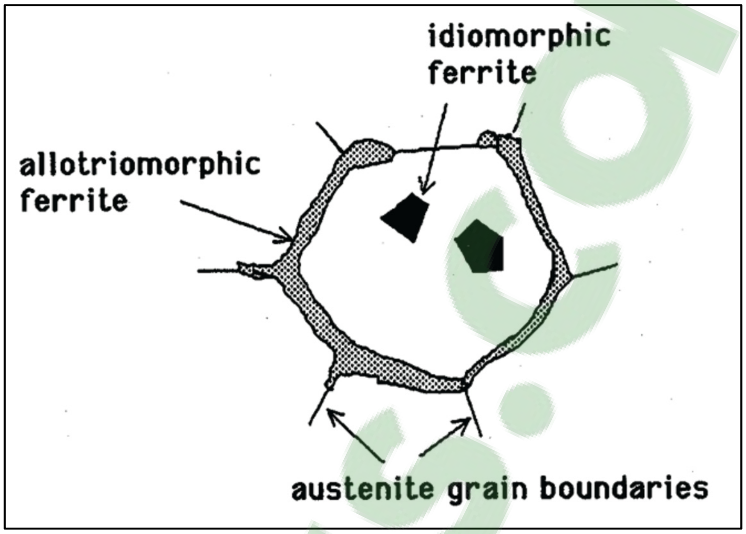

Figure 1.12 Nucleation of allotriomorphic and idiomorphic ferrite. (Bhadeshia, 2010a)

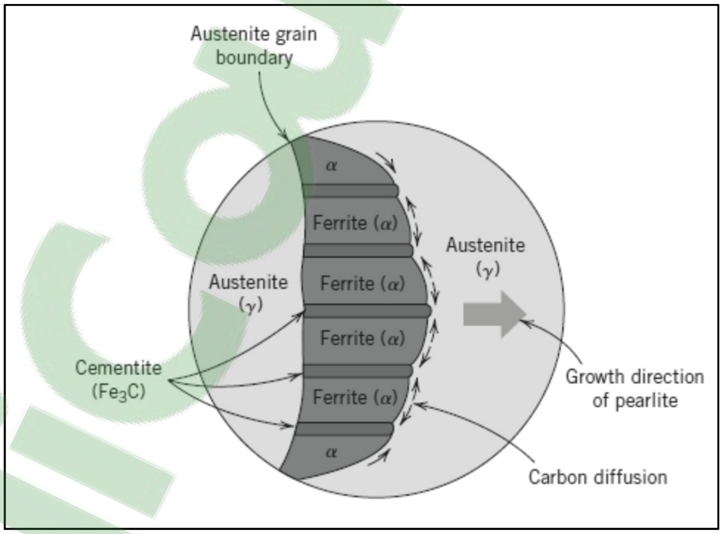

Figure 1.13 Representation of pearlite formation showing alternating layers of lamellar ferrite and cementite plates (Callister et Rethwisch, 2011)

1.6 Softening Mechanisms during Hot Deformation

In hot deformation, the process of softening and hardening may occur during the deformation itself. These processes are elaborated below.

1.6.1 Dynamic Recovery (DRV)

Dynamic recovery process occurs prior to recrystallization which causes changes in the microstructure of the deformed material. The process partially restores the properties to their values before deformation. Recovery is primarily due to rearrangement of dislocation structures. The recovery occurs in a series of events as shown in Fig. 1.14.

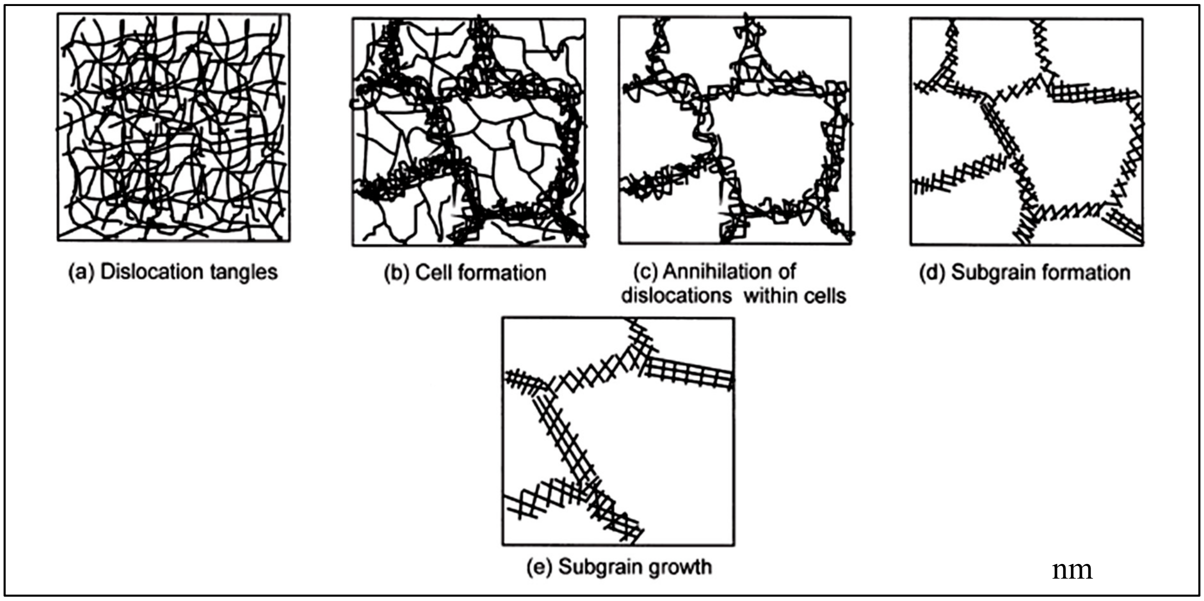
(a) Dislocation tangles (b) Cell formation (c) Annihilation of dislocations within cells (d) Subgrain formation

(e) Subgrain growth

Figure 1.14 Diagram showing various stages of the recovery process (Rollett et al., 2004)

In Fig. 1.14 (a), the deformation process causes dislocation tangles in the structures. In Fig. 1.14 (b), there is a rearrangement of the random dislocation structure into the cell structures. For high stacking fault energy (SFE) materials and during hot deformation, this can occur simultaneously with deformation. Fig. 1.14 (c) and (d), the strengthening of cell boundaries occurs into a well-developed subgrain boundary due to dislocation annihilation and rearrangement of dislocation into low energy configurations. In Fig. 1.14 (e), the subgrain starts growing during continued annealing, thus leading to an overall decrease in internal energy (Rollett et al., 2004).

The stress-strain curve in recovery is characterized by a rise followed by a steady state flow stress in Fig. 1.15. At an early stage during deformation, the dislocations interact and multiply, causing an increase in the flow stress. As the dislocation density rises, the driving force increases, which causes the rate of recovery to increase. This develops the microstructure of low angle boundary and subgrains. At a stage, rates of work hardening and recovery reach a dynamic equilibrium, the dislocation density remains constant and a steady state flow stress is obtained.

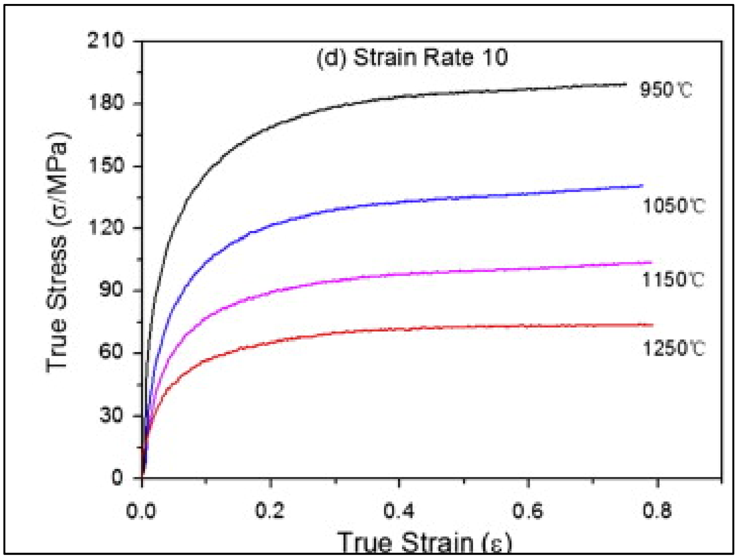

Figure 1.15 True stress–strain curves of 20MnNiMo steel under strain rate of 10 s^{-1}
(Wang et al., 2013)

1.6.2 Recrystallization

Recrystallization proceeds by the nucleation of strain-free grains and their subsequent growth to consume the deformed matrix. Recrystallization is divided into two types: continuous, where there is a homogeneous growth of deformed subgrains and discontinuous, where the recrystallization grains nucleate inhomogenously (Rollett et al., 2004). Taking in consideration of deformation conditions and temperatures, static, dynamic and metadynamic recrystallization occur in a material.

1.6.2.1 Static Recrystallization

Static recrystallization is one of the softening mechanisms which occur after unloading of material. Static recrystallization starts with the nucleation which is followed by the growth of dislocation free grains. The nucleation process is thermally activated and needs incubation time for nuclei to form. Increasing strain and deformation temperature decreases the static recrystallization time. Increase in strain rate introduces higher dislocation density and thus higher driving force (Morrison, 1972).

1.6.2.2 Dynamic Recrystallization

During hot deformation process like forging, microstructure control plays a vital role in controlling the properties of a material. Recrystallization that takes place during high temperature deformation such as forging, rolling, etc. of metals is known as Dynamic Recrystallization (DRX). DRX is one of the most important mechanisms of microstructure evolution. DRX emphases the hot ductility, aides in reconstituting of initial microstructure and refines the grain structure by movement of High Angle Grain Boundary (HAGB) resulting in improvement of mechanical properties. Materials with low Stacking Fault Energy (SFE) such as copper, nickel, and austenitic iron have low recovery rates. Such materials undergo DRX and new grains originate at the old grain boundaries. In these materials, cross slip of dislocation is difficult. Therefore, the ease of rearrangement and removal of dislocation by dynamic recovery is not possible.

During hot deformation, where at high temperatures thermally activated deformation and restoration processes occur, the microstructural evolution is dependent on the parameters such as deformation temperature (T) and strain rate ($\dot{\varepsilon}$) in addition to the strain (ε).

The strain rate and deformation temperature are often incorporated into a single parameter known as "Zener–Hollomon parameter (Z)", which is defined as in the equation (1.1):

$$Z = \dot{\varepsilon}\ exp\ (\frac{Qdef}{RT}) \tag{1.1}$$

Where $\dot{\varepsilon}$ is strain rate (s^{-1}), Q_{def} is activation energy for deformation, R is the universal gas constant, 8.314 J/mol.K and T is deformation temperature.

The stress-strain curve (Fig. 1.16) for a material undergoing dynamic recrystallization exhibits a broad peak, which is different as compared with a plateau in dynamic recovery. Under conditions of low Zener–Hollomon parameter (Z), multiple peaks may be exhibited at low strain rates (McQueen et Jonas, 1975). A critical deformation (ϵ_c) is necessary in order to initiate dynamic recrystallization which is less than peak stress (σ_{max}) of the stress-strain curve. ε_c decreases steadily with decreasing strain rates or Zener–Hollomon parameter, although at very low (creep) strain rates the critical strain may increase again. With the decrease in stress, the dynamic recrystallized grain size increases.

The size of dynamically recrystallized grains (D_R) increases with decreasing strain rate. Under high Z or increase in strain rate, the time available for thermal activation decreases whereas a decrease in temperature decreases the successful activation with decreasing amplitude of thermal fluctuation (Montheillet et Jonas, 1996).

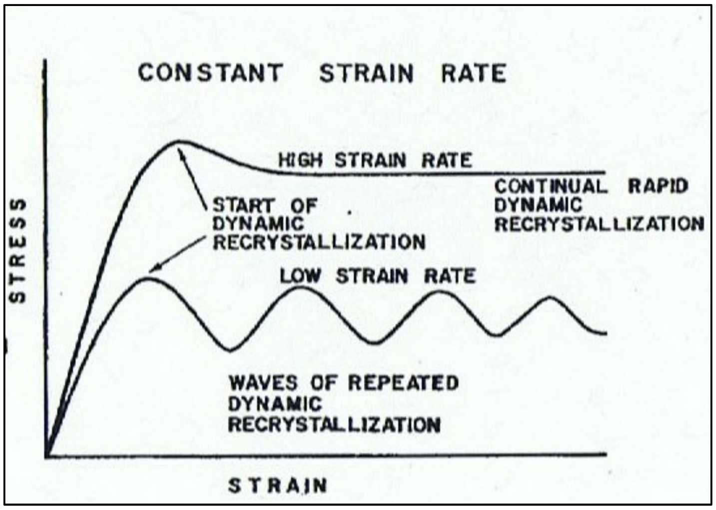

Figure 1.16 Flow curve showing DRX at high and low strain rate (Montheillet et Jonas, 1996)

The effect of temperature and strain rate has been reported by many researchers (ZHANG et al., 2013). It is reported that high deformation temperature and low strain rate (corresponds to low Z values), the critical driving force for DRX increases, thus enhancing the onset of dynamic recrystallization. This results in critical and peak stress occurring at lower strains whereas, at low temperatures and high strain rates (high Z value), the critical driving force decreases and the onset of DRX is delayed. (Fig. 1.17 (a) and (b)).

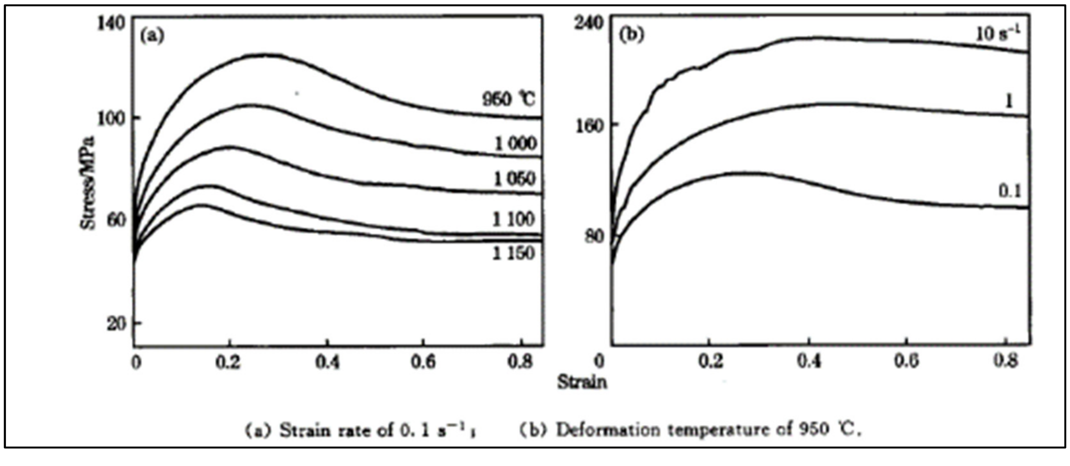

Figure 1.17 True stress- strain curves at different deformation temperatures and deformation rates of 38MnVS forging steel (ZHANG et al., 2013)

Dynamic recrystallization generally starts at old (High angle) grain boundaries by the bulging of the grain boundary. This process is similar to strain induced grain boundary migration which occurs due to differences in the dislocation density of two grains. New grains are subsequently nucleated at the boundaries of growing grains (Fig. 1.18 a & b). Thus, a thickening band of recrystallized grains are formed (Fig. 1.18 c). If there is a large difference between the initial grain size (D_o) and dynamically recrystallized grain size (D_R), then a necklace structure of grain may be formed and eventually, the material becomes fully recrystallized (Fig. 1.18 d).

Necklace structure on grain boundaries in Type 304 Austenitic Stainless Steels can be seen in Fig. 1.19 (a) and (b) (El Wahabi et al., 2005).

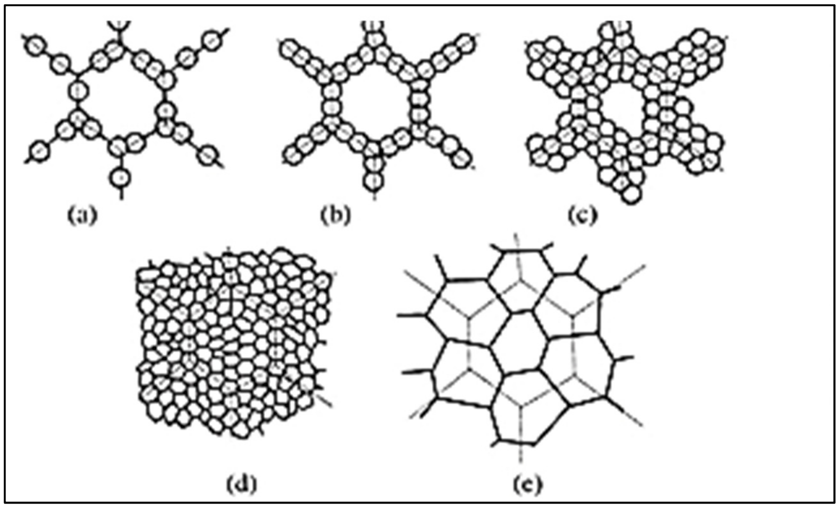

Figure 1.18 Illustration of DRX on grain boundaries (a)-(e)
(Humphreys et Hatherly)

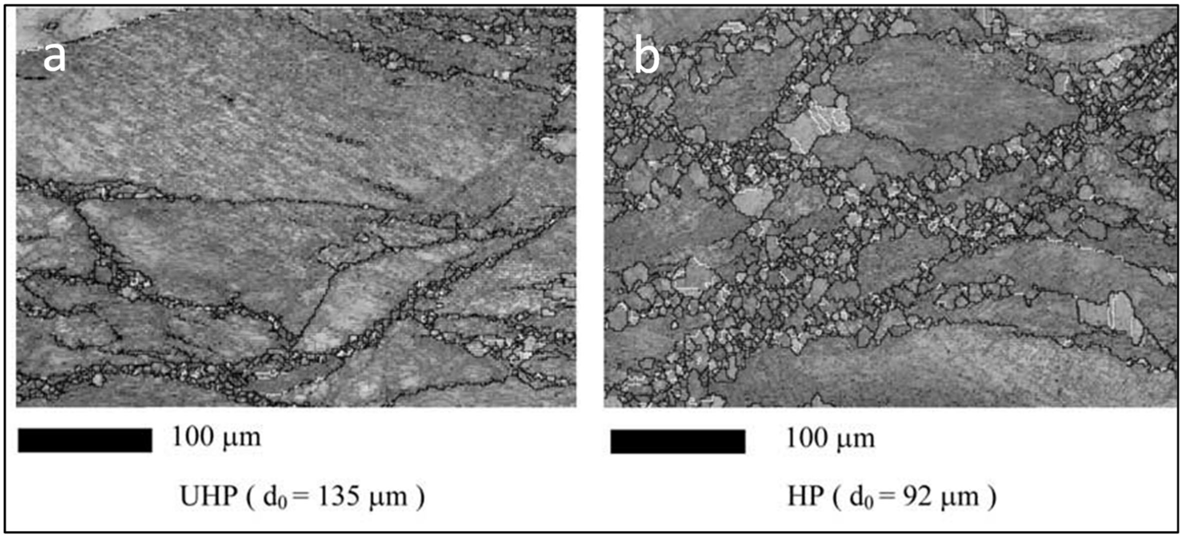

Figure 1.19 Dynamic recrystallization at prior grain boundaries (a) for Ultra High Purity and (b) for High Purity in Type 304 Austenitic Stainless Steels (El Wahabi et al., 2005)

Dynamic Recrystallization kinetics is also dependent on the initial grain size of the material. A study done by M.El Wahabi et al. (El Wahabi et al., 2005) on high purity (HP) and ultra-high purity (UHP) austenitic stainless steel with different initial grain size revealed that large initial grain size leads to a delay in the start of dynamic recrystallization in both alloys. The reason was due to a low fraction of grain boundary which acted as nucleation sites, due to which dynamic recovery took place (Fig. 1.20). They also concluded that small initial grain size (G.S.) leads to faster dynamic recrystallization and thus more softening process.

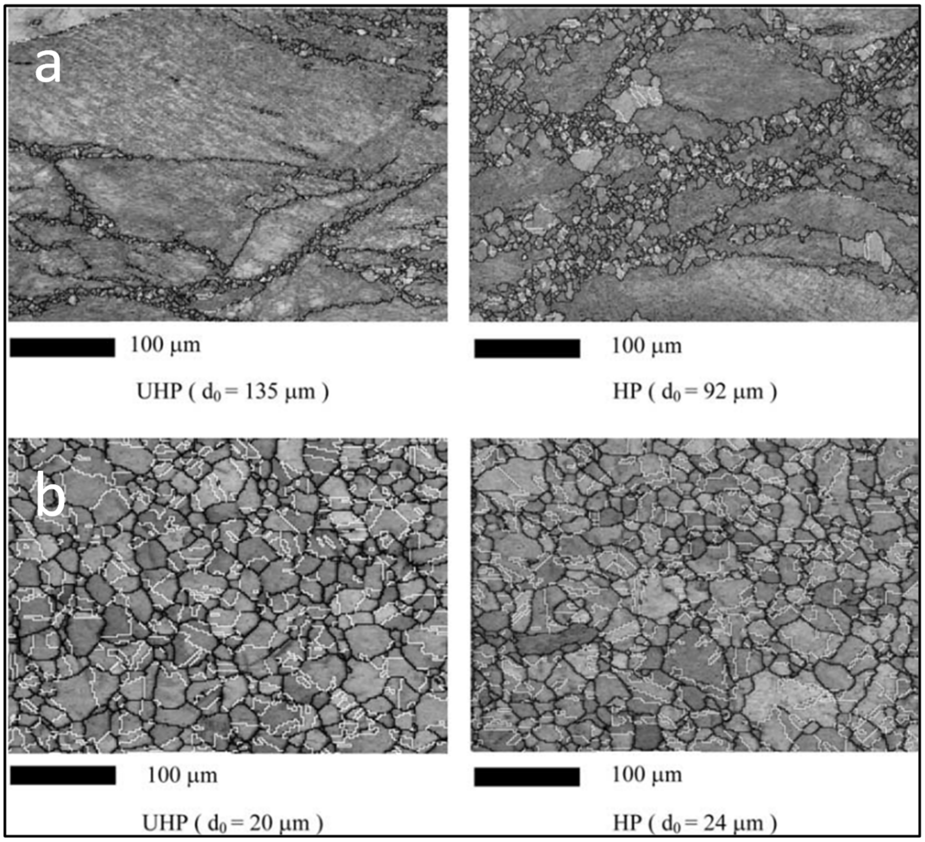

Figure 1.20 Orientation image mapping of UHP and HP at deformation equal to 1 deformed at 850˚C: (a) with big initial grain size; and (b) small initial grain size. Black lines: grain boundaries; gray lines: subgrain boundaries and white lines: twin boundaries (El Wahabi et al., 2005)

1.6.2.3 Metadynamic Recrystallization

This is a restoration process which occurs after the hot deformation. It often takes place very rapidly, specifically in industrial processes like multi-pass rolling, multi-axial forging etc. During softening process, if the critical strain for dynamic recrystallization is exceeded, the nuclei formed by dynamic recrystallization continue to grow when the specimen is unloaded. This strongly influences the microstructure properties like grain size and texture, mechanical properties like yield strength, fracture toughness etc. and phase transformation (e.g. in steels). The metadynamic recrystallization (MDRX) kinetics is most sensitive to strain rate and temperature.

The detailed explanation of the kinetics of MDRX process was given by Liu et al. (Liu et al., 2013). They proposed two possible mechanisms for the occurrence of MDRX. First, the metadynamic softening occurs and dislocation density before the second stage compression decreases with the increasing inter-pass time, thereby decreasing the yield flow stress of second stage compression with the increasing inter-pass time. The second one is that the grain size before the second stage compression increases with the increasing of inter-pass time due to metadynamic softening which causes the dynamically refined microstructure to coarsen.

The yield flow stress in the deformation process decreases with the increase of grain size. Therefore, long inter-pass time triggers full metadynamic softening as the dislocation structure established in the first stage compression is completely destroyed. This results in the flow stress-strain curve in the second stage compression similar to that in the first stage compression in order to rebuild the dislocation structure.

In order to quantify this, metadynamic softening fraction 'X' using 0.2% offset stress method is used as illustrated in Fig. 1.21. The metadynamic softening fraction is determined by the equation (1.2):

$$X=\frac{\sigma_m-\sigma_2}{\sigma_m-\sigma_1} \tag{1.2}$$

where σ_m (MPa) is flow stress at endpoint in first stage compression, σ_1 (MPa) and σ_2 (MPa) are offset flow stress for 1st and 2nd stage compression.

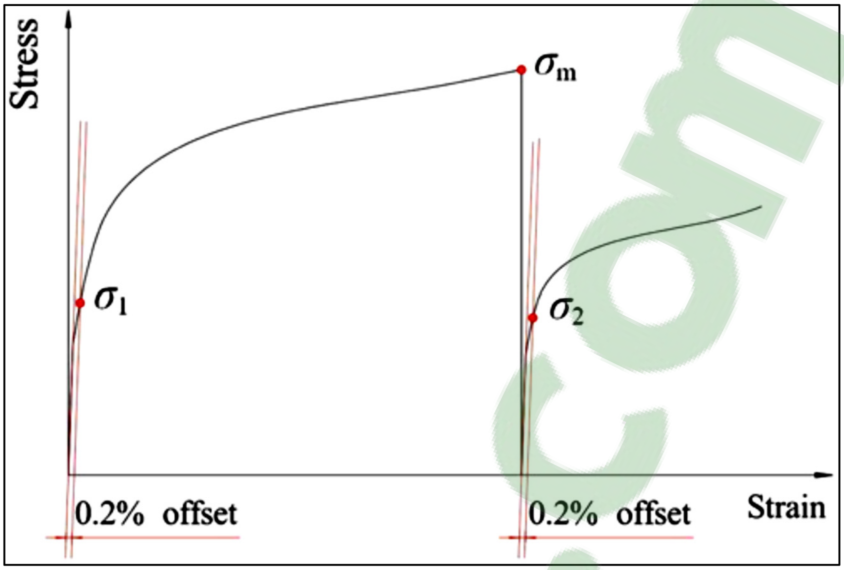

Figure 1.21 Determination of the metadynamic softening fraction using the 0.2% offset stress method (Liu et al., 2013)

1.6.3 Dynamic Transformation of Austenite phase

In the past, two routes for solid state processing of steels, i.e. deformation and transformation were thought to be independent of each other. In late 1950's, it was found that deformation had an influence on transformation which resulted in the development of Thermomechanical Controlled Processing (TMCP) in 1960's. It was then in 1980's when Priestner et al. (DeArdo, Ratz et Wray, 1982) proposed strain induced austenite (*γ*) to ferrite (*α*) transformation and termed it as 'Strain-induced Transformation to ferrite'. This transformation was then termed 'Deformation Induced Ferrite Transformation' and has been studied extensively by various researchers. (Dong, Sun et Weng, 2003; Dong et Sun, 2005; Weng, 2003; Yang et Wang, 2003).

In the late 1980's, Yada referred the transformation as Dynamic Transformation, i.e. transformation occurring during deformation. In their paper (Yada H), they found that DT ferrite could be produced in three plain carbon steels i.e. 0.003%C, 0.11%C and 0.14%C above paraequilibrium Ae_3. They found ferrite grains with a diameter of 1-2 μm with high densities of dislocations. In 1988, Yada et al. (Matsumura et Yada, 1987) did strip mill simulations with and without interpass times of 0.25, 1 and 5 s. They did the simulation at strain rates of 43 s^{-1}, 71 s^{-1}, 89 s^{-1}, 126 s^{-1} and 130 s^{-1} and at temperatures above paraequilibrium Ae_3. These simulations led to microstructures with fine ferrite grains in a matrix of martensite (prior austenite). The number of ferrite grains increased with strain and decreased with temperature. The microstructure after the second deformation revealed that the holding time refined the ferrite grains which were already present before second deformation (Fig. 1.22 (a)).

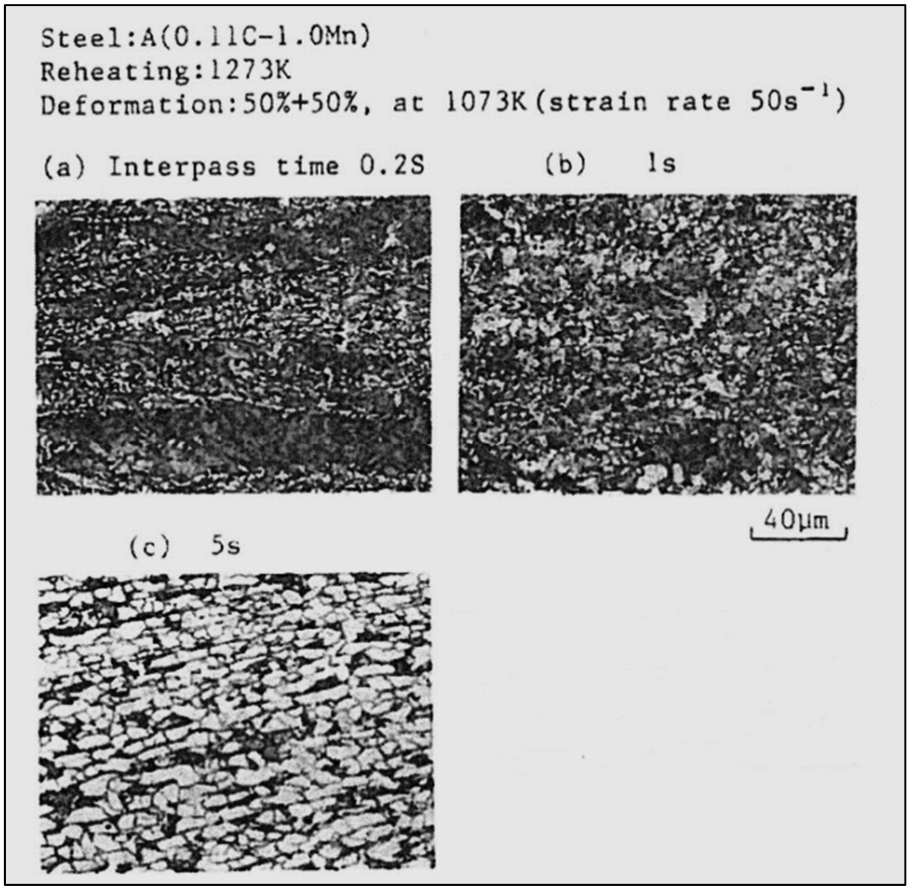

Figure 1.22 Effect of interpass time on the microstructure of steel after 2 pass hot deformation (Matsumura et Yada, 1987)

In the year 2000, Yada et al. (Yada, Li et Yamagata, 2000) returned to the same topic and did in situ X-ray diffraction to reveal γ-α transformation in three Fe-C alloys (0.0008, 0.096 and 0.29% C). They did hot torsion deformation at a temperature range of 600-700 °C i.e. above

Ae_3 temperature. The schematic diagram of in-situ X-ray experiment set up is presented in Fig. 1.23.

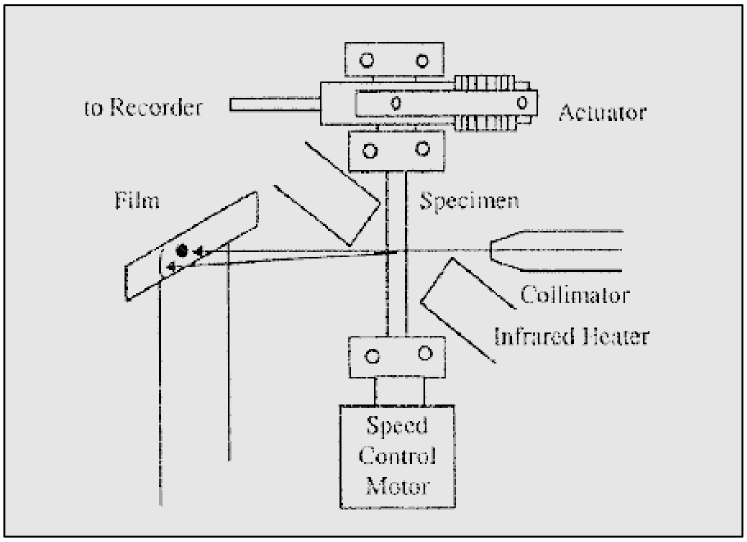

Figure 1.23 Schematic diagram of in-situ X-ray experimental setup (Yada, Li et Yamagata, 2000)

The experiments were performed at a static rate range from 0.01 to 0.09 s. Fig. 1.24 (a) shows the pattern of the specimen before heating. A strong diffraction line corresponding to (110) α-Fe can be observed. When the sample was fully austenized and held isothermally above Ae_3 without deformation, lines corresponding to $(111)\gamma - Fe$ can be observed in Fig. 1.24 (b). After the application of deformation at this temperature, a corresponding line (110) $_{\alpha\text{-Fe}}$ together with (111) $\gamma_{\text{-Fe}}$ appeared as shown In Fig. 1.24 (c). This clearly showed that γ -α transformed during hot deformation. (Yada, Li et Yamagata, 2000)

Since then, DT ferrite has been studied extensively by various groups all over the world at different deformation techniques like hot strip simulations (Basabe, Jonas et Ghosh, 2013; Ghosh, Aranas Jr et Jonas, 2016; Ghosh, Basabe et Jonas, 2014; Ghosh et al., 2013a; Ghosh et al., 2013b; Jonas et al., 2013) and compression tests (Park et al., 2013b; Park et al., 2013c) for different composition of steels at temperatures above Ae_3. In their detailed work, Chiradeep et al. (Ghosh et al., 2013b), examined the deformation behavior of high carbon steel [0.79%C] over a temperature range of 743 °C-823 °C deformed by torsion. The microstructural analysis showed the presence of Widmanstätten Ferrite along with cementite and martensite as shown in Fig. 1.25. Using EBSD analysis, they calculated the width of Widmanstätten Ferrite plate to be 200 nm as shown in Fig. 1.26.

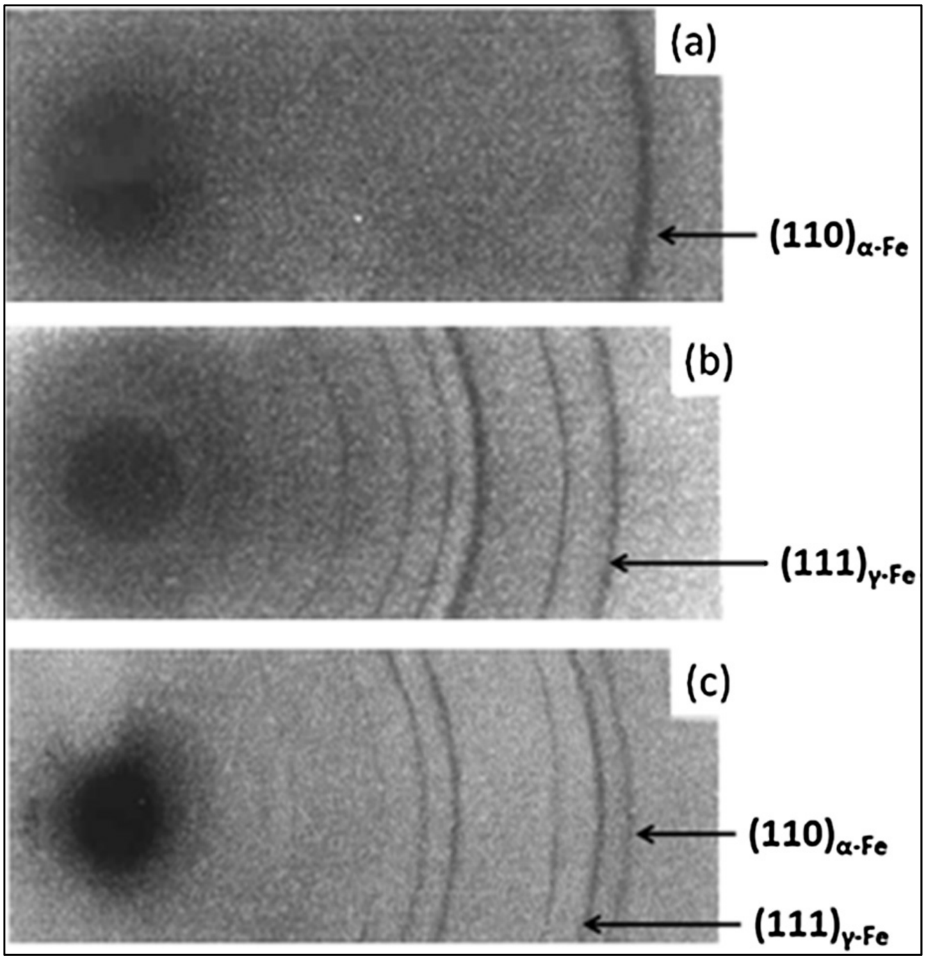

Figure 1.24 Typical X-ray diffraction patterns (a) before heating,
(b) at the austenitizing temperature (790 ºC), and
(c) on the application of torsional deformation at 720 ºC
(i.e. paraequilibrium Ae_3 + 40 ºC) temperature
(Yada, Li et Yamagata, 2000)

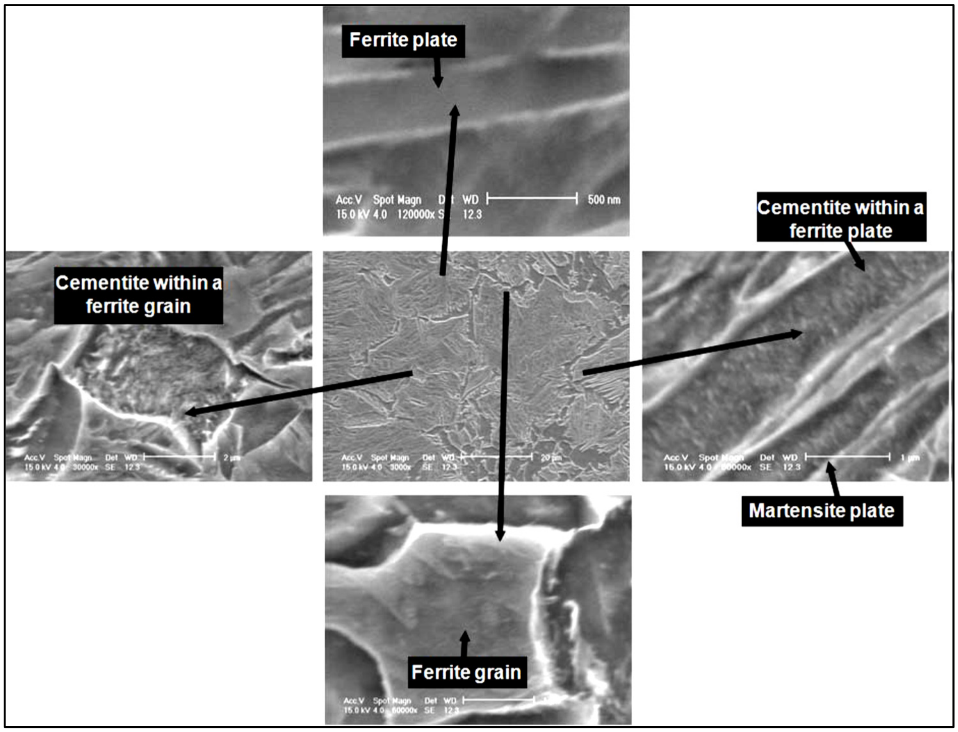

Figure 1.25 Scanning electron micrograph of a specimen deformed to a strain of 0.5 at 4 s^{-1} at 753 °C (Ae$_3$+20 °C). The deformed and quenched specimen contains Widmanstätten ferrite, cementite and martensite (Ghosh et al., 2013b)

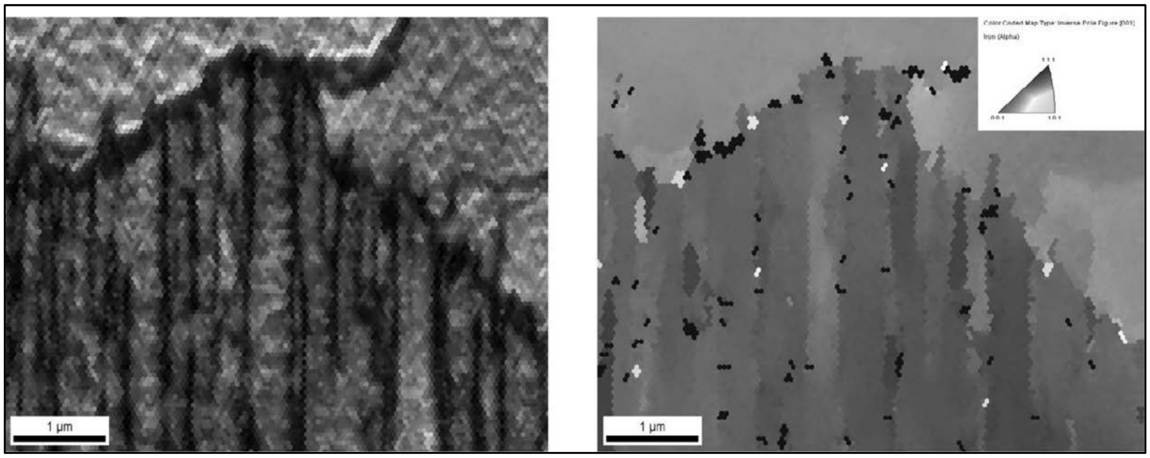

Figure 1.26 Appearance of a colony of DT Widmanstätten plates in an IQ map of 0.09C– 0.036Nb steel; (a) IPF map of the Widmanstätten plates and (b) EBSD, showing the small misorientations between the plates (Ghosh et al., 2013b)

They determined the critical strain for initiation of dynamic transformation on the basis of mathematical formulation developed by Poliak and Jonas (Poliak et Jonas, 1996). They found critical strain value of 0.25 under which no phase transformation took place. The authors did a close examination of their results using diffusion theory. They calculated diffusion distances of C and Mn in ferrite by the equation (1.3):

$$\bar{X} = \sqrt{Dt} \tag{1.3}$$

Where $\bar{X}$ is mean diffusion distance, t time and D diffusivity which is given by the equation (1.4):

$$D = D_o \exp(-\frac{Q}{RT}) \tag{1.4}$$

The diffusion distances calculated by them are shown in Fig. 1.27. It is evident that carbon takes 100 µs to diffuse to 100 nm in ferrite, whereas Mn can only diffuse a small fraction of a nanometer in that particular time. Thus, by this, they proved that interstitial diffusion mainly occurred which accounts for carbon diffusion rejection from ferrite to partition into austenite phase or form cementite.

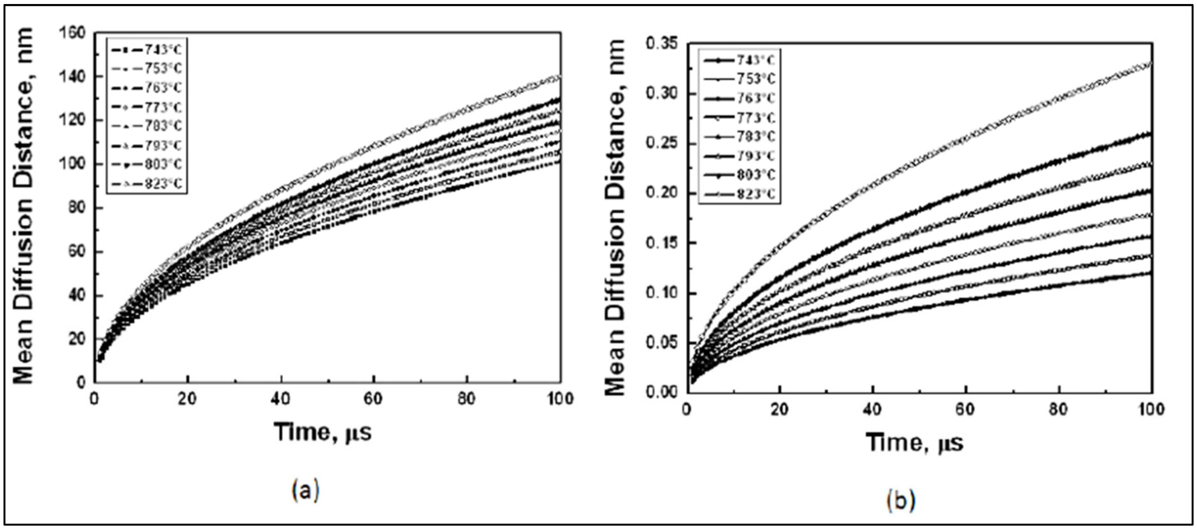

Figure 1.27 Estimated mean diffusion distances of (a) C and (b) Mn in ferrite over the experimental temperature range (Ghosh et al., 2013b)

C. Ghosh et al. (Ghosh, Basabe et Jonas, 2014) came up with a theory of DT of austenite. They proposed that the effect of hot deformation on the Gibbs energy of austenite can be estimated by assuming that the austenite continues to work harden after the initiation of the transformation and that its flow stress and dislocation density can be estimated from the experimental flow curve for the two-phase material. This results in higher austenite flow stresses and therefore higher dislocation densities. The dislocation densities in the regions that undergo transformation are higher than the average values. With this approach driving forces of about 200 J/mol are achieved and can thus readily account for transformation temperatures as much as 100 ºC above the Ae_3.

1.6.3.1 New theory for Dynamic Transformation

The theory described above could not justify fast forward transformation and slow reverse transformation, or the effect of stress on dynamic transformation etc. In addition to this, the dislocation theory was also not able to explain why DT occurs at strains of 0.10 to 0.3. At such low strains, it is difficult to assume any significant contribution made by stored energy of dislocations. In addition to these downsides, the critical strains for the initiation of DT decreased with increase in temperature, despite the fact that chemical driving forces oppose the transformation of unstable ferrite with increasing temperatures above Ae_3. Jonas et al. (Jonas et Ghosh, 2013) developed a new approach to resolve the above issues. They introduced three stress-related features to the previous model (Ghosh et al., 2013a).

First, is an additional driving force associated with the applied stress. Second, is shear accommodation work done in the austenite during the dynamic formation of Widmanstätten ferrite plates. Third, is the work of dilatation in austenite associated with the density decrease which follows ferrite formation as illustrated in Fig. 1.28.

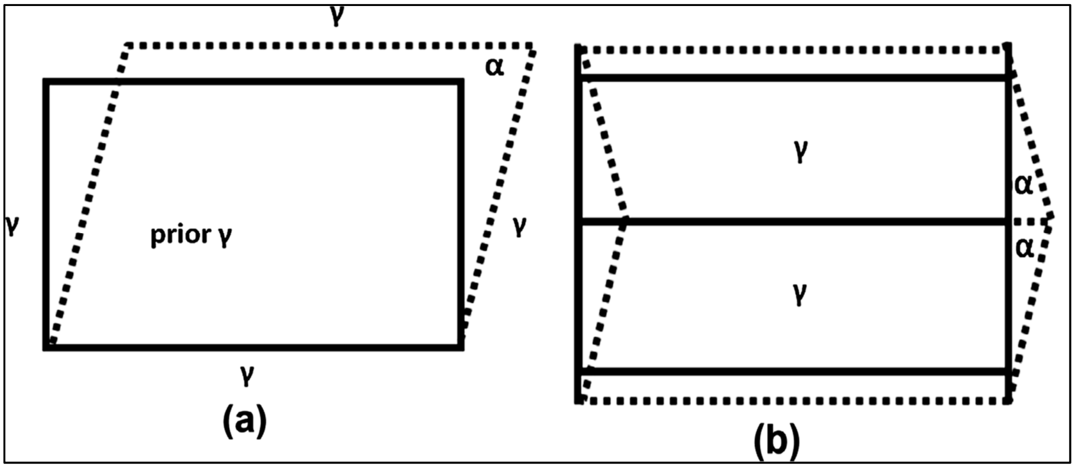

Figure 1.28 (a) a rectangle of prior austenite is transformed into a parallelogram of Widmanstätten ferrite as a result of application of a shear stress. The dilation (shown exaggerated) takes place in a direction perpendicular to the habit plane. (b) The geometry associated with the formation of a pair of "self-accommodating" plates (Jonas et Ghosh, 2013)

They compared their approach to the stored energy approach model and gave a significant explanation to issues as mentioned above. In the stored energy model as shown in Fig. 1.29 (a), the energy introduced by straining, increases the Gibbs energy of austenite and thereby transforms it to unstable ferrite. Prolonged holding after deformation results in retransformation of unstable ferrite to dislocation free austenite. The model developed by Jonas et al. is illustrated in Fig. 1.29 (b) and is summarized in the following: the stress developed at critical strain is sufficient to mechanically activate the fast forward and overcome chemical free energy difference between two phases as well as provide the energy required to accomplish work of dilation and shear of austenite. This process is athermal therefore it occurs very rapidly. Prolonged holding, results in retransformation according to diffusion control process and therefore very slow as compared to forward transformation (Jonas et Ghosh, 2013).

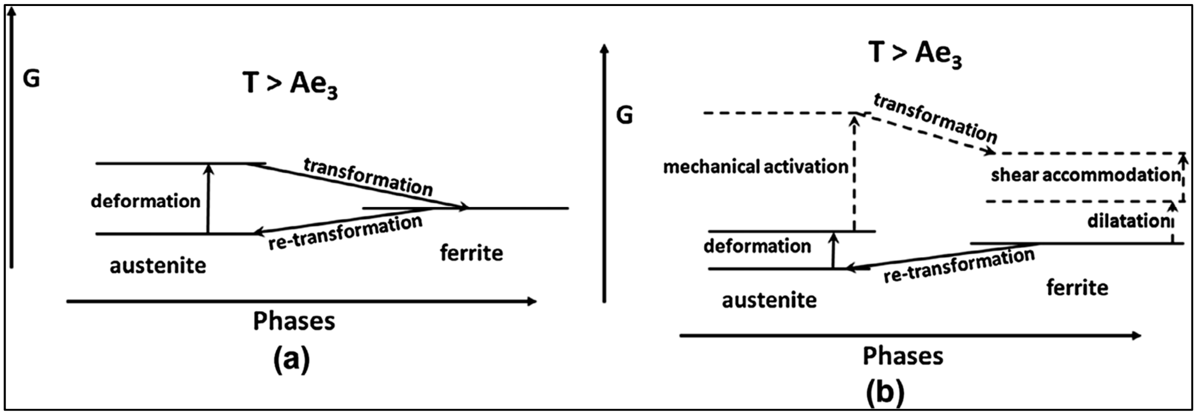

Figure 1.29 (a) Comparison of the Gibbs energies of deformed and undeformed austenite with that of undeformed ferrite at temperatures above the Ae3. Deformation increases the free energy of the austenite to a level above that of the otherwise unstable ferrite, leading to the occurrence of dynamic transformation. (b) The effect of mechanical activation on dynamic transformation (Jonas et Ghosh, 2013)

1.7 Constitutive Equations

For optimizing the microstructure and mechanical properties, determination of dynamic response under specified deformation conditions is a very critical phenomenon. Flow stress which is a key factor during hot deformation, changes with working variables such as strain, strain rate and deformation temperature. To measure this change in flow stress, mathematical relation should be set up to measure the response in regard to change in strain, strain rate and deformation temperature. Flow behavior is mainly due to work hardening or Dynamic softening mechanisms such as Dynamic recovery, Dynamic Recrystallization and Dynamic Transformation. Various models have been constructed to analyze these flow behaviors. Among these is Arrhenius type which was proposed by Jonas et al. (Jonas, Sellars et Tegart, 1969b) and subsequently used by many researchers to predict flow behavior of wrought materials (Lin, Chen et Zhong, 2008a; 2008b; 2008c; Lin, Ming-Song et Jue, 2008a; 2008b; 2008c; Lin, Chen et Zhong, 2008f) subjected to hot deformation. Due to easy availability of wrought mill products and fewer costs they are most researched materials as compared to the as-cast materials of which comparatively less research has been published due to cost, size of ingot and grain size.

1.8 Challenges and Objectives

The literature review provides elaborate work on various softening mechanisms occurring during hot deformation process. The major aim of the present work is focused to study the microstructure evolution of medium carbon low alloy steel in its *as-cast* form during ingot breakdown process. This work is aimed to provide various missing links to the scientific as well as industrial community. As described in section 1.2 and 1.3, that the ingot in *as-cast* form has heterogeneities such as cast microstructure, porosity, voids and macrosegregation. These heterogeneities are broken down using Ingot Breakdown Process. The microstructural and mechanical properties of material having these heterogeneities at this level of deformation have got very less attention. The occurrence of DRV and DRX has got tremendous attention for wrought alloys, but dedicated work for as-cast materials are very few. Due to this, there is also no precise material model which can be used to predict the mechanical behavior of the alloy and simulate this process. Therefore, in order to overcome this challenge, one part of this thesis is dedicated to study the softening mechanisms occurring during Ingot Breakdown Process, for the *as-cast* medium carbon low alloy steel which has a dendritic structure. In addition to it, the study will be focused to develop a precise material model which can predict the mechanical properties and also can be used for simulating deformation process specifically for the as-cast alloy.

Dynamic Transformation (DT) of austenite in various compositions of steel has been studied extensively. But, occurrence of DT in an *as-cast* alloy particularly on medium carbon low alloy steel has never been done. It is envisaged that large initial grain size of the starting material and the addition of various alloying elements, the effect of hot deformation on the DT of austenite would be significantly different than those of reported investigations on wrought structured material. Moreover, the effect of strain rate on the evolution of microstructure as a result of DT has not been reported. Strain rate change is one of the key factors for the change in stress value. The change is stress is directly responsible for the change in diffusion coefficients. The previous studies on diffusion focus only on temperature change and effect of strain rate or stress has not been studied. Therefore, the second objective of the study is to quantify the occurrence of DT of austenite and study the effect of strain rate of microstructure evolution.

The third objective is to determine the effect of alloying elements in DT transformation. Chromium is the dominant element present in the alloy used for the current investigation. Chromium is a ferrite stabilizer and is expected to enhance DT kinetics. However, this was never investigated. Therefore, the effect of Cr addition was studied in regards for its effect on the initiation of DT of austenite and its contribution to the DT kinetics.

CHAPTER 2

AN APPROACH TO DEVELOP HANSEL-SPITTEL CONSTITUTIVE EQUATION DURING INGOT BREAKDOWN OPERATION OF LOW ALLOY STEELS

Kanwal Chadha, Davood Shahriari, and Mohammad Jahazi

Department of Mechanical Engineering, École de Technologie Supérieure,
1100 Notre-Dame West, Montreal, Quebec, Canada H3C 1K3

Chapter published in *Frontiers in Materials Processing, Applications, Research and Technology*, Springer Singapore, December 2017

Abstract: The control of the final quality of a forged product requires an in-depth comprehension of quality of the initial cast ingot. Hot workability is an important property which can be evaluated by variation of strain, strain rate, and temperature. Modeling of forging process always needs to define constitutive models for the material involved. In this study, 42CrMo steel with dendritic microstructure was used to generate the flow stress curves. In order to provide accurate predictions of the thermal and mechanical parameters in the actual ingot break down operation, hot compression tests were carried out at uniform temperatures ranging from 1050 °C to 1200 °C and strain rates of 0.25 s^{-1} to 2 s^{-1}. Finally, Hansel-Spittel law was developed to represent the dependency of the material flow stress on the strain, strain rate and temperature. FE Simulation results reveal that the model is able to predict the adiabatic heating during deformation.

Keywords: As-cast structure, Low-alloy steel, Hansel-Spittel Model, constitutive equations, FEM simulation, Hot deformation.

2.1 Introduction

Hot workability is an important property to estimate materials plastic deformation ability, which is usually defined as the amount of deformation that a material can undergo without cracking and reach desirable mechanical properties and microstructure at a given temperature and strain rate is generally evaluated by various parameters like strain rate, strain and temperature. Forging of ingot after casting starts with ingot breakdown process which is generally performed at very high temperatures (0.75 of melting point "***MP***") so as to breakdown the chemical (macrosegregation) and microstructural structure (as-cast dendritic) inhomogeneity (Dieter, Kuhn et Semiatin, 2003). Flow characteristic of a hot forging process consists of strain hardening and softening due to dynamic processes like recrystallization and recovery, which basically determines the quality of a forging product. Constitutive relations are often used to model the forging process in order to describe the plastic flow properties of metals and alloys, many research groups have attempted to develop constitutive equations using various models to describe the flow behavior of various alloys using experimental data (Lin, Chen et Zhong, 2008a; 2008b; Lin et al., 2015; Rao et Hawbolt, 1992). Despite large efforts being made on the development of constitutive equations for 42CrMo, further investigation has to be done describing the behavior of 42CrMo in its as-cast structure at very high temperatures (~0.7 Mp) so as to describe the flow behavior during the ingot breakdown process. Therefore, the objective of this study is to investigate the nature of the influence of strain rate and temperature on compressive deformation characteristics of 42CrMo using hot compressive tests. A model describing the relationship between flow stress, strain rate, strain and temperature is proposed and used to simulate real time analysis of the process using Forge NxT 1.0® software.

2.2 Experimental

As-cast 42CrMo high strength steel was used for the present investigation. The composition of the alloy is shown in Table 2.1. The materials were provided by Finkl Steel Co., Sorel Tracy, Quebec, Canada. Cylindrical specimens were machined with a diameter of 10 mm and a height of 15mm. Hot compression tests were performed in Gleeble 3800 Thermomechanical Simulator at four different temperatures (1050, 1100, 1150 and 1200 °C) and four strain rates (0.25, 0.5, 1 and 2 s^{-1}). The heating rate was 2 °C/Sec till 1260 °C where it was maintained for 300 s so as to get homogenous temperature over the specimen. The specimen was then cooled to a respective deformation temperature at a cooling rate of 1 °C/Sec.

Table 2.1 Composition of as-cast 42CrMo (Wt.%)

C	Mn	Si	Mo	Cr	Ni	Other
0.35	0.84	0.41	0.44	1.90	Added	Microalloying

2.3 Results

For the present report, results from a deformation temperature of 1200 °C and 1150 °C at strain rates of 0.25 s^{-1} and 2 s^{-1} are considered. Stress-strain curve of hot compression tests (Fig. 2.1) reveals that at low strain rates, dynamic softening mechanisms get activated and results in stress drop after a peak stress. This is a typical recrystallization curve, which comprises of four states: the work hardening state, transition state, softening state and steady state. At high strain rates, the flow curves rise sharply and then attains a steady state. This type of flow curve resembles that of recovery behavior due to which the flow stress attains a steady state due to dislocation generation and annihilation process running simultaneously. Dislocations are particularly needed to build a reservoir of stored energy. This stored energy along with the thermal energy is useful breaking down the coarse grains and generating much finer recrystallized grains. High temperatures can provide sufficient driving force along with the dissolution of precipitates can lead to dislocation annihilation and thus softening can be seen as in Fig. 2.1 at a strain rate of 0.25 s^{-1}. However, higher strain rates do not show softening even at high temperatures due to the fact that critical driving force has not reached because of high Zener Hollomon factor, Z (McQueen et Jonas, 1975). Low strain rates promote sufficient driving force for the dislocation annihilation and thus softening can be seen in Fig 2.1(a).

2.4 Constitutive Equation of the flow stress

To investigate the deformation behavior of as-cast 42CrMo steel, there is a need to develop constitutive equations in order to simulate the process of the ingot breakdown process. Material constants of the constitutive equation can be derived from the stress-strain data obtained from the hot compression tests. To simulate bulk metal forming, Forge NxT 1.0® software is used which generally uses thermo-viscoplastic constitutive models under hot conditions. One of the most used models for bulk forming is Hansel-Spittel model. It is based on simple relation on three variables like strain, strain rate and temperature. It has been used for various alloys like AZ31 magnesium alloy (Cyganek et Tkocz, 2012), 20MoCrS4 (Meyer, Weise et Hahn, 1997), Al-0.7%Mg-0.4%Si aluminum alloy (El Mehtedi, Musharavati et Spigarelli, 2014), AA6082 alloy (Donati et al., 2013). The model was developed by Hansel and Spittel, commonly termed as HS equation (Hansel A, 1978) is given as:

$$\sigma = Ae^{m_1 T}\varepsilon^{m_2}\dot{\varepsilon}^{m_3}e^{\frac{m_4}{\varepsilon}}(1+\varepsilon)^{m_5 T}e^{m_7\varepsilon}\,\dot{\varepsilon}^{T m_8}T^{m_9} \tag{2.1}$$

where, $\sigma =$ Stress, ε = Strain, $\dot{\varepsilon}$ = Strain Rate, T= Deformation Temperature, A is the material consistency at given temperature (isothermal conditions assumed here), m_1 to m_9 define the material's sensitivity to temperature, m_5 defines coupling temperature and strain, m_8 term coupling temperature and strain rate, m_2, m_4 and m_7 define the material's sensitivity to strain and m_3 depends on the material's sensitivity to strain rate. Usually constants m_8 and m_9 are taken as zero.

The material constants were calculated using linear regression methods by Origin® software and are provided in Table 2.2. The constants were then applied in the equation for various values of strain, strain rate and temperature in order to find the values of stress. Fig. 2.1 shows the comparison between experiment and calculated flow stress curves developed by constitutive equations. The Hensel-Spittel model is able to describe the steady state phase of hot flow stress curves at high strain rate, whereas it was not able to take into account the softening behavior seen at lower strain rates with the difference of maximum ~ 14% between calculated and experimental flow stress. It can be observed that the model can fairly predict the peak stress at both the strain rates. The difference in the calculated peak stress and experimental peak stress is maximum ~7% at both higher and lower strain rates.

Table 2.2 Parameters of the Hansel-Spittel equation

A	*m1*	*m2*	*m3*	*m4*	*m5*	*m6*
2136.313	-0.00243	0.2315	0.1215	0.0001	-0.001	0.3235

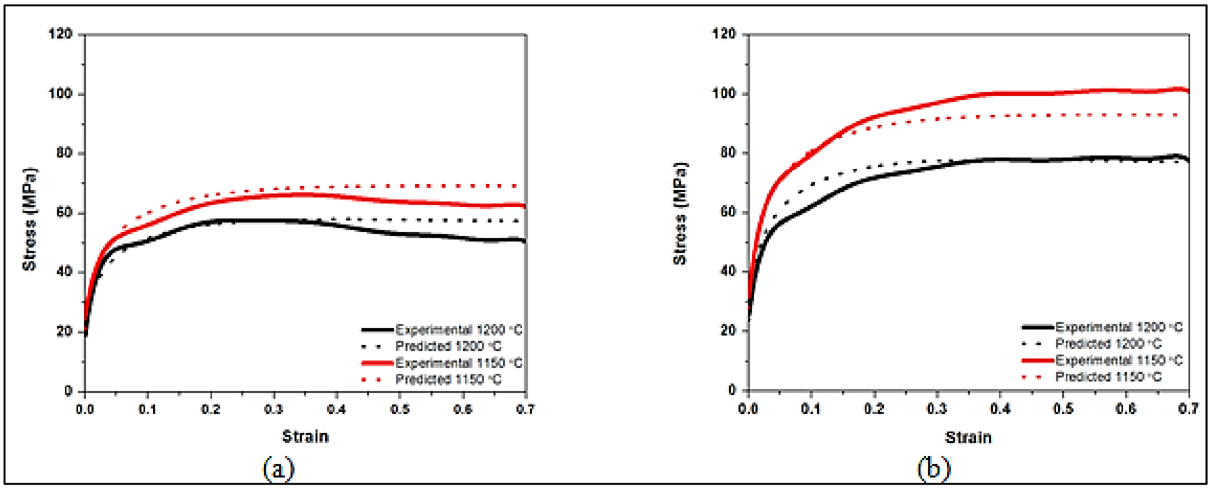

(a)

(b)

Figure 2.1 Flow curves of 42CrMo at strain rate of (a) 0.25 s^{-1} and (b) 2 s^{-1}

2.5 Numerical simulation of 42CrMo hot forging

Numerical simulations generally consist of various elements which present the real process. Among the various elements includes the geometrical models of the ingot, dies, material model and a set of boundary and initial conditions. The die temperature was kept similar to the deformation temperature. The density of the alloy is 7386.80465 Kg/m^3 and specific heat is 661.94 J/Kg/°K. Hansel-Spittel model was introduced in Forge NxT 1.0® software and two simulations at different strain rates, 0.25 s^{-1} and 2 s^{-1} at constant deformation temperature of 1200 °C were conducted. The temperature distribution map for final stage of deformation for strain rate of 0.25 s^{-1} and 2 s^{-1} with deformation temperature 1200 °C is shown in Fig. 2.2. It is apparent from the Fig. 2.2 that temperature distribution in case of higher strain rate is more homogenous than at lower strain rate. Deformation heating is usually generated in any alloy during deformation and is the function of strain rate (Dieter, Kuhn et Semiatin, 2003).

This heat generated is usually termed by adiabatic heating and causes higher heat in the sample thereby reducing the flow stress. Adiabatic heating is represented by the following equation:

$$\Delta T_{Adiabatic} = \frac{0.95 \int \sigma d\epsilon}{\rho C_p} \tag{2.2}$$

where, ΔT is the change in temperature, $\int \sigma d\varepsilon$ is the area under the uncorrected stress-strain curve, ρ is the density, C_p the specific heat and 0.95 is the fraction of mechanical work transformed to heat with remaining fraction going to microstructural changes.

Adiabatic heat calculated from the experimental data reveals that the temperature at the center at a strain rate of 0.25 s^{-1} and deformation temperature of 1200 °C is 7.19 °C at 0.25 $s^{-1}$and 14.5 °C at 2 s^{-1}. From the simulation results, the adiabatic heat generated due to hot compression at strain rate of 0.25 s^{-1} and 2 s^{-1} at a deformation temperature of 1200 °C is ~7 °C and ~15 °C. It is also observed that temperature distribution along the sample after a strain of 1 is not uniform at 0.25 s^{-1} whereas, it is significantly uniform at high strain rate (2 s^{-1}). This temperature distribution reveals that Hansel-Spittel equation significantly predicts the adiabatic heat generated during the deformation at low and high strain rates in case of as-cast 42CrMo alloy.

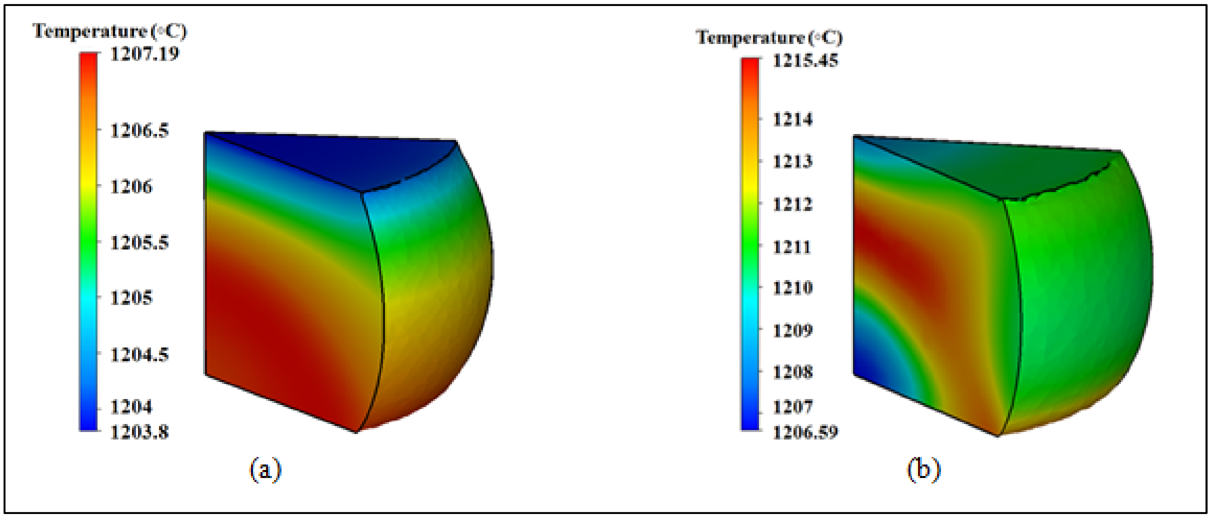

Figure 2.2 Simulated temperature distribution map of 42CrMo at strain rate of (a) 0.25 s^{-1} and (b) 2 s^{-1} at deformation temperature of 1200 °C

To verify the accuracy this model further, force versus time analysis was compared. Fig. 2.3 shows the force versus time plot of predicted and experimental data. From the plots, it was found that at lower strain rates, Fig. 2.3 (a), the difference in predicted and experimental values is 17%, whereas at higher strain rate, Fig. 2.3 (b), the difference shoots up to 37%. The indifference in the force reading between the experimental and predicted result is mainly due to the effect of friction during hot compression. It is well-known fact that friction plays a major role in stress-strain plots during hot compression (Yunping, Onodera et Chiba, 2010). From the experimental values, it was calculated that the friction effect was more at higher strain rates as compared to lower strain rates, which may have been the major cause of this deviation.

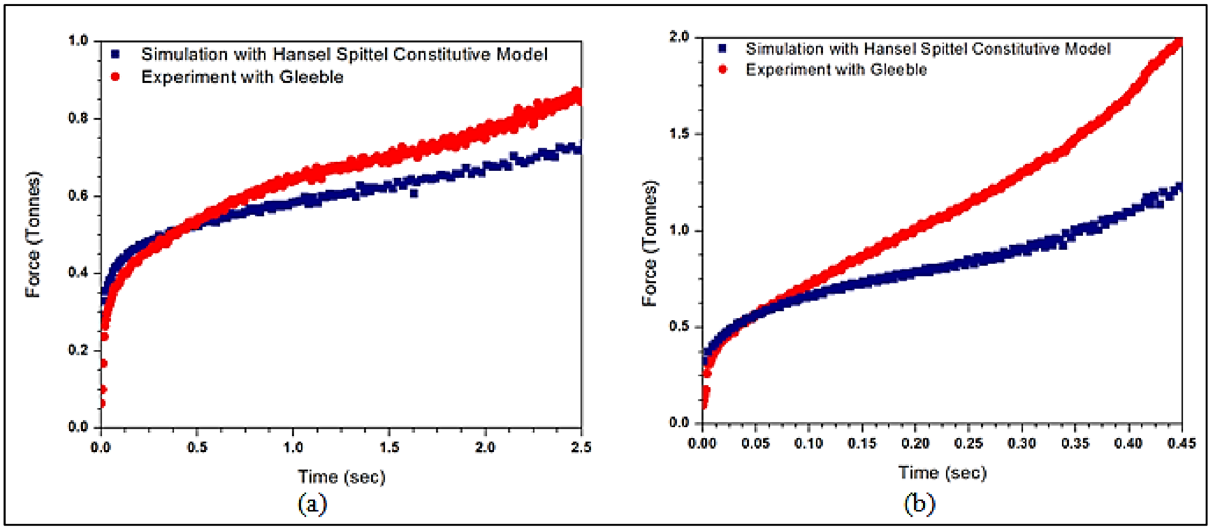

Figure 2.3 Force versus time plot of experimental and predicted at strain rate (a) 0.25 s^{-1} and (b) 2 s^{-1} at deformation temperature of 1200 °C.

2.6 Conclusions

1. Hot compression of as-cast 42CrMo alloy reveals that at low strain rates, dynamic recrystallization occurs, whereas at high strain rates recovery occurs.
2. Hansel-Spittel equation fairly predicts the flow curves up to peak stress. However, it is not able to predict softening of flow stress due to dynamic recrystallization.
3. Simulation results reveal that the model is able to predict the adiabatic heating during deformation, whereas it is not able to predict the force with the time.

CHAPTER 3

CONSTITUTIVE MODELLING OF INGOT BREAKDOWN PROCESS OF LOW ALLOY STEELS

Kanwal Chadha, Davood Shahriari, and Mohammad Jahazi

Department of Mechanical Engineering, École de Technologie Supérieure,
1100 Notre-Dame West, Montreal, Quebec, Canada H3C 1K3

Paper published in *La Metallurgia Italiana - International Journal of the Italian Association for Metallurgy*, April 2016

Abstract: In industrial ingot forging processes, the materials are subject to complex strain, strain-rate, and temperature histories. Understanding the behavior of the cast ingot during ingot breakdown operation during which the cast microstructure is converted into a wrought one, is of critical importance as it has a determining effect on the quality of the forged product. Finite element modeling (FEM) is a powerful numerical tool that can be used for the design or optimization of the ingot breakdown processes. However, the success in the application of FEM codes relies on the definition of an accurate plastic constitutive model used for the investigated alloy. Phenomenological constitutive models provide a definition of the flow stress based on empirical observations and their descriptions in the form of some mathematical functions. In this research, Arrhenius-Garofalo's equation is used as a constitutive model to generate the stress-strain curves of the forged material from the dendritic microstructure of a cast ingot made of medium carbon low alloy steel. The hyperbolic law in Arrhenius equation is most widely used to describe the relationship between the strain rate, flow stress and temperature, especially at high temperatures which can be represented by Zener-Hollomon parameter. In the current study, activation energy and other material constants are described as a polynomial equation to quantify the dependence of these parameters on the strain. In order to provide accurate predictions of the thermal and mechanical parameters in the actual ingot breakdown operation, hot compression tests were carried out on Gleeble^{TM} 3800 thermomechanical simulator with uniform temperatures ranging from 1050 ºC to 1200 ºC and strain rates from 0.25 s^{-1} to 2 s^{-1}, these being

representatives of the operating conditions of the application case. In particular, static and dynamic recrystallization which depend on energy stored in the grains were observed during hot deformation. The results show that the true stress-strain curves exhibit a peak stress at low strain rates when deformed at high temperatures, characteristic of dynamically recrystallized materials. Deformation at lower temperatures and at low strain rates resulted in strain hardening with no softening at any strain. The results demonstrate the significant influence of the choice of ingot breakdown parameters on the flow stress behavior such as peak flow stress, steady-state stress, deformation corresponding to peak and steady-state stresses.

3.1 Introduction

Hot workability is usually defined as the amount of deformation that a material can undergo without cracking and reach desirable mechanical properties and microstructure at a given temperature and strain rate. It is an important property to estimate the material's plastic deformation ability, which is generally evaluated by various parameters like strain rate, strain and temperature. In order to give a material a desired shape and property, hot deformation process is applied. The beginning stage of material processing starts with the casting process, after which forging is done till the desired shape.

Forging of a cast ingot starts with ingot breakdown process which is generally performed at very high temperatures (0.75 of melting point "M_P") so as to breakdown the chemical (macrosegregation) and microstructural (as-cast dendritic) inhomogeneity (Dieter, Kuhn et Semiatin, 2003). Flow characteristic of a hot forging process consist of strain hardening and softening due to dynamic processes like recrystallization and recovery which basically determines the quality of a forging product. Constitutive relations are often used to model forging process in order to describe the plastic flow properties of metals and alloys. Arrhenius equation is a phenomenological model which is mostly practiced due to the fact that it has reasonable number of material constants with limited experimental results. It was proposed by Jonas et al.(Jonas, Sellars et Tegart, 1969a). It is based on simple relation on three variables like strain, strain rate and temperature. However, the effect of strain was not introduced in the equation which was later modified by Sloof et al. (Slooff et al., 2007). This new model proved effective in predicting both hardening and softening characteristics. Many research groups have attempted to develop constitutive equations using Arrhenius model to describe the flow behavior of various alloys using experimental data. (Lin, Chen et Zhong, 2008a; 2008b; Lin et al., 2015; Rao et Hawbolt, 1992; Xiao et al., 2012). Despite large efforts being made on the development of constitutive equations for 42CrMo, further investigation has to be done describing the behavior of 42CrMo in its as-cast structure at very high temperatures (~0.7 Mp) so as to describe the flow behavior during the ingot breakdown process. Therefore, the objective of this study is to investigate the nature of the influence of strain rate and temperature on compressive deformation characteristics of as–cast 42CrMo using hot compression tests. A model describing the relationship between flow stress, strain rate, strain and temperature is proposed and used to simulate real time analysis of the process using Forge NxT 1.0® software which has not been done till date with the present model. The simulation results thus generated using the constitutive relations will be further used to analyze the adiabatic heating and force calculation in order to validate the model.

3.2 Experimental

The material used for the current investigation was an as-cast 42CrMo high strength steel. The composition of the alloy is shown in Table 3.1. The materials were provided by Finkl Steel Co., Sorel Tracy, Quebec, Canada. Cylindrical specimens were machined with a diameter of 10 mm and a height of 15 mm. Hot compression tests were performed in Gleeble 3800® Thermomechanical Simulator at four different temperatures (1050, 1100, 1150 and 1200 °C) and four strain rates (0.25, 0.5, 1 and 2 s^{-1}). The heating rate was 2 °C/sec till 1260 °C where it was maintained for 300 s so as to get homogenous temperature over the specimen. The specimen was then cooled to a respective deformation temperature at a cooling rate of 1 °C/sec.

Table 3.1 Composition of as-cast 42CrMo (Wt.%)

C	Mn	Si	Mo	Cr	Ni	Other
0.35	0.84	0.41	0.44	1.90	Added	Microalloying

3.3 Results and Discussions

In the present paper, results from deformation temperature of 1200 °C and 1150 °C at strain rates of 0.25 s^{-1} and 2 s^{-1} are considered. Stress-strain curve of hot compression tests (Fig. 3.1 ((a) & (b)) reveals that at low strain rates, dynamic softening mechanisms get activated and results in a stress drop after a peak stress. This is a typical recrystallization curve (McQueen et Jonas, 1975) which comprises of four stages due to the effect of work hardening and softening mechanisms as shown in Fig. 3.1 (c).

Stage I: Work hardening due to DRV (Work Hardening is higher than softening rate)
Stage II: Transition Stage (Work hardening is compensated by DRV and DRX)
Stage III: Softening (Stress Drops steeply due to mechanisms like DRV and DRX)
Stage IV: Steady state (Stress becomes steady due to balance between softening and hardening).

At high strain rates, the flow curves rise sharply and then attains a steady state. This type of flow curve resembles that of recovery behavior due to which the flow stress attains a steady state due to dislocation generation and annihilation process running simultaneously. Dislocations are particularly needed to build a reservoir of stored energy. This stored energy along with the thermal energy is required for breaking down the coarse grains and generating much finer recrystallized grains. High temperatures along with the dissolution of precipitates provide sufficient driving force for dislocation annihilation and thus softening can be seen as in Fig. 3.1 at a strain rate of 0.25 s^{-1}. However higher strain rates do not show softening even at high temperatures due to the fact that critical driving force has not reached because of high Zener Hollomon factor, Z (McQueen et Jonas, 1975). Low strain rates promote sufficient driving force for dislocation annihilation and thus softening can be seen in Fig. 3.1 (a).

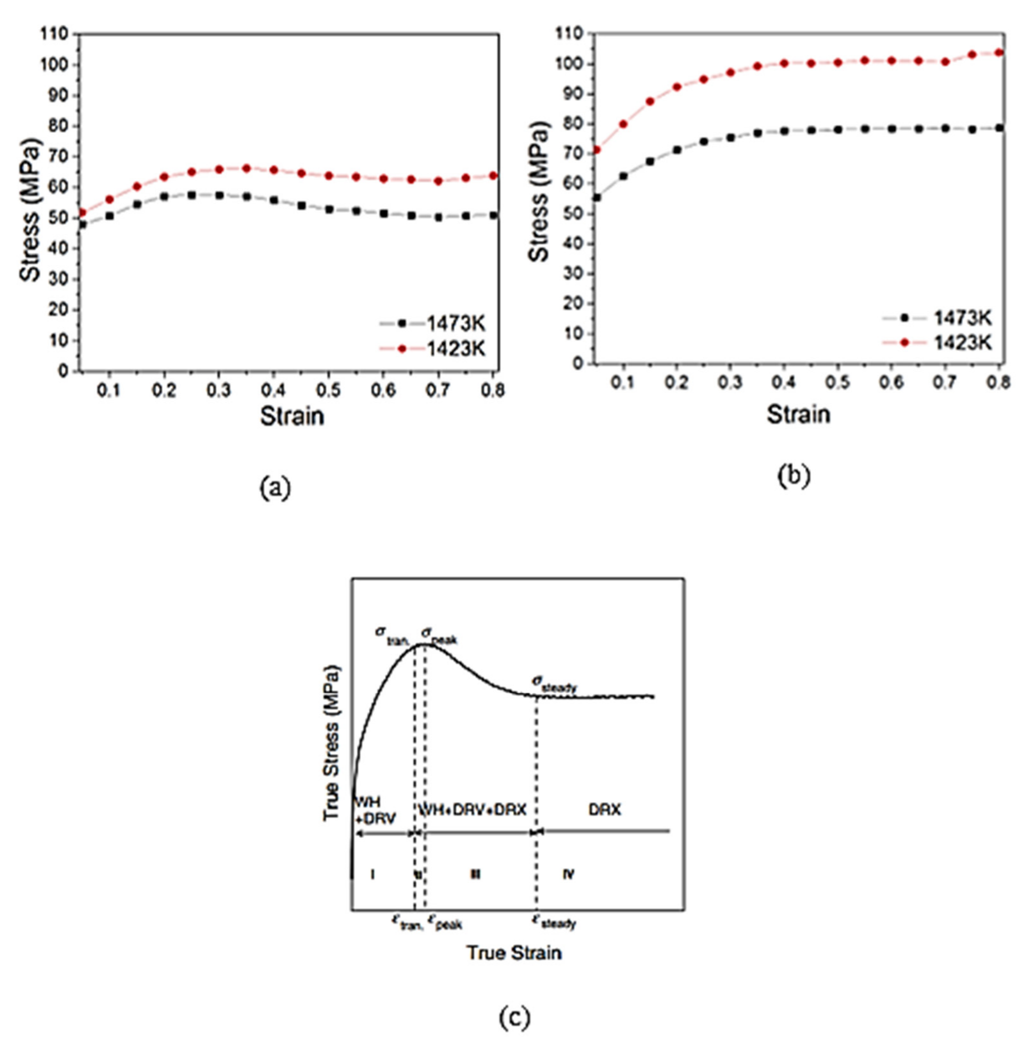

Figure 3.1 Experimental flow curves at a temperature of 1473K and 1423K at strain rate of (a) 0.25 s^{-1} and (b) 2 s^{-1}. (c) Typical flow stress curve at the elevated temperature (Lin, Chen et Zhong, 2008a)

3.4 Constitutive Equation of the flow stress

To investigate the deformation behavior of as-cast 42CrMo steel, there is a need to develop constitutive equations in order to simulate the process of ingot breakdown process. Material constants of the constitutive equation can be derived from the stress-strain data obtained from the hot compression tests. To simulate bulk metal forming, Forge NxT 1.0® software is used which generally uses thermo-viscoplastic constitutive models under hot conditions.

The effect of deformation temperature and strain rate on the deformation behavior can be expressed by Zener – Hollomon parameter (Z) (McQueen et Jonas, 1975) in an exponential form as follows:

$$Z = \dot{\varepsilon}\exp(\frac{Q}{RT}) \tag{3.1}$$

where, $\dot{\varepsilon}$ = Strain Rate, T= Deformation Temperature (K), Q is the activation energy for deformation (KJmol^{-1}), R is the universal gas constant (8.314 Jmol^{-1}K^{-1}).

Arrhenius-type model (Xiao et al., 2012) is used to describe the relationship between flow stress, deformation temperature and strain rate during high temperature deformation. It is given by

$$\dot{\epsilon} = AF(\sigma)\exp(-\frac{Q}{RT}) \tag{3.2}$$

Where:

$$\begin{aligned} F(\sigma) &= \sigma^{n_1} && (\alpha\sigma < 0.8) \\ F(\sigma) &= \exp(\beta\sigma) && (\alpha\sigma > 1.2) \\ F(\sigma) &= [\sinh(\alpha\sigma)]^{n} && (\text{for all } \sigma) \end{aligned} \tag{3.3}$$

It can be noted that the Eq. (3.2) does not take into the account deformation strain which has a significant impact on the flow stress, especially at the initial stage of deformation. In order to compensate this, the effect of strain accounted in order to increase the accuracy of the prediction and will be used in Eq. (3.8). In the present research, the data of flow stress, temperature and strain rate for the true strain between 0.05 to 0.8 with an interval of 0.05 were used for the construction of constitutive equations.

In order to find the constants, the value of *F(σ)* is put into Eq. (3.2) which gives the relationship of low-level stress ($\alpha\sigma < 0.8$) and high-level stress ($\alpha\sigma > 1.2$).

$$\dot{\varepsilon} = B\sigma^{n_1}$$
$$\dot{\varepsilon} = B' \exp(\beta\sigma) \tag{3.4}$$

B, B' and n_1 are material constants which are independent of deformation temperatures. These constants can be calculated by taking logarithm on both sides of Eq. (3.4).

$$\ln\sigma = \frac{ln\dot{\varepsilon}}{n_1} - \frac{lnB}{n_1}$$
$$\sigma = \frac{ln\dot{\varepsilon}}{\beta} - \frac{lnB'}{\beta} \tag{3.5}$$

In the present research, the strain of 0.05 is shown in order to show the solution procedures of the material constants. Plotting graphs of $ln\sigma$ vs $ln\dot{\varepsilon}$ and σ vs $ln\dot{\varepsilon}$, by linear regression method give the values of n_1 and β. The values are calculated using the average values of slope of parallel lines from different temperatures. Putting these values, the value of $\alpha = \beta / n_1$ can be found.

To calculate the value of Q, taking logarithm on both sides of Eq. (3.2) of the function for all values of stress and assuming it as independent of temperature.

$$\ln[sinh(\alpha\sigma)] = \frac{1}{n} ln\dot{\varepsilon} + \frac{Q}{nRT} - \frac{1}{n} lnA \tag{3.6}$$

Taking $ln\dot{\varepsilon}$ and 1/T are considered as two independent variables. Differentiating the above equation,

$$Q = nR \frac{\partial ln\dot{\varepsilon}}{\partial \ln[\sinh(\alpha\sigma)] \boldsymbol{T}} \tag{3.7}$$

$$n = \frac{\partial \ln[\sinh(\alpha\sigma)]}{\partial\left(\frac{1}{T}\right)} \dot{\boldsymbol{\varepsilon}}$$

(T and $\dot{\varepsilon}$ taken as independent variables)

Using this equation, plots of $\ln[\sinh(\alpha\sigma)]$ - $ln\dot{\varepsilon}$ and $\ln[\sinh(\alpha\sigma)]$ - $\left(\frac{1}{T}\right)$ can be generated and subsequently the value of *n* and *Q* can be found using regressed analysis of results from Fig. 3.3 ((a) & (b)). The value of the constant ln$A$ can be found from the intercept of $\ln[\sinh(\alpha\sigma)]$ - $ln\dot{\varepsilon}$ plots.

After calculating the constants $(\alpha, n, Q\ and\ A)$ in the above equation, the flow stress can be obtained. Eq. (3.2) does not take into account the effect of strain. Effect of strain is apparent on the flow stress due to the effect of strain hardening and softening. Therefore, in order to predict the flow stress, strain is compensated in material constants $(\alpha, n, Q\ and\ A)$ by:

$$\begin{aligned} \alpha &= B_0 + B_1\varepsilon + B_2\varepsilon + \cdots \ldots \ldots + B_m\varepsilon^m \\ n &= C_0 + C_1\varepsilon + C_2\varepsilon + \cdots \ldots \ldots + C_m\varepsilon^m \\ Q &= D_0 + D_1\varepsilon + D_2\varepsilon + \cdots \ldots \ldots + D_m\varepsilon^m \\ ln\,A &= E_0 + E_1\varepsilon + E_2\varepsilon + \cdots \ldots \ldots + E_m\varepsilon^m \end{aligned} \tag{3.8}$$

The order (*m*) of the polynomial is varied from one to nine. Selection of this polynomial should be done on the basis of analysis correction and generalization. In the present research, the value of the polynomial is taken as *m*=6 and are shown in Fig. 3.4 (a)-(d).

Using hyperbolic sine function, the constitutive model which relates flow stress and Zener-Hollomon parameter can be written as (Samantaray, Mandal et Bhaduri, 2009):

$$\sigma = \frac{1}{\alpha} \ln \left\{ \left(\frac{Z}{A}\right)^{1/n} + \left[\left(\frac{Z}{A}\right)^{\frac{2}{n}} + 1\right]^{1/2} \right\} \tag{3.9}$$

Then, flow stress values were predicted with varying temperature, strain and strain rate were predicted through Eqs. (3.1), (3.2), (3.8) and (3.9) and are presented in Fig. 3.5 in this present research.

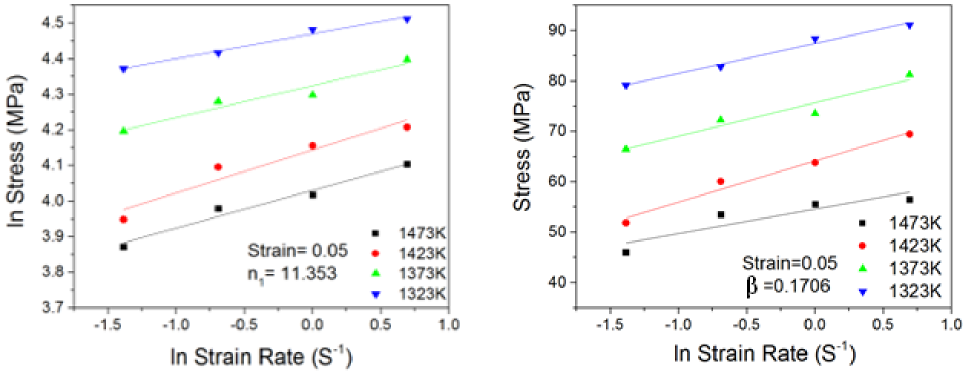

(a) **(b)**

Figure 3.2 Relationship of (a) ln (σ) and ln ($\dot{\varepsilon}$), (b) σ and ln ($\dot{\varepsilon}$)

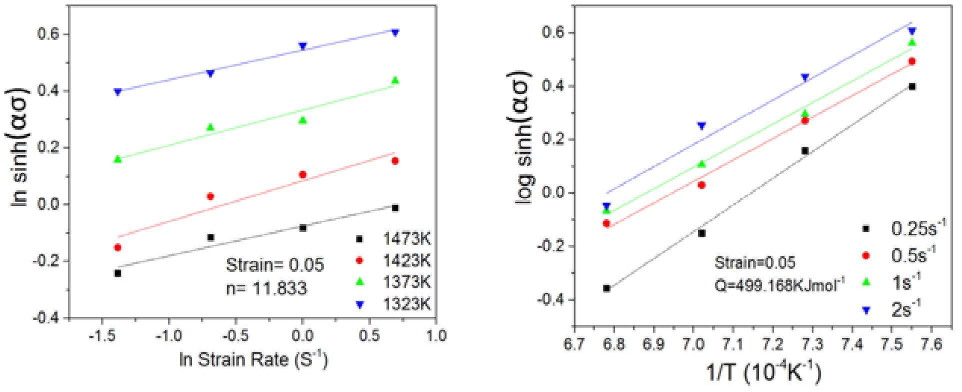

(a) **(b)**

Figure 3.3 Relationship of (a) ln sinh (ασ) and ln ($\dot{\varepsilon}$), (b) Ln sinh (ασ) and 1/T

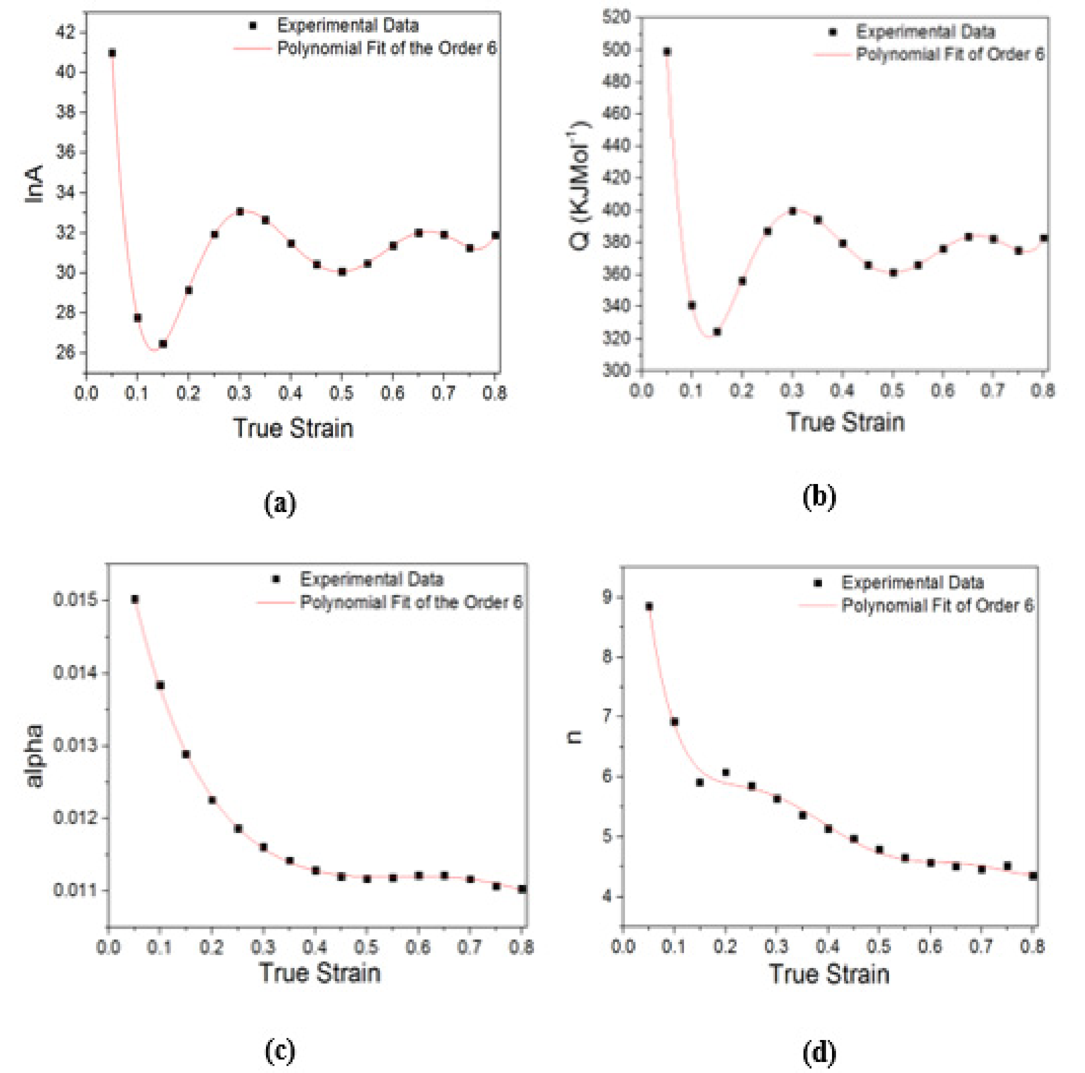

(a) (b) (c) (d)

Figure 3.4 Polynomial fit of variation of (a) *lnA*, (b) *Q*, (c) *α* and (d) *n* with strain

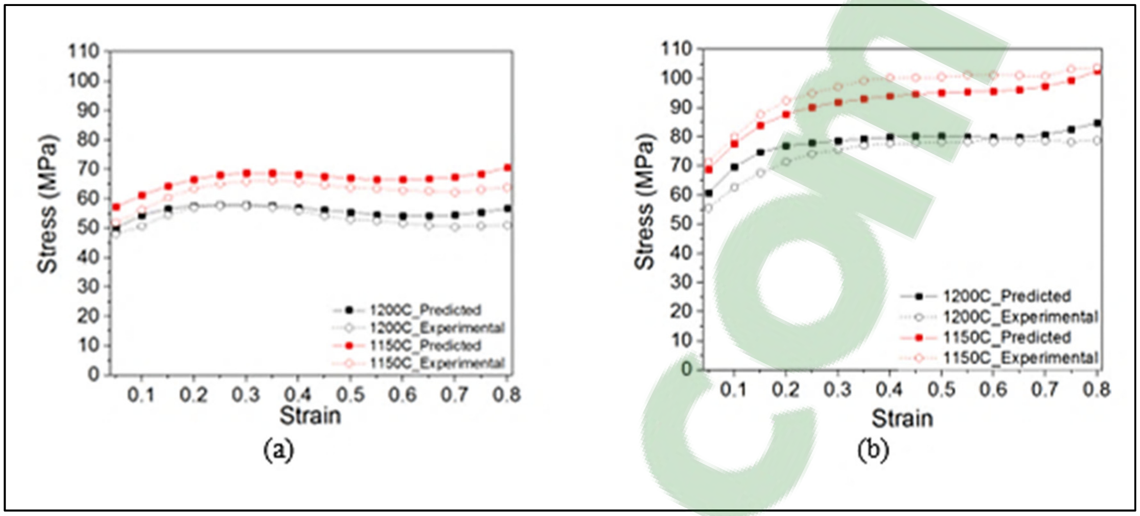

Figure 3.5 Predicted and Experimental flow curves of 42CrMo at a strain rate of (a) 0.25 s^{-1} and (b) 2 s^{-1}

The plots of the predicted and experimental values at temperatures of 1200 °C and 1150 °C and strain rates of 0.25 s^{-1} and 0.5 s^{-1} are shown in Fig. 3.5. It is observed that the Arrhenius equation predicts the stress values throughout the flow curves. It is very interesting to note that the model predicts the softening as well as friction behavior for all experimental data. The difference in the values of predicted and experimental data do not exceed beyond ~6.5% at all the points in the flow curves.

3.5 Numerical simulation of 42CrMo hot forging

Numerical simulations generally consist of various elements which present the real process. Among the various elements, includes the geometrical models of ingot, dies, material model and a set of boundary and initial conditions. The die temperature was kept similar to the deformation temperature. The density of the alloy is 7386.80465 Kg/m^3 and specific heat is 661.94 J/Kg/°K. Arrhenius Model was introduced in Forge NxT 1.0® software and two simulations at different strain rates, 0.25 s^{-1} and 2 s^{-1} at a constant deformation temperature of 1200 °C were conducted. The temperature distribution map for final stage of deformation for strain rate of 0.25 s^{-1} and 2 s^{-1} with deformation temperature 1200 °C is shown in Fig. 3.6. It is apparent from the Fig. 3.6 that temperature distribution in case of higher strain rate is more homogenous than at lower strain rate. Deformation heating is usually generated in any alloy during deformation and is the function of strain rate (Dieter, Kuhn et Semiatin, 2003). This heat generated is usually termed by adiabatic heating and causes higher heat in the sample thereby reducing the flow stress. Adiabatic heating is represented by the following equation:

$$\Delta T_{Adiabatic} = \frac{0.95 \int \sigma d\epsilon}{\rho C_p} \tag{3.10}$$

where ΔT is the change in temperature, $\int \sigma d\varepsilon$ is the area under the uncorrected stress-strain curve, ρ is the density, C_p the specific heat and 0.95 is the fraction of mechanical work transformed into heat with the remaining fraction going to microstructural changes. Adiabatic heat calculated from the experimental data reveals that the temperature at the center at a strain rate of 0.25 s^{-1} and deformation temperature of 1200 °C is 8.24 °C at 0.25 $s^{-1}$and 14.6 °C at 2 s^{-1}. From the simulation results, the adiabatic heat generated due to hot compression at strain rates of 0.25 s^{-1} and 2 s^{-1} at a deformation temperature of 1200 °C is ~8.4 °C and ~19.4 °C. It is also observed that the temperature distribution along the sample after a strain of 1 is not uniform at 0.25 s^{-1} whereas it is significantly uniform at high strain (2 s^{-1}). This temperature distribution reveals that the Arrhenius model predicts reasonably well the adiabatic heat generated during the deformation at low strain rates whereas in case of high strain rate, the difference in experimental and simulated is significantly higher.

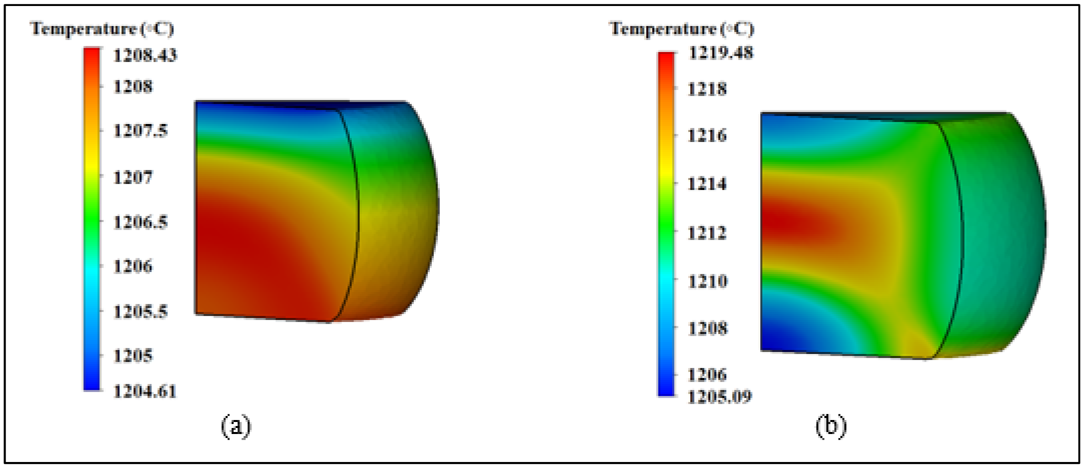

Figure 3.6 Simulated temperature distribution map of 42CrMo at a strain rate of (a) 0.25 s^{-1} and (b) 2 s^{-1} at a deformation temperature of 1200°C

To verify the accuracy this model further, force versus time analysis was compared. Fig. 3.7 shows the force versus time plot of predicted and experimental data. From the plots, it was found that at lower strain rates, Fig. 3.7 (a), the difference in predicted and experimental values is ~4% whereas at higher strain rate, Fig. 3.7 (b), the difference comes down to ~1%. The indifference in the force reading between the experimental and predicted result is mainly due to the effect of friction during hot compression. It is well-known fact that friction plays a major role in stress-strain plots during hot compression (Yunping, Onodera et Chiba, 2010). From the experimental values, it was calculated that the friction effect was more at higher strain rates as compared to lower strain rates, which is completely taken into the account by the Arrhenius Model.

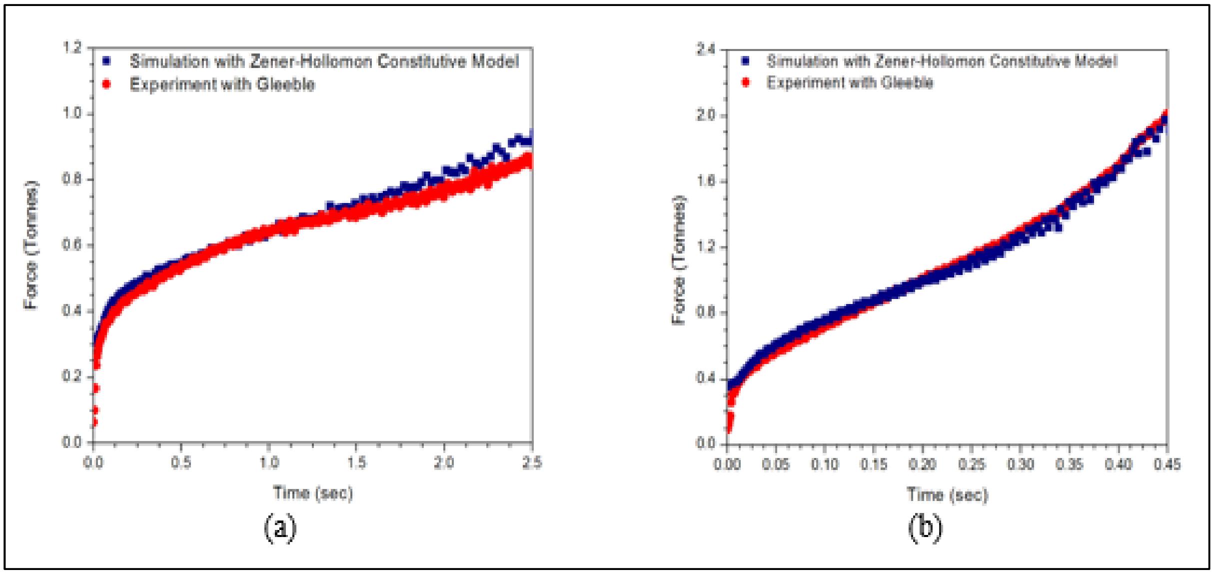

(a)

(b)

Figure 3.7 Force versus time plot of experimental and predicted at strain rate (a) 0.25 s^{-1} and (b) 2 s^{-1} at a deformation temperature of 1200 °C

3.6 Conclusions

1. Hot compression of as-cast 42CrMo alloy reveals that at low strain rates, dynamic recrystallization occurs, whereas at high strain rate recovery occurs.
2. Arrhenius model significantly predicts the flow curves. It is not only able to predict softening of flow stress due to dynamic recrystallization but takes into account the frictional effect at the end of deformation.
3. Simulation results reveal that the model is able to predict the adiabatic heating during deformation at a slow strain rate, but not at higher strain rates, where there is a large variation in values. It can significantly predict the force with the time at both strain rates.

CHAPTER 4

DEFORMATION AND RECRYSTALLIZATION BEHAVIOR OF THE CAST STRUCTURE IN LARGE SIZE, HIGH STRENGTH STEEL INGOTS: EXPERIMENTATION AND MODELING

Kanwal Chadha[a], Davood Shahriari[a], Rami Tremblay[b],
P.P. Bhattacharjee[c], and Mohammad Jahazi[a]

[a] Department of Mechanical Engineering, École de Technologie Supérieure,
1100 Notre-Dame West, Montreal, Quebec, Canada H3C 1K3
[b] Finkl Steel-Sorel Forge, Sorel Tracy, Quebec, Canada
[c] Indian Institute of Technology, Hyderabad, India

Paper published in *Metallurgical and Material Transactions A*, September 2017

Abstract: Constitutive modeling of the ingot breakdown process of large size ingots of high strength steel was carried out through comprehensive thermomechanical processing using Gleeble 3800® thermomechanical simulator, Finite Element Modeling (FEM), optical and Electron Back Scatter Diffraction (EBSD). For this purpose, hot compression tests in the range of 1473K (1200 ºC) to 1323K (1050 ºC) and strain rates of 0.25 s^{-1} to 2 s^{-1} were carried out. The stress-strain curves describing the deformation behavior of the dendritic microstructure of the cast ingot were analyzed in terms of the Arrhenius and Hansel-Spittel models which were implemented in Forge NxT 1.0® FEM software. The results indicated that the Arrhenius model was more reliable in predicting microstructure evolution of the *as-cast* structure during ingot breakdown, particularly the occurrence of dynamic recrystallization (DRX) process which was a vital parameter in estimating the optimum loads for forming of large size components. The accuracy and reliability of both models were compared in terms of correlation coefficient (R) and the average absolute relative error (ARRE).

Keywords: *As-cast* medium carbon low alloy steel, *as-cast* microstructure, constitutive model, FEM simulations, Arrhenius model, Hansel-Spittel model, Forge Nxt 1.0®

4.1 Introduction

Large size forged blocks made of medium carbon low alloy steel are extensively used in the automotive industry as die materials for the production of plastic injection components. In recent years, the demand for ever larger sized dies is continuously increasing. One of the major requirements of the industry is chemical homogeneity, uniform hardness, and grain size throughout the thickness of these large size forged blocks. Ingot casting followed by forging and quench and temper heat treatments are the main manufacturing steps in the production of the large sized blocks (Lin, Chen et Zhong, 2008e). The ingot breakdown process is generally conducted in order to convert the heterogeneous cast structure into a more uniform and refined microstructure. During ingot breakdown, several metallurgical phenomena may result in strengthening or weakening of the alloy. These include, work hardening (WH), phase transformation and precipitation, which often have strengthening effects while dynamic recovery (DRV), metadynamic recrystallization (MDRX), dynamic recrystallization (DRX), static recovery, and static recrystallization result in material softening (Marchattiwar et al., 2013; McQueen et Jonas, 1975; Poliak et Jonas, 2003a; 2003b).

In order to accurately predict microstructure evolution and flow stress behavior during the ingot breakdown process in large sized ingots, development of reliable constitutive models is essential. The constitutive models are usually integrated into FEM software in order to simulate the thermomechanical process of industrial sized ingots. However, very limited number of models have been integrated with the FEM software and therefore their applicability to determine microstructural conditions (*cast* vs. *wrought*) or alloy composition needs to be verified for accurate simulation of the deformation process (Han et al., 2013).

Analytical, phenomenological and numerical models are used to construct constitutive equations for different metals and alloys (Lin et Xiao-Min, 2011). While physics based and numerical models such as Zerilli-Armstrong (Lin et Chen, 2010; Samantaray, Mandal et Bhaduri, 2009), Preston-Tonks-Wallace (Preston, Tonks et Wallace, 2003; Price, Kearsley et

Burchell, 2013), or cellular automation (Li et al., 2012; Sabokpa et al., 2012) models provide accurate representation of the deformation behavior of a metal over large ranges of strain rates and temperatures; however, they require an enormous amount of data in order to derive the large number of material constants and properties which are not generally available in the literature. In contrast, phenomenological models have been investigated by many researchers due to their satisfactory precision, and relatively less number of constants which can be determined using the combination of a limited number of experiments and regression analysis (Lin et Chen, 2011).

Arrhenius (Li et al., 2015; McQueen et Ryan, 2002; Ying et al., 2013) and Hansel-Spittel models (El Mehtedi, Musharavati et Spigarelli, 2014; Hansel A, 1978) have been two of the most known phenomenological models and have been successfully used to predict flow behavior of a large family of alloys. However, these models have been exclusively used for *wrought* alloys and very little data is available for the prediction of stress-strain behavior of alloys in their *as-cast* structure (Li et al., 2015; Lin, Chen et Zhong, 2008a; 2008c; Lin et Liu, 2010; Lin, Ming-Song et Jue, 2008a; 2008c; McQueen et Ryan, 2002). Specifically, Y. Han et al. (Han et al., 2013) and W. Peng et al. (Peng et al., 2013) predicted the flow stress behavior of as-cast 904L steel and as-cast Ti-60 alloy, respectively. In both cases, the material model was based on Arrhenius model and no comparison was made with Hansel-Spittel or any other model. Moreover, Arrhenius model has been extensively used for *wrought* structured alloys and no reports exist for *as-cast* alloys, particularly for medium carbon steels like 42CrMo steel, where the maximum mean error between experimental and predicted results of peak stress of less than 2% have been reported (Lin, Ming-Song et Jue, 2008a; 2008c; Lin et Xiao-Min, 2011; Yuan-Chun et al., 2014). In most of the referenced studies, dynamic recovery and dynamic recrystallization behavior during hot deformation were predicted by the Arrhenius model. Hansel-Spittel model, on the other hand, has been employed in existing FEM packages (El Mehtedi, Musharavati et Spigarelli, 2014) and no reports are available on its development for predicting flow behavior during hot deformation for *as-cast* structured materials. Integration with FEM software in order to do simulations has been rarely investigated for Arrhenius model, whereas a few reports do exist for FEM simulations using Hansel-Spittel model (Duan et Sheppard, 2004; Marie et al., 2014; Opla et al., 2014). It is still unclear which type of constitutive equation would best describe the deformation behavior of an *as-cast* structure (the ingot breakdown stage) and particularly the occurrence of the different softening processes that take place, bringing major microstructural evolution during the conversion of the *cast* structure to a *wrought* structure. The wrought structure formed after the ingot breakdown stage will have a determining effect on the final properties of the forged block and therefore microstructure evolution from *as-cast* to *wrought* condition needs to be accurately quantified and the optimum material model and constants need to be identified.

In the present work, a combination of experimentation and simulation is used to study the constitutive behavior of the *as-cast* structure of a medium carbon high strength low alloy steel simulating the ingot breakdown process of large size forged ingots used as die material in the transport industry. The model which can better anticipate the flow curves during the deformation of an *as-cast* structure is determined. Specifically, Arrhenius and Hansel-Spittel constitutive models are developed using hot compression tests and then incorporated in FEM code Forge NxT 1.0®. The simulation results thus generated are further utilized to analyze the adiabatic heating and force vs. time analysis. In order to define the pertinence and the robustness of a broader range of deformation conditions, especially for large sized ingots where the temperature and strain rate varies from surface to center, stress-strain predictions and FEM simulations are carried out using a new set of experimental data. Similarly, a combination of optical and electron microscopy is utilized to validate the predictions of the models on the occurrence of the softening processes as suggested by the strain-strain curves. The results are compared to those obtained for similar alloys with *wrought* structure reported in the literature and analyzed in the framework of existing theories of recovery and recrystallization.

4.2 Materials and Methods

The material used for the current investigation was *as-cast* medium carbon low alloy steel. The detailed composition of the alloy is shown in Table 4.1.

Table 4.1 Composition of the Alloy

C	Mn	Si	Mo	Cr	Other
0.35	0.84	0.41	0.44	1.90	Microalloying

The materials were provided by Finkl Steel-Sorel Forge, Sorel, Quebec, Canada. Due to high segregation in the hot top region, the area was specifically chosen in order to have a similar chemical composition of the samples. In addition to this, columnar region shown with the letter ″A″ and ″D″ was selected for the present research in order to investigate its deformation characteristics. The specimen’s axis was kept perpendicular to the ingot axis as shown in Fig. 4.1. Cylindrical specimens with a diameter of 10mm and a height of 15 mm were used in order to ensure having the highest number of grains across the section of the specimen.

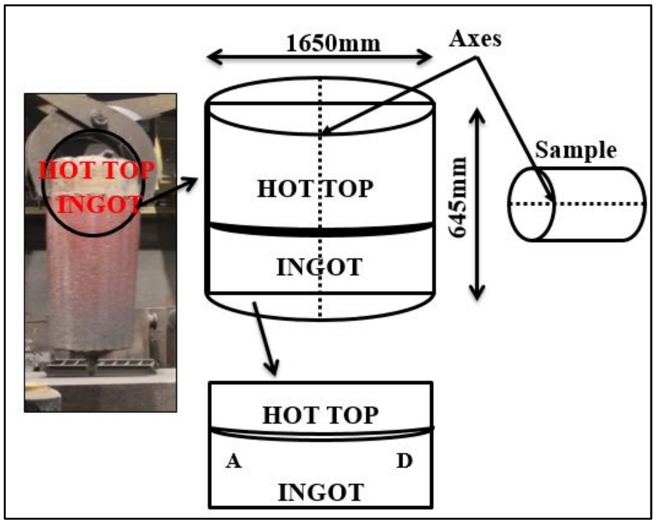

Figure 4.1 Schematic illustration depicting the position of the sample in the industrial sized ingot

As the main carbide forming elements in the investigated alloy are Mo and Cr, thermodynamic software Thermocalc® was used to determine the dissolution and the precipitation temperature of all possible carbides. It was found that all the carbides in this steel are dissolved at around 1273K (1000 °C) thereby confirming no presence of precipitates or carbides in the alloy at the deformation temperatures. In order to reveal initial macrostructure, the specimens were etched by 3% Nital solution and then, were observed using an optical microscope (AM Scope; Model: ZM-1TZ). To reveal microstructure through EBSD, the samples were polished mechanically using conventional techniques and then electropolished at room temperature using a mixture of perchloric acid and ethanol (1:9 by volume).

The electropolishing voltage and time were 25V and 15sec, respectively. The samples were placed in such a way that compression axis was parallel to the incident electron beam. EBSD characterization was performed with FEG-SEM (Carl Zeiss; Model: Supra 40) using TSL-OIM™ software. Hot compression tests were conducted based on the ASTM E209 standards with Gleeble 3800® thermomechanical simulator at four different temperatures, 1323K (1050 °C), 1373K (1100 °C), 1423K (1150 °C) and 1473K (1200 °C) (temperature readings were selected as per the industrial ingot forging using a FLIR® T650sc thermal camera) and four strain rates, 0.25 s^{-1}, 0.5 s^{-1},1 s^{-1} and 2 s^{-1}. The heating rate was maintained at $2Ks^{-1}$ (2 $°Cs^{-1}$) till 1533K (1260 °C) where it was maintained for 300 s. The specimens were then cooled to the deformation temperature at the rate of $1Ks^{-1}$ (1 $°Cs^{-1}$) before being compressed to a true strain of 0.8 and then water quenched immediately to preserve the deformed microstructure. Tantalum sheets of 0.1 mm thickness were used as a lubricant between the sample and the anvils (made of pure tungsten). The schematic diagram of the thermomechanical cycle is shown in Fig. 4.2.

In order to ensure maximum temperature uniformity over the entire length of the specimen, three sets of thermocouples, one at the center and another two at edges as shown in Fig. 4.3 were used to determine the optimum holding time of the target temperature.

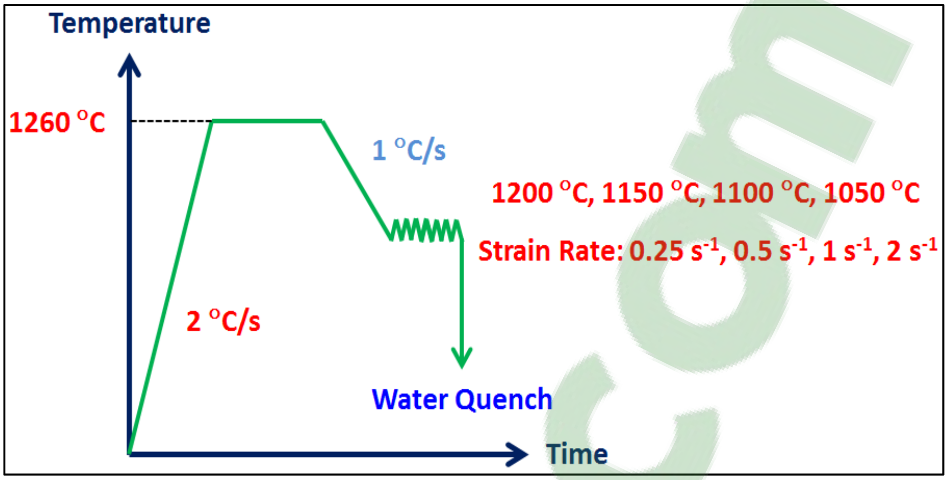

Figure 4.2 Schematic diagram of thermomechanical schedule for hot compression tests of as-*cast* medium carbon low alloy steel

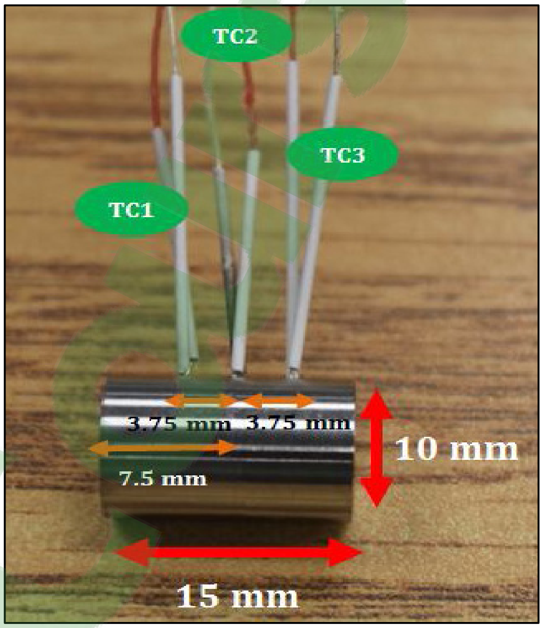

Figure 4.3 Schematic diagram of three thermocouples placed at different regions of the sample for precise measurement of holding time

The specimen was heated from the room temperature till 1533K (1260 °C) using center thermocouple for temperature measurement. At 1533K (1260 °C), the temperature readings of all three thermocouples were recorded and once the target temperature of

1533K (1260 °C) was reached, time was calculated till which all three thermocouples gave the same reading. This confirmed the best time for uniform heat distribution in the specimen. Thus, the time 300 s was used for homogenization in all experiments.

4.3 Results

4.3.1 As-cast microstructure

Fig. 4.4 shows the optical micrograph of the as-cast medium carbon low alloy steel from the columnar region of the ingot which reveals the presence of large sized dendrites with secondary dendrite arm spacing (SDAS) of ~200μm.

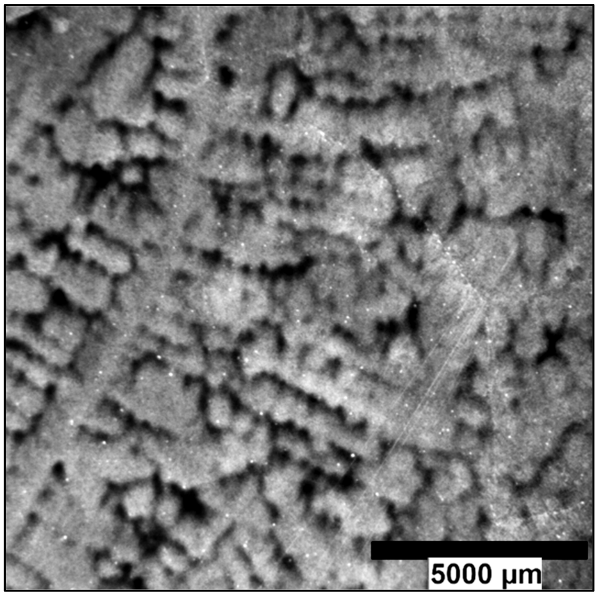

Figure 4.4 Initial macrostructure of *as-cast* medium carbon low alloy steel in the columnar region. The macrostructure consists of large sized dendrites

In order to observe the grains in the dendrites, EBSD was performed. The grain boundary map (Fig. 4.5) revealed that there is no specific grain boundary in the microstructure. In order to verify the influence of the initial coarse microstructure, repetitions of the hot compression test were performed.

The repetition tests at highest deformation temperatures of 1473K (1200 °C) and lowest strain rate of 0.25 s^{-1} do not show a significant change in the flow curves and the data is in the 5 % error range as can be seen in Fig. 4.6. This clarifies the fact that despite the microstructure is coarse, the repetitive curves prove coarseness does not affect the deformation characteristics.

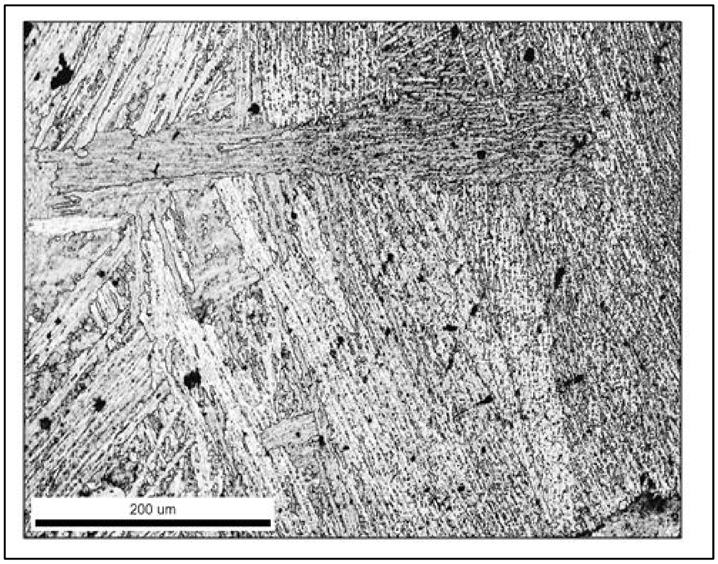

Figure 4.5 EBSD grain boundary map of initial microstructure of *as-cast* medium carbon low alloy steel. Black lines represent HAGBs. The microstructure can be observed with no grain boundaries

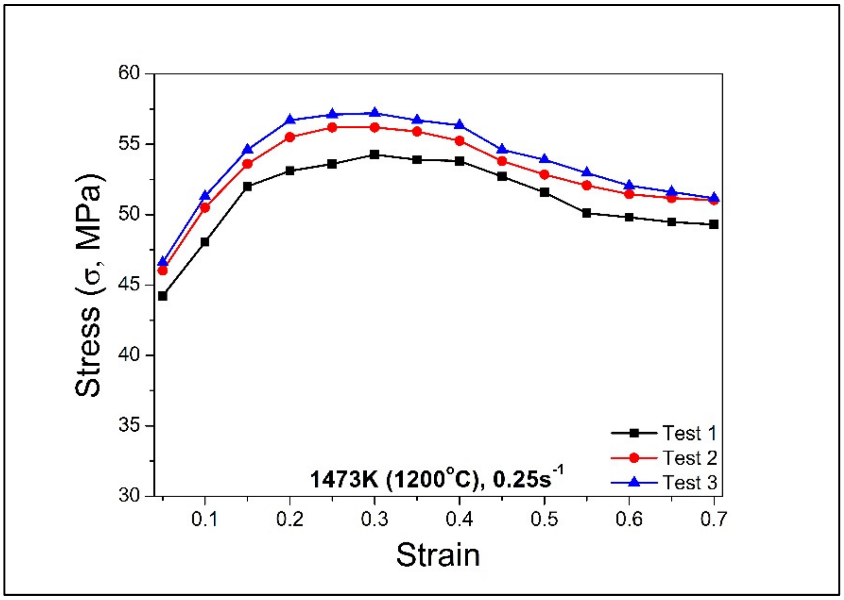

Figure 4.6 Comparison of repeated hot deformation tests at 1473K (1200 °C) and strain rate of 0.25 s^{-1} in order to observe the differences due to coarse microstructure

4.3.2 Flow Curves

For the present research, samples with their axis perpendicular to ingot axis were selected. The influence of the anisotropy of the dendrite orientation versus deformation axis (perpendicular or parallel) has been studied by Semiatin et al. (Semiatin et al., 2004b) in Nickel-based superalloys who observed a difference in the flow behavior from one case to another. While no similar data in available in the literature for steel ingots, the influence of anisotropy on flow behavior is not in the scope of the present research.

Fig. 4.7 depicts the flow curves obtained from the hot deformation tests carried out at temperatures of 1473K (1200 °C) (Fig. 4.7 (a)), 1423K (1150 °C) (Fig. 4.7 (b)), 1373K (1100 °C) (Fig. 4.7 (c)) and 1323K (1050 °C) (Fig. 4.7 (d)) using strain rates of 0.25 s^{-1},0.5 s^{-1}, 1 s^{-1} and 2 s^{-1}. It is observed from the curves that the flow stress increases with increasing strain rate but decreases with increasing deformation temperature. Analysis of the flow curves indicates that at a deformation temperature of 1473K (1200 °C) and 1423K (1150 °C) and for strain rates of 0.25 s^{-1} and 0.5 s^{-1}, the curves exhibit flow softening after initial work hardening. Peak stress was observed at a strain value of ~0.26 for 1473K (1200 °C) and at a strain value of ~0.32 for 1423K (1150 °C). The flow curves at 1473K (1200 °C), 1423K (1150 °C) and for the strain rate of 0.25 s^{-1} and 0.5 s^{-1} show a peak stress followed by a continuous decrease in the flow stress till the maximum strain of 0.8. This behavior is typical of the occurrence of dynamic recrystallization (McQueen et Jonas, 1975; Poliak et Jonas, 2003b).

In contrast, for tests carried out at different temperatures using higher strain rates, i.e. at 1 s^{-1} and 2 s^{-1}, no peak stress can be seen after initial work hardening but a steady state flow stress is observed indicating a balance of work hardening and dynamic recovery (Oh, Semiatin et Jonas, 1992). At deformation temperature of 1323K (1050 °C) and strain rates of 1 s^{-1} and 2 s^{-1} (Fig. 4.7 (d)), work hardening can be observed clearly. This is due to the fact that high strain rates indeed provide enough driving force for the dislocation generation, but low temperatures are insufficient to provide necessary dislocation movement for the annihilation to happen. In addition, due to the presence of alloying elements, precipitation can occur at lower temperatures, which may further pin down the dislocations (Dieter, Kuhn et Semiatin, 2003). In contrast, the flow behavior of similar alloy (42CrMo) during hot deformation in its *wrought* form, showed DRX behavior at all strain rates and temperatures as shown in Fig. 4.8 (Lin, Chen et Zhong, 2008c).

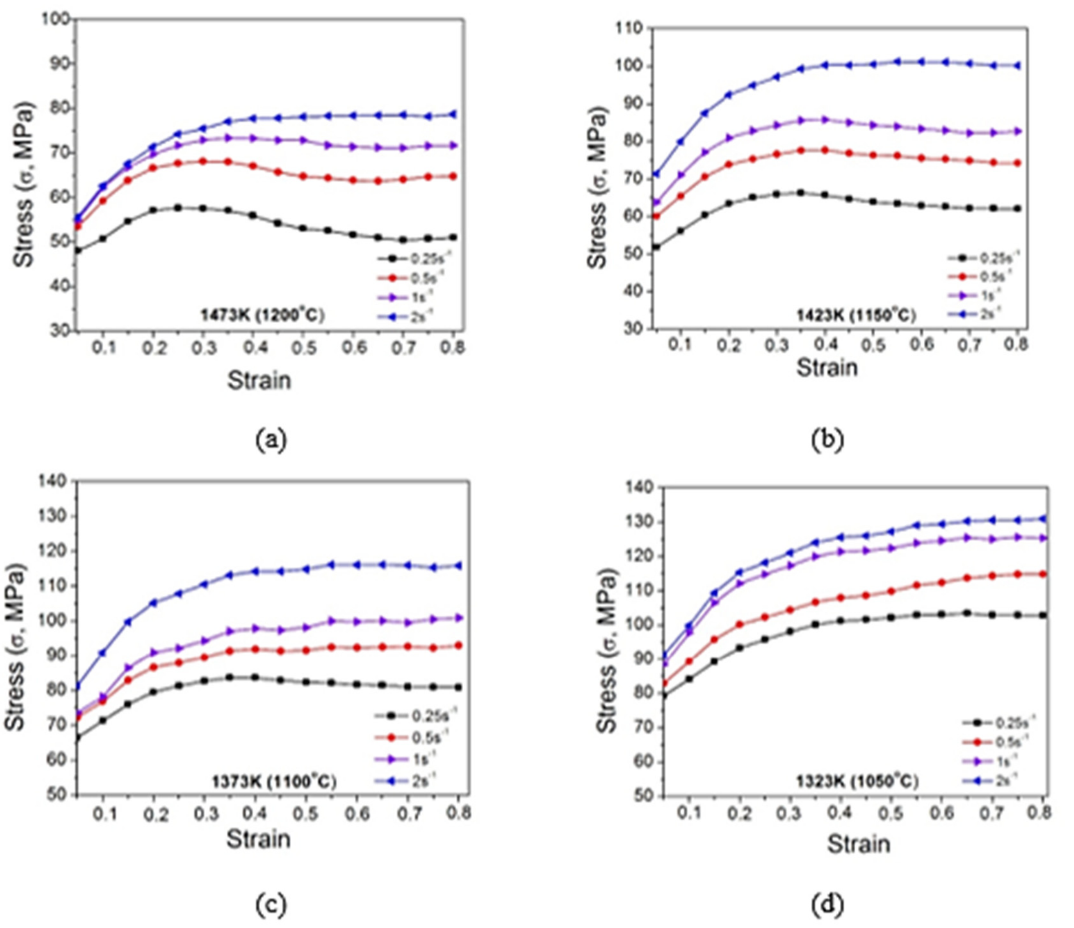

Figure 4.7 Stress-strain curves of *as-cast* medium carbon low alloy steel during hot isothermal compression at strain rates of 0.25 s^{-1}, 0.5 s^{-1}, 1 s^{-1} and 2 s^{-1} at deformation temperatures of (a) 1473K (1200 °C), (b) 1423K (1150 °C), (c) 1373K (1100 °C) and (d) 1323K (1050 °C)

DRX occurred easily at lower strain rates due to longer time for energy accumulation and higher mobilities at boundaries resulting in nucleation, the growth of dynamically recrystallized grains and dislocation annihilation. In addition to this, the peak strain decreased with the decrease in initial austenitic grain size, thereby showing a rapid occurrence of DRX when the grain size is fine because of the higher number of nucleation sites (Chen, Lin et Ma, 2012; Quan et al., 2011).

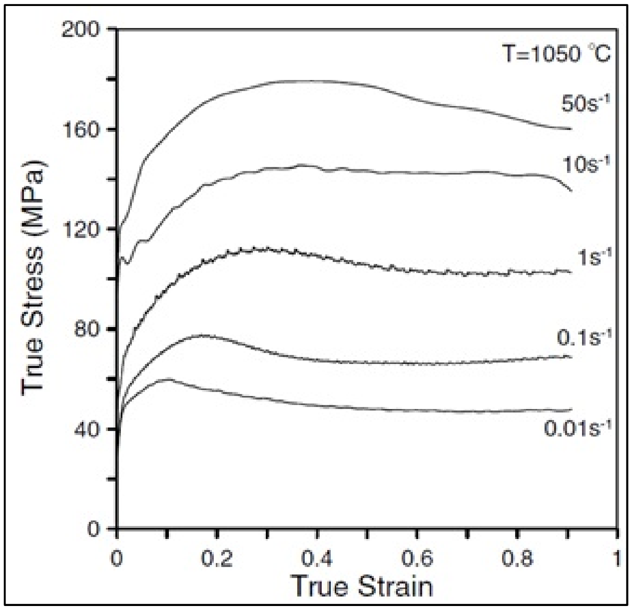

Figure 4.8 Typical stress-strain curve of *wrought* 42CrMo steel under different deformation temperatures and strain rates

4.4 Constitutive Equations

4.4.1 Arrhenius Equation

The effect of deformation temperature and strain rate on the deformation behavior can be expressed by Zener-Hollomon parameter (Z) (McQueen et Jonas, 1975) as follows:

$$Z = \dot{\varepsilon} \exp(\frac{Q}{RT}) \tag{4.1}$$

Where, $\dot{\varepsilon}$ = strain rate (s^{-1}), T= deformation temperature (K), Q = activation energy of deformation ($KJmol^{-1}$) and R is the universal gas constant (8.314 $Jmol^{-1}K^{-1}$).

Arrhenius-type model (Xiao et al., 2012) is used to describe the relationship between flow stress, deformation temperature and strain rate during high temperature deformation. It is given by,

$$\dot{\epsilon} \ = AF(\sigma)\exp(-\frac{Q}{RT}) \tag{4.2}$$

Generally, *F (σ)* is in the form of power function or exponential function or hyperbolic sine function as listed below:

$$\begin{aligned} &F(\sigma) = \sigma^{n_1} && (\alpha\sigma < 0.8) \\ &F(\sigma) = \exp(\beta\sigma) && (\alpha\sigma > 1.2) \\ &F(\sigma) = [\sinh(\alpha\sigma)]^{n} && (\text{for all } \sigma) \end{aligned} \tag{4.3}$$

Where, A, n_1, n, α and β are the material constants, with $\alpha = \beta / n_1$.

In the present research, the data of flow stress, temperature and strain rate for the true strain between 0.05 to 0.8 with an interval of 0.05 was used for the construction of constitutive equations**.** The values of material constants, A, n_1, n, α and β were calculated using regression analysis and are shown in Figs. 4.9 and 4.10 (The details of the calculation of the constants are described in Appendix A). The constants were calculated without taking into account the effect of strain. The effect of strain is apparent in the flow stress due to the effect of strain hardening and softening. Therefore, in order to predict the flow stress, strain is compensated in material constants ($\alpha, n, Q \ and \ A$) by:

$$\begin{aligned} \alpha &= B_0 + B_1\varepsilon + B_2\varepsilon^2 + \cdots \dots \dots + B_m\varepsilon^m \\ n &= C_0 + C_1\varepsilon + C_2\varepsilon^2 + \cdots \dots \dots + C_m\varepsilon^m \\ Q &= D_0 + D_1\varepsilon + D_2\varepsilon^2 + \cdots \dots \dots + D_m\varepsilon^m \\ ln\, A &= E_0 + E_1\varepsilon + E_2\varepsilon^2 + \cdots \dots \dots + E_m\varepsilon^m \end{aligned} \tag{4.4}$$

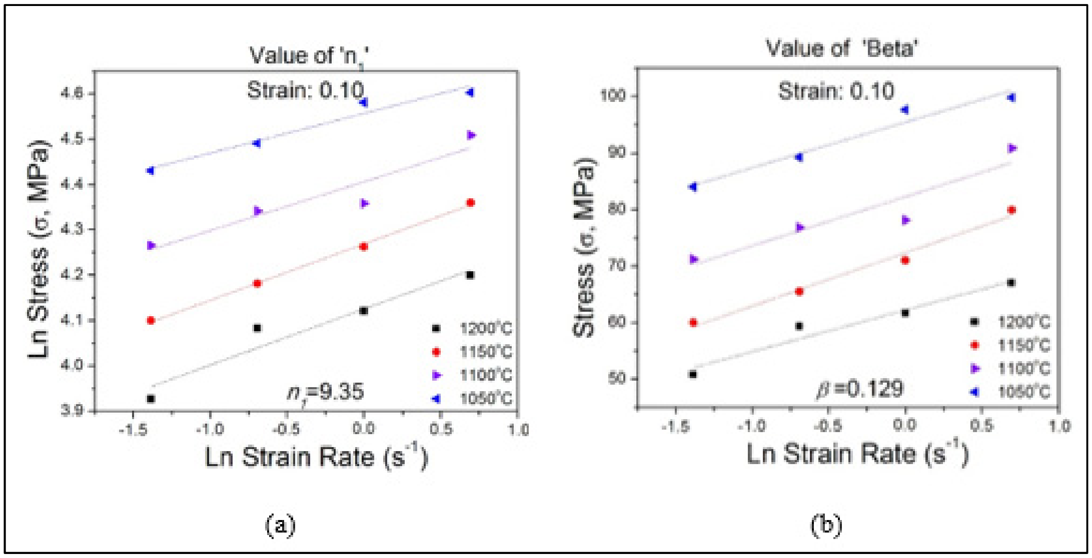

(a)

(b)

Figure 4.9 Relationship between (a) $ln\sigma$ vs $ln\dot{\varepsilon}$ and (b) σ vs $ln\dot{\varepsilon}$ at a strain of 0.10 and deformation temperatures of 1473K (1200 °C), 1423K (1150 °C), 1373K (1100 °C) and 1323K (1050 °C) of *as-cast* medium carbon low alloy steel

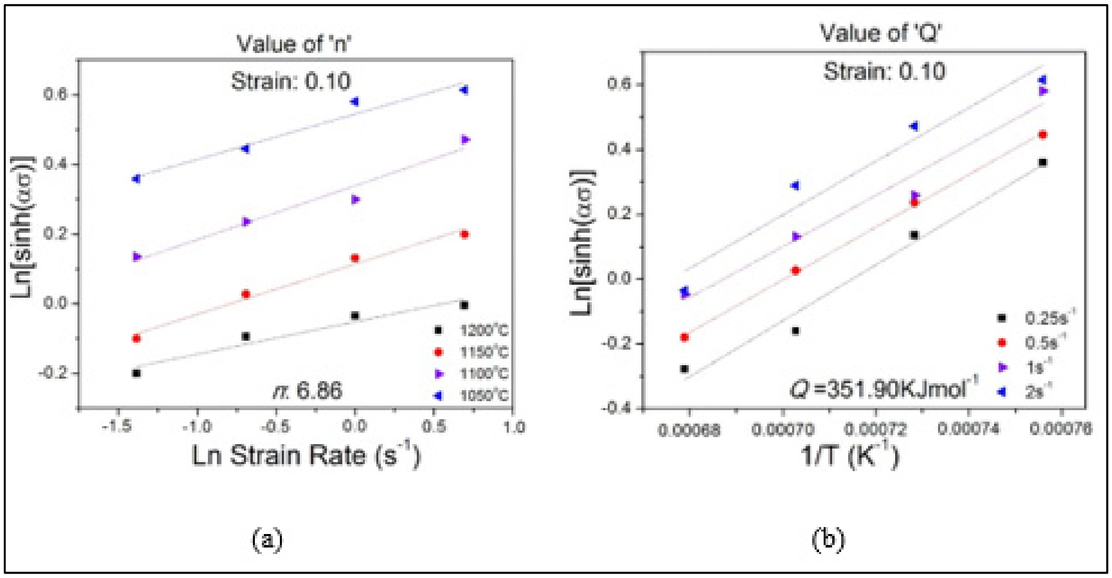

(a)

(b)

Figure 4.10 Relationship between (a) $\ln[sinh(\alpha\sigma)]$-$ln\dot{\varepsilon}$ (b) $\ln[sinh(\alpha\sigma)]$-$\left(\frac{1}{T}\right)$ at a strain of 0.10 and deformation temperatures of 1473K (1200°C), 1423K (1150 °C), 1373K (1100 °C) and 1323K (1050 °C) of *as-cast* medium carbon low alloy steel

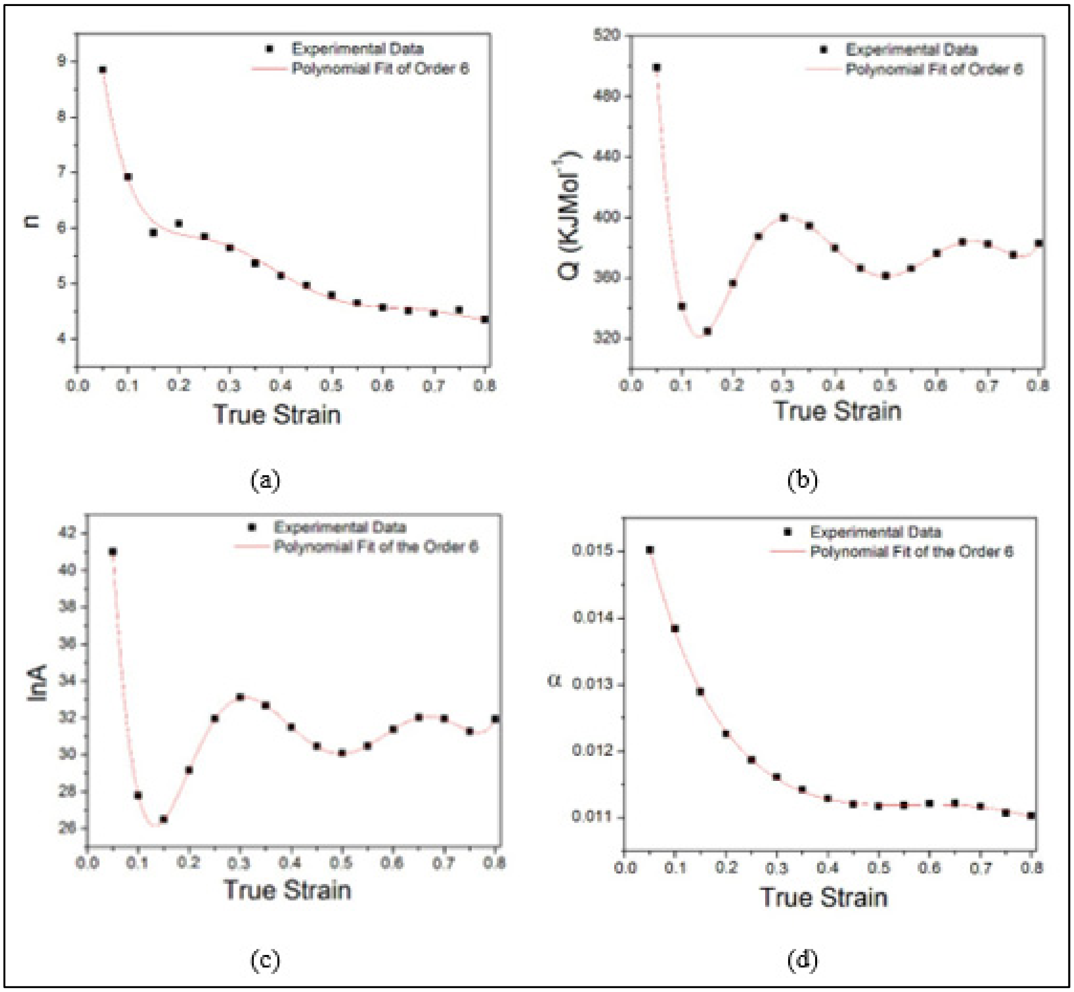

Figure 4.11 Polynomial fit of order 6 of variation of (a) *n*, (b) *Q*, (c) lnA and (d) α for hot compressed *as-cast* medium carbon low alloy steel. Black lines denote experimental data and red line denotes polynomial data

The order (*m*) of the polynomial varies from one to nine (Jonas et al., 2013; Poliak et Jonas, 1996). Selection of the '*m*' value is done on the basis of analysis correction and generalization. As shown in Fig. 4.11 (Chadha, Shahriari et Jahazi, 2016), in the present research, 6th order polynomial (*m*=6) provided the optimum correlation with the experimental results. An illustrative example of the 6th order is shown in Fig. 4.12 for activation energy, *Q* at a strain of 0.05. The values of the constants at strain value, $\varepsilon = 0.1$ have been mentioned in Table 4.2.

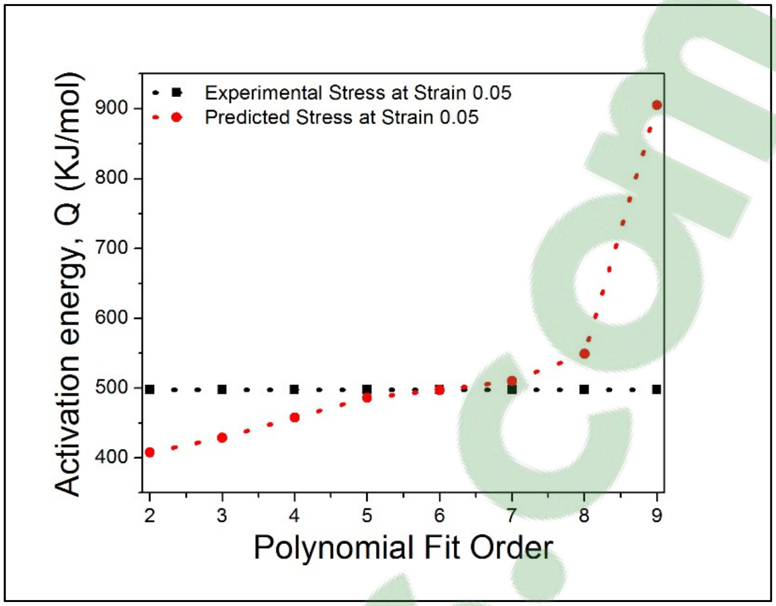

Figure 4.12 Graph of polynomial fit order (m) vs. activation energy, depicting the experimental and predicted values of activation energy, Q at a strain of 0.05

Table 4.2 Material constants in the Arrhenius model at strain, ε=0. 1

β(MPa^{-1})	n_1	α(MPa^{-1})	n	Q (KJmol^{-1})	lnA (s^{-1})
0.129	9.35	0.013	6.861	351.190	27.822

Using hyperbolic sine function, the constitutive model which relates the flow stress and Zener-Hollomon parameter can be written as (Samantaray, Mandal et Bhaduri, 2009):

$$\sigma = \frac{1}{\alpha}\ln \{(\frac{Z}{A})^{1/n} + \left[\left(\frac{Z}{A}\right)^{\frac{2}{n}} + 1\right]^{1/2}\} \tag{4.5}$$

Then, the flow stress values may be predicted with varying temperature, strain and strain rate through Eqs. (4.1), to (4.5) and are presented in Fig. 4.13.

4.4.2 Hansel-Spittel Model

Hansel-Spittel equation (Hansel A, 1978) (Eq. (4.5)) has many constants as compared to Arrhenius equation which needs to be calculated in order to derive the constitutive model. It is given by:

$$\sigma = A_o e^{m_1 T} \varepsilon^{m_2} \dot{\varepsilon}^{m_3} e^{\frac{m_4}{\varepsilon}} (1+\varepsilon)^{m_5 T} e^{m_6 \varepsilon} \dot{\varepsilon}^{m_7} T^{m_8} \qquad (4.6)$$

Where, $\sigma =$ stress (MPa), ε = strain, $\dot{\varepsilon}$ = strain rate (s^{-1}), T= deformation temperature (°C), A is the material consistency at given temperature (isothermal conditions assumed here), m_1 to m_8 define the material parameters. Usually, constants m_7 and m_8 are taken as zero (El Mehtedi, Musharavati et Spigarelli, 2014).

In order to calculate the material constants, multi-linear regression analyses were performed using Matlab® and Origin® 2015 software and are provided in Table 4.3. The constants were then used in the equation for various values of strain, strain rate and temperature in order to find the corresponding values of stress.

Table 4.3 Material constants of Hansel-Spittel model

A_o	m_1	m_2	m_3	m_4	m_5	m_6
8.3771	-0.00294	0.260017	0.142358	0.000101	-0.00157	0.70074

Fig. 4.13 shows the comparison between the stress values derived from both models. It can be seen that the Arrhenius model can precisely track the experimental data over the entire deformation temperature range of 1473K (1200 °C) to 1323K (1050 °C). The model takes into account the dynamic softening behavior of the material, which can be observed at high temperatures and low strain rates. The effect of recovery and strain hardening is also significantly predicted by this model. In contrast, the flow stress predicted using the Hansel-Spittel model shows significant differences in the experimental values. Specifically, the

prediction of dynamic recrystallization occurring in the material, at high temperature and low strain rates cannot be predicted using the Hansel-Spittel model. Instead, the stress-strain plot ends as a flat curve similar to a recovery curve. The model is also not able to predict the material behavior such as work hardening at low temperatures 1050 °C and high strain rates (2 s^{-1}) and a significant deviation (8% to 13%) can be observed between the experimental and predicted values. Previous studies on Hansel-Spittel model have been exclusively done only on *wrought* alloys and similar observations have been reported. In one of the studies done on C45 steel (Opla et al., 2014), the authors reported that the Hansel-Spittel model was inefficient to describe the steady-state phase of the hot flow stress curves. The authors also observed that the model did not take the account of the peak strain values, thereby indicating its inability to describe the onset of DRX. Based on the predictions, it can be concluded that Arrhenius model is much better in predicting the flow stress behavior during hot deformation of the *as-cast* medium carbon low alloy steel as compared to the Hansel-Spittel model.

4.5 Simulation

The flow characteristics of *as-cast* medium carbon low alloy steel can be seen through the flow curves generated using hot compression. The dependence of material properties and microstructural changes rely on parameters like strain rate, temperature, material and microstructural inhomogeneity. However, there are additional factors which also play a crucial role in determining the flow behavior that takes into account like die temperature, friction between die and workpiece, adiabatic heating, heat conduction, etc. In order to study the effect of some of these parameters on hot compression behavior, FEM simulation was conducted. Numerical simulations consist of various elements which represent the real ingot breakdown process. Amongst these, the geometrical models of the ingot, dies, material model and a set of boundary and initial conditions are included (Oh, Semiatin et Jonas, 1992).

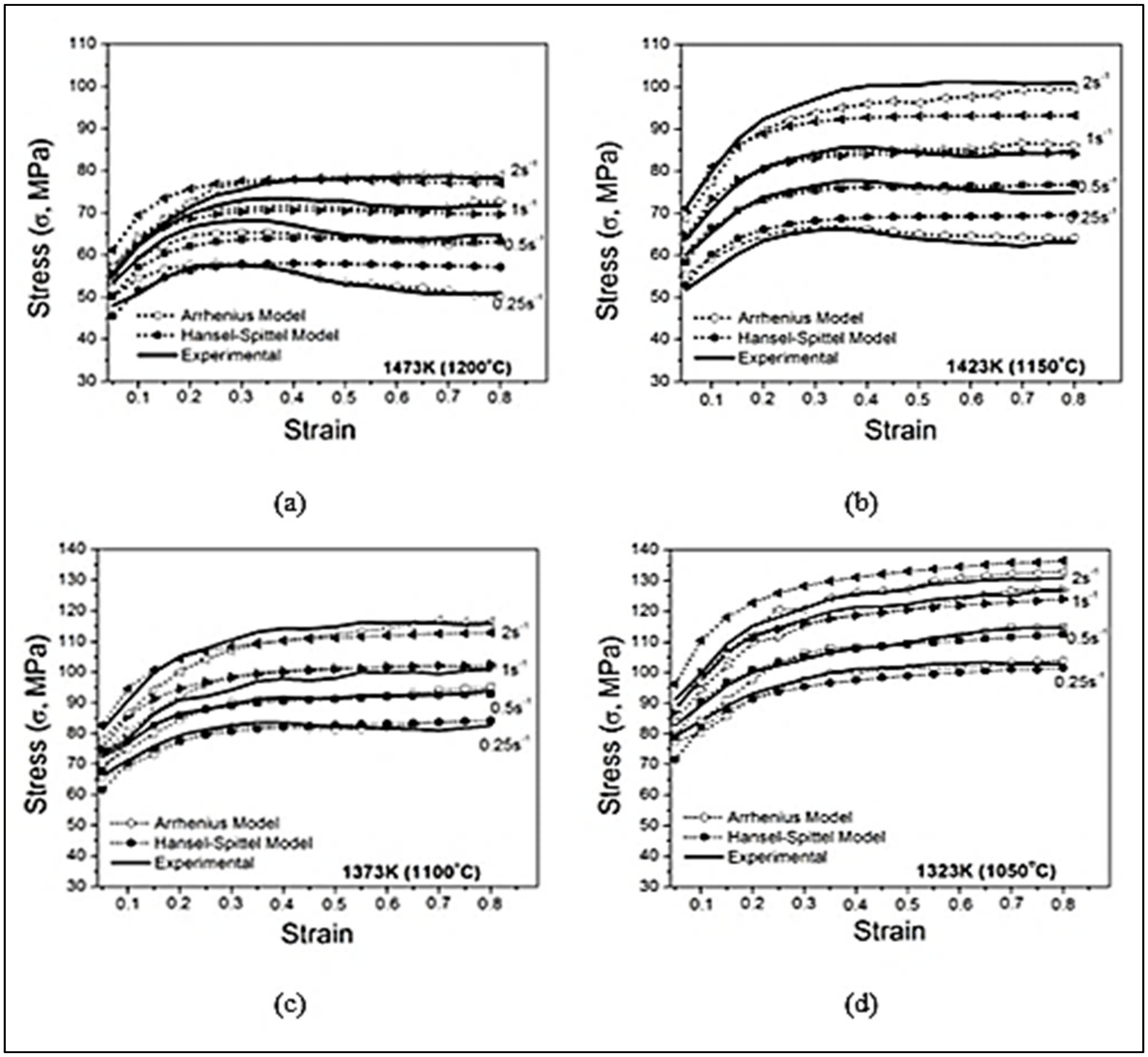

Figure 4.13 Comparison of flow curves between experimental and constitutive model predicted flow stress data for hot compressed *as-cast* medium carbon low alloy steel at a temperature of (a) 1200 °C, (b) 1150 °C, (c) 1100 °C and (d) 1050 °C. Continuous black line denotes experimental data, filled symbols denote Hansel-Spittel model data and blank symbols denote Arrhenius model data

In the present research, Forge NxT 1.0® was used to carry out FEM simulations of the ingot breakdown process using hot compression of cylindrical specimens to compare both Hansel-Spittel and Arrhenius models. The direction of the deformation during the ingot breakdown process is perpendicular to ingot axis which is similar to present deformation done on Gleeble 3800® Thermomechanical simulator. Since the implicit procedure is more accurate than the explicit method (Mahajan, Fourment et Chenot, 1998; Rojek et al., 2001), thereby it was selected to solve the set of FEM equations through iterations until the convergence criterion for each increment is satisfied. An eighth of the 3D model was used in order to reduce the calculation time. The results are extendable to full-size cylinder due to symmetry. Tetrahedral elements were used to discretize the geometrical model and adaptive remeshing was applied in order to avoid numerical locking. The upper anvil (die) moves along the central axis as a function of time while both upper and lower anvils are set as rigid bodies. The interface between tools and sample was assumed to follow the shear friction model. A constant friction factor of 0.3 was assumed between the dies and the sample. The temperature of the anvils was kept similar to the deformation temperature (isothermal forging). As the sample's heating during hot compression by Gleeble 3800® is in accordance with the accurate temperature control resistance heating method described in section 4.2, an adiabatic heating condition was imposed in the simulations. The thermophysical properties of the *as-cast* medium carbon low alloy (calculated by JMatPro®) are given in Table 4.4 and were implemented in the FEM code.

Table 4.4 Thermophysical properties of *as-cast* medium carbon low alloy steel used for FEM simulation

Physical Properties	Temperature Range(°C)	F(T)
ρ (Kg/m^3)	(950°C -1300°C)	-0.5234T+8040
K (W/m°K)		0.0119T+16.876
C_P (KJ/Kg)		0.1593T+470.75
α_L (10^{-6} 1/°K)		$3\times10^{-7}T^3-0.001T^2+1.0075T-309.13$

Deformation heating is usually generated in any alloy during deformation and is a function of the applied strain rate (Dieter, Kuhn et Semiatin, 2003). This generated heat, usually termed as adiabatic heating, results in a temperature increase in the sample thereby reducing the flow stress. The temperature increase due to adiabatic heating is represented by the following equation:

$$\Delta T_{Adiabatic} = \frac{0.95 \int \sigma d\epsilon}{\rho C_p} \tag{4.7}$$

where, ΔT is the change in temperature, $\int \sigma d\varepsilon$ is the area under the uncorrected stress-strain curve, ρ is the density (Kg/m^3), C_p the specific heat (J/Kg/°K) and 0.95 is the fraction of mechanical work transformed into heat with the remaining fraction going to microstructural changes (Dieter, Kuhn et Semiatin, 2003; Goetz et Semiatin, 2001; Mataya et Sackschewsky, 1994).

The adiabatic heating temperature calculated from the experimental data using Eq. (4.6) reveals that the temperature increase (ΔT) at the center of the specimen after deformation at 1200 °C is 8.24 °C at 0.25 s^{-1} and 14.5 °C at 2 s^{-1} as reported elsewhere (Chadha, Shahriari et Jahazi, 2016; K.Chadha, D.Shahriari et Jahazi, 2015). From the simulation results, the amount of temperature increase (ΔT) that occurs during hot compression at 1200°C for strain rates of 0.25 s^{-1} and 2 s^{-1} is 7 °C and 15 °C, respectively (Table 4.5) (Chadha, Shahriari et Jahazi, 2016; K.Chadha, D.Shahriari et Jahazi, 2015).

In the present research, simulation results of the specimen deformed at deformation temperature of 1150b°C and strain rates of 0.25bs^{-1} and 2bs^{-1} are presented. Adiabatic heating temperature for deformation temperature of 1150 °C as calculated from the experimental data using Eq. (4.6) reveals that the temperature increase (ΔT) at the center of the specimen after deformation is 8.36 °C at 0.25 s^{-1} and 19.02 °C at 2 s^{-1}.

Table 4.5 Values of adiabatic heating at different strain rates predicted by Hansel-Spittel model and Arrhenius model

Temperature	1200 °C		1150 °C	
Strain Rate	0.25 s^{-1}	2 s^{-1}	0.25 s^{-1}	2 s^{-1}
Experimental Adiabatic Heating	(8.24°C)	(14.5°C)	(8.36°C)	(19.02°C)
Hansel Spittel Model	(7°C)	(15°C)	(7.98°C)	(17.09°C)
Arrhenius Model	(8.4°C)	(19.4°C)	(9.38°C)	(21.7°C)

From the simulation results using Hansel-Spittel model, the amount of temperature increase that occurs during hot compression at 1150°C using strain rates of 0.25 s^{-1} and 2 s^{-1} is ~7.98 °C and 17.09 °C, respectively (Table 4.5) (Fig. 4.14 (a) & (b)). As shown in Fig. 4.14 (a), temperature increase along the sample after a strain of 0.8 is not uniform at a strain rate of 0.25 s^{-1}, whereas it is nearly uniform at a strain rate of 2 s^{-1} (Fig. 4.14 (b)). The temperature distribution map during deformation reveals that Hansel-Spittel model fairly predicts the adiabatic heat generated during the deformation of the *as-cast* medium carbon low alloy at both *low* and *high* strain rates.

Arrhenius model was also implemented in Forge NxT 1.0® software. From the simulation results, the temperature increase (ΔT) due to adiabatic heat generated due to hot compression at strain rates of 0.25 s^{-1}, 2 s^{-1} and at a deformation temperature of 1150 °C is ~9.38 °C and ~21.7 °C (Table 4.5) (Figs. 4.15 (a) & (b)). It is also observed that while temperature distribution map is not uniform at a strain rate of 0.25 s^{-1} (Fig. 4.15 (a)), it is significantly uniform at a strain rate of 2 s^{-1} (Fig. 4.15 (b)). The above findings indicate that the Arrhenius model also predicts relatively well the adiabatic heat generated during deformation for both strain rates. A difference of about 11% is observed between experimental and simulated values. The temperature distribution maps depict that both models were unable to simulate for low strain rates as the temperature distribution map is not uniform for both cases. The boundary conditions were indeed similar, only the incompatibility of the model can be pointed to be the primary cause of this inhomogeneity.

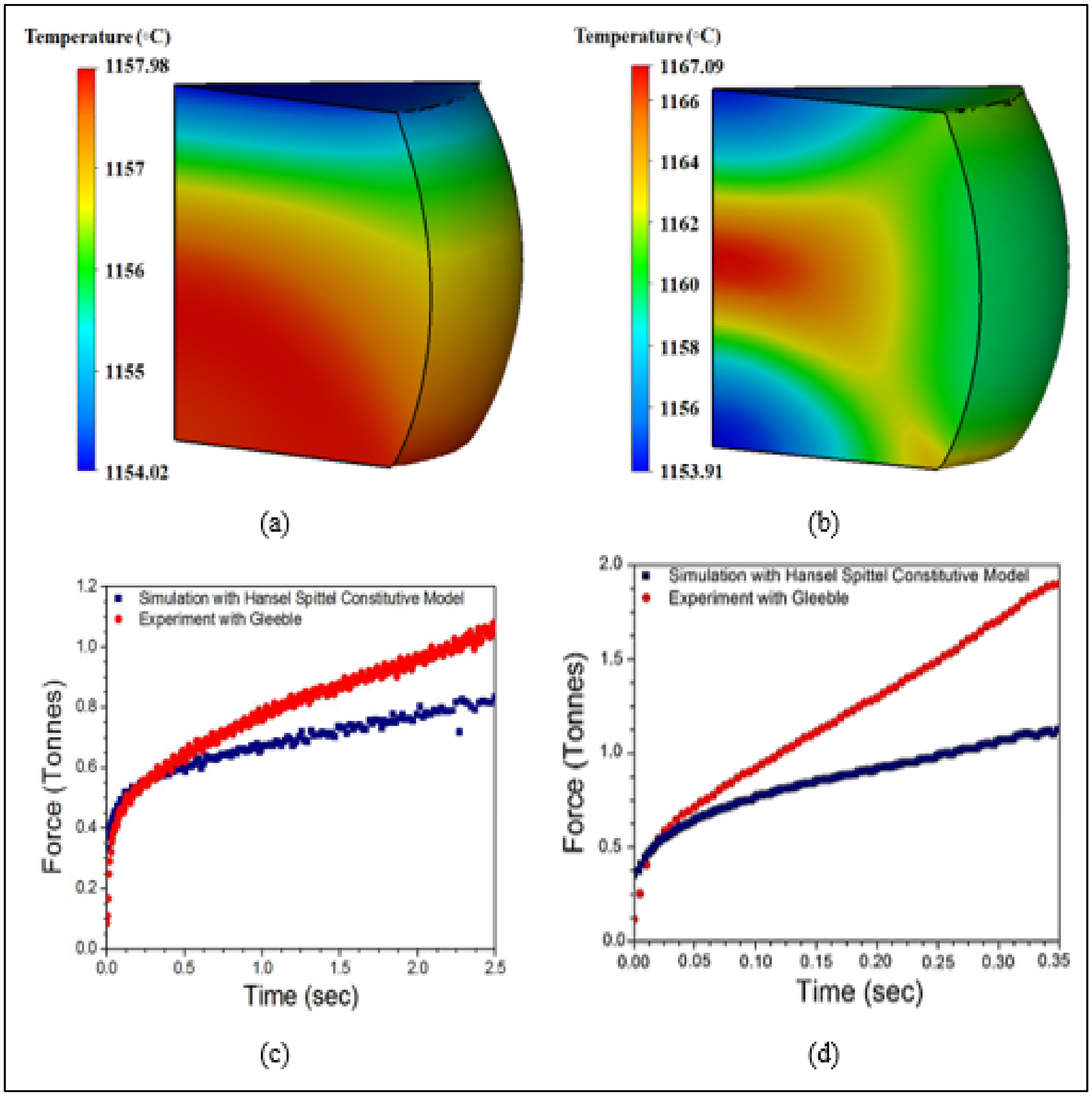

Figure 4.14 Simulated temperature distribution map of as-*cast* medium carbon low alloy steel predicted by Hansel-Spittel model at deformation temperature of 1150 °C and at a strain rate of (a) 0.25 s^{-1} and (b) 2 s^{-1}. Force versus time plot of experimental and predicted (Hansel-Spittel model) at a deformation temperature of 1150 °C and at strain rates of (c) 0.25 s^{-1} and (d) 2 s^{-1}

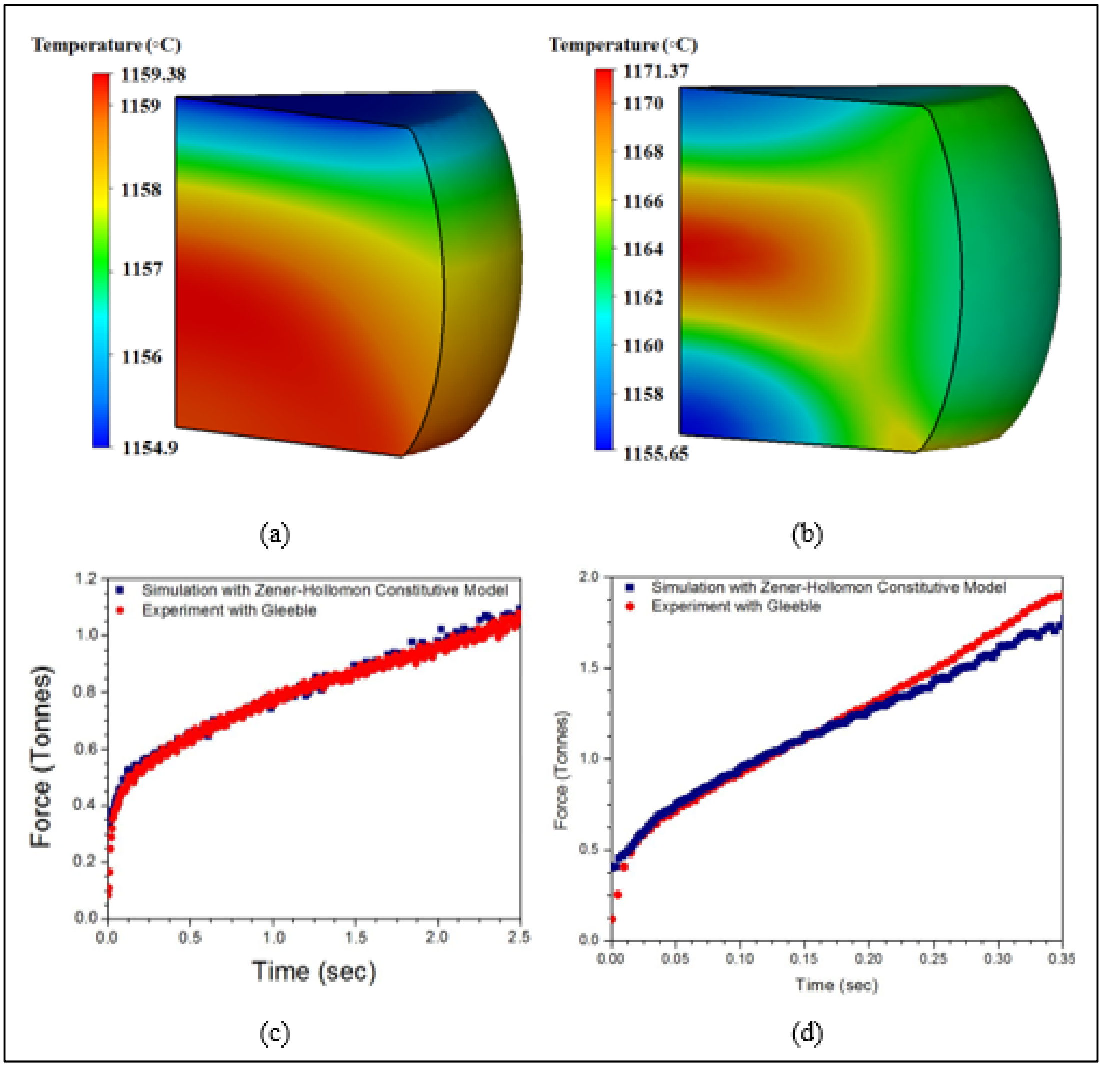

Figure 4.15 Simulated temperature distribution map of *as-cast* medium carbon low alloy steel predicted by Arrhenius model at deformation temperature of 1150 °C and at a strain rate of (a) 0.25 s^{-1} and (b) 2 s^{-1}. Force versus time plot of experimental and predicted (Arrhenius model) at a deformation temperature of 1150 °C using and strain rate of (c) 0.25 s^{-1} and (d) 2 s^{-1}

Figs. 4.14 ((c) & (d)) and Figs. 4.15 ((c) & (d)) shows the force versus time plots of the predicted (Hansel-Spittel (Fig. 14) and Arrhenius (Fig. 4.15)) model and experimental data at strain rates of 0.25 s^{-1} (c) and 2 s^{-1} (d), respectively. From the plots, it can be seen that at a strain rate of 0.25 s^{-1}, Fig. 4.14 (c), the difference in the predicted and experimental values is ~26% with the Hansel-Spittel model, whereas it is ~2% with the Arrhenius model (Fig. 4.15 (c)). At a strain rate of 2 s^{-1} (Fig. 4.14 (d)), this difference increases to

~41% for the Hansel-Spittel model, whereas with Arrhenius model the difference is ~5% (Fig. 4.15 (d)). It is well known that the role of the friction must be taken into account for the accurate determination of the flow curves during hot compression (Yunping, Onodera et Chiba, 2010). The difference in the force between the experimental and predicted values is assumed to be mainly due to the effect of friction during hot compression and can be justified by the experimental values. It is calculated that the friction effect at the strain rate of 2 s^{-1} is 0.395 while it is 0.266 for the strain rate of 0.25 s^{-1}. It is thus observed that the friction effect is completely taken into account by the Arrhenius model, but not fully by the Hansel-Spittel model, thus making it even more reliable to simulate adiabatic heat for *as-cast* medium carbon low alloy.

4.6 Discussion

Stress-strain curve of hot compression tests (Fig. 4.7 (a-d)) reveals that at low strain rates, dynamic softening mechanisms are activated and result in a stress drop after the peak stress. This is a typical dynamic recrystallization behavior (McQueen et Jonas, 1975) which is due to the effect of work hardening and softening mechanisms.

DRX is well observed in the hot compression tests of the *wrought* 42CrMo steel as_published in various articles recently. M.S. Chen et al. (Chen, Lin et Ma, 2012) and Y.C Lin et al. (Lin, Chen et Zhong, 2008c; 2008d; Lin, Ming-Song et Jue, 2008a; Lin et Xiao-Min, 2011; Lin, Chen et Zhong, 2008f) investigated the kinetics of dynamic recrystallization of *wrought* 42CrMo steel. They observed true stress-strain curves exhibiting peak stress at a small strain. After peak stress, the flow stresses decreased monotonically to higher strains, thus confirming the occurrence of dynamic flow softening processes. In the present research, the *as-cast* medium carbon low alloy steel showed similar trends in high temperatures (1200 °C & 1150 °C) and slow strain rates (0.25 s^{-1} & 0.5 s^{-1}).

However, a different behavior of flow stress was observed during deformation at higher strain rates. At high temperature and strain rates, e.g. at 1150 °C and 1 s^{-1}, the flow curves rise sharply and then attain a steady state, indicative of the occurrence of dynamic recovery rather than dynamic recrystallization. The EBSD grain boundary map of the specimen deformed at 1200 °C, 0.25 s^{-1} is shown in Fig. 4.16 (a), with the majority of the grains nucleated due to dynamic recrystallization (shown with red arrows).

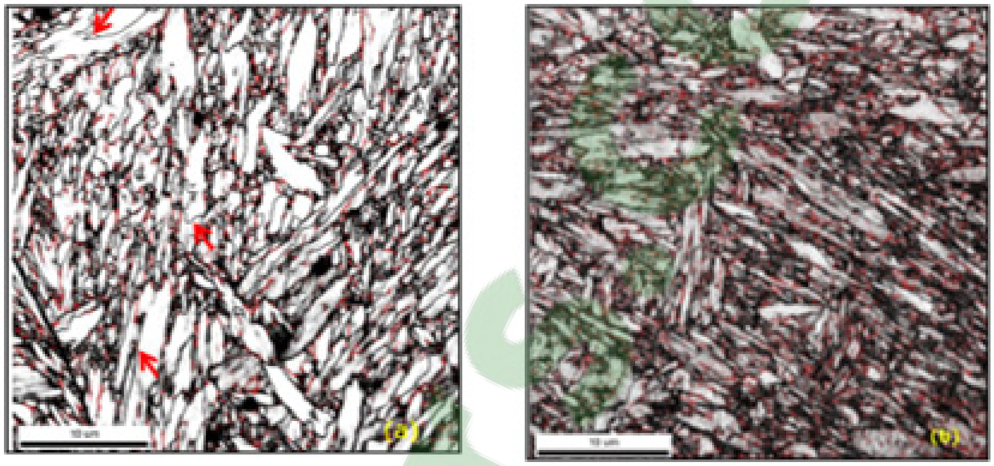

(a) (b)

Figure 4.16 EBSD grain boundary map of *as-cast* medium carbon low alloy steel deformed at (a) 1473K (1200 °C), 0.25 s^{-1} and (b) 1473K (1200 °C), 2 s^{-1}. Black lines denote HAGBs and red lines denote LAGBs

It can be observed that the new grains are nucleating from the bulged area of the grain boundary. In addition to it, grains are nucleating from prior austenite grains boundaries. The fraction of high angle grain boundaries (HAGBs having misorientation angle (θ) > 15 ^{o}) is 67.6% and that of low angle grain boundaries (LAGBs defined as 2 $^{o}\leq\theta\leq15$ ^{o}) is 32.4% for the deformed sample at 1200 °C, 0.25 s^{-1}. In contrast, at high strain rates (2 s^{-1}), grain nucleation cannot be observed and fraction of HAGBs is 39.2%, less than that observed at lower strain rate whereas fraction of LAGBs is higher at 60.8% (see Fig. 4.16(b)). Low strain rates provide sufficient time for dislocation annihilation and thus softening can be seen in flow curves (Fig. 4.7). However, at higher strain rates dynamic recrystallization is not observed even at high temperatures because the time required for nucleation and growth process to occur is insufficient (McQueen et Jonas, 1975).

Semiatin et al. (Semiatin et al., 2004a) reported in their research similar trend for transverse as-cast superalloy samples. They observed softening was mainly due to dynamic recrystallization at a strain rate of 0.1 s^{-1} which is in good agreement with the results obtained in the present research. Similar results have also been reported by Hotta et al. (Hotta et al., 2005), where it was observed that dynamic recrystallization occurred at low strain rates (10^{-1} - 10^{-3} s^{-1}) (i.e. low Z values), during hot compression of as-cast 9%Ni steel.

4.7 Model Validation

Generally, constitutive equations are derived in order to observe material behavior for various parameters other than the initial experimental parameters used for deriving the constants. Using the derived constants for FEM simulation for different parameters, the material behavior subjected to other deformation parameters at industrial scales can be revealed. Adiabatic heating and force calculations are a few elements which can be derived from the simulations of deformation process and can be further used to analyze and then optimize the parameters as per requirements.

In order to evaluate the validity of the proposed model, two new sets of experiments were carried out. The first set consisted of a strain rate of 0.8 s^{-1} and a deformation temperature of 1180 °C and the second one was selected with a strain rate of 0.05 s^{-1} and a deformation temperature of 1000 °C. The heating rate, holding time and cooling rate were kept similar to the original experimental cycle as shown in Fig. 4.2. The values of these parameters were then entered into the respective equations with the constants derived using original experimental data and the results are reported in Fig. 4.17 ((a) & (b)).

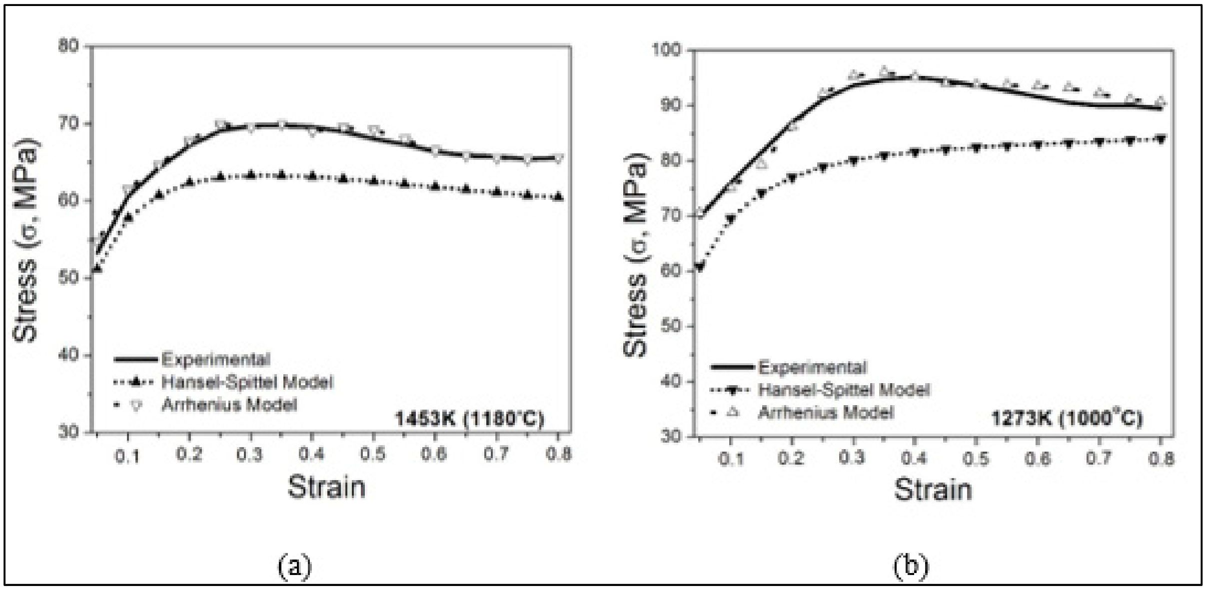

(a) (b)

Figure 4.17 Comparison of flow curves between experimental and predicted flow stress data at deformation temperature and strain rate of (a) 1180 ºC, 0.8 s^{-1} and (b) 1000 °C, 0.05 s^{-1}

It can be noted from the comparison plots that the Arrhenius model provides a very good prediction of experimental conditions in both events as compared to the Hansel-Spittel model. It is interesting to note that the Arrhenius model can anticipate the dynamic recrystallization behavior observed through stress-strain diagram of the as-cast material for both sets of new experimental data indicating that Arrhenius equation is better suited for predicting the stress-strain diagram of *as-cast* medium carbon low alloy steel during the hot deformation process. Using Forge NxT 1.0®, simulations were performed for the new experimental data using the proposed Hansel-Spittel and Arrhenius model constants.

The adiabatic heating and force vs. time graph are shown in Fig. 4.18 ((a) & (b)) for 1000 °C, 0.05 s^{-1} and Fig. 4.19 ((a) & (b)) for 1180 °C, 0.8 s^{-1}. Using Eq. 4.7, the increase in temperature at the core due to adiabatic heat was calculated to be 5.3K (5.3 °C) and 9.7K (9.7 °C) for deformation at 1000 °C and 1180 °C, respectively. Simulation results show that temperature increase values are very close to the theoretical calculations. The major differences lie in the force vs. time calculations where it can be observed that Arrhenius model is able to predict it much better than the Hansel-Spittel predictions.

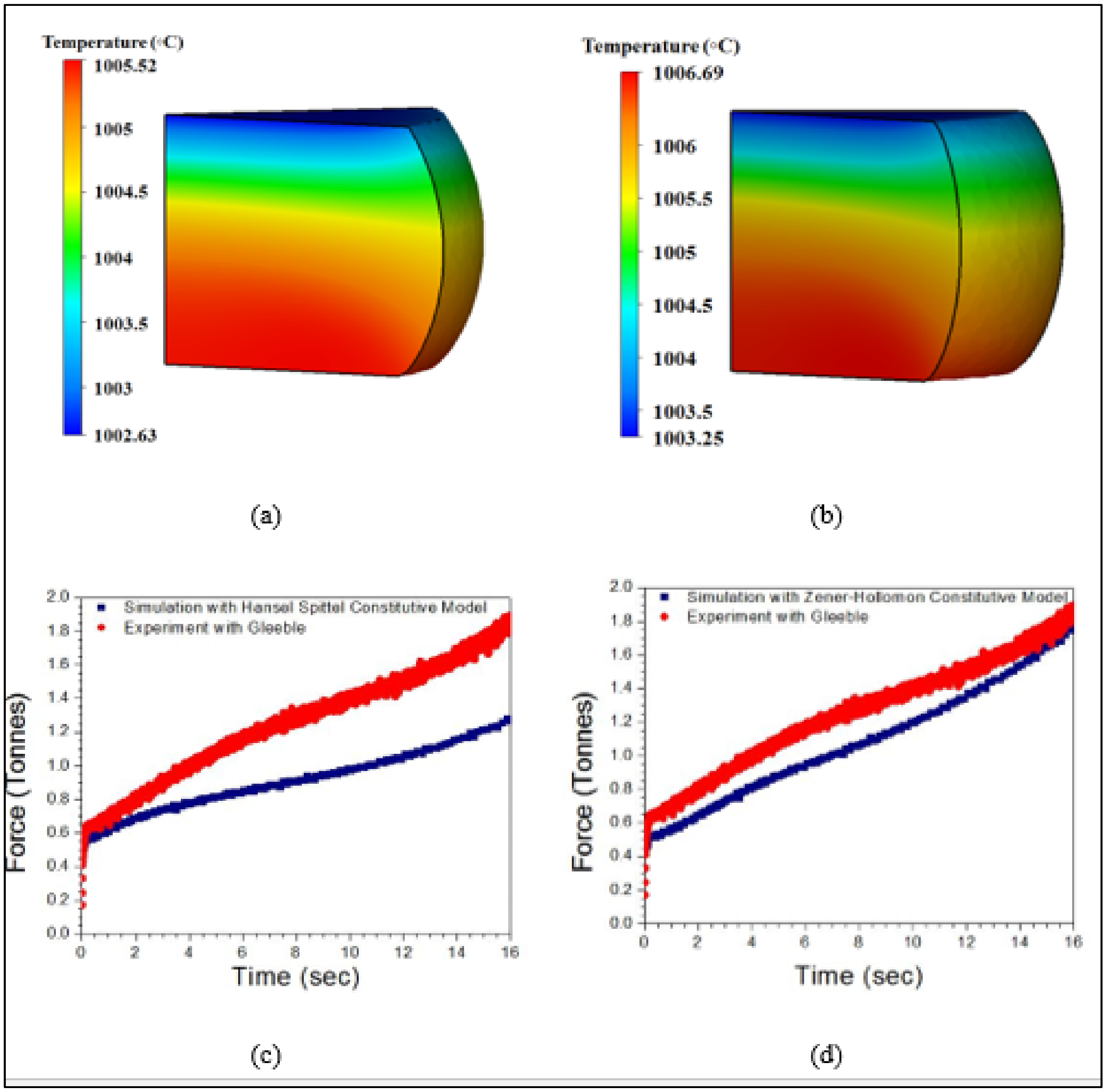

Figure 4.18 Simulated temperature distribution map of *as-cast* medium carbon low alloy steel at deformation temperature of 1000 °C and at a strain rate of 0.05 s^{-1} for (a) Hansel-Spittel model and (b) Arrhenius model. Force versus time plot of experimental and predicted at a strain rate of 0.05 s^{-1} and at a deformation temperature of 1000 °C using (c) Hansel-Spittel model and (d) Arrhenius model

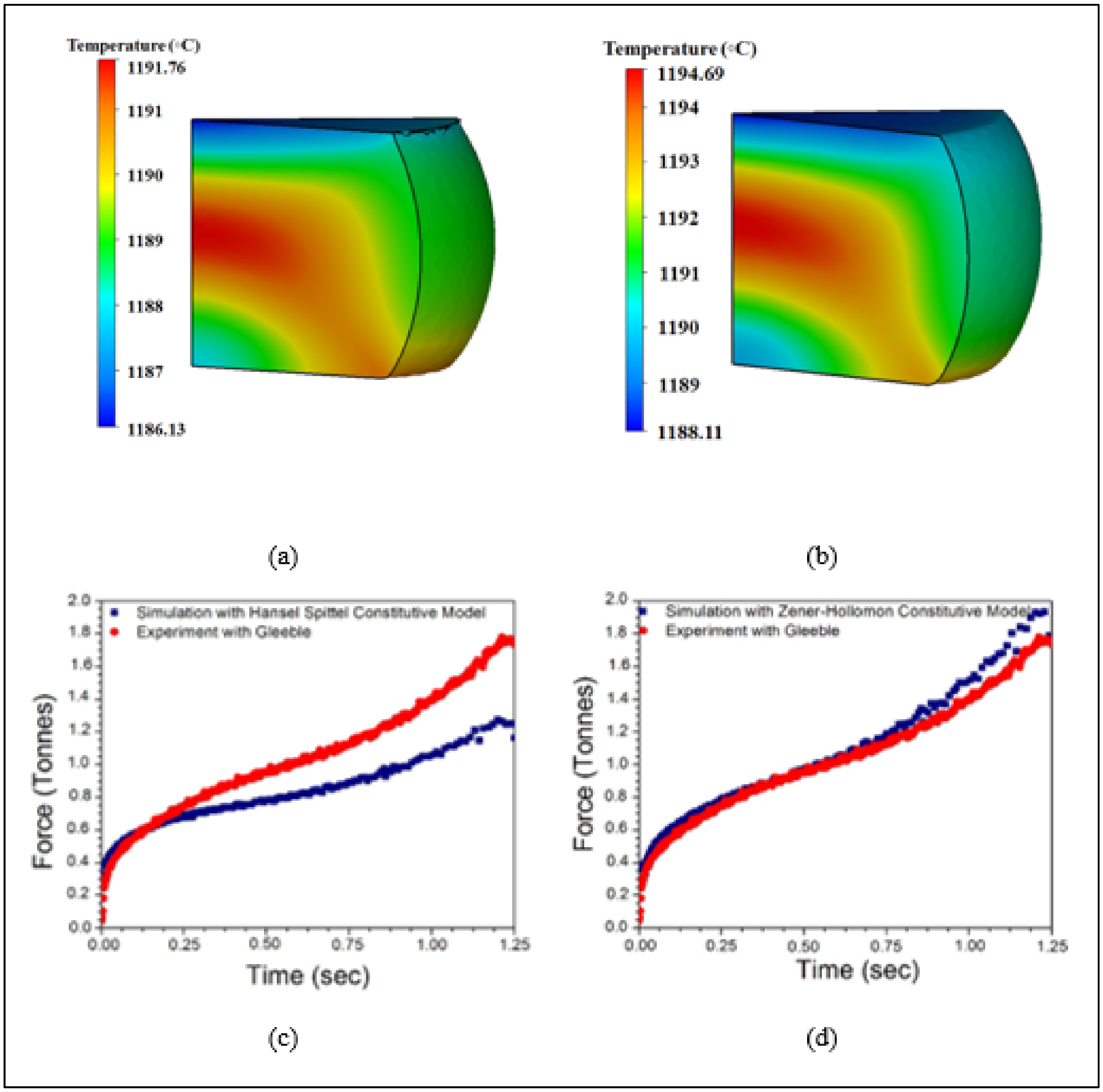

Figure 4.19 Simulated temperature distribution map of *as-cast* medium carbon low alloy steel at deformation temperature of 1180 °C and at a strain rate of 0.8 s^{-1} for (a) Hansel-Spittel model and (b) Arrhenius model. Force versus time plot of experimental and predicted at a strain rate of 0.8 s^{-1} and at a deformation temperature of 1180 °C using (c) Hansel-Spittel model and (d) Arrhenius model

Reliable prediction of loads by the FEM model requires accurate prediction of the flow stress. Therefore, the variability in flow stress values needs to be determined. To this end, the correlation coefficient (R) and absolute average error (Δ) were determined for the two models and are discussed in the following:

The correlation coefficient (R) is expressed as (Han et al., 2013):

$$R = \frac{\sum_{i=1}^{N}(\sigma_E^i - \bar{\sigma}_E)(\sigma_P^i - \bar{\sigma}_P)}{\sqrt{\sum_{i=1}^{N}(\sigma_E^i - \bar{\sigma}_E)^2 \sum_{i=1}^{N}(\sigma_P^i - \bar{\sigma}_P)^2}} \tag{4.8}$$

The absolute average error (Δ) is expressed as:

$$\Delta = \frac{1}{N}\sum_{i=1}^{N}\left|\frac{\sigma_E^i - \sigma_P^i}{\sigma_E^i}\right| X100 \tag{4.9}$$

Fig. 4.20 ((a) & (b)) shows the correlation between the experimental flow stress and predicted flow stress, which was obtained using the Arrhenius and the Hansel-Spittel models, respectively. It can be seen that most of the data points fall fairly close to the regression line and good correlation between experimental and predicted data can be obtained. The R value of Arrhenius model is 0.978 and that of the Hansel-Spittel model is 0.972.

Generally, the value of R indicates the strength of a linear relationship between the predicted and the experimental values. However, it is not always true that the higher value of R can indicate better results as the tendency of the model is often biased towards higher or lower values. Therefore, the absolute average error (Δ) was used as an unbiased statistical parameter which can further evaluate the predictability of the models (Samantaray, Mandal et Bhaduri, 2011).

Fig. 4.21 shows the Δ values at different strains for the two models. It can be observed that the average absolute error from the Hansel-Spittel model is higher than the ones from Arrhenius model. The absolute average error of the entire process was found to be 1.76% for the Arrhenius model and 3.17% for the Hansel-Spittel model. This finding further confirms that the Arrhenius model having a higher value of R and a lower value of Δ is more accurate and probably more suitable for the prediction of stress-strain curves during the hot deformation process of *as-cast* medium carbon low alloy steel.

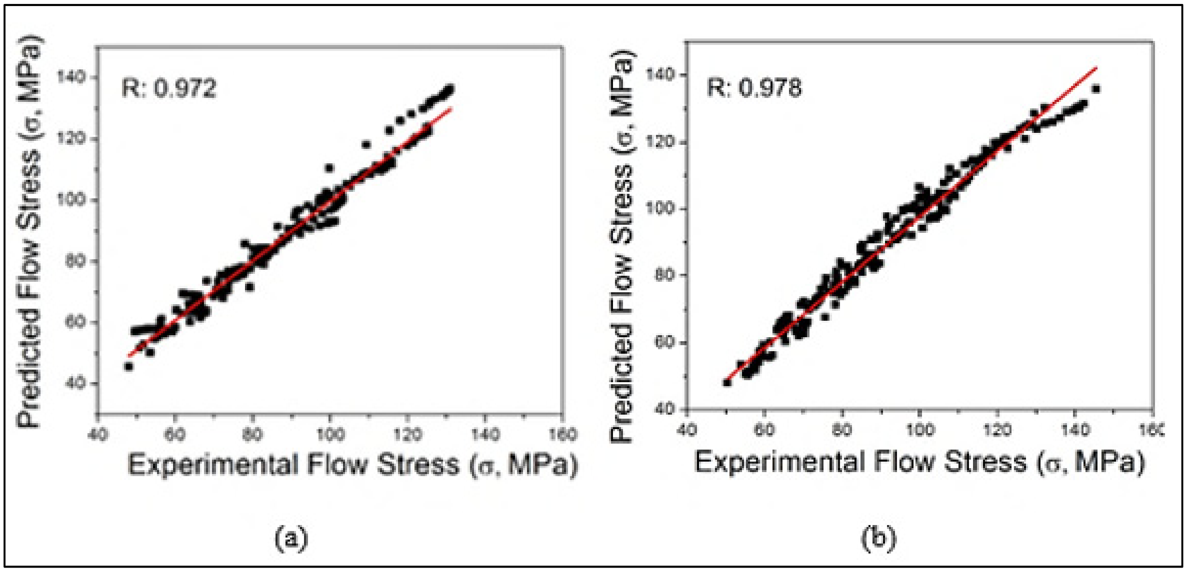

(a)

(b)

Figure 4.20 Correlation between the experimental and predicted flow stresses obtained from (a) Hansel-Spittel model and (b) Arrhenius model

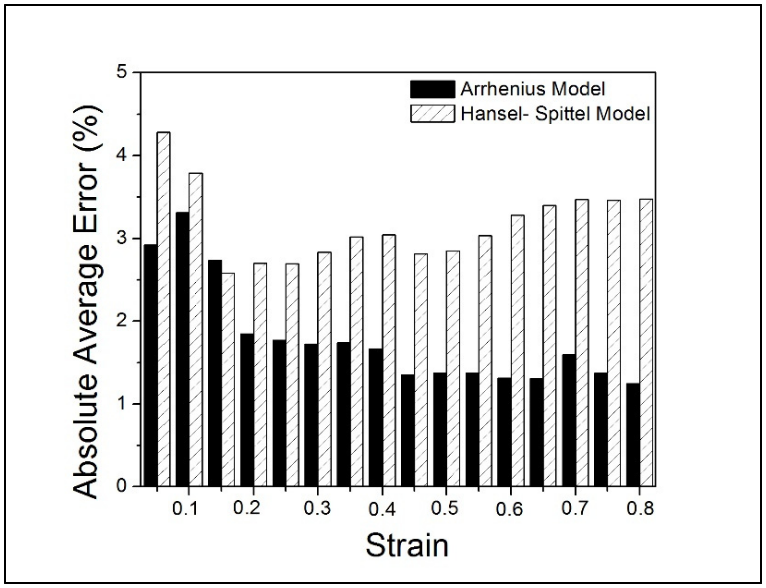

Figure 4.21 The absolute average error for the Arrhenius-type and Hansel-Spittel model at various strains for hot compressed *as-cast* medium carbon low alloy steel

4.8 Conclusions

The deformation behavior of an as-cast medium carbon low alloy steel was studied using isothermal compression tests and constitutive equations using Hansel-Spittel and Arrhenius equations were developed. The following conclusions can be drawn from the analysis:

1. The Hansel-Spittel model was used to predict high temperature flow stress of *as-cast* medium carbon low alloy steel. The model lacks the desired precision and reliability in predicting stress-strain curves which can be justified by the correlation coefficient (0.972) and the absolute error (3.17%).
2. Using the Arrhenius model, the effect of strain was considered in order to predict the flow behavior of *as-cast* medium carbon low alloy steel for various deformation parameters. The influence of strain on material constants (α, n, Q and A) with good correlation and precision could be determined using a sixth order polynomial.
3. The occurrence of dynamic recrystallization during the hot deformation process was demonstrated using grain boundary maps, EBSD and flow curves analyses. However, the Hansel-Spittel model failed to predict this while Arrhenius equation clearly does. Therefore, the Arrhenius model would be better suited for the FEM simulation of the process of ingot breakdown of large size ingots.

CHAPTER 5

INFLUENCE OF STRAIN RATE ON DYNAMIC TRANSFORMATION OF AUSTENITE IN AN AS-CAST MEDIUM CARBON LOW-ALLOY STEEL

Kanwal Chadha[a], Zaid Ahmed[a], Clodualdo Jr. Aranas[b],
Davood Shahriari[a], Mohammad Jahazi[a]

[a] Department of Mechanical Engineering, École de Technologie Supérieure,
1100 Notre-Dame West, Montreal, Quebec, Canada H3C 1K3
[b] Department of Mechanical Engineering, University of New Brunswick
Fredericton, NB E3B 5A3, Canada

Paper submitted for publication to Materialia, Feb 2018

Abstract: In this work, the effect of strain rate on the dynamic transformation (DT) of austenite to ferrite during high temperature forging of an as-cast medium carbon low alloyed steel was investigated. Hot deformation experiments were carried out in the 1150 °C to 1200 °C (400-450 °C above Ae_3) temperature range and 0.25 s^{-1} to 2 s^{-1} strain rate range using a Gleeble 3800® thermomechanical simulator. The critical strains for DT and dynamic recrystallization (DRX) were determined to be in the 0.08 to 0.18 strain range. A microstructural analysis was conducted using optical and electron microscopy. The kernel average misorientation (KAM) technique was applied to electron back-scattered diffraction (EBSD) images to quantify the internal misorientation of grains for the characterization of DT ferrite. Furthermore, it was found that an increase in strain rate decreased the amount of dynamically formed ferrite under the same applied strain and testing temperature. The obtained results were correlated with the influence of deformation parameters on carbon diffusivity and its impact on the growth of dynamically formed ferrite.

Keywords: Low-alloy steel, As-cast structure, Hot deformation, Dynamic transformation, Carbon diffusion, EBSD analysis.

5.1 Introduction

High strength steels used for the manufacturing of large size components such as turbine shafts are produced by ingot casting, followed by forging and quench and temper operations. The first step of the deformation process, called ingot breakdown, is carried out well above the Ae_3 temperature, and therefore produces major microstructural changes, such as dynamic recovery (DRV), dynamic recrystallization (DRX) and metadynamic recrystallization (MDRX) (Devadas, Samarasekera et Hawbolt, 1991; Laasraoui et Jonas, 1991; Sakai, Akben et Jonas, 1983). Deformation-induced transformation of austenite to ferrite, also known as dynamic transformation (DT), is an additional softening mechanism that needs to be taken into account. This phenomenon was first reported by Matsumara et al. and Yada et al. in the late 1980s (Matsumura et Yada, 1987; Yada, Li et Yamagata, 2000), and has attracted considerable interest in recent years (Ghosh, Aranas Jr et Jonas, 2016; Park et al., 2013c; Sun et al., 2014). However, most studies on DT are associated with wrought structures, and particularly rolled materials (Ghosh, Aranas Jr et Jonas, 2016; Ghosh et al., 2013a), and very limited data is available on the dynamic transformation of austenite in as-cast structures.

The occurrence and extent of DT depend on various parameters, such as alloy chemistry (Aranas Jr et Jonas, 2015; Ghosh, Basabe et Jonas, 2014) and grain size prior to deformation (Park et al., 2013a), as well as process parameters (temperature, strain and strain rate) (Grewal et al., 2016; Park et al., 2013c). The alloy composition significantly impacts the extent of DT. Ghosh et al. (Ghosh, Basabe et Jonas, 2014) studied the effect of carbon content on DT, and observed that at 0.15% to 0.40%wt. carbon, the Widmanstätten ferrite forms instantly from deformed austenite, whereas at a carbon content of 0.79%wt., the formation of ferrite was accompanied by that of cementite. Aranas et al. (Aranas Jr et Jonas, 2015) investigated the effect of Mn and Si on the occurrence of DT and reported that the presence of Mn increases not only the driving force, but also the thermodynamic energy barrier (i.e., the Gibbs energy difference between austenite and ferrite) for the occurrence of DT. On the other hand, Si increased the driving force, but decreased the thermodynamic energy barrier, thus proving to accelerate the DT process. N. Park et al. (Park et al., 2013a) observed that with a decrease in austenite grain size, the critical strain value decreased as well, implying that the onset of DT was accelerated. The effect of temperature and strain on DT was studied by Grewal et al. (Grewal et al., 2016), who observed that as the temperature increased beyond the obstacle peak, it became easier to form Widmanstätten plates. In another research, N. Park et al. (Park et al., 2013c) observed that under slow strain rate conditions, higher dynamic transformation was observed; however, their study was not focused on the effect of strain rate and its related mechanisms on DT.

The occurrence of DT was initially related to the influence of deformation on the stored energy of dislocations (Ghosh, Basabe et Jonas, 2014). However, it was later proven that the dislocations cannot accurately explain the dynamic transformation taking place well above the Ae_3 temperature. As a result, a new model known as transformation softening was proposed by Jonas et al. (Jonas et Ghosh, 2013). In this model, the driving force for DT is the net softening during the phase change, which is defined by the flow stress difference between the strain-hardened austenite and the yield stress of the freshly formed Widmanstätten ferrite (Jonas et Ghosh, 2013). Upon isothermal holding, DT ferrite can retransform back to austenite, the thermodynamically stable phase (Aranas Jr et Jonas, 2015; Aranas, Wang et Jonas, 2015). However, among the existing proposed mechanisms for DT, less attention has been paid to the influence of strain rate on carbon diffusivity and its effect on DT. For instance, the nucleation and growth of ferrite plates are also related to the diffusion of alloying elements such as carbon (Bhadeshia, 2010b). Furthermore, deformation under low strain rates means the specimen is under compression stress longer time than at higher strain rates. As a result, the evolution of the nucleated ferrite at critical strain will depend on the strain rate (Ohmori et al., 2004; Tsuji, Matsubara et Saito, 1997; Zhao et al., 2016).

The objectives of the present work are, therefore: i) to study dynamic transformation of austenite to ferrite in an as-cast structure, ii) to investigate and quantify the influence of strain rate on the nucleation and growth of the newly formed DT ferrite, and iii) to propose a mechanism which takes into account the role of solute diffusion (carbon) under various strain rates and its impact on the nucleation of DT ferrite.

5.2 Materials and Methods

The detailed composition of the as-cast medium carbon low-alloy steel used for the experiments is shown in Table 5.1, along with its orthoequilibrium and paraequilibrium temperatures. These were calculated using the FactSage thermodynamic software, employing the FSStel Database® (Bale et al., 2009). The materials were provided by Finkl Steel-Sorel Forge, Sorel, Quebec, Canada. Cylindrical specimens were machined from the central region of the as-cast ingot with diameters and heights of 10 mm and 15 mm, respectively. Hot compression tests were carried out using the Gleeble 3800® thermomechanical simulator following the procedures described in the ASTM E209.

Table 5.1 Composition of *as-cast* medium carbon low alloy steel (Alloy A) (wt. %)

C	Mn	Si	Mo	Cr	Other	Ae_3 Orthoequilibrium temperature	Ae_3 Paraequilibrium temperature
0.35	0.84	0.41	0.44	1.90	Microalloying	769.65ºC	748ºC

The schematic diagram of the thermomechanical cycle is shown in Fig. 5.1. Two temperatures, 1150 °C and 1200 °C, and three strain rates, 0.25 s^{-1}, 1 s^{-1} and 2 s^{-1}, were employed in the experiments. For reference, deformation temperatures were selected based on the actual parameters used during industrial ingot forging, which were measured using a FLIR® T650sc thermal camera. The thermomechanical procedure involved heating the sample to 1260 °C at a 2 ºC/s heating rate and soaking for 5 minutes to homogenize the temperature. The samples were then cooled to the deformation temperature at a rate of 1 °C/s before being compressed to a true strain of 0.8, followed by water quenching (Chadha et al., 2017b). 0.1 mm thick tantalum sheets were used as a lubricant between the sample and the tungsten anvils.

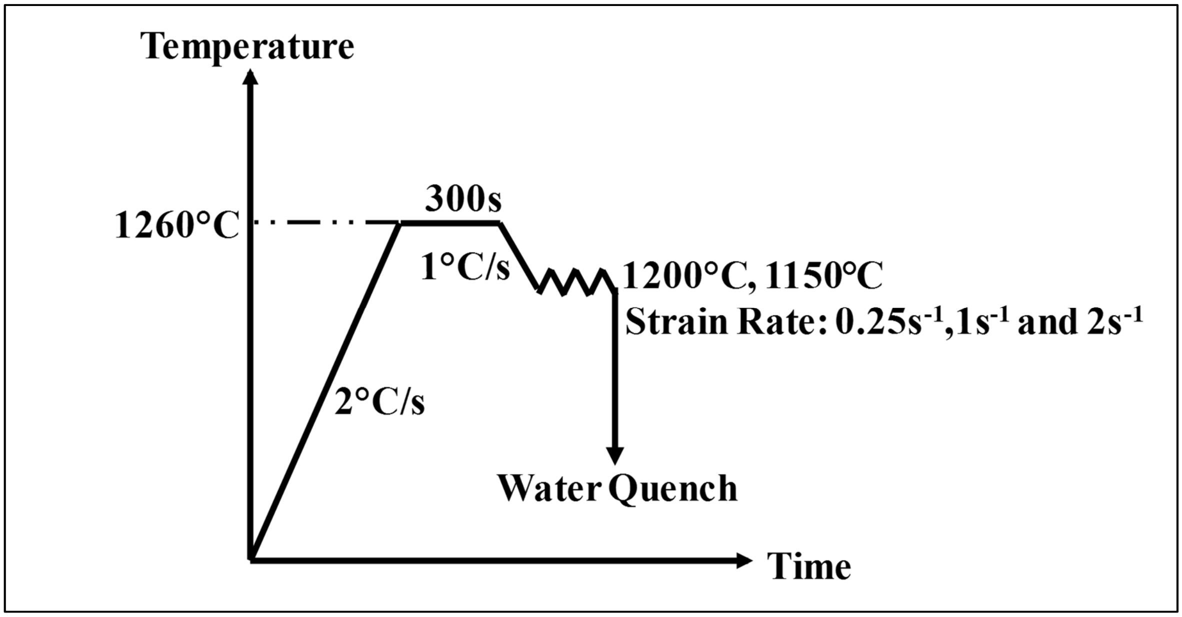

Figure 5.1 Schematic diagram of thermomechanical schedule for hot compression tests of *as-cast* medium carbon low alloy steel

The samples were polished mechanically using conventional techniques and then electropolished at room temperature using a mixture of Perchloric acid and ethanol (1:9 by volume) to reveal the microstructure by means of EBSD techniques. The electropolishing voltage and time were 25 V and 15 s, respectively. The samples were placed with their compression axis parallel to the incident electron beam. The EBSD analysis was performed using FEG-SEM (Carl Zeiss; Model: Supra 40) equipped with TSL-OIM^{TM} software. Fig. 5.2 presents the initial microstructure of the as-cast material before homogenization. The microstructure shows a coarse grain structure with no specific grain boundaries. In order to observe the microstructure of the material just before deformation, i.e., in homogenized condition, one sample was subjected to homogenization at 1260 °C for 5 minutes, followed by water quenching.

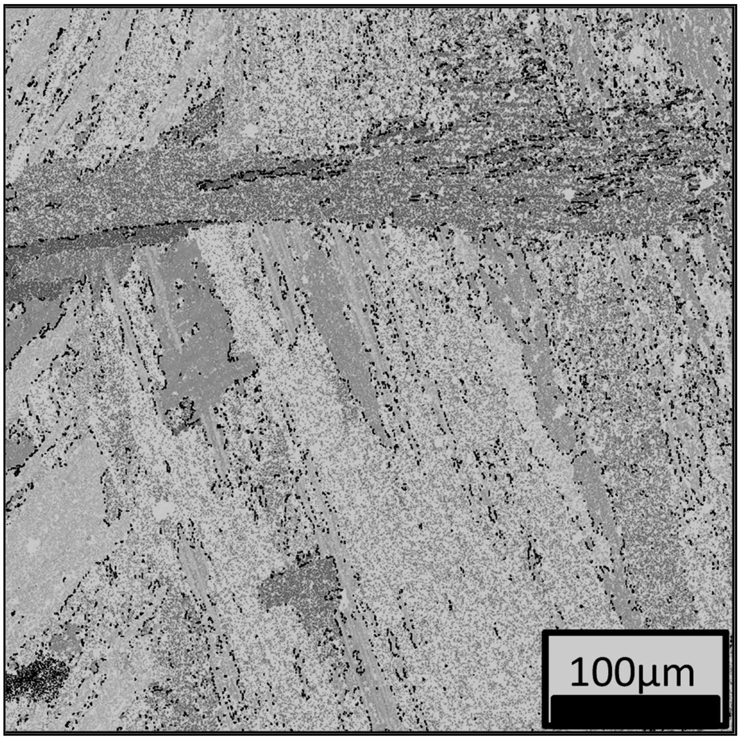

Figure 5.2 EBSD of initial microstructure of *as-cast* medium carbon low alloy steel in the columnar region. No specific grain boundaries can be observed in the microstructure. Black lines denote high angle grain boundaries

The homogenized grain boundary (G.B.) map of this microstructure is presented in Fig. 5.3 and shows very large grains. The low angle grain boundaries (LAGBs θ < 2°) are marked with red, while the high angle grain boundaries (HAGBs θ > 15°) are labelled in black. Grain size calculation was done using TSL software, employing the intercept method. The grain size distribution curves were drawn using TSL software, from which the minimum grain size of the material at respective deformation temperature and strain were calculated. The larger grains seen in the microstructure were manually separated out and drawn using GIMP® software, and then quantified using the image analysis software, MIP® (Tingdong, 2003). These grains are associated with the maximum grain size of the material at different deformation conditions.

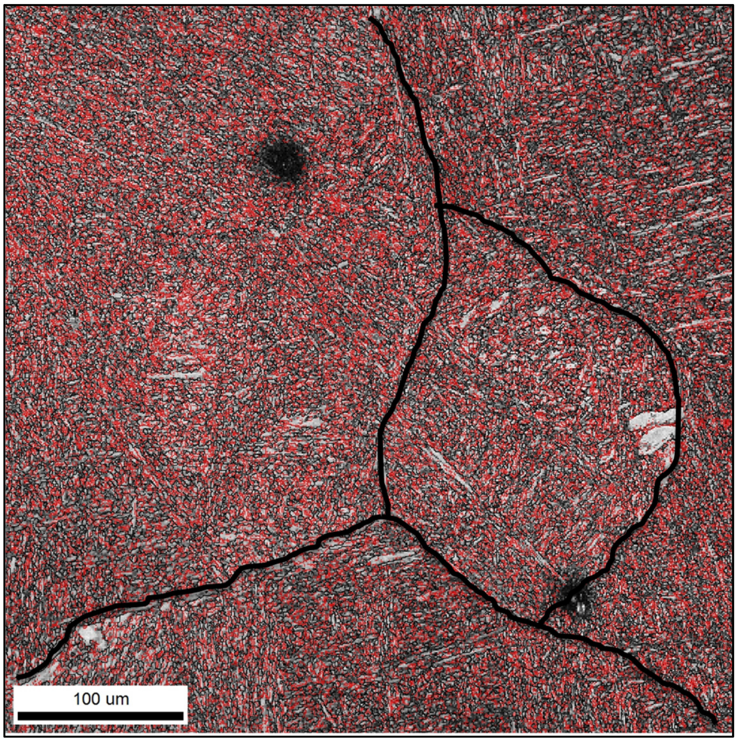

Figure 5.3 EBSD grain boundary map of *as-cast* medium carbon low alloy steel after austenizing at 1260 °C and then cooling to 1200 °C after which it was water quenched. Black lines denote HAGBs and red lines denote LAGBs

5.3 Results

5.3.1 Stress - Strain Curves

The flow stress-strain curves obtained after deformation at 1200 °C and 1150 °C, and strain rates of 0.25 s^{-1}, 1 s^{-1} and 2 s^{-1} are displayed in Fig. 5.4. Note that these temperatures are approximately 450 °C and 400 °C, respectively, above its paraequilibrium (Ae_3) temperature. The results show that the stress levels increase with an increase in strain rate; however, it decreases with an increase in temperature. The steady state flow was attained at a strain of about 0.5. At a strain rate of 0.25 s^{-1}, curves show an initial increase in stress, which is then accompanied by a gradual drop to a steady state value. With the increase in strain rate, true stress-true strain curves for both deformation temperatures show typical softening behavior. A stress drop of approximately 15% can be seen at testing conditions, employing the lowest strain rate and highest temperature, indicating the occurrence of dynamic softening phenomena.

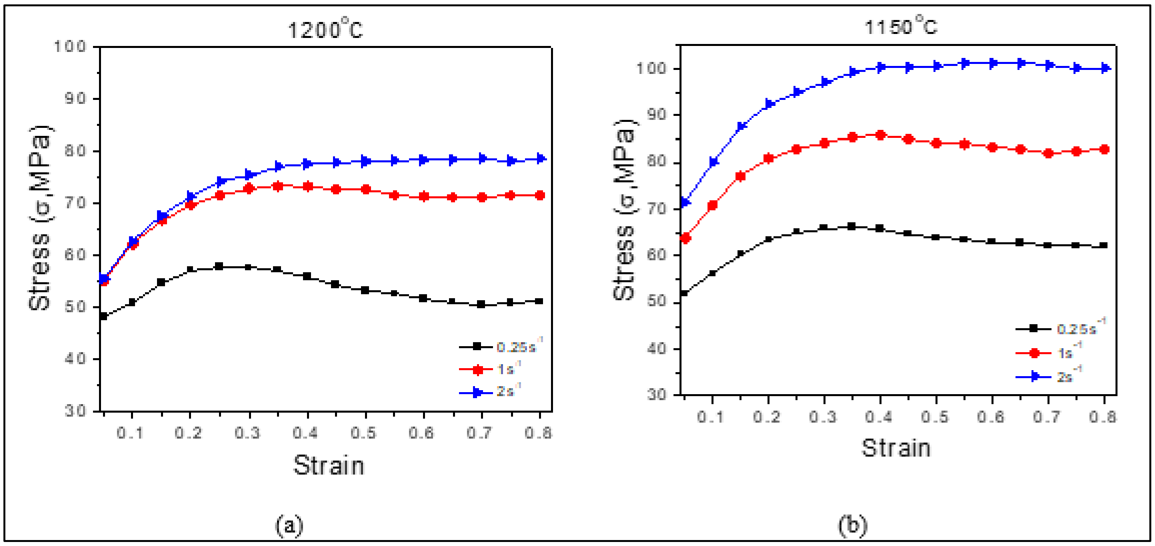

(a) (b)

Figure 5.4 Stress-strain curves of *as-cast* medium carbon low alloy steel during hot isothermal compression at strain rates of 0.25 s^{-1}, 1 s^{-1} and 2 s^{-1} at deformation temperatures of (a) 1200 °C, (b) 1150 °C

However, it is well established that during hot deformation of medium carbon low-alloy steels, in addition to DRX, the DT of austenite to ferrite, whose kinetics is much faster than DRX, may also occur (Aranas Jr et al., 2015). The double differentiation technique, proposed by Poliak and Jonas (Poliak et Jonas, 1996; 2003a), was used to evaluate the critical strains and stresses for the initiation of both DT and DRX. A dedicated script was developed in MATLAB® for analyzing the flow curves using this method.

In order to determine the critical stresses for the initiation of DT and DRX, the strain hardening rate, θ, was calculated by the following expression:

$$\theta = \left(\frac{\delta\sigma}{\delta\varepsilon}\right)_{\dot{\varepsilon}} \tag{5.1}$$

The minima were then calculated by taking the derivative of *θ,* (Ghosh, Basabe et Jonas, 2013; Jonas et al., 2013):

$$\left(\frac{\delta}{\delta\sigma}\right)\left(\frac{\delta\theta}{\delta\sigma}\right)=0 \tag{5.2}$$

The two minima shown in Fig. 5.5 (a) represent the critical stresses at which DT and DRX were initiated during deformation. The critical strains corresponding to these stresses were then calculated using the initial flow curves reported in Fig. 5.4.

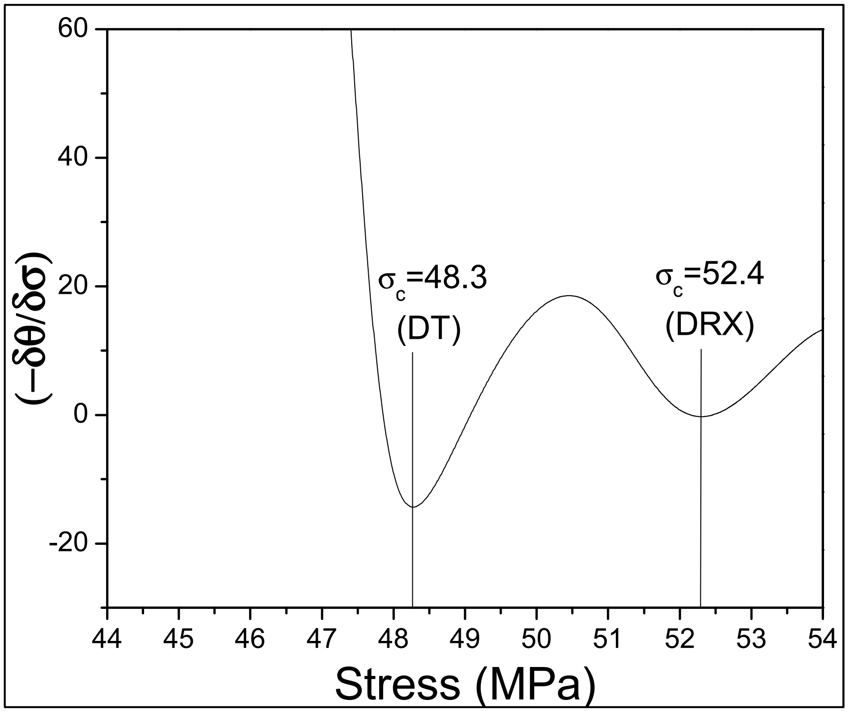

Figure 5.5 The double differentiation method employed in determination of the critical stresses and strains for DT and DRX. This experiment was carried out at 1200 °C and strain rate of $0.25s^{-1}$

The plots in Fig. 5.6 show variations of DT and DRX critical strains versus temperature and strain rate. This finding is in agreement with those reported by other researchers, who also showed that the critical strain for DT is less than that of DRX (Choi et al., 2003; Ghosh, Basabe et Jonas, 2013; Sun et al., 2008). Observations from the calculation of equations (5.1) and (5.2) of the present alloy show that the critical strain for DT is less than the one needed for DRX. In the present study the critical strains were 0.08 for DT and 0.13 for DRX at a deformation temperature of 1200 °C and a strain rate of 0.25 s^{-1}. From Fig. 5.6, it can be depicted that the critical strain for the initiation of DRX is higher than that for DT. It decreases with an increase in temperature and an increase in strain rate.

However, it must be noted that, the double differentiation technique is purely mathematical, and therefore microstructure analysis is needed to show the physical significance of critical strain on the evolution of the microstructure during hot deformation.

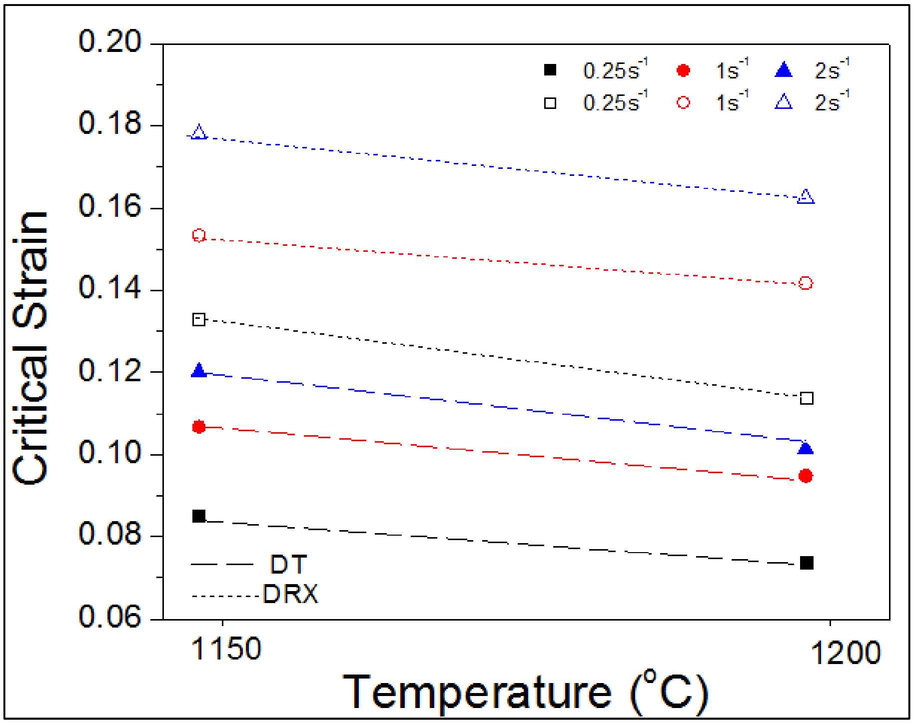

Figure 5.6 Critical stresses for dynamic transformation (DT) and dynamic recrystallization (DRX) determined over the temperature of 1150 °C to 1200 °C and strain rate of 0.25 s^{-1} to 2 s^{-1}

5.3.2 Microstructure Analysis

Fig. 5.7 shows the grain boundary map of the specimen deformed at 1200 °C and at strain rates of 0.25 s^{-1} (Fig. 5.7 (a)), 1 s^{-1} (Fig. 5.7 (b)) and 2 s^{-1} (Fig. 5.7 (c)). The microstructure shows prior austenite grain boundaries (shown in black), confirming the large grain size of prior austenite. At a higher strain rate (2 s^{-1}), a structure with a Widmanstätten type morphology is observed, which originates from the prior austenite grain boundaries and the interior of the grains. Note that ferrite plates were formed instead of martensitic structures due to the applied stress, which induces the displacive transformation of austenite to Widmanstätten ferrite. The width of these plates is affected by temperature due to the diffusion of alloying elements such as carbon. This observation is consistent with the results of numerous researchers described in Ref (Grewal et al., 2016). When the strain rate decreases to 1 s^{-1}, the microstructure becomes slightly coarser and the morphology appears to be mixed with lath and a few quasi-polygonal grains (see encircled area). At the lowest strain rate, a polygonal grain type morphology originating from the grain boundaries and from the interior of the grains was observed. Few polygonal grains show serrated and bulged grain boundaries, indicating the nucleation of new grains from these bulged areas of the grain boundaries (shown with red arrows). Comparative study of the features of the microstructure revealed that the Widmanstätten ferrite plates were finer at higher strain rates (e.g., Figs. 5.7 (b) & (c)). It is believed that this may be due to the disintegration of the deformation-induced Widmanstätten ferrite plates under high strain rate conditions, resulting in a finer structure (encircled in Fig. 5.7 (c)).

Fig. 5.8 shows the grain boundary map of the specimen deformed at 1150 °C and at strain rates of 0.25 s^{-1} (Fig. 5.8 (a)), 1 s^{-1} (Fig. 5.8 (b)) and 2 s^{-1} (Fig. 5.8 (c)). At a strain rate of 2 s^{-1} (Fig. 5.8 (c)), the microstructure is slightly finer than the one observed in Fig. 5.7 (c), i.e., Widmanstätten plates, nucleating from the prior austenite grain boundaries (highlighted with yellow arrow). At the intermediate strain rate, the microstructure is composed of lath and quasi-polygonal type ferrite. A comparison between the ferrite morphologies at deformation temperatures of 1150 °C and 1200 °C and strain rate of 0.25 s^{-1} showed that, while in both cases the dominant component of the microstructure is made of quasi-polygonal type ferrite, Widmanstätten plates are clearly visible in the sample deformed at 1150 °C and none in the one deformed at 1200 °C (Fig. 5.7 (a)).

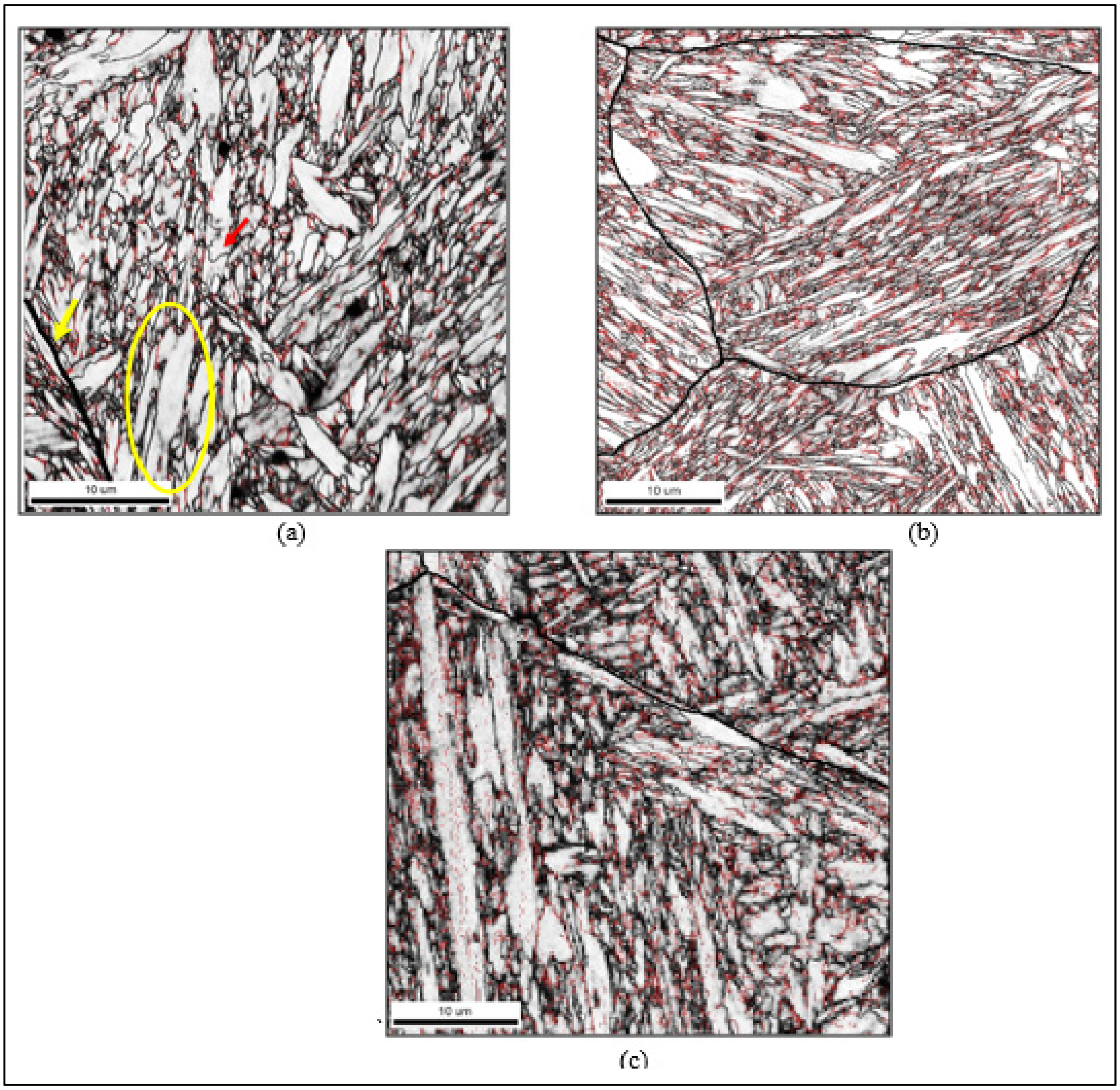

Figure 5.7 EBSD grain boundary map of *as-cast* medium carbon low alloy steel deformed at deformation temperature of 1200 °C at strain rate of (a) 0.25 s^{-1}, (b) 1 s^{-1} and (c) 2 s^{-1}. Black lines denote HAGB and red lines denote LAGB

Hot deformed microstructures at 1200 °C and 1150 °C for all the strain rates revealed a microstructure consisting of colonies of bainite laths with different morphologies, and polygonal grains in different orientations with respect to the loading directions.

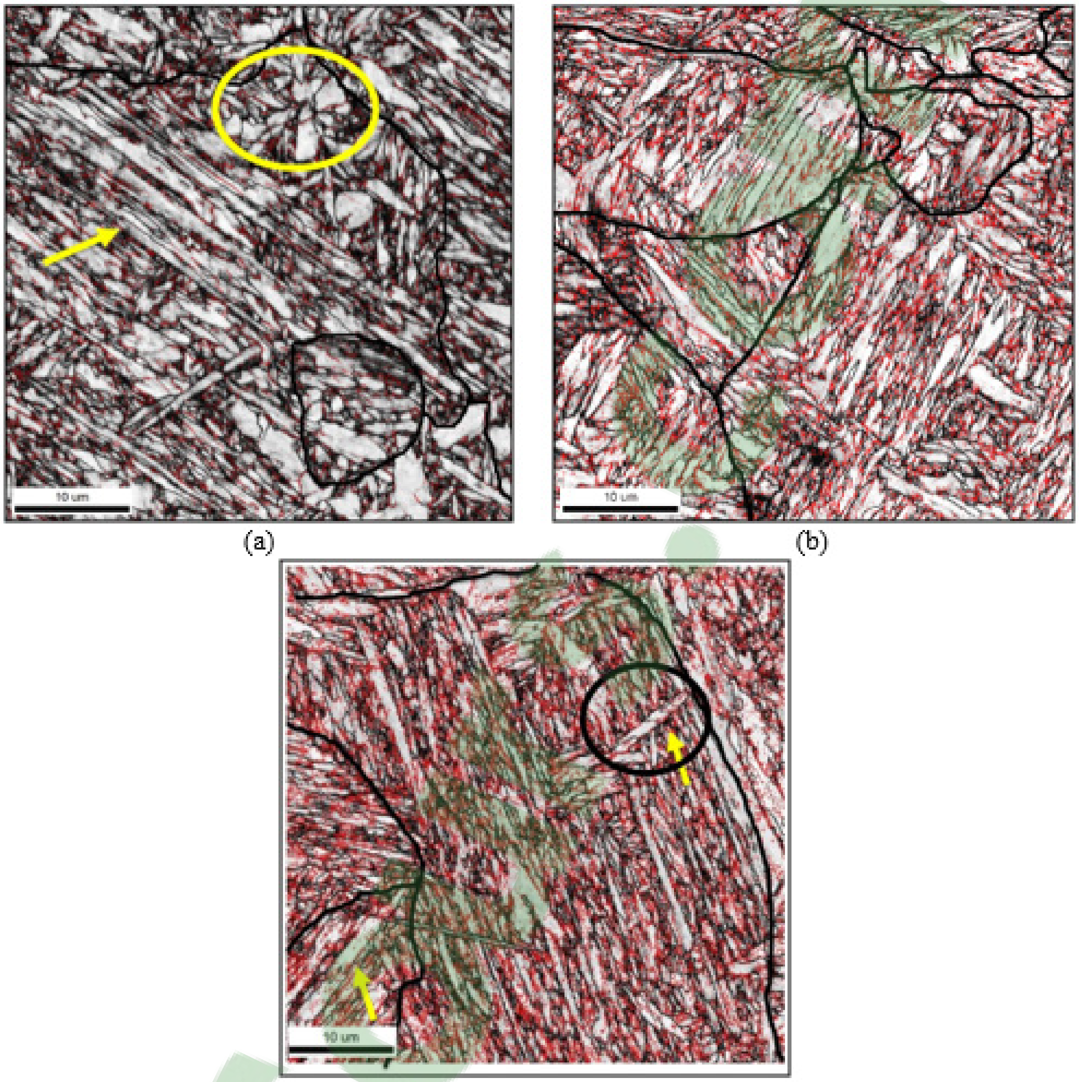

(a) (b) (c)

Figure 5.8 EBSD grain boundary map of *as-cast* medium carbon low alloy steel deformed at deformation temperature of 1150 °C and strain rate of (a) 0.25 s^{-1}, (b) 1 s^{-1} and (c) 2 s^{-1}. The black encircled region shows the disintegration of the Widmanstätten plate at high strain rate. Black lines denote HAGB and red lines denote LAGB.

A detailed microstructure analysis using EBSD grain boundary maps showed that at a strain rate of 0.25 s^{-1}, for the material deformed at 1200 °C, the entire microstructure was free from low angle grain boundaries (LAGBs), which could be an indication that the microstructure is fully recovered, although recrystallization and phase transformation may also contribute to a decrease in LAGBs. In contrast, LAGBs were still present in the sample deformed at 1150 °C and at a similar strain rate, suggesting that this temperature was insufficient to fully recover the microstructure. The polygonal grains displayed in Figs. 5.7 (a) and 5.8 (a) (0.25 s^{-1}) with few LAGBs or no LAGBs are strain-free grains. Their presence is probably due to the fact that a low strain rate and high temperature provide a sufficient driving force for recovery (Rollett et al., 2004). Figs. 5.7 (c) and 5.8 (c) show that significantly higher fractions of LAGBs are present in the grain boundary maps of the material deformed at higher strain rates (i.e., at 2 s^{-1}), which indicates that the internal structure of these lathes is highly deformed.

5.4 Discussion

5.4.1 Flow Curves Analysis

5.4.1.1 Effect of Strain Rate

An analysis of Fig. 5.6 shows that with the increase in strain rate from 0.25 s^{-1} to 2 s^{-1}, critical strains increase by about 40% (for T = 1200 °C). Here, it is important to note that although the critical strain for the initiation of DT is higher at higher strain rates ($\varepsilon_c = 0.103$ at 2 s^{-1} as compared to $\varepsilon_c = 0.073$ at 0.25 s^{-1} for T = 1200°C), the time to reach this critical strain is much shorter since the strain rate is higher (0.05s for 2 s^{-1} and 0.4s for 0.25 s^{-1}). The above results reveal a clear influence of strain rate on the initiation of DT. These observations are in contrast with some previous reports, which indicate that the strain rate does not affect the DT critical strains and/or the initiation of dynamic transformation (Basabe, Jonas et Ghosh, 2013; Jonas et al., 2013). The influence of strain rate on the formation of ferrite from deformed austenite can be justified in terms of the available time for dynamic transformation at lower strain rates and the diffusion of alloying elements. This will be discussed in detail in the next sections.

5.4.1.2 Effect of Temperature

The influence of temperature on the initiation of DT is illustrated in Fig. 5.6. The temperature effect on the critical strains associated with the initiation of DT is well established in the literature (Aranas Jr et Jonas, 2015; Aranas Jr et al., 2015; Aranas, Wang et Jonas, 2015; Ghosh, Aranas Jr et Jonas, 2016; Grewal et al., 2016; Jonas et Ghosh, 2013; Jr. et al., 2015). It has been reported that the critical strain increases with the temperature beyond Ae_3 to a maximum value, but then decreases until it reaches the delta ferrite formation temperature (Grewal et al., 2016). From a thermodynamic perspective, this could be related to the free energy for transformation. The evaluation of the energy barrier, defined here as the difference between the ΔG of ferrite and austenite, was calculated for the present steel using the FactSage thermodynamic software, employing the FSStel Database® (Bale et al., 2009). As shown in Fig. 5.9, ΔG for DT starts to decrease from 1090 °C.

The lower energy barrier value also results in less work hardening required for the transformation softening to take place in austenite. As indicated in Fig. 5.6, the critical strains at 1200 °C are lower than those at 1150 °C for all strain rates. Here, 1200 °C is closer to the delta ferrite formation temperature of this alloy, which is approximately 1480 °C, as calculated with the Thermocalc® Software, using the TCFE7 database (Andersson et al., 2002b). As the deformation temperature approaches the delta ferrite formation temperature, the Gibbs free energy of the deformed austenite gets very close to that of the delta ferrite, thereby easing the initiation of DT. However, it should be noted that the critical strain measured in this study is higher than that reported in the literature (0.11, compared to 0.08 for T = 1200 °C and $\dot{\varepsilon} = 1s^{-1}$) (Grewal et al., 2016; Jr. et al., 2015). The difference in the critical strain value is probably due to the higher carbon level in the present steel (0.34 %) as compared to the carbon level reported for low carbon steel (0.06 %) (Jr. et al., 2015). Indeed, as reported by Ghosh et al. (Ghosh, Basabe et Jonas, 2014), the resistance to DT increases with an increase in the carbon content of steel for the same testing temperature because carbon is an austenite stabilizer. Note that the addition of austenite stabilizers is known to decrease the Ae_3 temperature. Considering the fact that lower Ae_3 values delay the initiation of dynamic transformation, higher values of DT critical strain are therefore expected in the present steel.

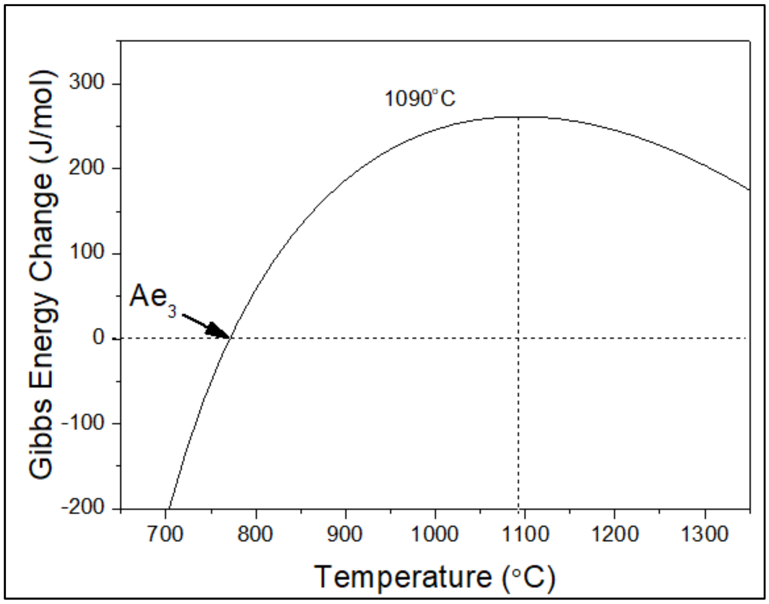

Figure 5.9 $\Delta G_{(\alpha-\gamma)}$ vs T for medium carbon low alloy steel showing the Gibbs energy obstacle opposing dynamic transformation

5.4.2 Analysis of Grain Boundary Maps

The grain size of the starting material (as-cast and homogenized) was about ~400 μm (Fig. 5.3). This value is very large in comparison with all other previous studies: 13 μm (Eghbali, 2010), 15 μm (Park et al., 2013a), 20 μm (Cai, Ding et Lee, 2011) and 65 μm (Sun et al., 2014). Based on the obtained results, the microstructure after deformation is expected to be composed of DRXed austenite and DTed ferrite. After quenching, the microstructure is expected to be composed of martensite and DTed ferrite. However, it is difficult to differentiate between martensite and dynamically transformed ferrite by using XRD, Optical or secondary electron imaging (Sun et al., 2014). In the present study, the EBSD technique, and specifically the Kernal Average Misorientation (KAM) (Schwartz et al.) method, was used to obtain internal misorientation between grains, and to therefore distinguish the BCT martensite from the BCC ferrite. Fig. 5.10 shows schematic representation of the KAM approach (Bhattacharjee et al., 2014; Schwartz et al.). The average misorientation of a given point with all points (Fig. 5.10 (a)) in the kernel or at the perimeter of the kernel is calculated with the provision that misorientations exceeding a given threshold value are excluded. In other words, by using KAM, grain size is defined based on a certain angle of grain boundaries and number of step sizes. In the present work, up to the third nearest neighbor (step size) was considered for calculating KAM values, and a threshold angle of 5° was used. To study the recovery behavior, only the area fractions with less than 2° misorientation (i.e., KAM ≤ 2°; green and blue regions) were considered.

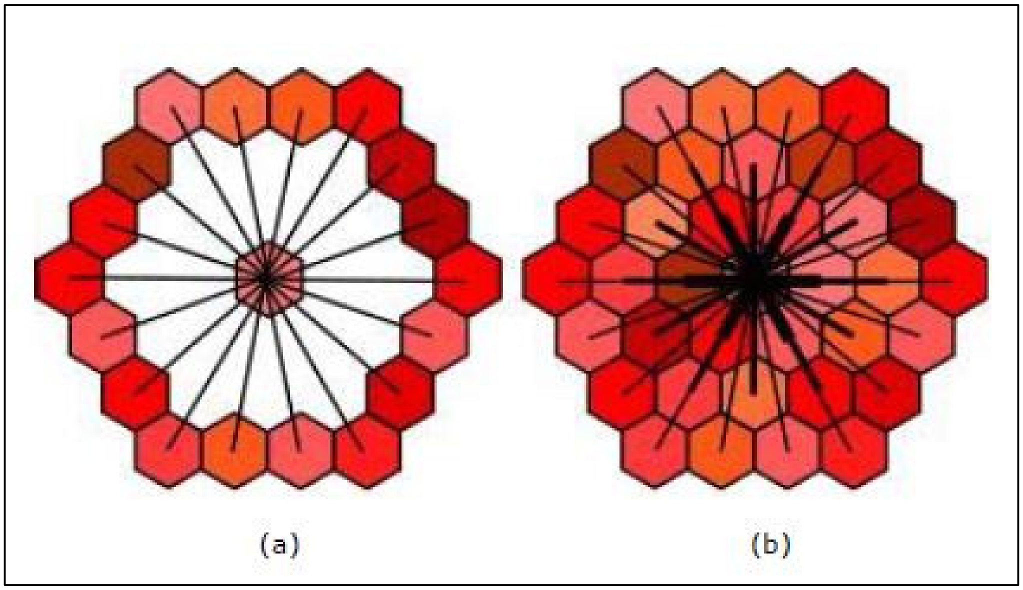

Figure 5.10 Schematic diagram showing (a) misorientation between a grain at the center and all other points at the perimeter of the kernel and (b) misorientation between a grain at the center and all points in the kernel

Using the above criteria, the dynamic recovery process of the two phases was studied, and a differentiation was made between ferrite and austenite. It is known that ferrite has a higher stacking fault energy (SFE) (Reick, Pohl et Padilha, 1998) than austenite, which would make dynamic recovery easier when it is further deformed to a higher strain (ε = 0.8). This leads to lower density of LAGBs within ferrite grains, which in turn leads to lower misorientation within the grain, as confirmed in the KAM map shown in Fig. 5.11. On the other hand, martensite laths (from prior austenite) which are formed due to shape deformation (displacive transformation) generate a higher amount of LAGBs, resulting in higher misorientations within the laths.

Fig. 5.11 (a) shows the KAM map for the specimen deformed at 1200 °C and at a strain rate of 0.25 s^{-1}. Quasi-polygonal ferrite grains, as observed on the Grain Boundary map (G.B. map) of Fig. 5.7 (a), a have <2° misorientation, thus confirming that they are recovered ferrite grains, whereas at 1200 °C and at a strain rate of 2 s^{-1}, as shown in Fig. 5.11 (c), the majority of the grains have a KAM between 3°-5°, signifying the presence of martensite due to untransformed austenite.

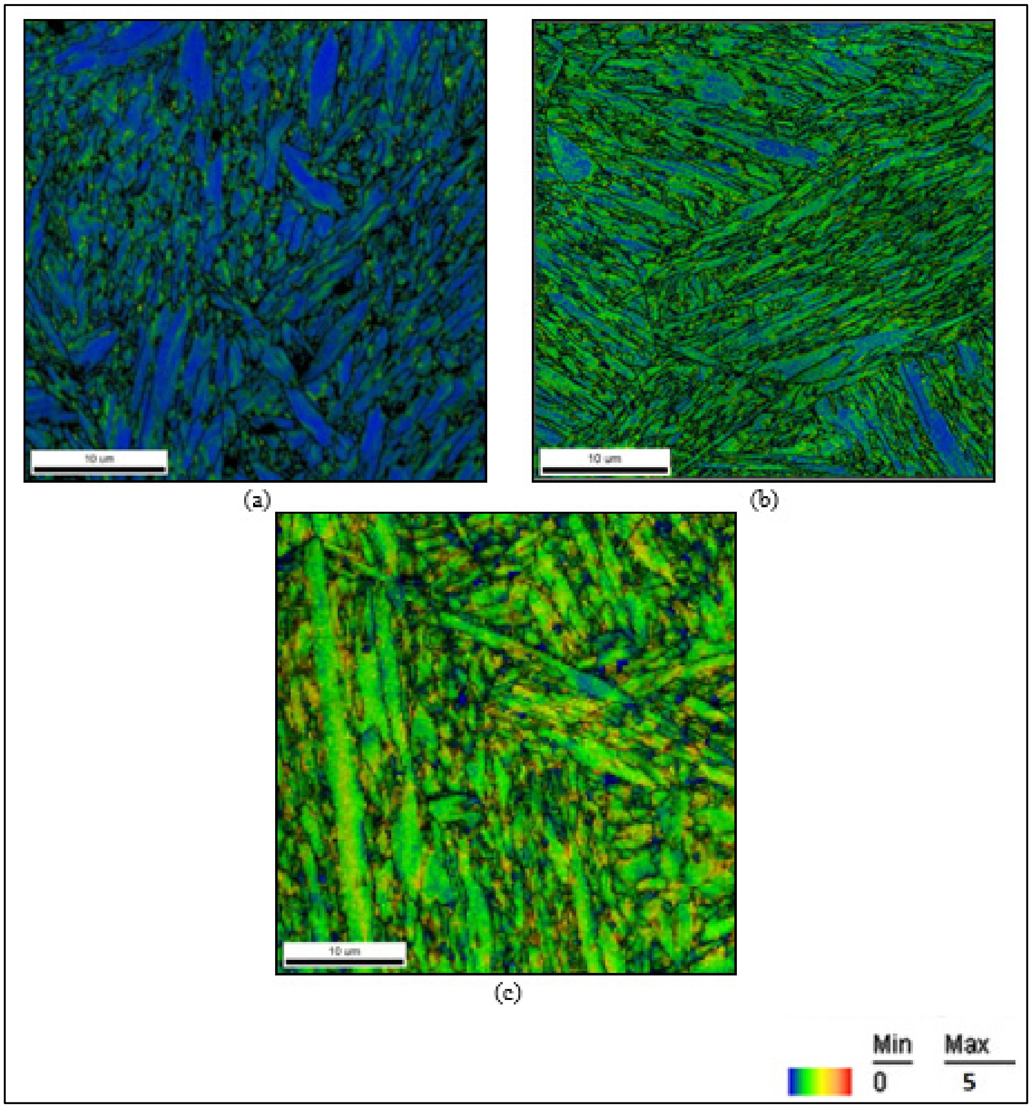

Figure 5.11 EBSD Kernal Average Map (KAM) of *as-cast* medium carbon low alloy steel deformed at deformation temperature of 1200 °C at strain rate of (a) 0.25 s^{-1}, (b) 1 s^{-1} and (c) 2 s^{-1}. Black lines denote HAGB

Fig. 5.12 shows the approximate fraction of ferrite (KAM values <2°) as a function of the Zener Hollomon parameter (Z parameter, equation (5.3) (Chadha et al., 2017b).

$$Z = \dot{\varepsilon}\exp(\frac{Q}{RT}) \tag{5.3}$$

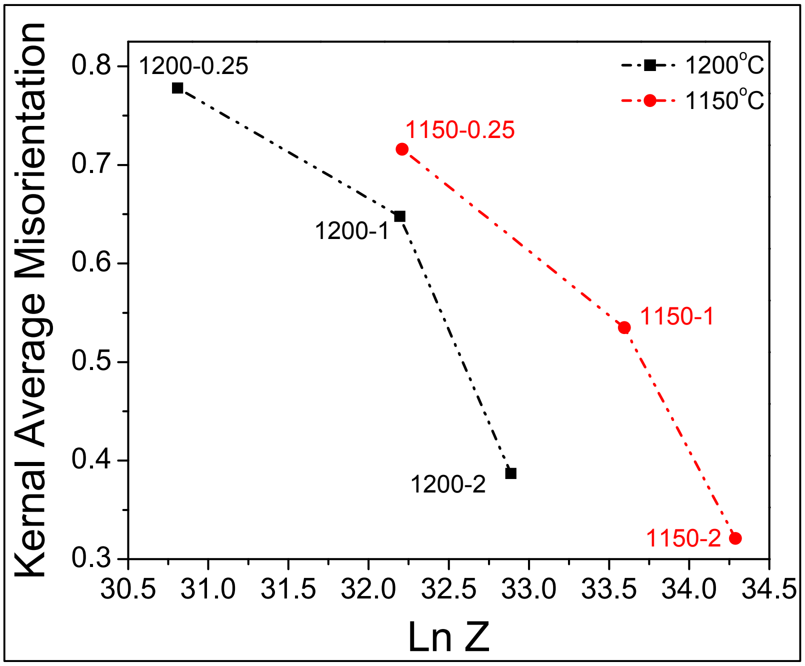

Figure 5.12 Graph of Kernal Average Misorientation fraction (KAM <2º) vs. Ln Z. The graph reveals the effect of strain rate and temperature on ferrite fraction

The area fraction of KAM with misorientations of less than 2° represent the fraction of ferrite. The ferrite fraction decreases as the strain rate increases, while it is higher at higher temperatures. For instance, at the strain rates of 0.25 s^{-1} and 2 s^{-1}, the ferrite volume fraction was around 77% and 38%, respectively. Similarly, at a constant strain rate of 0.25 s^{-1}, the ferrite fraction was respectively 77% and 72% at 1200 °C and 1150 °C. The above findings are consistent with those reported by N. Park et al. (Park et al., 2013b; Park et al., 2013c) who observed that with the decrease in the strain rate, the ferrite fraction increased in a 6Ni-0.1C steel. Considering that the growth of a dynamically transformed ferrite plate depends on the diffusion of alloying elements during deformation, and particularly that of carbon, the influence of the strain rate and temperature on the occurrence of DT can, therefore, be correlated to the diffusion of carbon during deformation. This will be discussed in the following section.

5.4.3 Influence of Strain Rate on Carbon Diffusion

Several authors have reported on increase in carbon diffusion with temperature (Aranas Jr et al., 2015; Ghosh, Aranas Jr et Jonas, 2016; Grewal et al., 2016; Jr. et al., 2015). Specifically, in DT studies on medium carbon low-alloy steels, it has been reported that carbon diffusivity increases by 8.6 times when the temperature increases from 900 °C to 1350 °C [1-7]. However, this increase is not solely associated with temperature change, but is also related to the applied stress. The influence of strain rate on carbon diffusivity can be quantified by plotting the diffusivity of carbon vs. strain graph. Indeed, as the stress values for each interval of strain vary with the strain rate, the effect of strain rate on carbon diffusion can be calculated by incorporating the respective stress values at a particular strain with respect to the individual strain rates, in the diffusion equations.

Lattice and pipe diffusion of carbon are the two important mechanisms by which solutes transfer to or away from stacking faults (Viswanathan et al., 2015). Lattice diffusion occurs when substitutional or interstitial atoms move to another lattice position, e.g., Fe atoms in Fe alloys, whereas pipe diffusion occurs when the atoms move via edge dislocations e.g. interstitial atoms like carbon in Fe alloys (Levine et MacCallum, 1960; Love, 1964). It has been reported by many researchers that interstitial atoms and solutes diffuse much faster through pipe diffusion than lattice diffusion due to higher activation energies required for the latter (http://nptel.ac.in/courses/113108052/module3/lecture17.pdf). Therefore, pipe diffusion plays the most important role, and is probably the dominant mechanism in the diffusion of solutes (Robinson et Sherby, 1969; Sauvage et Ivanisenko, 2007)

The effective diffusion is given by D_{eff} as;

$$D_{eff} = D_L f_L + D_P f_P \tag{5.4}$$

where *DL* and *DP* are respectively the lattice and pipe diffusion coefficients, f_L and f_P are fractions of atoms participating in the lattice and pipe diffusion processes, and f_L is given as unity and $f_P = 7.03125\left(\frac{\sigma}{\mu}\right)^2$ (Samantaray et al., 2011b).

The general expression for calculating *DL* and *DP* are presented in Appendix B, equations B 5 & B 6. In these equations, *b* represents the Burgers vector (*m*) and *μ* represents shear modulus (MPa). The equations for obtaining the values of *b* (eq. B 1) and *μ* (eq. B 3) under applied stress were proposed by Ashby and Frost (Ashby et al., 1978; Frost et Ashby, 1982). It is shown from the equations that when there is no stress, there is no pipe diffusion. Table 5.2 shows all the required variables for the calculation of *DL* and *DP* of carbon.

Table 5.2 Temperature, Pressure Coefficients, and Material Data for Carbon in Medium Carbon Low alloy steel

Parameters	Values
Bulk Modulus K_0(MPa) (Andersson et al., 2002b)	1.6×10^5
Shear Modulus μ_0(MPa) (Andersson et al., 2002b)	7.6×10^4
Pressure Dependence $\frac{d\mu}{d\sigma_s}$ (Frost et Ashby, 1982)	1.8
Pressure Dependence $\frac{dK}{d\sigma_s}$ (Frost et Ashby, 1982)	4.8
Temperature Dependence $\frac{T_M dK}{K_0 dT}$ (Andersson et al., 2002b)	0.15
Temperature Dependence $\frac{T_M d\mu}{\mu_0 dT}$ (Andersson et al., 2002b)	-0.46
Activation Volume $V_p^*\left(\frac{m^3}{mole}\right)$ (Ridley et Stuart, 1970)	1.3×10^{-6}
Burger's Vector, b_0 (m) (Frost et Ashby, 1982)	2.5×10^{-10}
Pre-Exponential of pipe diffusion, $a_p D_{0p}$ $\left(\frac{m^4}{s}\right)$ (Brandes, Brook et Paufler, 1993; Frost et Ashby, 1982)	5.7×10^{-24}
Activation energy of pipe diffusion, Q_{p0} $\left(\frac{KJ}{mole}\right)$ (Frost et Ashby, 1982)	88.8
Pre-exponential of lattice diffusion for Carbon D_{0L} $\left(\frac{m^2}{s}\right)$ (Brandes, Brook et Paufler, 1993)	7.9×10^{-7}
Activation energy of lattice diffusion for Carbon, Q_L $\left(\frac{KJ}{mole}\right)$ (Brandes, Brook et Paufler, 1993)	148
Melting point of medium carbon low alloy steel, T_M $[K(°C)]$ (Andersson et al., 2002b)	1768

The diffusivity due to *DL*, *DP* and the corresponding effective diffusion (*Deff*) are shown in Fig. 5.13 for a deformation temperature of 1200 °C and a strain rate of 0.25 s^{-1}. It can be seen that D_L is constant while D_P changes with change in stress value at constant temperature. Specifically, D_P was found to be 6.8 times faster than D_L, indicating the significance of D_P. Since lattice diffusion is constant for a particular temperature and independent of the stress level, only the variations of D_P will be considered for other temperatures.

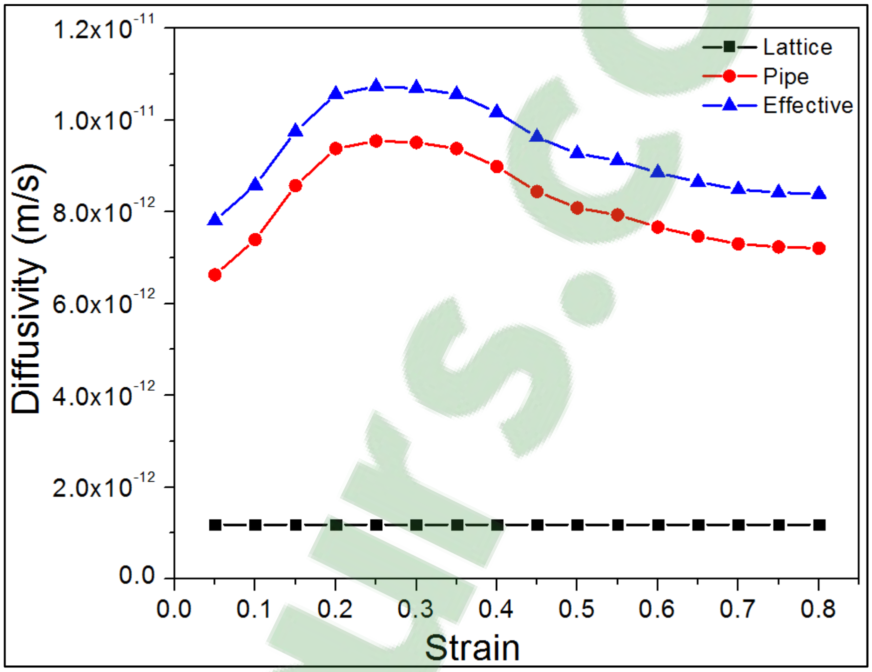

Figure 5.13 Graph depicting diffusivity due to lattice diffusion, pipe diffusion and effective diffusion with regard to strain for 1200 °C and 0.25 s^{-1}. Due to the absence of stress, D_L is constant throughout the strain values

Diffusivity due to pipe diffusion (eq. B 6) for a deformation temperature of (a) 1200 °C and (b) 1150 °C, respectively, at various strain levels, is shown in Fig 5.14. It can be seen that at a constant temperature, the diffusivity of carbon increases with an increase in the strain rate. The equations used to calculate D_P have stress as a variable, thereby indicating that any change in the stress value should significantly change the diffusivity values at a constant temperature. Therefore, the application of the compressive stress during deformation accelerates the pipe diffusion process (i.e., D_P increases). The obtained results are in good agreement with those reported by Tingdong (Tingdong, 2003), who for a series of low carbon steels, observed that the diffusion coefficient of impurity-vacancy complex was three times larger under applied stress than under stress-free conditions.

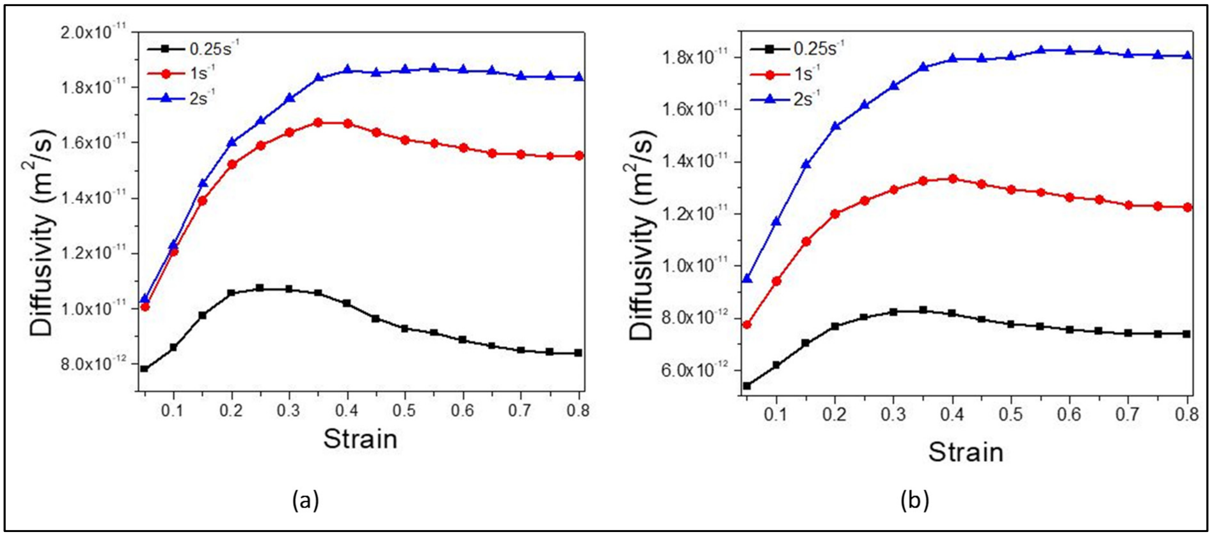

(a)

(b)

Figure 5.14 Graph depicting Diffusivity due to pipe diffusion vs strain for (a) 1200 º C and (b) 1150 º C

Fig. 5.15 shows the distances over which carbon atoms can diffuse under lattice and pipe diffusion at 1200 °C and at a strain rate of 0.25 s^{-1}. It can be seen that the lattice diffusion distance varies from 0.48 µm (at $\varepsilon = 0.05$) to 1.90 µm ($\varepsilon = 0.8$) at 1200 °C, whereas the pipe diffusion distance varies from 1.15 µm (at $\varepsilon = 0.05$) to 4.80 µm ($\varepsilon = 0.8$). Specifically, at a strain of 0.8, the distance traveled by pipe diffusion is ~2.4 times higher than that by lattice diffusion. Figs. 5.16 ((a) & (b)) shows the variation of diffusion distance, x (µm) due to pipe diffusion vs. strain at a deformation temperature of (a) 1200 °C and (b) 1150 °C. The results indicate that the diffusion distance traveled by carbon atoms decreases when the strain rate increases. As shown in Fig. 5.14, as the stress increases, the diffusivity increases, but with the increase in strain rate, the trend is opposite. Furthermore, it appears that the time available for the diffusion is less at high strain rates than at slower strain rates. For example, at a strain of 0.8, this time is 0.4 s at 2 s^{-1} while it is 3.2 s at 0.25 s^{-1}. This indicates that the governing mechanism controlling the diffusion of carbon from ferrite, after transformation, is mainly dislocation pipe diffusion. This finding is in agreement with those reported by other researchers who identified dislocation pipe diffusion as the governing mechanisms during hot deformation of other steels (Lesuer et al., 2001; Samantaray et al., 2011a; Sauvage et Ivanisenko, 2007).

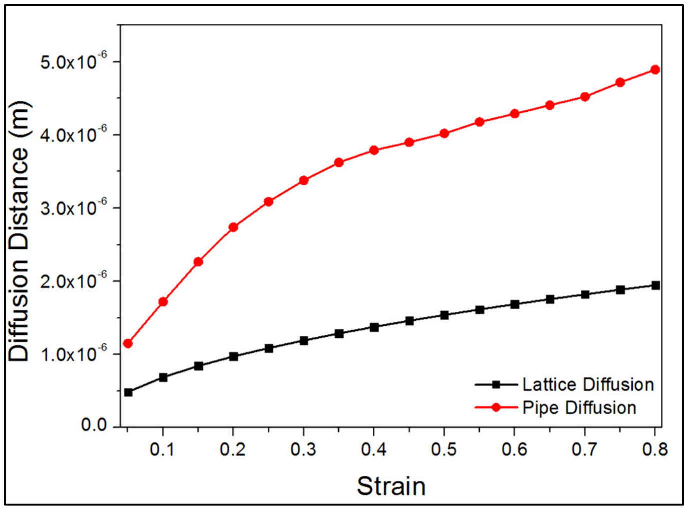

Figure 5.15 Graph depicting diffusion distance of carbon atom with respect to the strain for deformation temperature of 1200 ºC and 0.25 s^{-1}

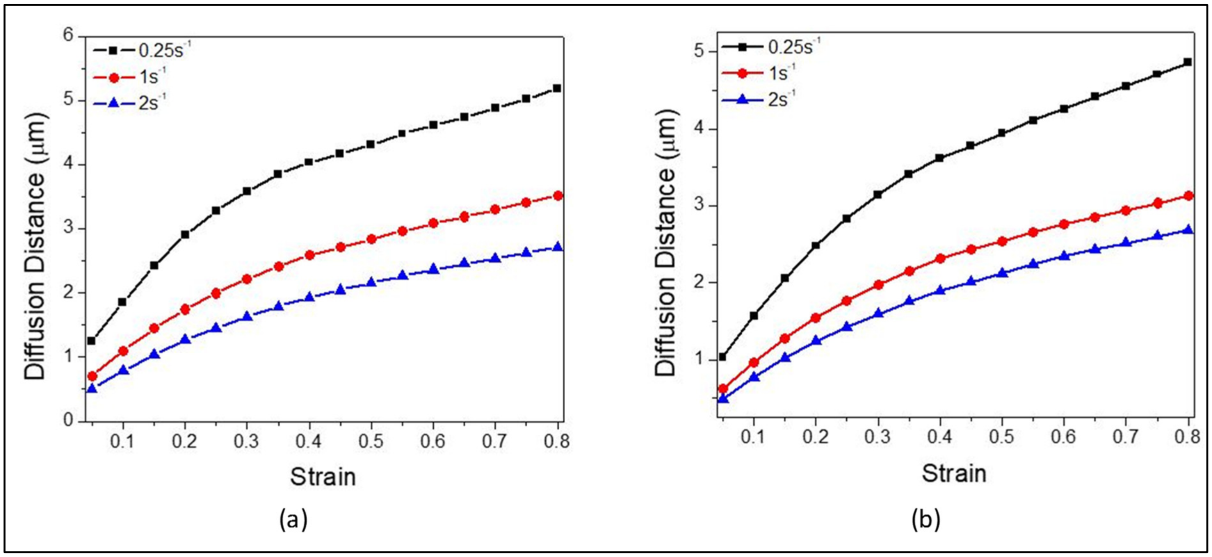

Figure 5.16 Graph depicting diffusion distance of carbon w.r.t strain for (a) 1200ºC and (b) 1150ºC

Finally, Figs. 5.17 ((a) & (b)) show the variation of diffusion distance, *x* (μm), due to pipe diffusion vs. deformation time, t (s) for a strain rate of 0.25 s^{-1}. An analysis of the graph shows that with an increase in both temperature and deformation time, the diffusion distance of carbon atoms increases. This finding could be correlated with the higher volume fraction of ferrite obtained after deformation at a strain rate of 0.25 s^{-1}, where the deformation time is 8 times higher, than when the deformation was applied with a strain rate of 2 s^{-1}.

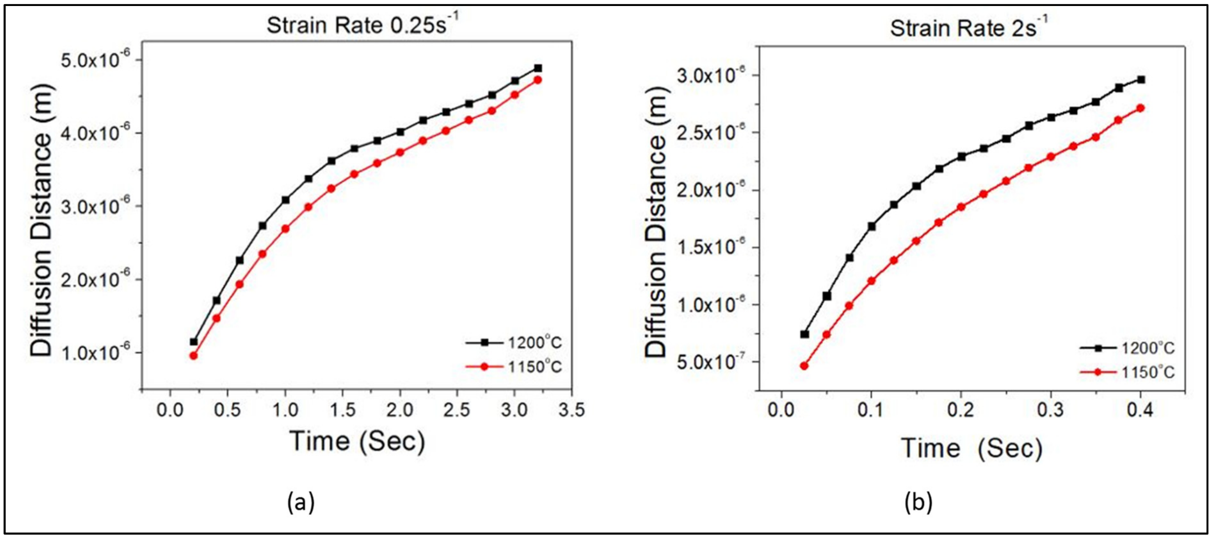

(a) (b)

Figure 5.17 The variation of diffusion distance, x (m) due to pipe diffusion coefficient vs. deformation time, t (sec) for (a) 0.25 s^{-1} and (b) 2 s^{-1}

5.4.4 Evaluation of the DT Ferrite Grain Size

The nucleation and growth of DT ferrite depends on several factors, such as temperature, stress level, alloying elements, holding time, etc. These have been studied in detail by various researchers (Ghosh, Aranas Jr et Jonas, 2016). Due to the complexity of separating the individual effects of these factors, the present results account for the influence of carbon diffusion in the nucleation and growth of ferrite. The evolution of ferrite grain size is certainly related to the diffusion distance of carbon (Bhadeshia, 1985; Ghosh, Aranas Jr et Jonas, 2016). In this study, a new mechanism is proposed in order to relate the grain size to the diffusion distance. To that end, the following assumptions are made:

1. The grain size at the critical strain for DT (i.e., at $\varepsilon = 0.1$) is assumed as the smallest average grain size in the GB map (Figs. 5.7 & 5.8).

2. The largest average grain size for the strain of $\varepsilon = 0.8$ is the grain size of the large grains observed in the GB map (Figs. 5.7 & 5.8).

The calculation followed the procedure described in the *Materials and Methods* section.

As per the diffusion calculation presented in Fig. 5.15, the critical strain for the occurrence of DT corresponds to the minimum distance traveled by the carbon atoms, whereas the highest strain corresponds to the maximum distance travelled by the carbon atoms.

Fig. 5.18 shows the plot of the smallest and largest average grain sizes with respect to the diffusion distance of carbon for strain rates of (a) 0.25 s^{-1} and (b) 2 s^{-1}. It can be seen that with the increase in the strain rate, the diffusion distance of carbon decreases with respect to the smallest or largest average grain size. The relation between the grain size evolution and the diffusion distance of carbon for strain rates of (a) 0.25 s^{-1} and (b) 2 s^{-1} is shown schematically in Fig. 5.19.

During deformation at the lowest strain rate, i.e., 0.25 s^{-1} (Fig. 5.19 (a)), at the stage I, nucleation of DT Widmanstätten ferrite plates from the prior austenite grain boundaries (PAGBs) starts. The nucleated plates are “self-accommodating plates”, which form due to the shear and dilatation of austenite (Jonas et Ghosh, 2013). At this stage, the diffusion distance (1.85 μm, Fig. 5.18) is greater than the smallest average grain size (1.11 μm), and therefore, the carbon atoms can diffuse out of the Widmanstätten ferrite plates from both the width and the leading edges. With increasing deformation, the nucleated DT Widmanstätten ferrite continues to expand both from the edges and the width, while at the same time, more nucleation of DT Widmanstätten ferrite takes place from the PAGBs, as well as in the interior of the grains. This has been related to the occurrence of variable amounts of stored energy within different parts of large grains, due to the activation of different slip systems (Basabe, Jonas et Ghosh, 2013; Essadiqi et Jonas, 1988). The width and the length of the plates keep on increasing from all directions until they start to coalesce with other plates to form grains. Specifically, in stage II, the diffusion distance of carbon (5.26 μm) is significantly greater than that of the largest average grain size (4.26 μm), therefore the plates

coalesce into grains, and a lath structure is produced. The features of the lath type structure are clearly visible in Fig. 5.7 (a), and partially in Fig. 5.8 (a).
During deformation at the highest strain rate, i.e., 2 s^{-1} (Fig. 5.19 (b)), at stage I, nucleation of DT Widmanstätten ferrite grains from the PAGBs initiates from the critical strain of $\varepsilon = 0.1$. At this stage, the diffusion distance (0.58 μm) is smaller than the smallest average grain size (0.77 μm), and therefore, carbon atoms cannot diffuse out of the ferrite from the width direction, whereas they can diffuse out from the leading edges. Moreover, the growth rate of the Widmanstätten plate depends on the diffusivity of carbon atoms (Saunders et al., 2003). As a result, the plates tend to increase in the leading edge in the direction of the applied stress. Further straining causes more nucleation of the DT Widmanstätten ferrite due to the activation of more slip systems. Here, the plates are not seen growing in the width direction, and therefore, no grains are formed, as in case of low strain rate (0.25 s^{-1}). With the increase in strain, the plates start to disintegrate as they further increase lengthwise (Grewal et al., 2016). Clear evidence of this behavior is shown in Figs. 5.7 (c) and 5.8 (c), where long and thin Widmanstätten ferrite plates and their gradual disintegration are clearly visible.

In summary, the formation mechanism of ferrite grains is a two-step process, where ferrite nucleates first as Widmanstätten type laths, and in the second stage the laths coalesce due to the least misorientation between two adjacent ferrite plates and convert into granular morphology (Aranas Jr et al., 2015; Basabe, Jonas et Ghosh, 2013; Grewal et al., 2016; Jr. et al., 2015). However, the coalescence process cannot be accomplished during high strain rate deformations due to the higher misorientation difference between two adjacent laths produced by intense straining, whereas at higher temperature and lower strain rates, the microstructure is in recovery state.

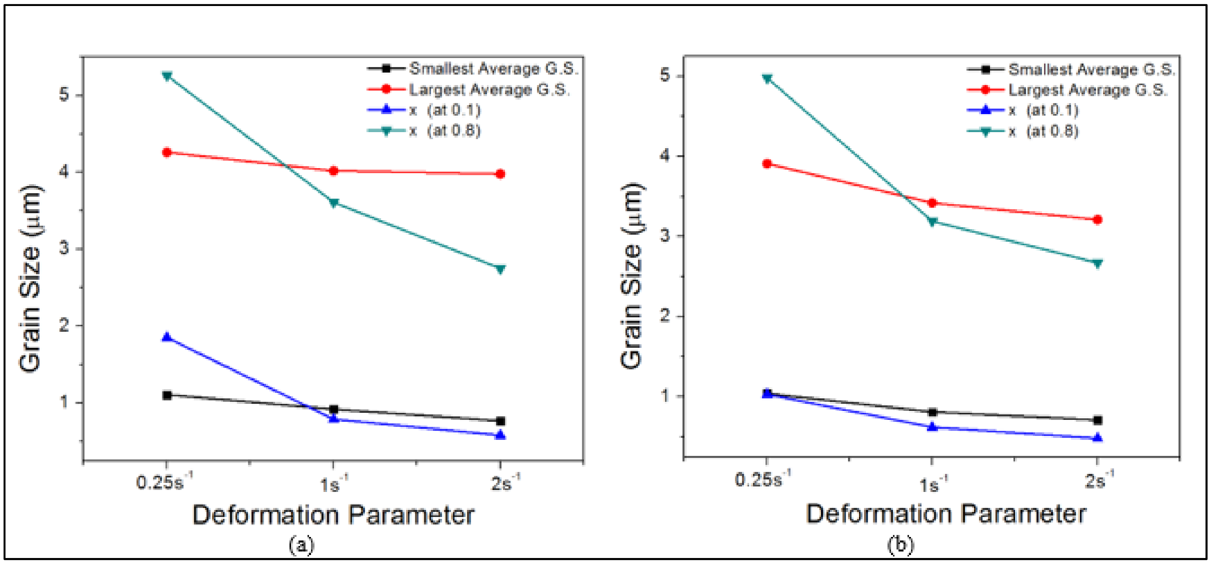

(a) (b)

Figure 5.18 Graph depicting correlation of grain size and diffusion distance w.r.t the strain rate for (a) 1200 ºC and (b) 1150 ºC

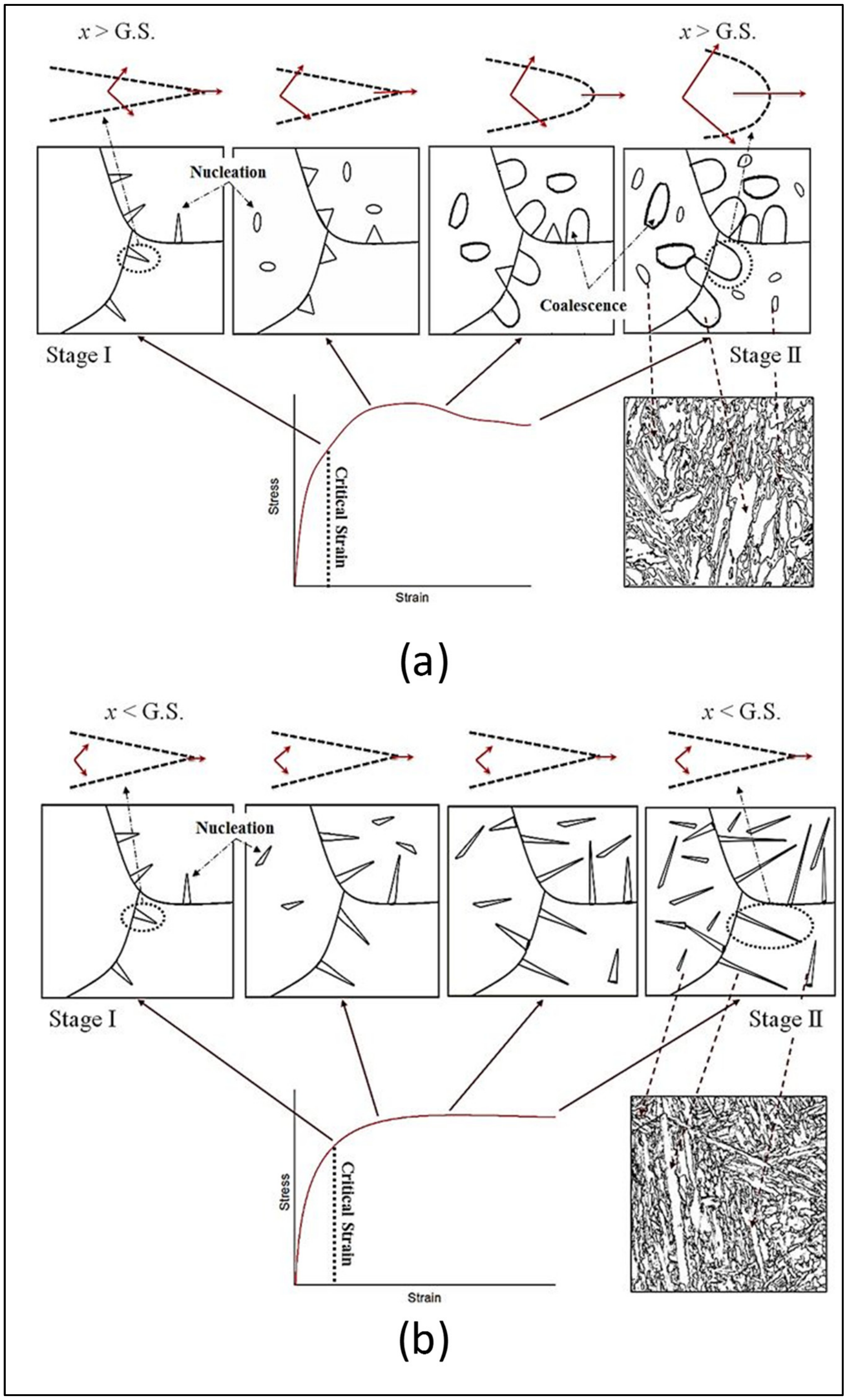

Figure 5.19 Schematic depicting the hypothesis to relate G.S. (grain size) and *x* (diffusion distance of carbon) for the strain rate of (a) 0.25 s^{-1} and (b) 2 s^{-1}. Red arrows represent diffusion of carbon atoms from the Widmanstätten grains (dashed lines)

5.5 Conclusions

In the present work, the possible occurrence of dynamic transformation of austenite to ferrite in the as-cast structure of a large size ingot of medium carbon alloy steel and the influence of strain rate on the occurrence of DT was investigated. The following conclusions can be drawn from this study:

- An analysis of flow curves by the double differentiation method and a microstructural analysis with an EBSD-KAM approach showed the occurrence of DT even in very large grain size materials.
- An investigation of microstructure evolution with the KAM technique showed the influence of processing parameters on dynamic transformed ferrite fraction. High strain rates resulted in a reduction in dynamically transformed ferrite fractions. Moreover, more ferrite was observed at around 1200 °C which is close to the formation temperature of delta ferrite.
- The strain rate has a significant influence on the morphology of the DT ferrite: a higher strain rate shows the Widmanstätten morphology, while at a lower strain rate, a quasi-polygonal morphology was formed due to the plate coalescence mechanism.
- A coarser microstructure with a quasi-polygonal morphology at lower strain rates and higher temperature was attributed to carbon diffusion and larger prior austenite grain size.
- A diffusion analysis of carbon during high temperature deformation showed higher diffusivity but shorter diffusion distances at high strain rates and temperatures.
- The ferrite fraction was correlated with the diffusion distance of carbon atoms: granular ferrite plates were formed with a higher diffusion distance of carbons atoms, whereas with a lower diffusion distance of carbon atoms, Widmanstätten ferrite laths were formed.
- Diffusivity and diffusion distance calculations and their correlation with grain size shows that the rate of change of stress due to change in strain rate has an influence on

the DT ferrite and its growth, although other factors, including temperature, applied stress, alloying element, etc., can affect as well.

CHAPTER 6

ON THE ROLE OF CHROMIUM IN DYNAMIC TRANSFORMATION OF AUSTENITE

Kanwal Chadha [a], Davood Shahriari [a], C. Jr. Aranas [b],
Louis-Philippe Lapierre-Boire [c], Mohammad Jahazi [a]

[a] Department of Mechanical Engineering, École de Technologie Supérieure,
1100 Notre-Dame West, Montreal, Quebec, Canada H3C 1K3
[b]Department of Mechanical Engineering, University of New Brunswick
Fredericton, NB, E3B 5A3, Canada
[c]Finkl Steel - Sorel, 100 McCarthy, Saint-Joseph-de-Sorel, QC, J3R 3M8, Canada

Manuscript submitted to Journal of Materials Science, (April 2018)

Abstract: The effect of Chromium (Cr) on the dynamic transformation (DT) of austenite to ferrite at temperatures up to 430 °C above Ae_3 was studied in a medium-carbon low-alloy steel. Hot compression tests were performed using Gleeble 3800® thermomechanical simulator followed by microstructural examinations using electron microscopy (FESEM-EBSD). Driving force calculation using austenite flow stress and ferrite yield stress on an inverse absolute temperature graph indicated that Cr increases the driving force for the transformation of austenite to ferrite; however, when the influence of stress and thermodynamic analysis are taken into account, it was observed that Cr increases the barrier energy and therefore, emerges as a barrier to the transformation. An analysis, based on lattice and pipe diffusion theories is presented that quantifies the role of stress on the diffusivity of Cr and is compared with other the main alloying elements such as C, Si and Mn and its impact, positive or negative, on the DT barrier energy. Finally, a comparison is made on the differential effects of temperature and stress on the initiation of DT in medium-carbon low-alloy steels.

Key words: Dynamic transformation, Medium-carbon low-alloy steel, Phase transformation, Stress induced diffusion, As-cast structure.

6.1 Introduction

Generally, the transformation of ferrite at temperatures lower than Ae_3 depends upon various deformation conditions such as deformation temperature, prior austenite grain size, strain rate, precipitates, and so forth. The occurrence of dynamic transformation (DT) of austenite to ferrite at temperatures above Ae_3 was first reported by Yada et al. (Matsumura et Yada, 1987; Yada, Li et Yamagata, 2000) using in-situ X-ray examinations during torsion testing. In recent years, this field has attracted a considerable attention and various research have been reported on DT of austenite to ferrite in steels (Ghosh, Aranas Jr et Jonas, 2016; Park et al., 2013c; Sun et al., 2014), and also on other alloys where deformation-induced transformation from a soft to hard or hard to soft phase occurs (Guo et al.).

To date, several models have been proposed to account for the occurrence of DT above Ae_3 temperatures in steels. Hanlon et al. (Hanlon, Sietsma et Zwaag, 2001) and Ghosh et al. (Ghosh et al., 2013a) reported that increase in Gibbs energy during deformation was responsible for DT, and related it to the stored energy from dislocation generation during deformation. However, it was later observed that transformation was initiated at the critical strain levels of ~0.1, at which the dislocation-based model did not prove significant to justify the description of the phenomenon.

Recently, Aranas et al. (Aranas Jr et Jonas, 2015) proposed that the driving force for the transformation can be calculated from the flow stress difference between the strain hardened austenite and the yield stress of Widmanstätten ferrite. In their model, the chemical free energy difference between austenite and Widmanstätten ferrite, the lattice dilatation work, and shear accommodation work associated with the transformation, were opposing factors to the driving force. On the role of alloying elements, they found that Si increased the driving force, whereas Mn decreased the net driving force. Despite extensive research on effect of alloying element on DT kinetics, the role of Cr on DT as an important alloying element in medium-carbon steels has not been discussed. Moreover, the role of stress on solute mobility has not been fully treated in the existing DT models while, this aspect appears to be of significant importance (K. Chadha, 2018). The present work inscribes in this context and has for main objective to study the effect of Cr on the driving force and barrier energy to DT of austenite to ferrite. The analysis will then be expanded to compare and evaluate the diffusion distance and diffusivity of Cr with other elements such as C, Si and Mn, while considering the stress involved during hot deformation and provide more insight into the driving force and barrier energy theories of DT.

6.2 Materials and methods

The material used for the current investigation was an as-cast medium-carbon low-alloy steel (Labelled as, "HCr (High Chromium) alloy steel"). In order to evaluate the effect of addition of Cr, Low Cr "LCr (Low Chromium) alloy steel" with 0.1 wt. % Cr and remaining alloying elements in same wt. % as HCr alloy steel, was considered. The detailed compositions of both the HCr alloy steel and the LCr alloy steel are shown in Table 6.1. The specimens of HCr alloy steel were provided by Finkl Steel-Sorel Forge, Sorel, Quebec, Canada.

Table 6.1 Composition of *as-cast* medium carbon low alloy steel (wt. %)

Alloy	C	Mn	Si	Mo	Cr	Other
HCr	0.35	0.84	0.41	0.44	1.90	Microalloying
LCr	0.35	0.84	0.41	0.44	0.1	Microalloying

Cylindrical specimens were machined with a diameter of 10 mm and a height of 15 mm. Hot compression tests were conducted based on the ASTM E209 standards with Gleeble 3800® thermomechanical simulator. The samples were heated at 2 °C s^{-1} till 1260 °C and then held 300 s for homogenization. The specimens were then cooled to the deformation temperature (1200 °C or 1150 °C) at the rate of 1 °Cs^{-1} before being compressed to a true strain of 0.8 and strain rate of 1 s^{-1}. They were then water quenched immediately to preserve the deformed microstructure. The Schematic of the thermomechanical cycle is shown in Fig. 6.1.

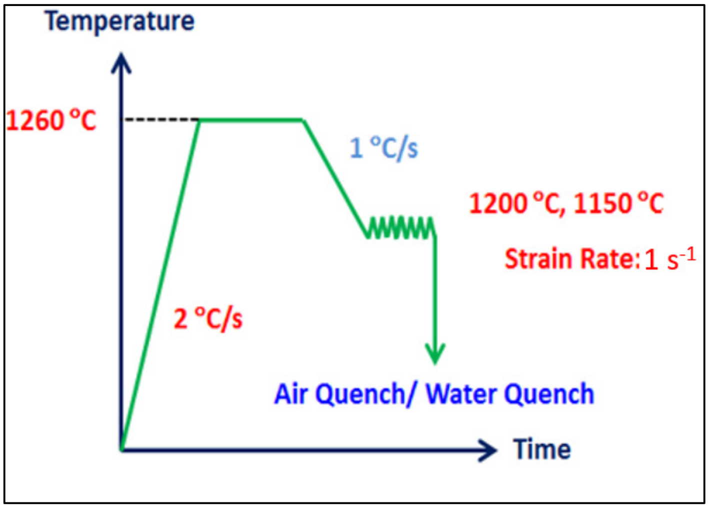

Figure 6.1 Schematic diagram of thermomechanical schedule for hot compression tests of medium-carbon low-alloy steel (HCr)

To reveal the microstructure through Electron Back Scatter Diffraction (EBSD), the samples were polished mechanically using conventional techniques and then electropolished at room temperature using a mixture of Perchloric acid and ethanol (1:9 by volume). The electropolishing was done at 25 V and 15 s. The samples were placed in such a way that compression axis was parallel to the incident electron beam. EBSD characterization was performed with FEG-SEM (Carl Zeiss; Model: Supra 40) using TSL-OIM^{TM} software. Low angle grain boundaries (LAGB's >2°) are illustrated in red and high angle grain boundaries (HAGB's >15°) are shown in black. LCr alloy steel has been considered in order to compare with HCr alloy steel, therefore, predicted results are used for this alloy. To compare the properties of these alloys, JMatPro$^{®}$ Software (Saunders et al., 2003) was used to calculate the flow stress analysis for LCr alloy steel, flow stress *per phase* and thermodynamic calculations for both alloys.

6.3 Results and Discussions

6.3.1 Stress- Strain Curves

The flow stress-strain data obtained after deformation at 1200 °C and 1150 °C and a strain rate of 1 s^{-1} using Gleeble 3800® thermomechanical simulator for HCr alloy steel and predicted results of LCr alloy steel are displayed in Fig. 6.2. The results reveal that the flow stress levels for both alloys increase with a decrease in the deformation temperature. Moreover, it can be seen that the flow stress is higher for HCr alloy steel than that of LCr alloy steel for both deformation temperatures, which indicates that the increase in wt. % of Cr increases the mechanical properties of the alloy. However, all stress-strain curves present a hardening stage followed by a peak stress and then a stress drop of ~3% indicating the occurrence of one or more softening processes in the material e.g., DRX (Chadha et al., 2017a) and DT. The occurrence of DT for HCr alloy steel has already been reported in a previous study (K. Chadha, 2018) and the associated critical strain (~0.1) for the initiation of DT of austenite was determined. The values of the critical strain will be used in the present study for further calculations.

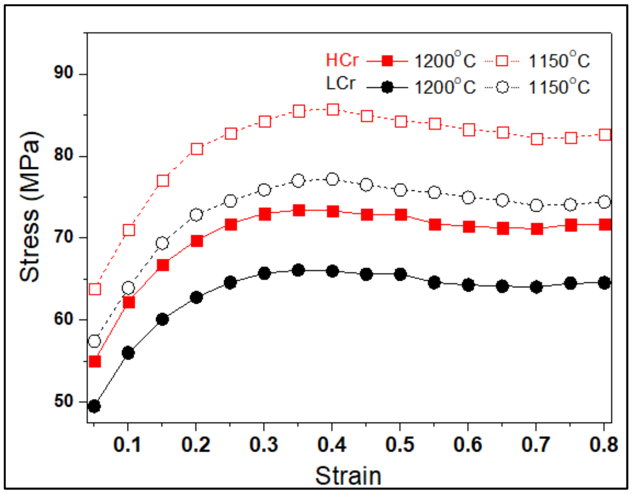

Figure 6.2 Stress-strain curves of medium carbon low-alloy steel during hot isothermal compression at strain rate of 1 s^{-1} at deformation temperatures of 1200 °C and 1150 °C

6.3.2 Net Driving Force for Dynamic Transformation

In the composition of the HCr alloy steel, austenite stabilizers such as Mn, Ni, N and Co (KOSKENNISKA, 2014; Song et al., 2016), which should hinder ferrite formation, and ferrite stabilizers like Si, Mo and Cr (KOSKENNISKA, 2014), which should promote ferrite formation, are present. The effects of Mn and Si on dynamic transformation of austenite was studied by Aranas et al. (Aranas Jr et Jonas, 2015), who reported that Mn as austenite stabilizer significantly increased the driving force as well as the total barrier energy (TBE) for DT, while Si as ferrite stabilizer marginally increased the driving force but significantly reduced the total barrier energy (TBE) for the occurrence of DT. Due to this, the net effect of addition of Mn was found to be smaller as compared to that of Si. Therefore, in order to quantify the impact of Cr on DT, its driving force and contribution to the TBE need to be calculated.

Aranas et al. (Aranas Jr et Jonas, 2015) calculated the driving force by plotting the austenite flow stress and ferrite yield stress against inverse absolute temperature using Wray et al. data (Wray, 1984). In order to compare the chemical free energy difference, the driving force (in MPa) was converted into units of $Jmol^{-1}$ using the conversation factor (1 MPa = 1 MJm^{-3}=7.2 $Jmol^{-1}$) (Ghosh, Aranas Jr et Jonas, 2016). The driving force calculation requires values of austenite flow stress at 0.1 (approximate critical strain for dynamic transformation) and ferrite yield stress at temperatures above Ae_3. Since the yield stress of ferrite cannot be measured experimentally above the Ae_3 temperature as it is in the austenitic region, therefore, in the present investigation, the values of *ferrite yield stress* were predicted using JMat Pro® software flow stress *per phase* analysis tool.

Fig. 6.3 (a & b) shows the graph of austenite flow stress and ferrite yield stress at deformation temperatures of 1200 °C and 1150 °C and strain rate of 1 s^{-1}. The inverse of absolute temperature for HCr alloy steel (Fig. 6.3 (a)) and LCr alloy steel (Fig. 6.3 (b)) are plotted against the stress (MPa). The driving force for the transformation of austenite can be calculated from the diagrams by measuring the vertical distance between austenite flow stress (strain = 0.1) and ferrite yield stress. The results reveal that the increase of Cr content from 0.1 wt. % to 1.9 wt. % increased the driving force marginally by ~6 Jmol^{-1} at 1200 °C and ~3 Jmol^{-1} at 1150 °C, relatively.

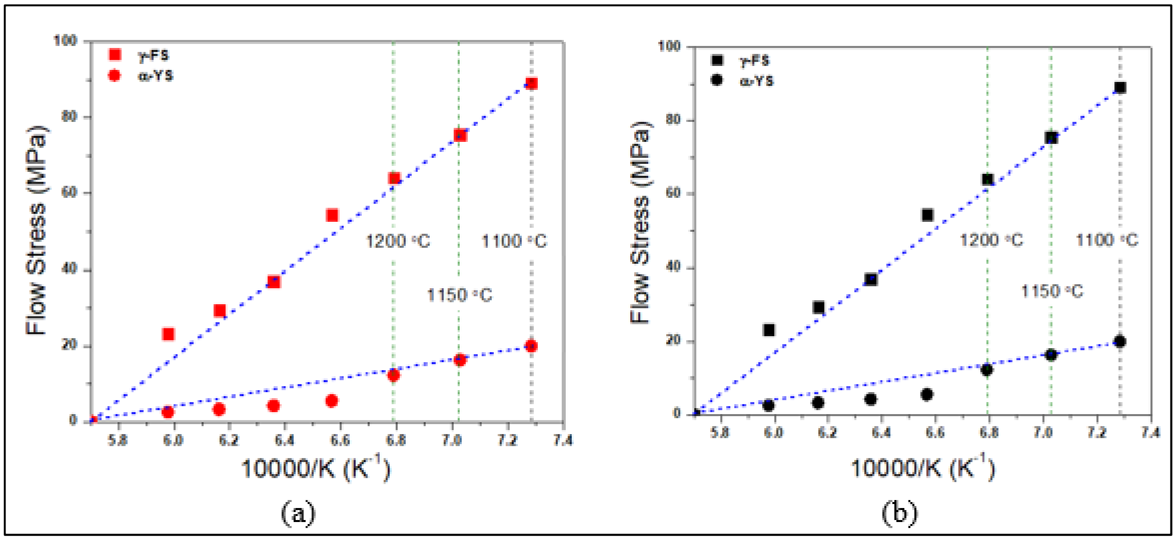

(a) (b)

Figure 6.3 Driving force calculations for (a) HCr alloy steel and (b) LCr alloy steel. The driving force is calculated by subtracting the ferrite yield stress from the austenite flow stress at critical strain of 0.1

There are three types of barrier energies to the transformation of ferrite: 1) work done to accommodate localized shearing during transformation, 2) dilatation work imposed on surrounding austenite by the expansion of lower density ferrite, and 3) chemical free energy between phases ($\Delta G_{\gamma-\alpha}$) (Jonas et Ghosh, 2013). The work consumed in accommodating the process of shearing and the dilatation associated with ferrite formation was evaluated using the austenite flow stress developed at the measured critical strain of 0.1. The shear accommodation work per unit volume w_s was calculated using the following relation (Jonas et Ghosh, 2013):

$$w_s = m \times \sigma_{0.1} \times \gamma \tag{6.1}$$

where, $\gamma = 0.22$, is the shear strain involved in the transformation of austenite to ferrite (Bhadeshia, 2002), and m = 0.5, the Schmid factor at which the grains are most favorably orientated with respect to the applied stress (Aranas Jr et Jonas, 2015). w_s is expressed in the units of Jmol^{-1}.

The dilatation work per unit volume, w_d, was calculated for both alloys in a similar manner as shear accommodation work. The orientation factors for both alloys were assumed to be, λ = $\sqrt{m}$ = 0.707 (for m = 0.5). The factor was calculated for a dilatation strain of 3% using the relation (Jonas et Ghosh, 2013):

$$w_d = \lambda \times \sigma_{0.1} \times 0.03 \tag{6.2}$$

The chemical free energy difference between phases ($\Delta G_{\gamma-\alpha}$) was determined to be maximum at 1090 °C (K. Chadha, 2018). The maxima at 1090 °C indicates that at this temperature, the transformation of austenite to ferrite is most difficult to occur. Chemical free energy difference ($\Delta G_{\gamma-\alpha}$) vs. temperature graph is shown in Fig. 6.4, for both alloys. Since the maxima of the chemical free energy difference was 1090 °C, and to make the graph easier to understand, the values of the temperature in the graph (Fig. 6.4) is shown as deformation temperature minus 1100 °C (I.e. close of 1090°C). It can be seen that, with the addition of 1.9 wt. % Cr, the barrier to transformation increases by ~13.7 Jmol^{-1} at 1200 °C and by 15.1 Jmol^{-1} at 1150 °C. It is also interesting to note that at the maxima, the increase in chemical free energy difference between LCr and HCr has maximum value i.e. 17.35 Jmol^{-1} and this value keeps decreasing (10.21 Jmol^{-1} at 1300 °C) as the temperature nears delta ferrite formation temperature (~1480 °C for both alloy steels). This indicates that, the effect of Cr addition gets reduced as the deformation temperature is increased. The decrease in the values of chemical free energy difference for both alloys with increasing temperature signifies that the barrier to DT is decreased as the deformation temperature nears delta ferrite temperature.

The combined effect of these barriers to the transformation was calculated as the sum of $w_s + w_d + \Delta G_{\gamma-\alpha}$.

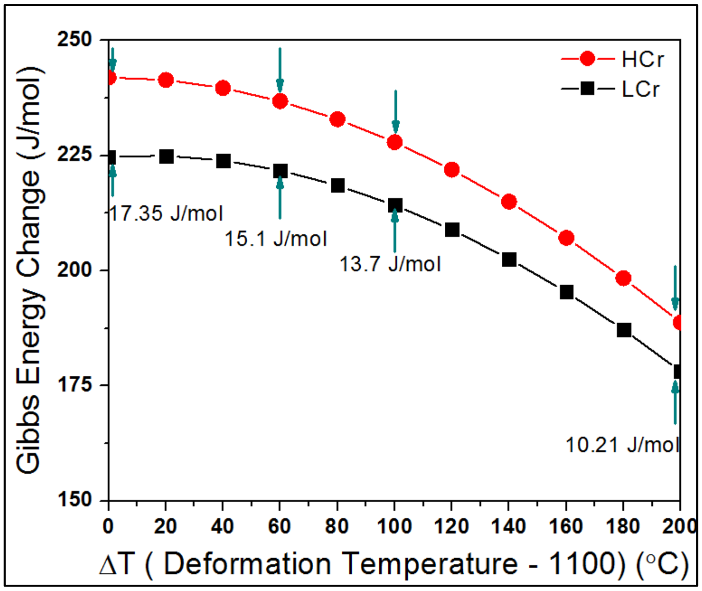

Figure 6.4 $\Delta G_{(\alpha-\gamma)}$ vs ΔT (deformation temperature-1100 °C) for HCr alloy steel and LCr alloy steel, showing the Gibbs energy obstacle opposing dynamic transformation

Driving force data, TBE and net driving force for both alloys, were calculated, and the results are shown in Figs. 6.5 ((a) & (b)), for temperatures of 1200 °C (a) and 1150 °C (b), respectively. It can be seen from Fig. 6.5 (a) that the net driving force at 1200 °C is higher by 15.67 $Jmol^{-1}$ for LCr relative to that of HCr alloy. The decrease in the net driving force at 1200 °C per 1 wt. % Cr is approximately 8.7 $Jmol^{-1}$. As the TBE is relatively low for LCr alloy steel as compared to that of HCr alloy, a higher net driving force was observed, despite of having lower driving force (Fig. 6.3 (b)). Similar trends are observed in Fig. 6.5 (b) (1150 °C) where, the net driving force is higher for LCr alloy steel by 22.19 $Jmol^{-1}$ relative to that of HCr alloy steel. The decrease in the net driving force at 1150 °C per 1 wt. % Cr is approximately 12.3 $Jmol^{-1}$. The results clearly reveal that while the increase in wt. % of Cr increases the driving force marginally, it significantly increases the TBE of the transformation of ferrite, which ultimately leads to reduction in the net driving force. Therefore, it appears that while Cr is a ferrite stabilizer, it finally acts as a barrier to the dynamic transformation of ferrite.

Although the above analysis provides significant information regarding the effect of alloying elements, understanding the underlying mechanisms of their effect on the dynamic transformation kinetics and resulting microstructure is necessary. To do so, diffusion analysis of each element was carried out with respect to strain under the application of the applied stress.

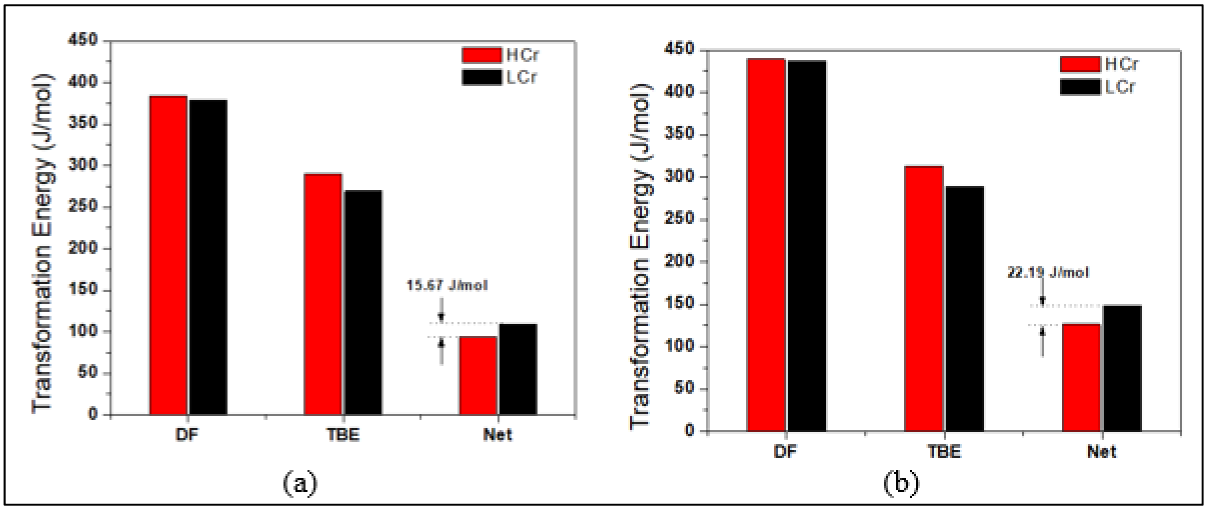

Figure 6.5 Graph depicting the driving force (DF), total barrier energy (TBE) and Net driving force for HCr alloy steel and LCr alloy steel at deformation temperatures of (a) 1200 °C and (b) 1150 °C

6.3.3 Diffusion Analysis of alloying elements

In DT studies on medium-carbon low-alloy steels, it has been reported that carbon diffusivity increases by nearly 8.6 times when the temperature increases from 900°C to 1350°C (Aranas Jr et al., 2015; Grewal et al., 2016; Jr. et al., 2015). However, the studies focussing on this increase consider temperature as the only variable, and do not consider the contribution of stress on the diffusivity of the alloying elements. F. Masoumi et al. calculated the effect of stress on diffusion of Ni in Ni-based superalloy (Masoumi et al., 2017), where it was found that with the application of a compressive stress of about 187.5 MPa, the diffusion of Ni increased by 25 times. Since the application of stress plays a significant role in the diffusion of the alloying elements, therefore, diffusion of Cr and its effect on the phenomenon of DT is studied below.

When analyzing diffusion coefficients, distinction must be made between lattice and pipe diffusion behaviors as they are the two most important mechanisms by which solutes transfer to or away from stacking faults (Viswanathan et al., 2015). Amongst these two, pipe diffusion, is probably the dominant mechanism in the diffusion of solutes (Robinson et Sherby, 1969). The effective diffusion coefficient, given by D_{eff}, can be defined as the sum of the lattice and pipe diffusion by the following equation:

$$D_{eff} = D_L f_L + D_P f_P \tag{6.3}$$

where, D_L and D_P are respectively lattice and pipe diffusion coefficients, f_L and f_P are fraction of atoms participating in the lattice and pipe diffusion processes. f_L is given as unity and $f_P = 7.03125\left(\frac{\sigma}{\mu}\right)^2$ (Samantaray et al., 2011b).

The general expressions for calculating D_L and D_{Peff} ($D_P f_P$) are provided in Table 6.2, equations 6.8 & 6.9. In these equations, b represents burgers vector (m) and μ represents shear modulus (MPa). The equations for obtaining the values of b (eq. 6.4) and μ (eq. 6.6) under applied stress were proposed by Ashby and Frost (Ashby et al., 1978; Frost et Ashby, 1982). It is depicted from the equations that, when there is no stress, there is no pipe diffusion. Table 6.3 shows all the required variables for the calculation of D_L and D_P of Cr, Si and Mn (Andersson et al., 2002a; Béjina et al., 1997; Beswick, Shalders et Swaddle, 1996; Frost et Ashby, 1982; Posner, 2012; Smitll et Hales, 1975; Taniguchi, Hara et Senoo, 2013) where, the diffusivity and diffusion distances calculated using Eqs. 6.8 and 6.9 for these three elements are compared with carbon values obtained from (K. Chadha, 2018). Tingdong (Tingdong, 2003) reported that the variations of lattice diffusion coefficient at a specific temperature could be considered independent of the stress level (i.e. constant). Thus, in this study, only the variations of D_P will be considered for both temperatures.

Table 6.2 Pipe and lattice diffusion equations

$b(\sigma) = b_0 exp\left(-\frac{\sigma}{3K}\right)$	(6.4)
$K(T,\sigma) = K_0\left[1 + \frac{T_M dK}{K_0 dT}\left(\frac{T-300}{T_M}\right)\right] + \frac{\sigma dK}{K_0 d\sigma}$	(6.5)
$\mu(T,\sigma) = \mu_0\left[1 + \frac{T_M dK}{\mu_0 dT}\left(\frac{T-300}{T_M}\right)\right] + \frac{\sigma d\mu}{\mu_0 d\sigma}$	(6.6)
$Q_p = Q_{p0} + \sigma V_p^*$	(6.7)
$D_L = D_{0L} exp\left(-\frac{Q_L}{RT}\right)$	(6.8)
$D_{Peff} = \frac{10}{b^2}\left(\frac{\sigma}{\mu}\right)^2 a_p D_p$	(6.9)
$a_p D_p = a_p D_{0p} exp\left(-\frac{Q_p}{RT}\right)$	(6.10)

In Figs. 6.6 (a-c), the influences of temperature and strain levels on diffusivity due to pipe diffusion (eq. 6.9) are illustrated for the three elements (carbon considered as reference) for HCr alloy steel. It is interesting to note that the diffusivity of Cr is significantly lower than that of Si and Mn at both temperatures by 800 and 200 times, respectively and ~3000 times lower than that of carbon. The results stating lower diffusivity of Cr and Mn as compared to Si corroborates well with the findings that with the addition of Cr (present research) and Mn (Aranas Jr et Jonas, 2015), the barrier energy to DT increased, whereas it decreased with the addition of Si (Aranas Jr et Jonas, 2015).

Table 6.3 Temperature, Pressure Coefficients, and Material Data for Cr, Mn and Si in Medium Carbon Low alloy steel

Parameters	Cr	Mn	Si
Bulk Modulus K_0(MPa) (Andersson et al., 2002b)	1.68×10^5	1.67×10^5	1.68×10^5
Shear Modulus μ_0(MPa)	1.26×10^5	8.1×10^4	6.37×10^4
Pressure Dependence $\frac{d\mu}{d\sigma_s}$	1.5	2.4	1.5
Pressure Dependence $\frac{dK}{d\sigma_s}$ (Frost et Ashby, 1982)	4.5	5.1	5
Temperature Dependence $\frac{T_M dK}{K_0 dT}$ (Andersson et al., 2002b)	-0.62	-0.45	0.51
Temperature Dependence $\frac{T_M d\mu}{\mu_0 dT}$ (Andersson et al., 2002b)	-0.5	-0.25	-0.078
Activation Volume $V_p^* \left(\frac{m^3}{mole}\right)$	5.5×10^{-6}	6.9×10^{-6}	2.2×10^{-6}
Burger's Vector, b_0 (m) (Frost et Ashby, 1982)	2.5×10^{-10}	2.5×10^{-10}	3.83×10^{-10}
Pre-Exponential of pipe diffusion, $a_p D_{0p}$ $\left(\frac{m^4}{s}\right)$	6.9×10^{-24}	10^{-23}	5.27×10^{-19}
Activation energy of pipe diffusion, Q_{p0} $\left(\frac{KJ}{mole}\right)$ (Frost et Ashby, 1982)	203.2	171.6	327.36
Pre-exponential of lattice diffusion D_{0L} $\left(\frac{m^2}{s}\right)$	2.8×10^{-5}	4.03×10^{-5}	0.9
Activation energy of lattice diffusion, Q_L	308	260	496
Melting point, T_M $[K(°C)]$ (Andersson et al., 2002b)	2163	1519	1687

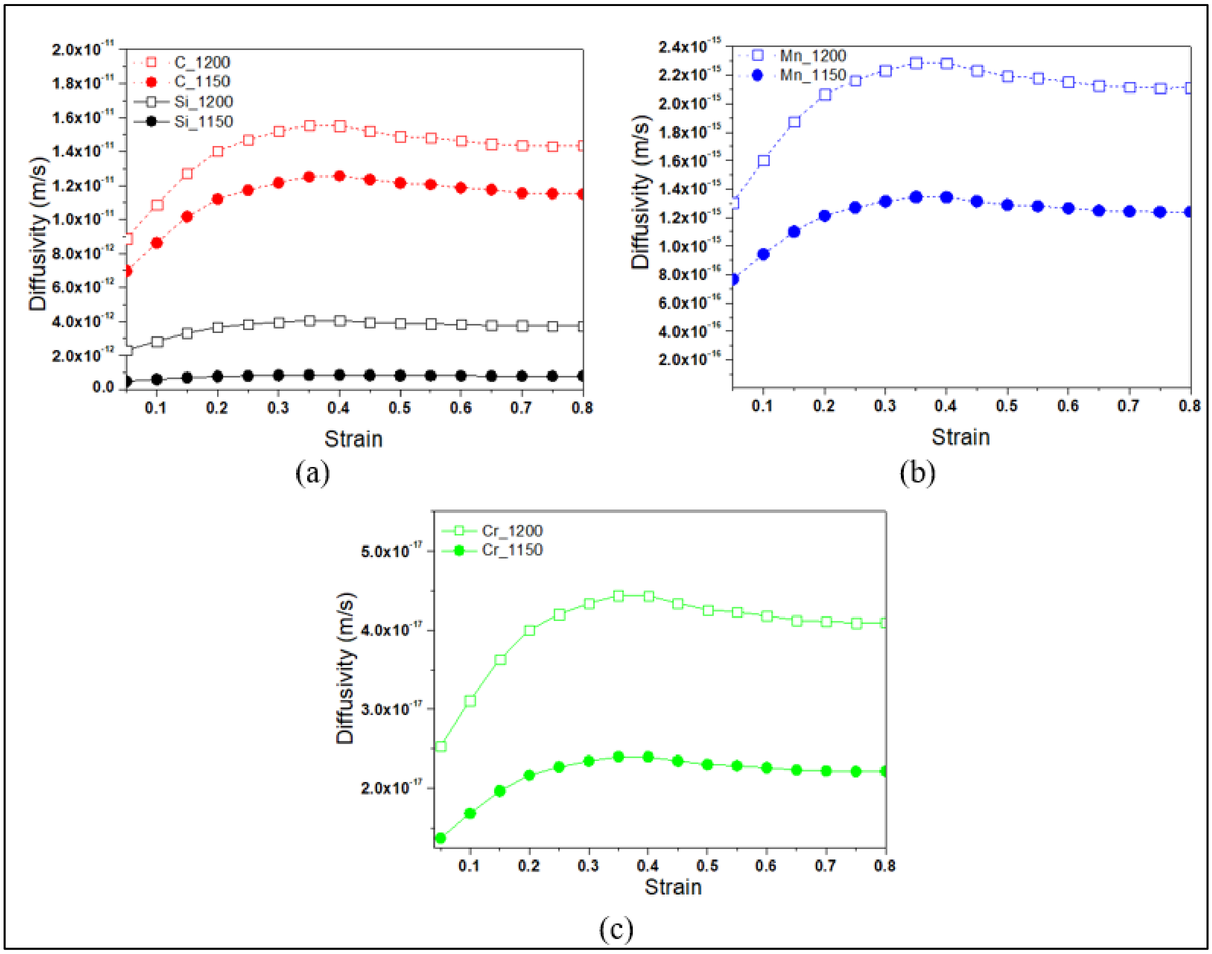

(a)

(b)

(c)

Figure 6.6 Graph depicting diffusivity due to pipe diffusion vs. strain for (a) C and Si, (b) Mn and (c) Cr at deformation temperatures of 1200 °C and 1150 °C for HCr alloy steel

Fig. 6.7 ((a) & (b)) shows the variation of diffusion distance, $x = \sqrt{D_{Peff} \times \frac{\varepsilon}{\dot{\varepsilon}}}$ (m) of Si (a), Cr (b) and Mn (b), atoms due to pipe diffusion at deformation temperatures of 1200 °C and 1150 °C, respectively. It can be seen that the diffusion distance of Cr varies from 1.12 nm (at $\varepsilon = 0.05$) to 5.7 nm ($\varepsilon = 0.8$) at 1200 °C. Upon comparing the diffusion distance at a strain of 0.8, the distance travelled by Cr is ~20 and ~100 times lower than that of Mn and Si, respectively and ~210 times lower than that of carbon atoms. It is clear that such differences in the solute mobility will affect its effectiveness in the overall kinetics of the transformation process. The grain boundary map for HCr alloy steel is shown in Fig. 6.8 for the deformation temperature of 1200 °C and strain rate of 1 s^{-1}, where the maximum average grain size (average grain size of only large grains of the map, marked by red circle) is ~8.1 µm and minimum average grain size (average grain size of small grains of the map, marked as black circle) is ~2.4 µm. The diffusion distance of Cr and Mn is ~400 and ~50 times less than that of the minimum average grain size, whereas diffusion distance of Si is ~1.5 times less that of minimum average grain size. Thus, it can be said that elements such as Cr and Mn would not be able to diffuse out of grains (minimum or maximum average) during transformation, which further confirms that addition of Cr can impede the DT of austenite and the growth of DTed ferrite during further straining due to its sluggish diffusion.

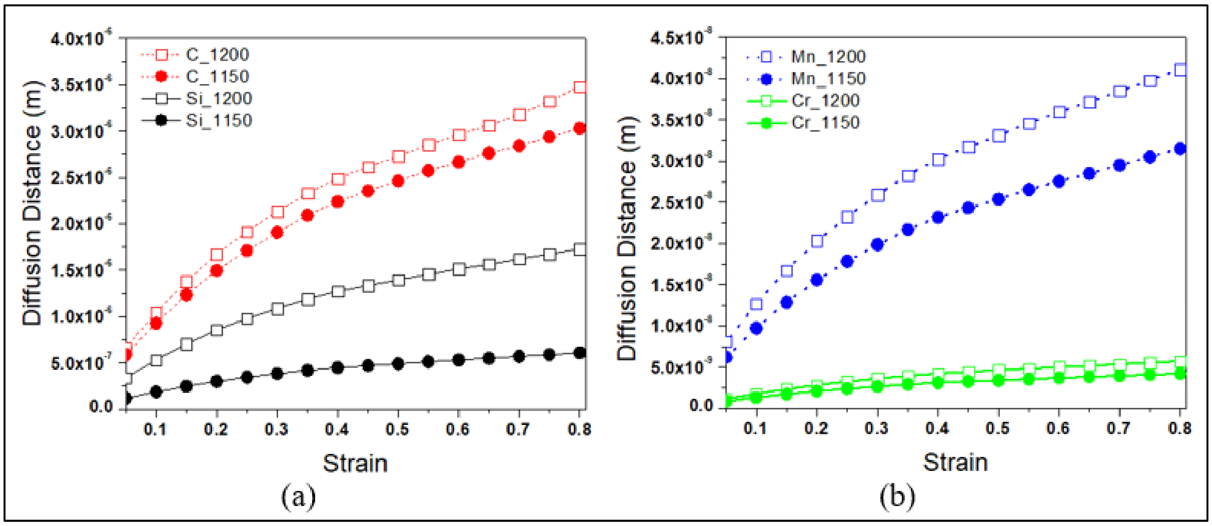

(a) (b)

Figure 6.7 Graph depicting diffusion distance of (a) C and Si and (b) Mn and Cr, vs. strain for deformation temperatures of 1200 ºC and 1150 ºC for HCr alloy steel

The above findings of diffusivity and diffusion distances of various solutes gives a new insight into the analysis of the driving force and barrier energy model for explaining the occurrence of DT. The model predicted that Si promotes the DT (Aranas Jr et Jonas, 2015) whereas Mn (Aranas Jr et Jonas, 2015) and Cr (present study) have a detrimental effect on it. This can be explained by the differences in the diffusivity of these three elements: during transformation, since the diffusivity of Si is high, the Si atoms can much faster diffuse out of the austenite matrix as compared to Cr or Mn atoms.

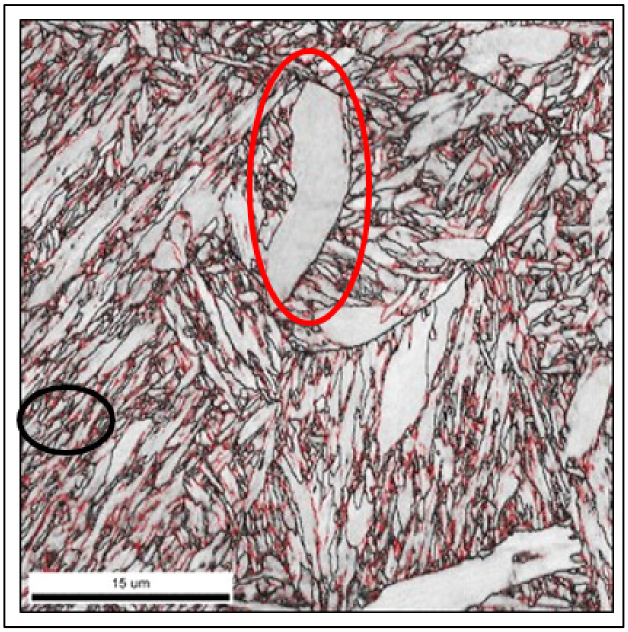

Figure 6.8 EBSD grain boundary map of HCr alloy steel deformed at deformation temperature of 1200 °C and strain rate of 1 s^{-1}. The HAGBs are shown in black and LAGBs are shown in red

The effect of Cr on the initiation of DT can be calculated by calculating the strength of the austenite matrix. The strength can be determined by adding the work done for the dilatation and shear accommodation energy (Work $_{D+SA}$) during the deformation. Work $_{D+SA}$ was calculated using the eqs. (6.1) & (6.2), and then was compared for HCr alloy steel and LCr alloy steel and the results are reported in Fig. 6.9. It can be seen that, Work $_{D+SA}$ for HCr alloy steel is higher by 8.68 $Jmol^{-1}$ and 7.53 $Jmol^{-1}$ at deformation temperatures of 1150 °C and 1200 °C, respectively. This finding signifies that the increase in wt. % of Cr increases the strength of austenite matrix, resulting in a higher austenite flow stress at the strain of 0.1. The higher strength of the austenite matrix impedes the formation of Widmanstätten ferrite, which occurs through shear accommodation and dilatation process (Jonas et Ghosh, 2013).

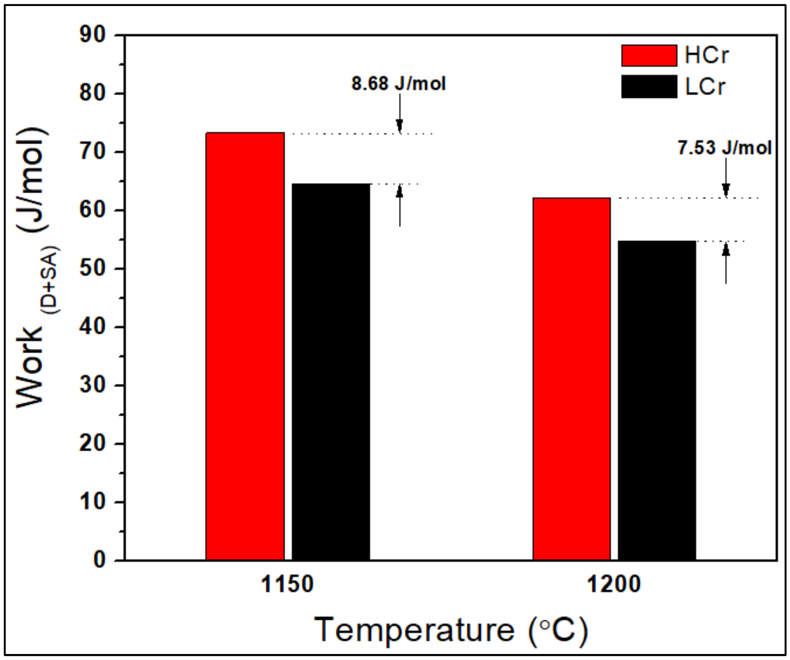

Figure 6.9 Graph depicting effect of addition of Cr on work done by shear accommodation and dilatation of austenite matrix for HCr alloy steel and LCr alloy steel at deformation temperatures of 1200 °C and 1150 °C

The strength of austenite can be correlated with the critical stress and critical strain of the initiation of DT. The critical strain used to calculate Work $_{\text{D+SA}}$ is determined by double differentiation technique (Poliak et Jonas, 1996). It has been reported that the double differentiation technique overestimates the critical stress and strain since it requires the formation of about 5% of the dynamic phase in order for the operation of the softening mechanism to be detectable (Aranas et al., 2017). In order to overcome this barrier, the critical stresses are calculated by the total barrier energy method, which provides exact moment that transformation begins.

The critical stress and strain for the initiation of DT are calculated by total barrier energy method using the following equation:

$$E_{DF} = E_B \tag{6.11}$$

where, E_{DF} is the driving force and E_B is the energy of the barrier to the transformation. By substituting the equations for the driving force and barrier energy (eqs. (6.1) and (6.2)), the above equation can be expressed as:

$$\sigma_c - \sigma_{\beta-YS} = \Delta G_{\gamma-\alpha} + w_s + w_d \tag{6.12}$$

where, σ_c is the critical stress for transformation, $\sigma_{\beta-YS}$ is the yield stress of ferrite as calculated above.

The critical stress calculated by eq. (6.5) was compared with the critical stress calculated by double differentiation equation for LCr alloy steel and HCr alloy steel at deformation temperatures of 1150 °C and 1200 °C (K. Chadha, 2018). It was found that the critical stresses obtained from total barrier energy method (eq. (6.5) and shown in Table 6.4) are significantly less as compared to the ones calculated by double differentiation method. From Table 6.5, it can be observed that the critical stresses for initiation of DT of austenite are lower for LCr alloy steel as compared to that of HCr alloy steel for both temperatures. With the above findings, it is inevitable to conclude that with the increase in Cr the initiation of DT of austenite is delayed.

Table 6.4 Comparison between critical stresses (σ_C) obtained using double differentiation [10]
and the barrier energy method for HCr alloy steel

Temperature	$\sigma_C -$ Double Differentiation	$\sigma_C -$ Barrier Energy
1150 °C	68.21 MPa	59.47 MPa
1200 °C	62.11 MPa	52.20 MPa

Table 6.5 Comparison between critical stresses (σ_C) obtained the barrier energy method for LCr and HCr alloy steels

Temperature	$\sigma_C -$ LCr	$\sigma_C -$ HCr
1150 °C	57.48 MPa	59.47 MPa
1200 °C	50.64 MPa	52.20 MPa

6.4 New Model for Dynamic Transformation

In a study by Ghosh et al. (Ghosh et al., 2013b) on the diffusion analysis of C and Mn during the DT of austenite, it was found that C atoms takes about 100 μs to diffuse a distance of 100 nm, whereas, Mn atoms diffuse a distance of only 0.12 nm in the same period of time. Due to low diffusion distance of substitutional element, it was considered that the DT of austenite was a displacive phenomenon and diffusion (specifically of substitutional elements) does not play any role during the transformation. The diffusion calculations done to calculate the diffusion distances in that study employed only lattice diffusion coefficient parameters and the effect of stress (pipe diffusion) was not considered. In the present study, it was revealed that the diffusion distances for C (1.04×10^{-6} m), Si (0.53×10^{-6} m), Mn (12×10^{-9} m) and Cr (1.7×10^{-9} m) at 100μs ($\varepsilon = 0.1\, and\, \dot{\varepsilon} = 1s^{-1}$, $\frac{\varepsilon}{\dot{\varepsilon}} = 0.1\, s\, or\, 100$ μs) are much greater than those reported by Ghosh et al. (Ghosh et al., 2013b), since the contribution of stress to the diffusional kinetics is taken into consideration. With this finding, it can be said that the DT of austenite to ferrite is not only due to displacive transformation, but also includes diffusion of the alloying elements (e.g. substitutional elements like Si, Mn and Cr) as an additional contribution. The schematic representing the DT phenomenon is shown in Fig. 6.10. During hot deformation at temperatures of 1200 °C and 1150 °C, the austenite matrix (Fig. 10 (a)) composed of interstitial (C) and substitutional (Si, Cr and Mn) alloying elements is deformed by the action of stress. As the stress increases, the atoms of alloying elements like C (interstitial atom) and Si (substitutional atoms) start to diffuse from the austenite matrix, thus making the transformation easier (Fig. 6.10 (b)). However, elements like Cr and Mn (substitutional atoms), which have relatively lower diffusivity, remain in the austenite matrix, and thus make the austenite matrix stronger. This leads to an increase in the barrier energy due to shear accommodation and dilatation (Fig. 6.10 (c)) and thus acts to impede the DT of austenite. After shear accommodation and dilatation, the austenite matrix is converted into Widmanstätten ferrite (Fig. 6.10 (d)) (Jonas et Ghosh, 2013). The nucleation of Widmanstätten ferrite starts from the prior austenite grain boundary (PAGB) (Fig. 6.10 (e)). Due to the effect of stress w.r.t. to strain rate and corresponding diffusion of carbon (schematic adopted from (K. Chadha, 2018)), the Widmanstätten ferrite starts to grow. At slow strain rates, the diffusion distance of C is less w.r.t. the grain size, which results in the formation of Quasi polygonal ferrite (QPF) (Fig. 6.10 (f)), however, at high strain rates, the diffusion distance of carbon is high w.r.t. to the grain size, which results in the formation of Widmanstätten Ferrite with long plates are formed (Fig. 6.10 (g)).

6.5 Conclusions

In the present work, the effect of Cr on the dynamic transformation of austenite was studied for two medium-carbon low-alloy steels. With the driving force model and diffusion analysis the following conclusions were drawn:

1. Increase in the wt. % of Cr from 0.1 to 1.9 wt. % in the alloy increased only marginally the driving force for ferrite formation, whereas, it significantly increased the barrier energy to the transformation, which signifies that the addition of Cr lowers the net driving force for the DT of austenite. The net decrease on the driving force at deformation temperatures of 1200 °C and 1150 °C per 1 wt. % Cr is approximately 8.7 and 12.3 $Jmol^{-1}$, respectively.
2. Diffusion analysis indicated that Cr has the least diffusivity during hot deformation in the austenite matrix and therefore resulting in lower values of diffusion distance as compared to Mn and Si. Due to this, the Cr atoms cannot move out of relatively large grains and thereby, impede DT phenomenon.
3. The lower diffusivity of Cr and Mn atoms result in lower diffusion out of the austenite matrix, thus resulting as barrier to the transformation through shearing and dilatation of austenite as compared to Si, where higher values of diffusivity and diffusion distance make the shearing and dilatation of austenite matrix easier. Slower diffusivity leads to sluggish diffusion of Cr atoms and it causes the austenite matrix to be stronger which eventually impedes DT phenomenon.

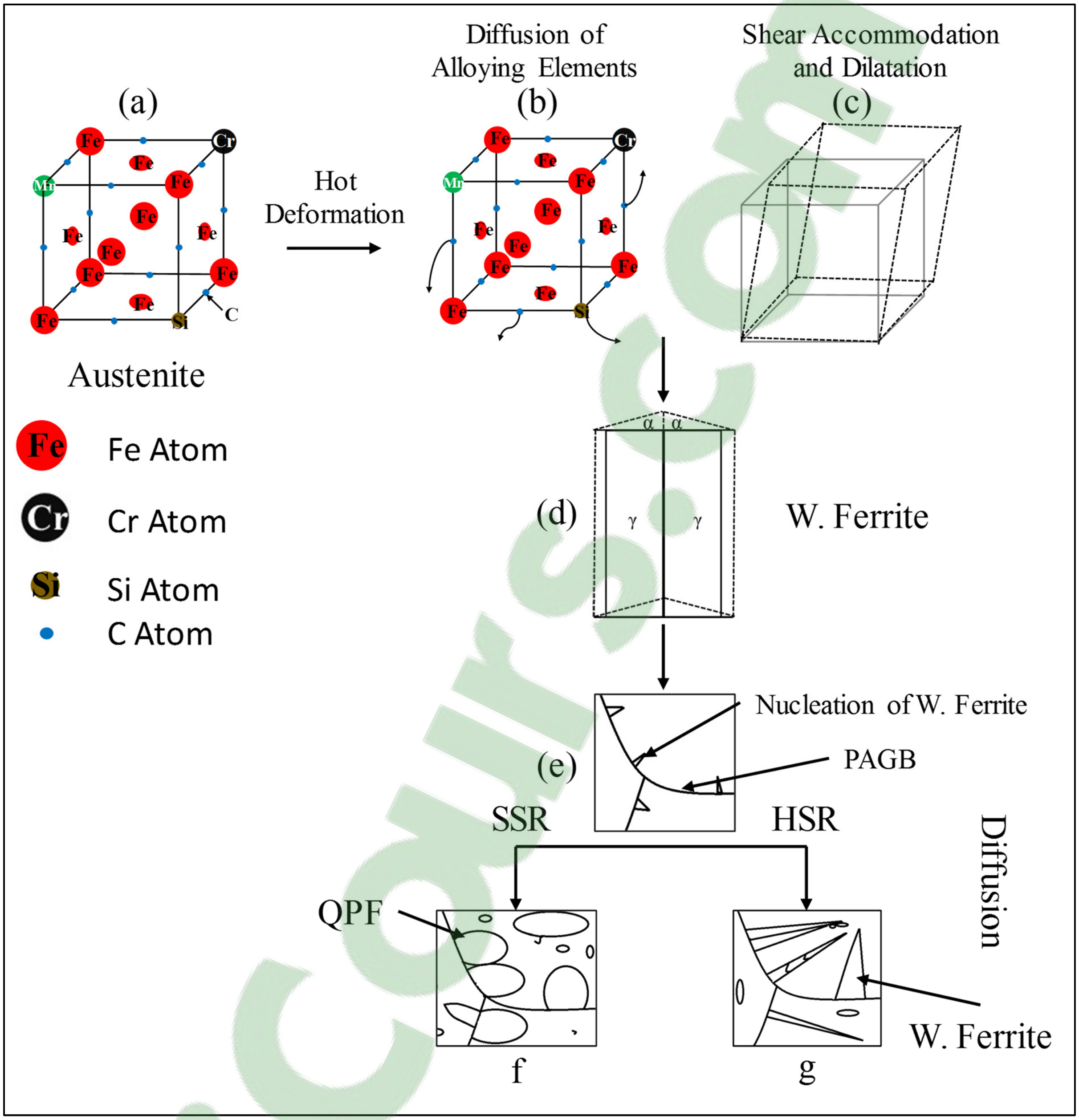

Figure 6.10 Schematic diagram of the DT phenomenon. The austenite matrix (a) when subjected to hot deformation at 1200 °C and 1150 °C, leads to the diffusion of alloying elements like C and Si, whereas, Cr and Mn stay in the matrix due to sluggish diffusivity (b). After shear accommodation and dilatation (c), the austenite matrix is converted into Widmanstätten ferrite (W. Ferrite) (d), which starts to nucleate from prior austenite grain boundary (PAGB) (e). Due to the effect of stress w.r.t. to strain rate, the Widmanstätten ferrite starts to grow and at slow strain rate (SSR) (f), Quasi polygonal ferrite (QPF) and at high strain rate (HSR) (g), Widmanstätten Ferrite (W. Ferrite) are formed

CONCLUSIONS

In the present work, the fundamental softening processes occurring during thermomechanical processing of the as-cast structure of medium carbon low alloy steels was studied using both simulation and experimentation. Enlisted are the compiled conclusions that were drawn from this research:

1. Hot compression of as-cast 42CrMo alloy reveals that at low strain rates, dynamic recrystallization occurs, whereas at high strain rates recovery occurs.
2. It was shown that the Hansel-Spittel model, commonly used for modeling wrought structures, lacks the desired precision and reliability in predicting stress-strain curves of as-cast structures.
3. It was demonstrated that the Arrhenius model, could efficiently predict the flow behavior of *as-cast* medium carbon low alloy steel for various deformation parameters. The influence of strain on material constants (α, n, Q and A) with good correlation and precision was determined using a sixth order polynomial. Therefore, the Arrhenius model would be better suited for the FEM simulation of the process of ingot breakdown of large size ingots.
4. Analysis of flow curves by double differentiation method and microstructural analysis with an EBSD-KAM approach showed the occurrence of DT even in very large grain size materials.
5. Investigation of microstructure evolution by KAM technique showed the influence of processing parameters on dynamically transformed ferrite fraction. High strain rates and low deformation temperature resulted in the reduction in dynamically transformed ferrite fraction.
6. Strain rate has a significant influence on the morphology of the DT ferrite: the higher strain rate shows Widmanstätten morphology, while at a lower strain rate quasi polygonal morphology was formed due to the plate coalescence mechanism. The Coarser microstructure with quasi polygonal morphology at lower strain rates and higher temperature was attributed to carbon diffusion and larger prior austenite grain size.

7. The ferrite fraction was correlated with the diffusion distance of carbon atoms: granular ferrite plates were formed with a higher diffusion distance of carbons atoms, whereas with a lower diffusion distance of carbon atoms, Widmanstätten ferrite laths were formed.
8. Diffusivity and diffusion distance calculations and its correlation with grain size shows that the rate of change of stress due to change in strain rate has significant influence on the DT ferrite and its growth.
9. Addition of Cr in the alloy increased the driving force for the transformation by ~26 J/Mol and ~30 J/Mol for 1200 °C and 1150 °C. The addition of Cr also leads to increase in the barrier energy to transformation by. Therefore, while Cr is a ferrite stabilizer, it actually has a negative impact on dynamic transformation.
10. Diffusion analysis was done for Si, Cr and Mn. It was found that Cr has the least diffusivity followed by Mn during the hot deformation as compared to Si. Similar observation was seen for the diffusion distance of Cr and Mn in comparison to that of Si i.e. Cr has least diffusion distance followed by Mn and Si, thereby, these two elements, namely, Cr and Mn act as a barrier to shearing and dilation of austenite which ultimately results as a barrier to DT phenomenon.

ANNEX I

MODELING METADYNAMIC RECRYSTALLIZATION OF A DIE STEEL DURING INGOT BREAKDOWN PROCESS

Kanwal Chadha, Davood Shahriari, and Mohammad Jahazi

Department of Mechanical Engineering, École de Technologie Supérieure,
1100 Notre-Dame West, Montreal, Quebec, Canada H3C 1K3

Paper published *in Numerical Methods in Industrial Forming Processes*
MATEC Web Conf. Volume 80, 2016

Abstract: Ingot forging processes often consist of several successive deformation steps with high interpass times, during which metadynamic recrystallization (MDRX) occurs. Two-stage isothermal compression tests were carried out at 1150 °C and 1200 °C with strain rates of 0.25-2 s^{-1} and interpass times of 5-25 s. Based on the experimental results, a material model for MDRX is proposed. The constitutive model was implemented in Forge NxT 1.1$^{®}$ software to simulate the multistage compression. Results from the material model are consistent with the numerical analysis and experimental results.

1. Introduction

Forging of ingot after casting process starts with ingot breakdown process which is generally performed at very high temperatures (0.75 of melting point "M_P") so as to breakdown the chemical (macrosegregation) and microstructural structure (as-cast dendritic) inhomogeneity (Dieter, Kuhn et Semiatin, 2003). The forging process usually consists of various deformation passes which includes interpass periods between deformations. During interpass periods, dynamic recovery (McQueen et Jonas, 1975), static recrystallization (Lin, Chen et Zhong, 2008d) and metadynamic recrystallization (Beladi, Cizek et Hodgson, 2011; Gao et al., 2000; Lin, Chen et Zhong, 2009; Zhou et Baker, 1995) may occur. Hot workability is defined as the amount of deformation that a material can undergo without cracking and reach desirable mechanical properties and microstructure at a given temperature and strain rate. It is generally evaluated by various parameters like strain rate, strain, temperature and interpass time. It is therefore a challenging task to determine the optimum thermomechanical route to apply in order to achieve the desired mechanical property keeping in view the microstructural changes and softening mechanisms involved. Kinetic equations are often used to describe the plastic flow properties of metals and alloys. Many research groups have attempted to develop kinetic equations using Avrami equation to describe the flow behavior of various alloys using experimental data (Cho et Yoo, 2001; Elwazri, Essadiqi et Yue, 2004; Lin, Chen et Zhong, 2009; Liu et al., 2013). Despite large efforts being made on the development of kinetic equations for wrought ferrous alloys, little information is available on the flow behavior of as-cast structures at very high temperature (~0.7 M_p) and prolonged interpass times. This corresponds to the ingot breakdown process during which the porosities inherited from solidification are close, macrosegregation levels are reduced and the as-cast structure is converted into a much finer and more isotropic wrought structure. The objective of this study is to investigate the influence of strain rate, temperature and interpass time on compressive deformation characteristics of as-cast 42CrMo using double hit hot compressive tests. Avrami equation describing the relationship of flow stress, strain rate, strain, interpass time and temperature was investigated and used to simulate real time analysis of the ingot breakdown process using FEM analysis.

2. Experimental

The composition of the as-cast 42CrMo high strength steel is shown in Table A I-1. The specimens were provided by Finkl Steel Co., Sorel Tracy, Quebec, Canada. Cylindrical specimens were machined with a diameter of 10mm and a height of 15 mm. Hot compression tests were performed in Gleeble^{TM} 3800 Thermomechanical Simulator at temperatures of 1150 °C and 1200 °C, strain rates of 0.25, 0.5, and 2 s^{-1} and interpass times of 5,15 and 25 s. The heating rate was 2 °C/s till 1260 °C where it was maintained for 300 s so as to get homogenous temperature over the specimen. The specimen was then cooled to a respective deformation temperature at a cooling rate of 1 °C/s. Water quench was done at the end of the deformation so as to freeze the microstructure.

Table A I-6 Composition of as-cast 42CrMo (Wt. %)

C	Mn	Si	Mo	Cr	Ni	Other
0.35	0.84	0.41	0.44	1.90	Added	Microalloying

3. Results and Discussions

3.1 Flow Stress-Strain Curves

For the present report, results from deformation temperature of 1200 °C at a strain rate of 0.25 s^{-1} and interpass times of 5, 15 and 25 s are considered. Stress- strain curve of double hit hot compression tests (Fig. A I-1) reveals that the yield flow stress of the second hit is higher than that of the first hit deformation. It can be seen that in the second hit, the yield flow stress generally decreases with the increase in the interpass time. The results point out a fact that metadynamic softening increases with an increase in the interpass time. It is interesting to note that at interpass time of 25 s, much of the metadynamic softening has taken place and the value of the yield flow stress of the second hit deformation is very close to the yield flow stress of the first hit deformation. This behavior can be explained by the fact that the dislocation density decreases with an increase in the interpass time. This results in low yield flow stress during second hit deformation (Lin, Chen et Zhong, 2009).

3.2 Effect of Temperature on Metadynamic Softening

The metadynamic softening fraction *X* is determined by taking 0.2% offset-stress method. The value of *X* is calculated by:

$$\boldsymbol{X = \frac{\sigma_m - \sigma_2}{\sigma_m - \sigma_1}} \qquad \text{(A I-1)}$$

where σ_m (MPa) is the flow stress at the endpoint in the first hit deformation, σ_1(MPa) and σ_2 (MPa) are the offset yield flow stress for the first and second hit compression respectively.

The effect of temperature at the strain rate of 0.25 s^{-1} is shown in Fig. A I-2. It can be seen that with an increase in temperature, the metadynamic softening fraction increases. For different temperatures (1200 °C and 1150 °C) and interpass time of 15 s, the metadynamic softening fraction values are 69.5% and 57.2%, respectively. This is due to the fact that, increase in the deformation temperature causes an increase in the diffusion of the atoms which make migration of the boundaries easier thereby benefitting the growth of the dynamically formed grains (Liu et al., 2013).

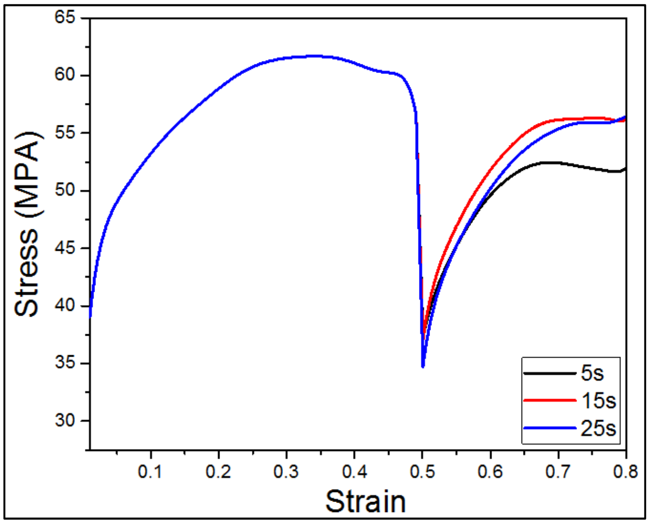

Figure A I-11 Flow stress-strain curves in double hit hot compression at a temperature of 1200 °C and strain rate of 0.25 s^{-1}

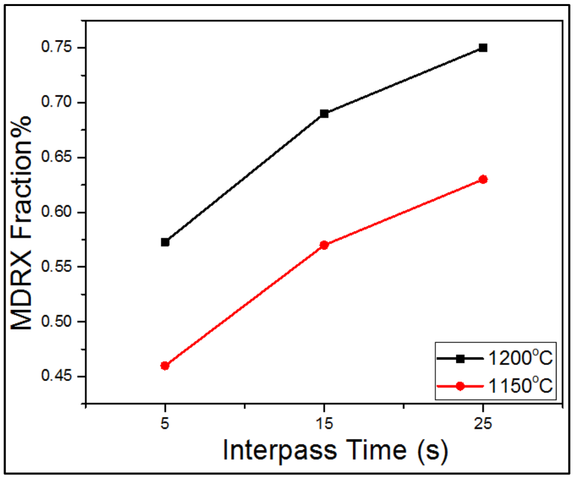

Figure A I-12 Effect of deformation temperature on metadynamic softening

4. Kinetic Equation of Metadynamic Recrystallization

In order to characterize the metadynamic softening behavior of as-cast 42CrMo steels, the Avrami equation is applied. The equation is in the following form:

$$\boldsymbol{X_m = 1 - exp[-0.693\left(\frac{t}{t_{0.5}}\right)^n]} \tag{A I-2}$$

where X_m is the metadynamic softening fraction (%), t is the interpass time (s), n is the material dependent constant, $t_{0.5}$ is the time for metadynamic softening fraction of 50% (s) which is expressed as:

$$\boldsymbol{t_{0.5} = A\dot{\varepsilon}^p exp(\frac{Q_m}{RT})} \tag{A I-3}$$

where, Q_m is the activation energy for metadynamic recrystallization (KJmol^{-1}), T is the absolute deformation temperature (°K), and R is the universal gas constant (Jmol^{-1}°K^{-1}), p and A are the material dependent constants.

The values of $t_{0.5}$ and n in Eq. (A I-2), A, Q_m and p in Eq. (A I-3) were calculated by linear regression method presented in Figs. A I-3 and A I-4 and as described in various published papers (Elwazri, Essadiqi et Yue, 2004; Lin, Chen et Zhong, 2009; Liu et al., 2013).

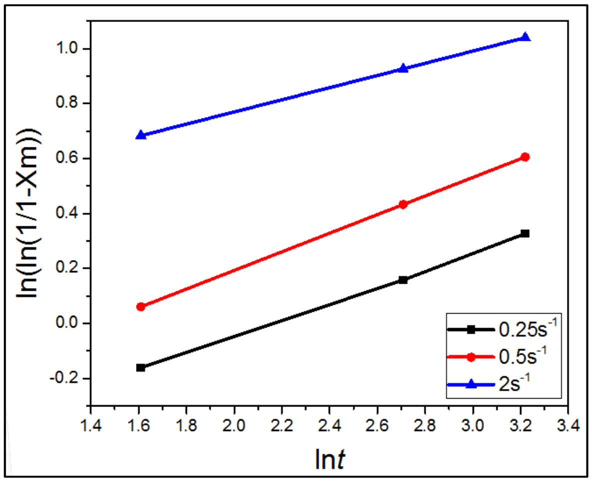

Figure A I-13 Relationship between ln (ln (1/1-*Xm*)) and ln*t* at deformation temperature of 1200 °C

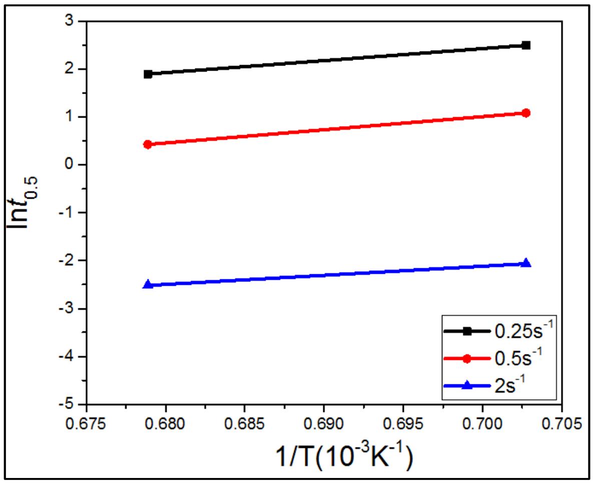

Figure A I-14 Relationship between ln$t_{0.5}$ and 1/T

The values of the constants calculated using linear regression method are shown in Table A I-2.

Table A I-7 Values of constants derived from the regression analysis

n	*Q_m*	*p*	*LnA*
0.27	185853	-0.318	-2.019

The equations of metadynamic softening fraction and the time for 50% softening for as-cast 42CrMo steels are represented as follows:

$$X_m = 1 - exp[-0.693\left(\frac{t}{t_{0.5}}\right)^{0.27}] \qquad \text{(A I-4)}$$

$$t_{0.5} = 0.1328\dot{\varepsilon}^{-0.318}exp(\frac{185853}{RT}) \qquad \text{(A I-5)}$$

The comparison of the experimental and calculated $t_{0.5}$ at various deformation parameters is shown in Fig. A I-5. The calculated results are in good agreement with the experimental results, thereby confirming that the kinetic equation is able to predict the model for metadynamic behavior of as-cast 42CrMo steel.

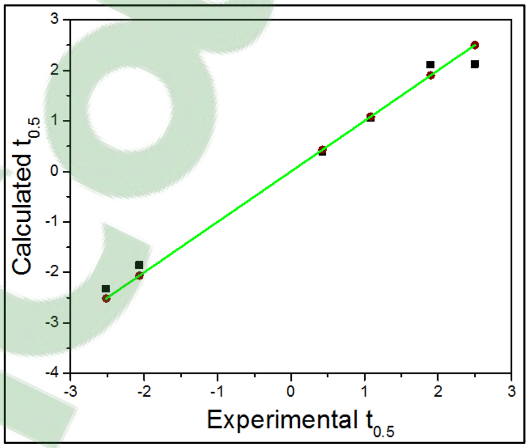

Figure A I-15 The comparison of the calculated and experimental $t_{0.5}$. Green line with brown symbols represent experimental values and black symbols represent calculated values.

5. FEM Simulation for Recrystallization Behavior of 42CrMo

In this study, the Forge NxT 1.1® software is used to carry out FEM simulation of hot compression of cylindrical specimen. An eighth of the 3D model is considered instead of a whole geometry to simulate the hot compression test because of the symmetrical features of the specimen, saving the computational time and getting the sufficient accuracy. The tetrahedral element is used to discrete the geometry model. The upper die moved along the central axis of model while both upper and lower dies are set as a rigid body. The friction coefficient between the dies and the sample is assumed as 0.4. Since the sample is very small and its heating during hot compression by Gleeble™ 3800 is in accordance with the accurate temperature control resistance heating method, an adiabatic heating condition is imposed in this simulation. Physical and thermo-physical properties are critical parameters for any hot deformation simulations. So, the material property data (as a function of temperature) are calculated by JMatPro® and then directly input into the FEM code. The implementation of the flow stress constitutive equations of as-cast 42CrMo steel according to Arrhenius constitutive model (Chadha, Shahriari et Jahazi, 2016) and the recrystallization model in the FEM software are accomplished by user subroutine. Fig. A I-6 ((a) & (b)) represents total recrystallization (RX) fraction under 1200 °C at different strain rate. The recrystallization fractions in the center of the specimen under 1200 °C at strain rate 2 s^{-1} nearly achieve 90%. It can be seen that the recrystallized zone will enlarge as the strain rate reduces.

According to Fig. A I-7, recrystallization region with strain rate 0.25 s^{-1} at 1200 °C in the center is almost complete (100%) and the size of this zone is approximately with a diameter 3 mm and a length of 1.5 mm.

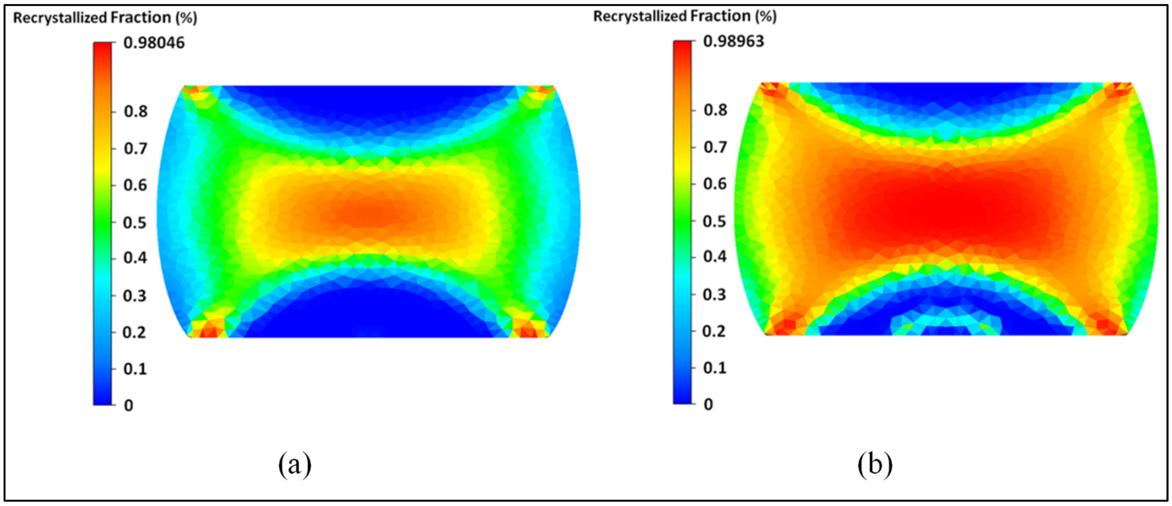

Figure A I-16 FEM simulation results of recrystallization fraction distribution under 1200 °C at the strain rate of (a) 0.25 s^{-1} and (b) 2 s^{-1}

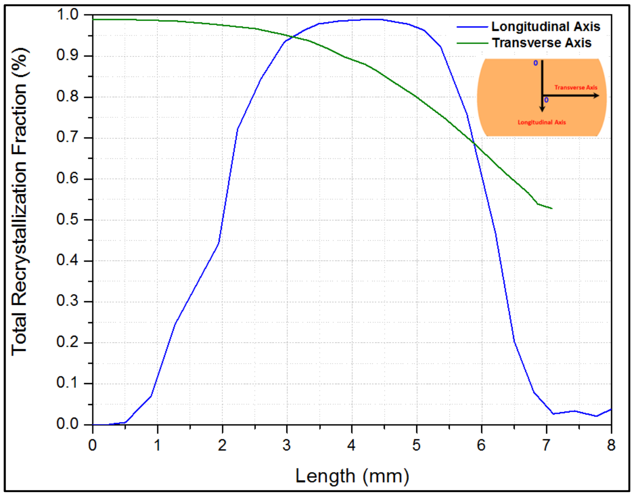

Figure A I-17 Predicted recrystallized region in the deformed specimen under 1200 °C at the strain rate of 0.25 s^{-1}

Total recrystallization volume fraction of as-cast 42CrMo steel by FEM simulation under various strain rates at deformation temperature 1200 °C is illustrated in Fig. A I-8.

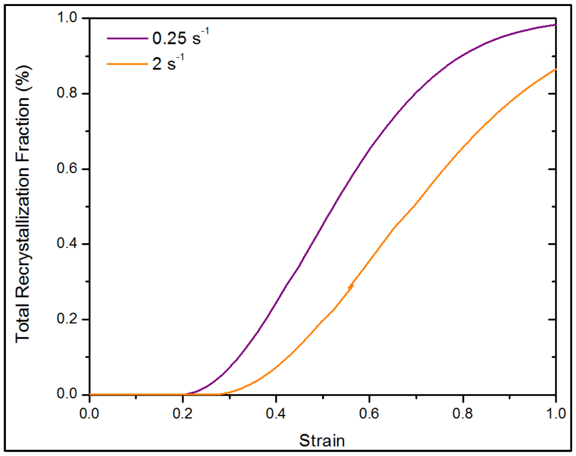

Figure A I-8 Volume fraction of total recrystallization fraction at the center of the deformed sample under 1200 °C at the strain rate of 0.25 s^{-1} and 2 s^{-1}

It shows the total volume fraction of recrystallization increases with the increasing of the strain. It approves at lower strain rate, total RX fraction tends to be complete and close to 100%. The main reason for this phenomenon is that higher strain rates lead to increase work hardening rate and decrease the time for recrystallization. So, the recrystallized nucleus at high strain rate has no enough time to fully grow up. Finally, there is a good agreement between the predicted value by FEM simulation results and the experimental data.

6. Conclusions

Double hit hot compression tests of as-cast 42CrMo steel was conducted using Gleeble^{TM} 3800 Thermomechanical Simulator. Deformation temperature of 1200 °C and 1150 °C, strain rates of 0.25, 0.5 and 2 s^{-1} and interpass times of 5, 15 and 25 s were selected so as to investigate the effect of deformation parameters on metadynamic recrystallization. Using experimental conditions, the Avrami equation was obtained to characterize the metadynamic behavior.

The following are the main conclusions of the research:

a. With an increase in temperature, strain rate and interpass time, the metadynamic softening fraction increased.
b. Maximum metadynamic softening occurs at temperature of 1200 °C at an interpass time of 25 s.
c. Avrami equation developed is in good agreement with the experimental and calculated results.
d. Integrating with the material kinetic models in the Forge NxT 1.1® software is developed to analyze the microstructure evolution under various hot deformation conditions.

APPENDIX A

Arrhenius-type model (Xiao et al., 2012) is used to describe the relationship between flow stress, deformation temperature and strain rate during high temperature deformation. It is given by

$$\dot{\epsilon} \ = AF(\sigma)\exp(-\frac{Q}{RT}) \qquad \text{(A 1)}$$

Generally, $F(\sigma)$ is in the form of power function or exponential function or hyperbolic sine function as listed below:

$$\begin{aligned} F(\sigma) &= \sigma^{n_1} && (\alpha\sigma < 0.8) \\ F(\sigma) &= \exp(\beta\sigma) && (\alpha\sigma > 1.2) \\ F(\sigma) &= [\sinh(\alpha\sigma)]^{n} && (\text{for all } \sigma) \end{aligned} \qquad \text{(A 2)}$$

Where, A, n_1, n, α and β are the material constants, with $\alpha = \beta / n_1$.

In order to find the constants, the value of $F(\sigma)$ is put into Eq. (A 2) which gives the relationship of low-level stress ($\alpha\sigma < 0.8$) and high-level stress ($\alpha\sigma > 1.2$).

$$\begin{aligned} \dot{\varepsilon} &= B\sigma^{n_1} \\ \dot{\varepsilon} &= B' \exp(\beta\sigma) \end{aligned} \qquad \text{(A 3)}$$

B, B' and n_1 are material constants which are independent of deformation temperatures. These constants can be calculated by taking logarithm on both sides of Eq. (A 3).

$$\begin{aligned} \ln\sigma &= \frac{\ln\dot{\varepsilon}}{n_1} - \frac{\ln B}{n_1} \\ \sigma &= \frac{\ln\dot{\varepsilon}}{\beta} - \frac{\ln B'}{\beta} \end{aligned} \qquad \text{(A 4)}$$

Plotting graphs of $ln\sigma$ vs $ln\dot{\varepsilon}$ and σ vs $ln\dot{\varepsilon}$, by the linear regression method gives the values of n_1 and β. The values are calculated using the average values of slope of parallel lines from different temperatures. Putting these values, value of $\alpha = \beta / n_1$ can be found.

In order to calculate the value of Q, logarithm on both sides of Eq. (A 2) of the function is taken for all values of stress and then assuming it as independent of temperature gives,

$$ln[sinh(\alpha\sigma)] = \frac{1}{n} ln\dot{\varepsilon} + \frac{Q}{nRT} - \frac{1}{n} lnA \tag{A 5}$$

$ln\dot{\varepsilon}$ and 1/T are considered as two independent variables. Differentiating the above equation gives,

$$n = \left. \frac{\partial ln\dot{\varepsilon}}{\partial\, ln[sinh(\alpha\sigma)]} \right|_T \tag{A 6}$$

$$Q = nR \left. \frac{\partial\, ln[sinh(\alpha\sigma)]}{\partial\left(\frac{1}{T}\right)} \right|_{\dot{\varepsilon}} \tag{A 7}$$

(T and $\dot{\varepsilon}$ taken as independent variables)

Using these equations, plots of $ln[sinh(\alpha\sigma)]$-$ln\dot{\varepsilon}$ and $ln[sinh(\alpha\sigma)]$-$\left(\frac{1}{T}\right)$ can be generated and subsequently the value of n and Q can be found using regression analysis of experimental results. The value of the constant lnA can be found from the intercept of $\ln[\sinh(\alpha\sigma)]$-$ln\dot{\varepsilon}$ plots.

APPENDIX B

In order to estimate the diffusion distance of carbon using effective, pipe and lattice diffusion parameters (Eq. 5.4), the coefficients used are determined as follows:

$$b(\sigma_s) = b_0 exp\left(-\frac{\sigma_s}{3K}\right) \tag{B 1}$$

$$K(T,\sigma_s) = K_0\left[1+\frac{T_M dK}{K_0 dT}\left(\frac{T-300}{T_M}\right)\right]+\frac{\sigma_s dK}{K_0 d\sigma_s} \tag{B 2}$$

$$\mu(T,\sigma_s) = \mu_0\left[1+\frac{T_M dK}{\mu_0 dT}\left(\frac{T-300}{T_M}\right)\right]+\frac{\sigma_s d\mu}{\mu_0 d\sigma_s} \tag{B 3}$$

$$Q_p = Q_{p0} + \sigma_s V_p^* \tag{B 4}$$

$$D_L = D_{0L} exp\left(-\frac{Q_L}{RT}\right) \tag{B 5}$$

$$D_{Peff} = \frac{10}{b^2}\left(\frac{\sigma_s}{\mu}\right)^2 a_p D_p \tag{B 6}$$

$$a_p D_p = a_p D_{0p} exp\left(-\frac{Q_p}{RT}\right) \tag{B 7}$$

LIST OF BIBLIOGRAPHICAL REFERENCES

Andersson, Jan-Olof, Thomas Helander, Lars Höglund, Pingfang Shi et Bo Sundman. 2002a. « Thermo-Calc & DICTRA, computational tools for materials science ». *Calphad,* vol. 26, nº 2, p. 273-312.

Andersson, Jan Olof, Thomas Helander, Lars Höglund, Pingfang Shi et Bo Sundman. 2002b. « Thermo-Calc & DICTRA, computational tools for materials science ». *Calphad,* vol. 26, nº 2, p. 273-312.

Aranas, Clodualdo, Anes Foul, Baoqi Guo, Ameth Fall, Mohammad Jahazi et John J. Jonas. 2017. « Determination of the critical stress for the initiation of dynamic transformation in commercially pure titanium ». *Scripta Materialia,* vol. 133, p. 83-85.

Aranas Jr, Clodualdo, et John J. Jonas. 2015. « Effect of Mn and Si on the dynamic transformation of austenite above the Ae_3 temperature ». *Acta Materialia,* vol. 82, p. 1-10.

Aranas Jr, Clodualdo, Tuan Nguyen Minh, Rupanjit Grewal et John Joseph Jonas. 2015. « Flow Softening-based Formation of Widmanstätten Ferrite in a 0.06%C Steel Deformed Above the Ae_3 ». *ISIJ International,* vol. 55, nº 1, p. 300-307.

Aranas, Jr Clodualdo, Tong Wang et John Joseph Jonas. 2015. « Effect of Interpass Time on the Dynamic Transformation of a Plain C–Mn and a Nb Microalloyed Steel ». *ISIJ International,* vol. 55, nº 3, p. 647-654.

Ashby, Mo F, RA Verrall, HH Schloessin, EH Rutter, KHG Ashbee, SH White, SAF Murrell et A Kelly. 1978. « Micromechanisms of flow and fracture, and their relevance to the rheology of the upper mantle ». *Philosophical Transactions for the Royal Society of London. Series A, Mathematical and Physical Sciences*, p. 59-95.

Bale, C. W., E. Bélisle, P. Chartrand, S. A. Decterov, G. Eriksson, K. Hack, I. H. Jung, Y. B. Kang, J. Melançon, A. D. Pelton, C. Robelin et S. Petersen. 2009. « FactSage thermochemical software and databases — recent developments ». *Calphad,* vol. 33, nº 2, p. 295-311.

Basabe, Vladimir Vinicio, John Joseph Jonas et Chiradeep Ghosh. 2013. « Formation of Strain-induced Ferrite in Low Carbon Steels at Temperatures Above the Ae_3 ». *ISIJ International,* vol. 53, nº 12, p. 2233-2241.

Béjina, F, P Raterron, J Zhang, O Jaoul et RC Liebermann. 1997. « Activation volume of silicon diffusion in San Carlos olivine ». *Geophysical research letters,* vol. 24, nº 21, p. 2597-2600.

Beladi, Hossein, Pavel Cizek et Peter D Hodgson. 2011. « New insight into the mechanism of metadynamic softening in austenite ». *Acta Materialia,* vol. 59, n° 4, p. 1482-1492.

Beladi, Hossein, GL Kelly, A Shokouhi et PD Hodgson. 2004. « The evolution of ultrafine ferrite formation through dynamic strain-induced transformation ». *Materials Science and Engineering: A,* vol. 371, n° 1-2, p. 343-352.

Beswick, Colin L, Richard D Shalders et Thomas W Swaddle. 1996. « Volume profile for substitution in labile chromium (III) complexes: Reactions of aqueous [Cr (Hedta) OH2] and [Cr (edta)]-with thiocyanate ion ». *Inorganic chemistry,* vol. 35, n° 4, p. 991-994.

Bhadeshia, H. K. D. H. 1985. « Diffusion-controlled growth of ferrite plates in plain-carbon steels ». *Materials Science and Technology,* vol. 1, n° 7, p. 497-504.

Bhadeshia, H. K. D. H. 1987. « Diffusional and displacive transformations ». *Scripta Metallurgica,* vol. 21, n° 8, p. 1017-1022.

Bhadeshia, H.K.D.H. 2010a. « Allotriomorphic Ferrite ». In *http://www.msm.cam.ac.uk/phase-trans/index.html*.

Bhadeshia, H.K.D.H. 2010b. « Widmansatten Ferrite Undergraduate Lecture Notes, http://www.msm.cam.ac.uk/phase-trans/index.html ».

Bhadeshia, HKDH. 2002. « Material factors ». *ASM International, Member/Customer Service Center, Materials Park, OH 44073-0002, USA, 2002.*, p. 3-10.

Bhattacharjee, Pinaki Prasad, M. Zaid, G. D. Sathiaraj et B. Bhadak. 2014. « Evolution of Microstructure and Texture During Warm Rolling of a Duplex Steel ». *Metallurgical and Materials Transactions A,* vol. 45, n° 4, p. 2180-2191.

Brandes, EA, GB Brook et P Paufler. 1993. « Smithells Metals Reference Book. Butterworth-Heinemann Ltd., Oxford, 1992. 1746 Seiten, Preis 150£, ISBN 0-7506-1020-4 ». *Crystal Research and Technology,* vol. 28, n° 4, p. 530-530.

Cai, Ming Hui, Hua Ding et Young Kook Lee. 2011. « Dynamic Strain-Induced Ferrite Transformation during Hot Compression of Low Carbon Si-Mn Steels ». *MATERIALS TRANSACTIONS,* vol. 52, n° 9, p. 1722-1727.

Callister, William D, et David G Rethwisch. 2011. *Materials science and engineering*, 5. John Wiley & Sons NY.

Chadha, K, D Shahriari, R Tremblay, PP Bhattacharjee et M Jahazi. 2017a. « Deformation and recrystallization behavior of the cast structure in large size, high strength steel ingots: experimentation and modeling ». *Metallurgical and Materials Transactions A,* vol. 48, nº 9, p. 4297-4313.

Chadha, K., D. Shahriari et M. Jahazi. 2016. « Constitutive Modelling of Ingot Breakdown Process of Low Alloy Steels ». *La Metallurgia Italiana - International Journal of the Italian Association for Metallurgy,* vol. 4, p. 5-12.

Chadha, K., D. Shahriari, R. Tremblay, P. P. Bhattacharjee et M. Jahazi. 2017b. « Deformation and Recrystallization Behavior of the Cast Structure in Large Size, High Strength Steel Ingots: Experimentation and Modeling ». *Metallurgical and Materials Transactions A,* vol. 48, nº 9, p. 4297-4313.

Chen, Ming-Song, Y. C. Lin et Xue-Song Ma. 2012. « The kinetics of dynamic recrystallization of 42CrMo steel ». *Materials Science and Engineering: A,* vol. 556, p. 260-266.

Cho, Sang-Hyun, et Yeon-Chul Yoo. 2001. « Metadynamic recrystallization of austenitic stainless steel ». *Journal of materials science,* vol. 36, nº 17, p. 4279-4284.

Choi, J. K., D. H. Seo, J. S. Lee, K. K. Um et W. Y. Choo. 2003. « Formation of ultrafine ferrite by strain-induced dynamic transformation in plain low carbon steel ». *ISIJ International,* vol. 43, nº 5, p. 746-754.

Choo, W-Y, K-K Um, J-S Lee, D-H Seo et J-K Choi. 2001. « Enhancement of fine ferrite formation by strain induced dynamic transformation and mechanical properties of fine grained steel ». In *ISUGS 2001: International Symposium on Ultrafine Grained Steels*. p. 2-9.

Cyganek, Z., et M. Tkocz. 2012. « The effect of AZ31 alloy flow stress description on the accuracy of forward extrusion FE simulation results ». *Archives of Metallurgy and Materials,* vol. 57, nº 1, p. 199-204.

DeArdo, Anthony J, GA Ratz et PJ Wray. 1982. *Thermomechanical processing of microalloyed austenite: Proceedings of the International Conference on the Thermomechanical Processing of Microalloyed Austenite*. Metallurgical Society of AIME.

Devadas, C, IV Samarasekera et EB Hawbolt. 1991. « The thermal and metallurgical state of steel strip during hot rolling: Part III. Microstructural evolution ». *Metallurgical Transactions A,* vol. 22, nº 2, p. 335-349.

Dieter, G. E., H. A. Kuhn et S. L. Semiatin. 2003. *Handbook of Workability and Process Design*. Asm International.

Donati, Lorenzo, Antonio Segatori, Mohamad El Mehtedi et Luca Tomesani. 2013. « Grain evolution analysis and experimental validation in the extrusion of 6XXX alloys by use of a lagrangian FE code ». *International Journal of Plasticity,* vol. 46, n^{o} 0, p. 70-81.

Dong, H. 2001. « Ultra-fine grained steels and properties ». In *ISUGS 2001: International Symposium on Ultrafine Grained Steels*. p. 18-25.

Dong, Han, Xin-jun Sun et Y Weng. 2003. « Deformation induced ferrite transformation-phenomena and theory ». *IRON AND STEEL-BEIJING-,* vol. 38, n^{o} 10, p. 56-67.

Dong, Han, et Xinjun Sun. 2005. « Deformation induced ferrite transformation in low carbon steels ». *Current Opinion in Solid State and Materials Science,* vol. 9, n^{o} 6, p. 269-276.

Duan, Xinjian, et Terry Sheppard. 2004. « The influence of the constitutive equation on the simulation of a hot rolling process ». *Journal of Materials Processing Technology,* vol. 150, n^{o} 1–2, p. 100-106.

Eghbali, B. 2010. « Study on the ferrite grain refinement during intercritical deformation of a microalloyed steel ». *Materials Science and Engineering: A,* vol. 527, n^{o} 15, p. 3407-3410.

El Mehtedi, M., F. Musharavati et S. Spigarelli. 2014. « Modelling of the flow behaviour of wrought aluminium alloys at elevated temperatures by a new constitutive equation ». *Materials & Design,* vol. 54, n^{o} 0, p. 869-873.

El Wahabi, Mohamed, Laurent Gavard, Frank Montheillet, JM Cabrera et JM Prado. 2005. « Effect of initial grain size on dynamic recrystallization in high purity austenitic stainless steels ». *Acta materialia,* vol. 53, n^{o} 17, p. 4605-4612.

Elwazri, AM, E Essadiqi et S Yue. 2004. « Kinetics of metadynamic recrystallization in microalloyed hypereutectoid steels ». *ISIJ international,* vol. 44, n^{o} 4, p. 744-752.

Essadiqi, E., et J. J. Jonas. 1988. « Effect of deformation on the austenite-to-ferrite transformation in a plain carbon and two microalloyed steels ». *Metallurgical Transactions A,* vol. 19, n^{o} 3, p. 417-426.

Frost, Harold J, et Michael F Ashby. 1982. *Deformation mechanism maps: the plasticity and creep of metals and ceramics*. Pergamon press.

Gao, F, Y Xu, B Song et K Xia. 2000. « Thermodynamic study of the critical nucleus size for metadynamic recrystallisation ». *Materials Science and Engineering: A,* vol. 277, n^{o} 1, p. 33-37.

Ghosh, Chiradeep, Clodualdo Aranas Jr et John J. Jonas. 2016. « Dynamic transformation of deformed austenite at temperatures above the Ae_3 ». *Progress in Materials Science,* vol. 82, p. 151-233.

Ghosh, Chiradeep, Vladimir V. Basabe et John J. Jonas. 2013. « Determination of the Critical Strains for the Initiation of Dynamic Transformation and Dynamic Recrystallization in Four Steels of Increasing Carbon Contents ». *steel research international,* vol. 84, nº 5, p. 490-494.

Ghosh, Chiradeep, Vladimir V. Basabe et John J. Jonas. 2014. « Thermodynamics of dynamic transformation of hot deformed austenite in four steels of increasing carbon contents ». *Materials Science and Engineering: A,* vol. 591, p. 173-182.

Ghosh, Chiradeep, Vladimir V. Basabe, John J. Jonas, Young-Min Kim, In-Ho Jung et Stephen Yue. 2013a. « The dynamic transformation of deformed austenite at temperatures above the Ae_3 ». *Acta Materialia,* vol. 61, nº 7, p. 2348-2362.

Ghosh, Chiradeep, Vladimir V. Basabe, John J. Jonas, Stephen Yue et Xiang Y. Xiong. 2013b. « Dynamic Transformation Behavior of a Deformed High Carbon Steel at Temperatures Above the Ae₃ ». *ISIJ International,* vol. 53, nº 5, p. 900-908.

Goetz, R. L., et S. L. Semiatin. 2001. « The adiabatic correction factor for deformation heating during the uniaxial compression test ». *Journal of Materials Engineering and Performance,* vol. 10, nº 6, p. 710-717.

Grewal, Rupanjit, Clodualdo Aranas Jr, Kanwal Chadha, Davood Shahriari, Mohammad Jahazi et John J. Jonas. 2016. « Formation of Widmanstätten ferrite at very high temperatures in the austenite phase field ». *Acta Materialia,* vol. 109, p. 23-31.

Guo, Baoqi, SL Semiatin, John J Jonas et Stephen Yue. « Dynamic transformation of Ti–6Al–4V during torsion in the two-phase region ». *Journal of Materials Science*, p. 1-11.

Han, Ying, Guanjun Qiao, JiaPeng Sun et Dening Zou. 2013. « A comparative study on constitutive relationship of as-cast 904L austenitic stainless steel during hot deformation based on Arrhenius-type and artificial neural network models ». *Computational Materials Science,* vol. 67, p. 93-103.

Hanlon, David N., Jilt Sietsma et Sybrand van der Zwaag. 2001. « The Effect of Plastic Deformation of Austenite on the Kinetics of Subsequent Ferrite Formation ». *ISIJ International,* vol. 41, nº 9, p. 1028-1036.

Hansel A, Spittel T. 1978. « Kraft- und Arbeitsbedarf bildsamer Formgeburgsverfahren.Leipzig ». *VEB DeutscherVerlag fur Grundstoffindustrie*.

Hillert, Mats, et John Ågren. 2004. « On the definitions of paraequilibrium and orthoequilibrium ». *Scripta Materialia,* vol. 50, nº 5, p. 697-699.

Hotta, S., T. Murakami, T. Narushima, Y. Iguchi et C. Ouchi. 2005. « Effects of Dynamic Recrystallization on γ Grain Refinement and Improvement of Micro Segregation of As Cast Austenite in 9% Ni Steel ». *ISIJ International,* vol. 45, nº 3, p. 338-346.

« http://nptel.ac.in/courses/113108052/module3/lecture17.pdf ».

http://www.calphad.com/iron-carbon.html.

Hultgren, Axel. 1947. « Isothermal transformation of austenite ». *Transactions of the American Society for Metals,* vol. 39, p. 915-1005.

Humphreys, FJ, et M Hatherly. « Hot Deformation and Dynamic Restoration-Chapter 13 ».

Hurtuk, D.J. (911-917). *Steel Ingot Casting Casting, ASM Handbook.* , 15. ASM International.

Jonas, J. J., C. M. Sellars et W. J. M. Tegart. 1969a. « Strength and structure under hot-working conditions ». *Metallurgical Reviews,* vol. 14, nº 130, p. 1-24.

Jonas, JJ, CM Sellars et WJ McG Tegart. 1969b. « Strength and structure under hot-working conditions ». *Metallurgical Reviews,* vol. 14, nº 1, p. 1-24.

Jonas, John J., et Chiradeep Ghosh. 2013. « Role of mechanical activation in the dynamic transformation of austenite ». *Acta Materialia,* vol. 61, nº 16, p. 6125-6131.

Jonas, John J., Chiradeep Ghosh, Xavier Quelennec et Vladimir V. Basabe. 2013. « The Critical Strain for Dynamic Transformation in Hot Deformed Austenite ». *ISIJ International,* vol. 53, nº 1, p. 145-151.

Jr., Clod Aranas, Rupan Grewal, Kanwal Chadha, D. Shahriari, M. Jahazi et J.J. Jonas. 2015. « Formation of Widmanstätten Ferrite in a C-Mn Steel at Temperatures High in the Austenite Phase Field ». In *Proceedings of the International Conference on Solid-Solid Phase Transformations in Inorganic Materials (PTM 2015).* (Whistler, BC), p. 613-620.

K. Chadha, Z. Ahmed, C. Jr. Aranas, D. Shahriari, M. Jahazi. 2018. « Influence of Strain Rate in Dynamic Transformation of Austenite in an As-Cast Medium Carbon Low Alloy Steel ». *Accepted for Publication in Materialia.*

K.Chadha, D.Shahriari et M. Jahazi. 2015. « An Approach to Develop Hansel-Spittel Constitutive Equation during Ingot Breakdown Operation of Low Alloy Steels ». In *FiMPART*. (Hyderabad, India). Springer.

Veuillez sélectionner un type de document autre que « Generic » afin de faire afficher la référence bibliographique.

Krauss, George. 1999. « Martensite in steel: strength and structure ». *Materials science and engineering: A,* vol. 273, p. 40-57.

Laasraoui, A, et JJ Jonas. 1991. « Prediction of steel flow stresses at high temperatures and strain rates ». *Metallurgical transactions A,* vol. 22, n° 7, p. 1545-1558.

Lesuer, DR, CK Syn, JD Whittenberger, M Carsi, OA Ruano et OD Sherby. 2001. « Creep behavior of Fe–C alloys at high temperatures and high strain rates ». *Materials Science and Engineering: A,* vol. 317, n° 1, p. 101-107.

Levine, H. S., et C. J. MacCallum. 1960. « Grain Boundary and Lattice Diffusion in Polycrystalline Bodies ». *Journal of Applied Physics,* vol. 31, n° 3, p. 595-599.

Li, Hong-Ying, Dong-Dong Wei, Yang-Hua Li et Xiao-Feng Wang. 2012. « Application of artificial neural network and constitutive equations to describe the hot compressive behavior of 28CrMnMoV steel ». *Materials & Design,* vol. 35, p. 557-562.

Li, Yu-fei, Zhen-hong Wang, Lin-ying Zhang, Chao Luo et Xin-chun Lai. 2015. « Arrhenius-type constitutive model and dynamic recrystallization behavior of V–5Cr–5Ti alloy during hot compression ». *Transactions of Nonferrous Metals Society of China,* vol. 25, n° 6, p. 1889-1900.

Lin, Y. C., Ming-Song Chen et Jue Zhong. 2008a. « Constitutive modeling for elevated temperature flow behavior of 42CrMo steel ». *Computational Materials Science,* vol. 42, n° 3, p. 470-477.

Lin, Y. C., Ming-Song Chen et Jue Zhong. 2008b. « Effect of temperature and strain rate on the compressive deformation behavior of 42CrMo steel ». *Journal of Materials Processing Technology,* vol. 205, n° 1–3, p. 308-315.

Lin, Y. C., Ming-Song Chen et Jue Zhong. 2008c. « Prediction of 42CrMo steel flow stress at high temperature and strain rate ». *Mechanics Research Communications,* vol. 35, n° 3, p. 142-150.

Lin, Y. C., Ming-Song Chen et Jue Zhong. 2008d. « Study of static recrystallization kinetics in a low alloy steel ». *Computational Materials Science,* vol. 44, n° 2, p. 316-321.

Lin, Y. C., Ming-Song Chen et Jue Zhong. 2009. « Study of metadynamic recrystallization behaviors in a low alloy steel ». *Journal of Materials Processing Technology,* vol. 209, n° 5, p. 2477-2482.

Lin, Y. C., et Xiao-Min Chen. 2010. « A combined Johnson–Cook and Zerilli–Armstrong model for hot compressed typical high-strength alloy steel ». *Computational Materials Science,* vol. 49, n° 3, p. 628-633.

Lin, Y. C., et Xiao-Min Chen. 2011. « A critical review of experimental results and constitutive descriptions for metals and alloys in hot working ». *Materials & Design,* vol. 32, n° 4, p. 1733-1759.

Lin, Y. C., Kuo-Kuo Li, Hong-Bin Li, Jian Chen, Xiao-Min Chen et Dong-Xu Wen. 2015. « New constitutive model for high-temperature deformation behavior of inconel 718 superalloy ». *Materials & Design,* vol. 74, n° 0, p. 108-118.

Lin, Y. C., et Ge Liu. 2010. « A new mathematical model for predicting flow stress of typical high-strength alloy steel at elevated high temperature ». *Computational Materials Science,* vol. 48, n° 1, p. 54-58.

Lin, Y. C., Chen Ming-Song et Zhong Jue. 2008a. « Constitutive modeling for elevated temperature flow behavior of 42CrMo steel ». *Computational Materials Science,* vol. 42, n° 3, p. 470-7.

Lin, Y. C., Chen Ming-Song et Zhong Jue. 2008b. « Effect of temperature and strain rate on the compressive deformation behavior of 42CrMo steel ». *Journal of Materials Processing Technology,* vol. 205, n° 1-3, p. 308-15.

Lin, Y. C., Chen Ming-Song et Zhong Jue. 2008c. « Prediction of 42CrMo steel flow stress at high temperature and strain rate ». *Mechanics Research Communications,* vol. 35, n° 3, p. 142-50.

Lin, Y. C., et Chen Xiao-Min. 2011. « A critical review of experimental results and constitutive descriptions for metals and alloys in hot working ». *Materials & Design,* vol. 32, n° 4, p. 1733-59.

Lin, YC, Ming-Song Chen et Jue Zhong. 2008e. « Effect of temperature and strain rate on the compressive deformation behavior of 42CrMo steel ». *Journal of materials processing technology,* vol. 205, n° 1-3, p. 308-315.

Lin, Yong-cheng, Ming-song Chen et Jue Zhong. 2008f. « Flow stress behaviors of 42CrMo steel during hot compression ». *Journal of Central South University (Science and Technology),* vol. 39, n° 3, p. 549-53.

Liu, J, YG Liu, H Lin et MQ Li. 2013. « The metadynamic recrystallization in the two-stage isothermal compression of 300M steel ». *Materials Science and Engineering: A,* vol. 565, p. 126-131.

Love, G. R. 1964. « Dislocation pipe diffusion ». *Acta Metallurgica,* vol. 12, n° 6, p. 731-737.

Mahajan, P., L. Fourment et J. L. Chenot. 1998. « Implicit scheme for contact analysis in non-steady state forming ». *Engineering Computations,* vol. 15, n° 7, p. 908-924.

Maidorn, C., et D. Blind. 1985. « Solidification and segregation in heavy forging ingots ». In *Ninth MPA-Seminar on the Safety of the Pressure Boundary of Light Water Reactors, 13-14 Oct. 1983*. (Netherlands), 2 Vol. 84, p. 285-96. Coll. « Nucl. Eng. Des. (Netherlands) ». < http://dx.doi.org/10.1016/0029-5493(85)90199-2 >.

Marchattiwar, A., A. Sarkar, J. K. Chakravartty et B. P. Kashyap. 2013. « Dynamic Recrystallization during Hot Deformation of 304 Austenitic Stainless Steel ». *Journal of Materials Engineering and Performance,* vol. 22, n° 8, p. 2168-75.

Marie, S., R. Ducloux, P. Lasne, J. Barlier et L. Fourment. 2014. « Inverse analysis of forming processes based on FORGE environment ». In *17th Conference of the European Scientific Association on Material Forming, ESAFORM 2014, May 7, 2014 - May 9, 2014*. (Espoo, Finland) Vol. 611-612, p. 1494-1502. Coll. « Key Engineering Materials »: Trans Tech Publications Ltd. < http://dx.doi.org/10.4028/www.scientific.net/KEM.611-612.1494 >.

Masoumi, F., D. Shahriari, M. Jahazi, J. Cormier et B. C. D. Flipo. 2017. « On the Occurrence of Liquation During Linear Friction Welding of Ni-Based Superalloys ». *Metallurgical and Materials Transactions A,* vol. 48, n° 6, p. 2886-2899.

Mataya, M. C., et V. E. Sackschewsky. 1994. « Effect of internal heating during hot compression on the stress-strain behavior of alloy 304L ». *Metallurgical and Materials Transactions A,* vol. 25, n° 12, p. 2737-2752.

Matsumura, Yoshikazu, et Hiroshi Yada. 1987. « Evolution of Ultrafine-grained Ferrite in Hot Successive Deformation ». *Transactions of the Iron and Steel Institute of Japan,* vol. 27, n° 6, p. 492-498.

McQueen, H. J., et J. J. Jonas. 1975. « Recovery and Recrystallization during High Temperature Deformation ». In *Treatise on Materials Science & Technology*, sous la dir. de R.J, Arsenault. Vol. Volume 6, p. 393-493. Elsevier. < http://www.sciencedirect.com/science/article/pii/B9780123418067500143 >.

McQueen, H. J., et N. D. Ryan. 2002. « Constitutive analysis in hot working ». *Materials Science and Engineering: A,* vol. 322, n° 1–2, p. 43-63.

Meyer, L. W., A. Weise et F. Hahn. 1997. « Comparison of constitutive flow curve relations in cold and hot forming ». In *5th International Conference on Mechanical and Physical Behaviour of Materials Under Dynamic Loading, 22-26 Sept. 1997.* (France), C3 Vol. 7, p. 13-20. Coll. « J. Phys. IV, Colloq. (France) »: Editions de Physique.

Montheillet, F, et JJ Jonas. 1996. « Dynamic recrystallization ». *Encyclopedia of applied physics,* vol. 16, p. 205-225.

Moore, JJ, et NA Shah. 1983. « Mechanisms of formation of A-and V-segregation in cast steel ». *International metals reviews,* vol. 28, n° 1, p. 336-356.

Morrison, WB. 1972. « RECRYSTALLIZATION OF A LOW-C STEEL IN THE AUSTENITE RANGE ». *J IRON STEEL INST,* vol. 210, n° 8, p. 618-623.

Nakao, Y, et H Miura. 2011. « Nano-grain evolution in austenitic stainless steel during multi-directional forging ». *Materials Science and Engineering: A,* vol. 528, n° 3, p. 1310-1317.

Oh, S. I., S. L. Semiatin et J. J. Jonas. 1992. « An analysis of the isothermal hot compression test ». *Metallurgical Transactions A,* vol. 23, n° 3, p. 963-975.

Ohmori, Akio, Shiro Torizuka, Kotobu Nagai, Naoshi Koseki et Yasuo Kogo. 2004. « Effect of deformation temperature and strain rate on evolution of ultrafine grained structure through single-pass large-strain warm deformation in a low carbon steel ». *Materials transactions,* vol. 45, n° 7, p. 2224-2231.

Opla, Petr, Ivo Schindler, Toma Petrek, Petr Kawulok, Filip Vanura, Rostislav Kawulok et Stanislav Rusz. 2014. « Hot deformation behaviour of steel C45 at high strains ». In *23rd International Conference on Metallurgy and Materials, METAL 2014, May 21, 2014 - May 23, 2014.* (Brno, Czech republic), p. 383-388. Coll. « METAL 2014 - 23rd International Conference on Metallurgy and Materials, Conference Proceedings »: TANGER Ltd.

Park, N., S. Khamsuk, A. Shibata et N. Tsuji. 2013a. « Effect of austenite grain size on kinetics of dynamic ferrite transformation in low carbon steel ». *Scripta Materialia,* vol. 68, n° 8, p. 611-614.

Park, Nokeun, Sunisa Khamsuk, Akinobu Shibata et Nobuhiro Tsuji. 2013b. « Occurrence of dynamic ferrite transformation in low-carbon steel above Ae_3 ». *Scripta Materialia,* vol. 68, n° 7, p. 538-541.

Park, Nokeun, Akinobu Shibata, Daisuke Terada et Nobuhiro Tsuji. 2013c. « Flow stress analysis for determining the critical condition of dynamic ferrite transformation in 6Ni–0.1C steel ». *Acta Materialia,* vol. 61, n° 1, p. 163-173.

Peng, Wenwen, Weidong Zeng, Qingjiang Wang et Hanqing Yu. 2013. « Comparative study on constitutive relationship of as-cast Ti60 titanium alloy during hot deformation based on Arrhenius-type and artificial neural network models ». *Materials & Design,* vol. 51, p. 95-104.

Pickering, Edward John. 2013. « Macrosegregation in steel ingots: the applicability of modelling and characterisation techniques ». *ISIJ international,* vol. 53, n° 6, p. 935-949.

Poliak, E. I., et J. J. Jonas. 1996. « A one-parameter approach to determining the critical conditions for the initiation of dynamic recrystallization ». *Acta Materialia,* vol. 44, n° 1, p. 127-136.

Poliak, E. I., et J. J. Jonas. 2003a. « Critical strain for dynamic recrystallization in variable strain rate hot deformation ». *ISIJ International,* vol. 43, n° 5, p. 692-700.

Poliak, E. I., et J. J. Jonas. 2003b. « Initiation of dynamic recrystallization in constant strain rate hot deformation ». *ISIJ International,* vol. 43, n° 5, p. 684-691.

Posner, Esther S. 2012. « EXPERIMENTS AND APPLICATIONS OF CHROMIUM DIFFUSION IN SPINEL ». UNIVERSITY OF ARIZONA.

Preston, D. L., D. L. Tonks et D. C. Wallace. 2003. « Model of plastic deformation for extreme loading conditions ». *Journal of Applied Physics,* vol. 93, n° 1, p. 211-20.

Price, M. C., A. T. Kearsley et M. J. Burchell. 2013. « Validation of the Preston–Tonks–Wallace strength model at strain rates approaching ~1011 s−1 for Al-1100, tantalum and copper using hypervelocity impact crater morphologies ». *International Journal of Impact Engineering,* vol. 52, p. 1-10.

Quan, Guo-Zheng, Gui-Sheng Li, Tao Chen, Yi-Xin Wang, Yan-Wei Zhang et Jie Zhou. 2011. « Dynamic recrystallization kinetics of 42CrMo steel during compression at different temperatures and strain rates ». *Materials Science and Engineering: A,* vol. 528, n° 13–14, p. 4643-4651.

Rao, K. P., et E. B. Hawbolt. 1992. « Development of Constitutive Relationships Using Compression Testing of a Medium Carbon Steel ». *Journal of Engineering Materials and Technology,* vol. 114, n° 1, p. 116-123.

Reick, Wolfgang, Michael Pohl et Angelo Fernando Padilha. 1998. « Recrystallization and Related Phenomena. Recrystallization-Transformation Combined Reactions during

Annealing of a Cold Rolled Ferritic-Austenitic Duplex Stainless Steel ». *ISIJ International,* vol. 38, nº 6, p. 567-571.

Ridley, N, et H Stuart. 1970. « Partial molar volumes from high-temperature lattice parameters of iron–carbon austenites ». *Metal Science Journal,* vol. 4, nº 1, p. 219-222.

Robinson, S. L., et O. D. Sherby. 1969. « Mechanical behavior of polycrystalline tungsten at elevated temperature ». *Acta Metallurgica,* vol. 17, nº 2, p. 109-125.

Rojek, J., O. C. Zienkiewicz, E. Oñate et E. Postek. 2001. « Advances in FE explicit formulation for simulation of metalforming processes ». *Journal of Materials Processing Technology,* vol. 119, nº 1–3, p. 41-47.

Rollett, Anthony, FJ Humphreys, Gregory S Rohrer et M Hatherly. 2004. *Recrystallization and related annealing phenomena*. Elsevier.

Sabokpa, O., A. Zarei-Hanzaki, H. R. Abedi et N. Haghdadi. 2012. « Artificial neural network modeling to predict the high temperature flow behavior of an AZ81 magnesium alloy ». *Materials & Design,* vol. 39, p. 390-396.

Sakai, T, MG Akben et JJ Jonas. 1983. « Dynamic recrystallization during the transient deformation of a vanadium microalloyed steel ». *Acta Metallurgica,* vol. 31, nº 4, p. 631-641.

Samantaray, D., S. Mandal et A. K. Bhaduri. 2009. « A comparative study on Johnson Cook, modified Zerilli-Armstrong and Arrhenius-type constitutive models to predict elevated temperature flow behaviour in modified 9Cr-1Mo steel ». *Computational Materials Science,* vol. 47, nº 2, p. 568-76.

Samantaray, Dipti, Sumantra Mandal et A. K. Bhaduri. 2011. « A critical comparison of various data processing methods in simple uni-axial compression testing ». *Materials & Design,* vol. 32, nº 5, p. 2797-2802.

Samantaray, Dipti, C Phaniraj, Sumantra Mandal et AK Bhaduri. 2011a. « Strain dependent rate equation to predict elevated temperature flow behavior of modified 9Cr-1Mo (P91) steel ». *Materials Science and Engineering: A,* vol. 528, nº 3, p. 1071-1077.

Samantaray, Dipti, C. Phaniraj, Sumantra Mandal et A. K. Bhaduri. 2011b. « Strain dependent rate equation to predict elevated temperature flow behavior of modified 9Cr-1Mo (P91) steel ». *Materials Science and Engineering: A,* vol. 528, nº 3, p. 1071-1077.

Saunders, N, UKZ Guo, X Li, AP Miodownik et J-Ph Schillé. 2003. « Using JMatPro to model materials properties and behavior ». *Jom,* vol. 55, nº 12, p. 60-65.

Sauvage, X., et Y. Ivanisenko. 2007. « The role of carbon segregation on nanocrystallisation of pearlitic steels processed by severe plastic deformation ». *Journal of Materials Science,* vol. 42, nº 5, p. 1615-1621.

Schwartz, Adam J., Mukul Kumar, Brent L. Adams et David P. Field. *Electron Backscatter Diffraction in Materials Science: Springer Science 2010*

Semiatin, S. L., D. S. Weaver, P. N. Fagin, M. G. Glavicic, R. L. Goetz, N. D. Frey, R. C. Kramb et M. M. Antony. 2004a. « Deformation and recrystallization behavior during hot working of a coarse-grain, nickel-base superalloy ingot material ». *Metallurgical and Materials Transactions A (Physical Metallurgy and Materials Science),* vol. 35A, nº 2, p. 679-93.

Semiatin, S. L., D. S. Weaver, R. C. Kramb, P. N. Fagin, M. G. Glavicic, R. L. Goetz, N. D. Frey et M. M. Antony. 2004b. « Deformation and recrystallization behavior during hot working of a coarse-grain, nickel-base superalloy ingot material ». *Metallurgical and Materials Transactions A,* vol. 35, nº 2, p. 679-693.

Slooff, F. A., J. Zhou, J. Duszczyk et L. Katgerman. 2007. « Constitutive analysis of wrought magnesium alloy Mg-Al4-Zn1 ». *Scripta Materialia,* vol. 57, nº 8, p. 759-762.

Smitll, A. F., et R. Hales. 1975. « Diffusion of Manganese in Type 316 Austenitic Stainless Steel ». *Metal Science,* vol. 9, nº 1, p. 181-184.

Song, Hyejin, Seok Su Sohn, Jai-Hyun Kwak, Byeong-Joo Lee et Sunghak Lee. 2016. « Effect of Austenite Stability on Microstructural Evolution and Tensile Properties in Intercritically Annealed Medium-Mn Lightweight Steels ». *Metallurgical and Materials Transactions A,* vol. 47, nº 6, p. 2674-2685.

Sun, L., K. Muszka, B. P. Wynne et E. J. Palmiere. 2014. « Effect of strain path on dynamic strain-induced transformation in a microalloyed steel ». *Acta Materialia,* vol. 66, p. 132-149.

Sun, Xinjun, Haiwen Luo, Han Dong, Qingyou Liu et Yuqing Weng. 2008. « Microstructural Evolution and Kinetics for Post-dynamic Transformation in a Plain Low Carbon Steel ». *ISIJ International,* vol. 48, nº 7, p. 994-1000.

Taniguchi, Yoshihiro, Kimihiko Hara et M Senoo. 2013. *High pressure liquids and solutions*. Elsevier.

Tingdong, Xu. 2003. « Creating and destroying vacancies in solids and non-equilibrium grain-boundary segregation ». *Philosophical Magazine,* vol. 83, nº 7, p. 889-899.

Tsuji, N, Y Matsubara et Y Saito. 1997. « Dynamic recrystallization of ferrite in interstitial free steel ». *Scripta materialia,* vol. 37, n° 4.

Viswanathan, G. B., R. Shi, A. Genc, V. A. Vorontsov, L. Kovarik, C. M. F. Rae et M. J. Mills. 2015. « Segregation at stacking faults within the γ′ phase of two Ni-base superalloys following intermediate temperature creep ». *Scripta Materialia,* vol. 94, n° Supplement C, p. 5-8.

Wang, Meng-han, Yu-feng Li, Wen-hao Wang, Jie Zhou et Akihiko Chiba. 2013. « Quantitative analysis of work hardening and dynamic softening behavior of low carbon alloy steel based on the flow stress ». *Materials & Design,* vol. 45, p. 384-392.

Weng, Yuqing. 2003. « Microstructure refinement of structural steel in China ». *ISIJ international,* vol. 43, n° 11, p. 1675-1682.

Wray, P. J. 1984. « HIGH TEMPERATURE PLASTIC-FLOW BEHAVIOR OF MIXTURES OF AUSTENITE, CEMENTITE, FERRITE, AND PEARLITE IN PLAIN-CARBON STEELS ». *Metallurgical transactions. A, Physical metallurgy and materials science,* vol. 15 A, n° 11, p. 2041-2058.

Xiao, X., G. Q. Liu, B. F. Hu, X. Zheng, L. N. Wang, S. J. Chen et A. Ullah. 2012. « A comparative study on Arrhenius-type constitutive equations and artificial neural network model to predict high-temperature deformation behaviour in 12Cr3WV steel ». *Computational Materials Science,* vol. 62, p. 227-234.

Yada H, Matsumura Y, Senuma T. In: Proc of the int conf on martensitic transformation, JIM; 1986. p. 515. « ».

Yada, Hiroshi, Chun Ming Li et Hiroshi Yamagata. 2000. « Dynamic γ→α Transformation during Hot Deformation in Iron–Nickel–Carbon Alloys ». *ISIJ International,* vol. 40, n° 2, p. 200-206.

Yang, Zhongmin, et Ruizhen Wang. 2003. « Formation of ultra-fine grain structure of plain low carbon steel through deformation induced ferrite transformation ». *ISIJ international,* vol. 43, n° 5, p. 761-766.

Ying, Han, Qiao Guanjun, Sun JiaPeng et Zou Dening. 2013. « A comparative study on constitutive relationship of as-cast 904L austenitic stainless steel during hot deformation based on Arrhenius-type and artificial neural network models ». *Computational Materials Science,* vol. 67, p. 93-103.

Yuan-Chun, Huang, Y. C. Lin, Deng Jiao, Liu Ge et Chen Ming-Song. 2014. « Hot tensile deformation behaviors and constitutive model of 42CrMo steel ». *Materials & Design,* vol. 53, p. 349-56.

Yunping, Li, E. Onodera et A. Chiba. 2010. « Friction Coefficient in Hot Compression of Cylindrical Sample ». *Materials Transactions,* vol. 51, n° 7, p. 1210-15.

ZHANG, Tong-bo, SHEN Yong, LIU Pan, Qi-long YONG et Yao-zong BAO. 2013. « New type austenite dynamic recrystallization of microalloyed forging steels 38MnVS during forging process ». *Journal of Iron and Steel Research, International,* vol. 20, n° 5, p. 57-60.

Zhao, Lijia, Nokeun Park, Yanzhong Tian, Akinobu Shibata et Nobuhiro Tsuji. 2016. « Combination of dynamic transformation and dynamic recrystallization for realizing ultrafine-grained steels with superior mechanical properties ». *Scientific Reports,* vol. 6, p. 39127.

Zheng, Chengwu, Namin Xiao, Luhan Hao, Dianzhong Li et Yiyi Li. 2009. « Numerical simulation of dynamic strain-induced austenite–ferrite transformation in a low carbon steel ». *Acta Materialia,* vol. 57, n° 10, p. 2956-2968.

Zhou, LX, et TN Baker. 1995. « Effects on dynamic and metadynamic recrystallization on microstructures of wrought IN-718 due to hot deformation ». *Materials Science and Engineering: A,* vol. 196, n° 1, p. 89-95.